NUCLEAR INSTRUMENTS & METHODS

A JOURNAL ON ACCELERATORS, INSTRUMENTATION
AND TECHNIQUES IN NUCLEAR PHYSICS

EDITOR: K. SIEGBAHN - UPPSALA

VOLUME 12

JUNE 1961 — JULY 1961

NORTH-HOLLAND PUBLISHING COMPANY — AMSTERDAM

PRINTED IN THE NETHERLANDS
DRUKKERIJ MEIJER N.V. - WORMERVEER AND AMSTERDAM

64-06911

NUCLEAR INSTRUMENTS AND METHODS

Per.
QC
786
N883
v. 12-13

EDITORIAL BOARD:

J. B. ADAMS (CERN)
F. A. ALSINA (Buenos Aires)
E. AMALDI (Rome)
H. L. ANDERSON (Chicago)
K. T. BAINBRIDGE (Cambridge, Mass.)
P. R. BELL (Oak Ridge)
R. E. BELL (Montreal)
A. BERTHELOT (Saclay)
H. BRINKMAN (Groningen)
E. H. COOKE–YARBOROUGH (Harwell)
S. DE BENEDETTI (Pittsburgh)
M. DE HEMPTINNE (Louvain)
A. DE-SHALIT (Rehovoth)
M. DEUTSCH (Cambridge, Mass.)
S. DU TOIT (Pretoria)
B. S. DŽELEPOV (Leningrad)
W. GENTNER (Heidelberg)
P. C. GUGELOT (Amsterdam)
H. HALBAN (Paris)
O. HAXEL (Heidelberg)
P. HUBER (Basel)
S. KIKUCHI (Tokyo)
J. KOCH (Copenhagen)
M. S. KOZODAEV (Moscow)
S. LIVINGSTON (Cambridge, Mass.)
E. M. MCMILLAN (Berkeley)
M. G. MEŠČERJAKOV (Moscow)
P. B. MOON (Birmingham)
M. L. OLIPHANT (Canberra)
W. PAUL (Bonn)
A. S. RAO (Bombay)
G. SALVINI (Rome)
P. SAVIĆ (Belgrade)
P. SCHERRER (Zürich)
CH. SCHMELZER (CERN)
R. TANGEN (Oslo)
D. TAYLOR (Northampton)
V. I. VEKSLER (Moscow)
G. VON DARDEL (CERN)
O. WERNHOLM (Stockholm)
R. R. WILSON (Cornell)
S. D. WINTER (Saclay)

JUNE 1961 VOLUME 12 (1961) No. 1

GREGG M. SINCLAIR LIBRARY
UNIVERSITY OF HAWAII
D-7-63

NUCLEAR INSTRUMENTS & METHODS

A JOURNAL ON ACCELERATORS, INSTRUMENTATION AND TECHNIQUES IN NUCLEAR PHYSICS

EDITOR: K. SIEGBAHN - UPPSALA

CONTENTS

STANLEY C. BAKER, QUENTIN A. KERNS, FREDERICK A. KIRSTEN, DICK A. MACK and THOMAS A. NUNAMAKER, Test routines and monitoring for a large counter experiment 1

STANLEY C. BAKER, FREDERICK A. KIRSTEN, DICK A. MACK and CLYDE WIEGAND, An electronic data-acquisition system for use with a complex nuclear physics experiment. . . . 11

STANLEY C. BAKER, A transistor coincidence-discriminator circuit for 10^{-8}-second pulses 20

ARTHUR E. BJERKE, QUENTIN A. KERNS and THOMAS A. NUNAMAKER, A solid-state chronotron for digitizing time delays 25

QUENTIN A. KERNS and GERALD C. COX, A triggered nanosecond light source 32

FRANK EVANS and FREDERICK A. KIRSTEN, An 1800-bit buffer store and readout system. . 39

ARPAD BARNA, J. HOWARD MARSHALL and MATTHEW SANDS, A multifold coincidence-veto circuit using transistors 43

JACK H. ELLIOTT, Thick junction radiation detectors made by ion drift 60

J. BENVENISTE, R. BOOTH and A. C. MITCHELL, Observations on the response of two p–n junction diodes to protons 67

R. M. BRUGGER and J. E. EVANS, MTR phased chopper velocity selector. 75

R. E. HOLLAND, The design of bunching magnets 103

HERBERT L. ANDERSON, Alpha particle thickness gauge using a solid state detector 111

C. D. ZERBY, A. MEYER and R. B. MURRAY, Intrinsic line broadening in NaI(Tl) gamma-ray spectrometers 115

F. F. LIU and F. J. LOEFFLER, Transistorized linear gate for photomultiplier pulses . . . 124

THOMAS A. RABSON, Utilization of tunnel diodes in fast trigger circuits 127

S. MARGULIES and J. R. EHRMAN, Transmission and line broadening of resonance radiation incident on a resonance absorber 131

F. TINTA, N. MARTALOGU, R. DUMITRESCU and T. MAGDA, On the natural pulsing of cyclotron external beams in the nanosecond range . . 138

ROLF NORDHAGEN, Simple scheme for using the selective storage of a multichannel pulse height analyser in coincidence counting . . 151

A. PAULIN, Betriebszustände des Mikrotrons mit geteiltem Magnet (racetrack microtron) 155

W. L. RAUTENBACH, Experimental verification of the space charge law ($I = k(e/m)^{\frac{1}{2}}V^{\frac{3}{2}}$) for ion beams from a plasma ion source 169

M. A. MEYER, J. A. M. DE VILLIERS and A. J. VAN DER WALT, Hodoscope system for experiments on the scattering of cosmic ray mumesons. Part III – Theory of the hodoscope 180

ZIEMOWID SUJKOWSKI, Adaptation of a $\pi\sqrt{2}$ beta-ray spectrometer for coincidence experiments 187

A. H. F. MUGGLETON and F. A. HOWE, The preparation of thin ^{18}O targets 192

G. J. F. LEGGE, A stable 0.1 % beam current integrator for the range 0.1 to 20 μA . . . 195

Letters to the Editor

E. BROOKS SHERA, Further comments on accidental coincidences in fast-slow coincidence systems 198

R. E. BELL, Higher order events in coincidence counting 199

R. EVANGELISTI and G. SACERDOTI, Proposal for a storage ring for relativistic charged particles 201

Book Reviews 203

NORTH-HOLLAND PUBLISHING COMPANY — AMSTERDAM

NUCLEAR INSTRUMENTS AND METHODS

A journal on accelerators, instrumentation and techniques in nuclear physics

EDITOR: K. SIEGBAHN, UPPSALA

EDITORIAL BOARD:

J. B. ADAMS (CERN)
F. A. ALSINA (Buenos Aires)
E. AMALDI (Rome)
H. L. ANDERSON (Chicago)
K. T. BAINBRIDGE (Cambridge Mass.)
P. R. BELL (Oak Ridge)
R. E. BELL (Montreal)
A. BERTHELOT (Saclay)
H. BRINKMAN (Groningen)
E. H. COOKE-YARBOROUGH (Harwell)
S. DE BENEDETTI (Pittsburgh)
M. DE HEMPTINNE (Louvain)
A. DE-SHALIT (Rehovoth)
M. DEUTSCH (Cambridge Mass.)
S. DU TOIT (Pretoria)
B. S. DŽELEPOV (Leningrad)
W. GENTNER (Heidelberg)
P. C. GUGELOT (Amsterdam)
H. HALBAN (Paris)
O. HAXEL (Heidelberg)
P. HUBER (Basel)
S. KIKUCHI (Tokyo)
J. KOCH (Copenhagen)
M. S. KOZODAEV (Moscow)
S. LIVINGSTON (Cambridge Mass.)
E. M. MCMILLAN (Berkeley)
M. G. MEŠČERJAKOW (Moscow)
P. B. MOON (Birmingham)
M. L. OLIPHANT (Canberra)
W. PAUL (Bonn)
A. S. RAO (Bombay)
G. SALVINI (Rome)
P. SAVIĆ (Belgrade)
P. SCHERRER (Zürich)
CH. SCHMELZER (CERN)
R. TANGEN (Oslo)
D. TAYLOR (Northampton)
V. I. VEKSLER (Moscow)
G. VON DARDEL (CERN)
O. WERNHOLM (Stockholm)
R. R. WILSON (Cornell)
S. D. WINTER (Saclay)

INSTRUCTIONS FOR CONTRIBUTORS

Contributions may be sent to the Editor, Professor K. Siegbahn, Institute of Physics, University of Uppsala, Sweden, either directly or through the intermediation of one of the members of the Editorial Board. Contributions may be written in English, French or German but should always, except for very short papers, be supplied with a brief abstract in English. Figures should be in inked original drawings or glossy prints and they should be sufficiently large. Contributors should make sure that important details in drawings and photographs will show up clearly in the diminished copy used by the publisher.

Books for review should be sent to Professor Siegbahn.

Objective and descriptive material on endeavours and product developments from the industry for the section "Spotlight on Industry" should be sent directly to the publishers, North-Holland Publishing Company, P.O. Box 103, Amsterdam.

Nuclear Instruments and Methods is published monthly. The subscription price of a volume of 360 pages is $ 17.00 (130 s), postage free.

Subscriptions should be sent to the publishers, North-Holland Publishing Company, P.O. Box 103, Amsterdam, or to any subscription-agent.

No part of this issue may be reproduced in any form, by print, photoprint, microfilm or any other means without written permission from the publisher.

Tracerlab

Low Background Beta Counting System

omni/guard

- **BACKGROUND LESS THAN 0.3 CPM**
- **1″ OR 2″ SAMPLES**
- **MANUAL OR AUTOMATIC SYSTEMS**

Guaranteed ultra low background, *guaranteed* high efficiency counting, compact shielding, automatic or manual operation, a choice of sample sizes . . . all these advantages are combined in the new Omni/Guard System from Tracerlab. This new system utilizes the very latest Tracerlab instruments . . . the new Multi/Matic Sample Changer, the Omni/Guard Anti-Coincidence Flow Counter and the new Omni/Guard Scaler. Each is the most advanced in its field. Small wonder the new Tracerlab Omni/Guard System outperforms all other low background Beta counting systems.

With the new Tracerlab Omni/Guard System it is possible to assay solid beta samples *with counting rates of less than 1 c.p.m.* You'll get superb counting efficiency (even for low energy beta rays, C^{14}, S^{35} etc.) because of the ultra thin Mono/Mol Windows of the Omni/Guard Flow Counter (<125 $\mu g/cm^2$). Very low background coupled with high counting efficiency means less starting material is needed, lower activity levels can be measured and counting time is substantially reduced. Yet the new Tracerlab Omni/Guard System is moderately priced and economical to operate and maintain.

The Tracerlab Omni/Guard System may be combined with a variety of standard readouts; Tracer/Matic timers; Time and Count printers and Time, Count and Count Per Minute printers.

By extending the range of detection sensitivity further than ever before the new Tracerlab Omni/Guard System opens a new era of instrumental analysis. You should have complete information on this latest Tracerlab development. *Write for Tracerlab Omni/Guard Bulletin*

Tracerlab

Tracerlab Keleket

1601 Trapelo Road, Waltham 54, Massachusetts
2030 Wright Avenue, Richmond 3, California

VISIT TRACERLAB BOOTHS 22 and 23, HEALTH PHYSICS SHOW, JUNE 13—16, RIVIERA HOTEL, LAS VEGAS

"In addition to omni/guard see the newest developments in effluent systems."

NON-OVERLOADING

LINEAR PULSE AMPLIFIER NE 5202 of the Fairstein type.

Designed for scintillation spectrometry and pulse height analysis studies, this new wide band amplifier features high gain, high gain stability, good linearity, low noise, excellent non-overloading characteristics, and operation at high duty cycles. Based on a double delay line differentiated system, it consists of three high gain feedback groups and a white cathode follower output. Premium tubes and the highest workmanship are used throughout.

Check these data;

Overload performance: Fastest recovery of any available amplifier (5 microseconds for 100 times overload).
Maximum Voltage Gain: 50,000.
Gain Control Range: 1,200: 1 with coarse & fine controls.
Gain Drift: Better than 0.25% per week with stabilised supply
Gain Stability: Better than 1% for 10% change in mains voltage.

Input noise rms:	40 microvolts
Output voltage:	± 100 volts
Output rise time:	0.2 microseconds
Output pulse width:	1.2 microseconds
Integral linearity:	0.15%
Output impedence:	17 ohms

Also available, the following companion units:

Pre-amplifier and cathode follower NE 5202A; Single-channel pulse height selector NE 5102; Highly stabilised EHT supply NE 5302; Scanning Scintillation spectrometer NE 8601; Ratemeter NE 5401; Complete assembly for C14 and H3 counting.

Write for Bulletins and New Illustrated Price List

Nuclear Enterprises (G.B.) Ltd.

BANKHEAD MEDWAY, SIGHTHILL, EDINBURGH, 11, SCOTLAND - TEL.: CRA 5262

Associate Company: Nuclear Enterprises Ltd., 550 Berry Street, Winnipeg 21, Canada.

ndh 709

NORTH-HOLLAND BOOKS

Imperfections in Crystals

by H. G. VAN BUEREN, *Philips Laboratories, Eindhoven*

CONTENTS

Part I: General properties of lattice imperfections

Part II: Imperfections in metals

Part III: Imperfections in non-metallic crystals

XVIII + 675 PAGES, NUMEROUS PHOTOGRAPHS - GUILDERS 55.— (10S.)

ASK YOUR BOOKSELLER OR:

NORTH-HOLLAND PUBLISHING COMPANY - AMSTERDAM

SOLE DISTRIBUTION IN U.S.A.: INTERSCIENCE PUBLISHERS INC. - NEW YORK

he first portable, "desk-top" 400-channel pulse height analyzer

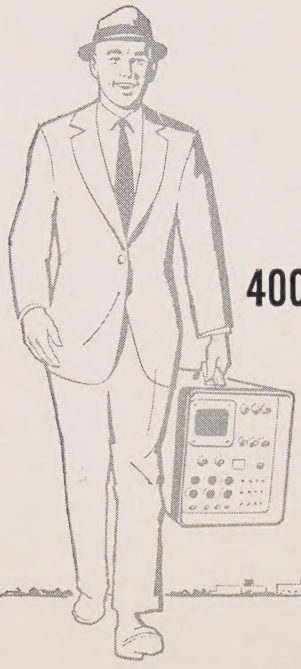

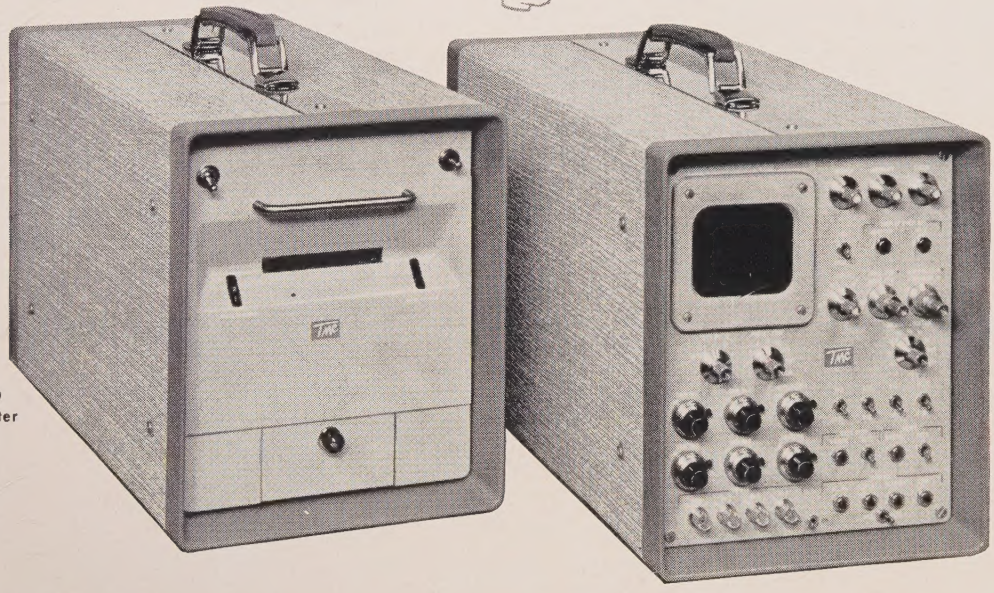

Model 500
decimal printer

Model 404
pulse height analyzer

— the TMC Model 404

ne new TMC Model 404 is the most portable pulse ight analyzer you can own. Take it and use it anywhere. ith its all-transistor, printed circuitry and 400-channel emory in a package just over a cubic foot, this analyzer small enough to operate on your desk. *All* the instruents needed for an experiment can be carried easily by e person.

ne Model 404 has a magnetic core memory that can be used in sub-groups of two or four; four separate inputs and associated amplifiers; internal pulse routing circuitry pushbutton data transfer and display overlap; very low power requirements and many "system" advantages. And it can be used with the new solid state detectors.

For readout, use its companion unit, the Model 500 Decimal Printer; a high speed paper tape punch; strip chart or X-Y recorders; or an IBM electric typewriter.

LITERATURE ON REQUEST

TMC TECHNICAL MEASUREMENT CORPORATION

441 WASHINGTON AVENUE NORTH HAVEN, CONNECTICUT

High accuracy
Maximum flexibility

FEATURED BY

200-Channel Pulse Height Analyzer-mod. C31-CISE

- spectrum storage in 200 channels; 16 bits per channel ferrite memory
- independent spectrum storage in two sets of 100 channels (100′ and 100″)
- spectrum storage of the input pulses in either undelayed or delayed coincidence with other external pulses
- simultaneous storage of two independent spectra, one in the first and the other in the second 100 channel set, by using optional mixer
- spectrum storage in the first 100 channel set with automatic transfer in the second 100 channel set of the pulses coincident with other external driving pulses
- three dimensional-coincident energy spectra with 10 × 20 channel memory subgrouping
- optional possibility to store ten spectra of 20 channels each, shifting from one spectrum to the following in a time sequence triggered by an external programmer
- optional possibility to connect, in place of the normal pulse height to time input Converter, a time-of-flight unit for neutron spectrography
- optional possibility to obtain the automatic programming of device's operation by using an external programmer
- 0.5% linearity through 60 V range
- 1/3 channel per day maximum drift
- Dead Time:
variable:
$20 + 0.5\ N + T\ \mu$ sec, where:
N = channel number
T = rise time protection (μ sec);
fixed: $120 + T\ \mu$ sec
- simultaneous oscilloscope display
- optional strip-chart recorder
- printing performed by a modified « Olivetti Lexicon » electrical typewriter

BEFORE YOU DECIDE contact our technical staff

LABEN Laboratori Elettronici e Nucleari S.r.l.
MILANO - VIA AMADEO 41 - TELEFONO 712494/95

AEI INSTRUMENTATION INFORMATION SERVICE

Transistorized....
4-5 litre ionization chamber
AEI GAMMA MONITORS

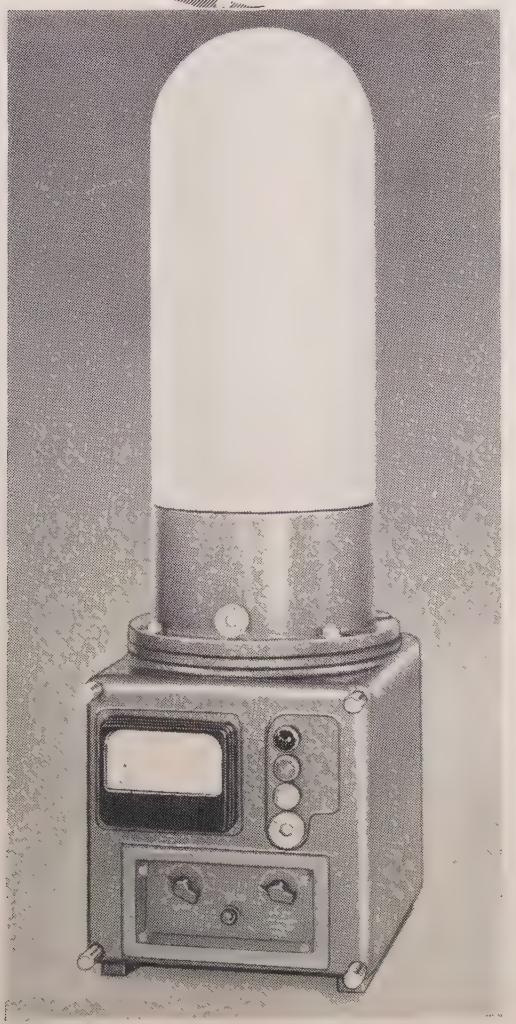

Designed for area radiation monitoring, the type GM2 logarithmic gamma monitor has a 5-decode scale with a maximum sensitivity of 100μ R/hr. The large and sensitive ionization chamber is filled with argon/air to ensure optimum flatness of gamma energy response. Circuitry is transistorized apart from the electrometer input stage which is used as a cathode follower feeding directly into a negative feedback amplifier to obtain maximum stability. An instrument failure alarm is incorporated and over-rides the trips to prevent spurious radiation alarms. Also available as a linear monitor type GM1.

Full details of types GM1 and GM2 monitors are given in Publication 2454-1 available from
AEI Instrumentation Division,
Process Control Department,
P.O. Box One, Harlow, Essex.

◀ GM2 logarithmic gamma monitor with ion chamber mounted on the splash proof case ; it can also be mounted remotely.

AEI | **Instrumentation Division**
Associated Electrical Industries Limited

SC/136

CDC's PROVEN PERFORMANCE

100-CHANNEL PULSE HEIGHT ANALYZER

CHALK RIVER KICKSORTER

Manufactured by Computing Devices of Canada, Limited, from specifications prepared by Atomic Energy of Canada, Limited.

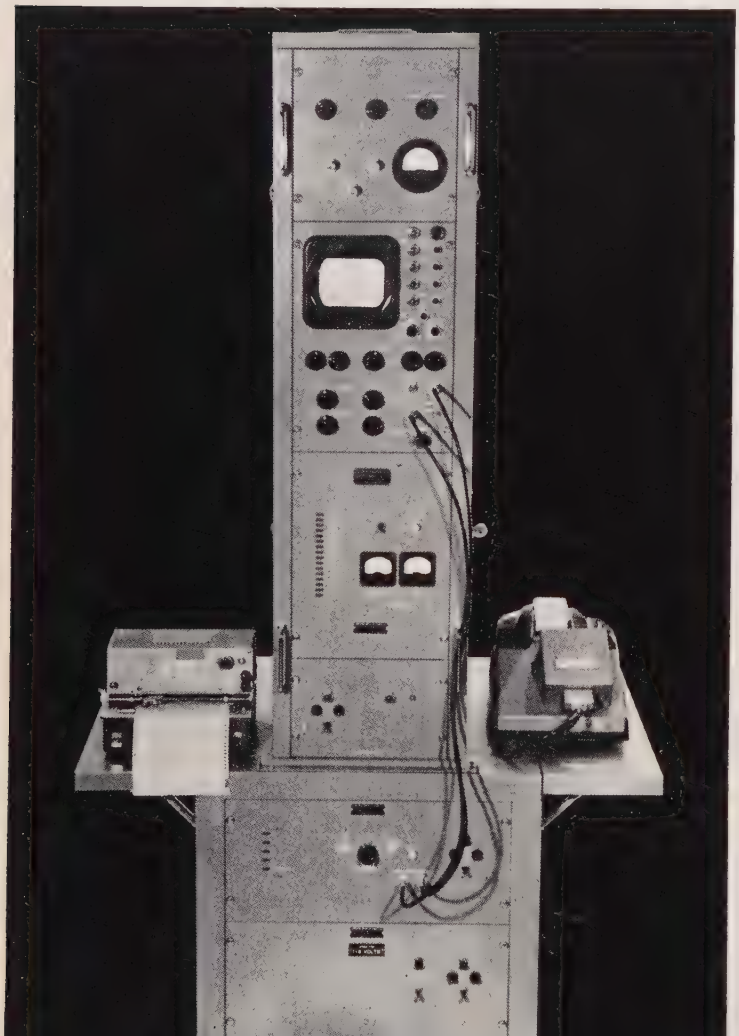

The convenience and speed of automatic printout can be obtained by adding a Decimal Scaler, a Print Control Unit, and an Electric Printer as accessories, shown with the Kicksorter. Provision is also made in the circuitry for the addition of a Pen Recorder for more accurate analog output.

88% TRANSISTORIZED

- Printed Circuitry
- Low Maintenance—High Reliability
- Low Power Consumption—120 Watts
- No Ventilation or Cooling Problems

VERSATILE DATA PRESENTATION

- Oscilloscope Display
- Binary Manual count readout allows the count on any channel to be displayed in digital form.
- Magnetic Core Memory—65,535 counts can be stored per channel.
- Permanent Count Storage—sixteen magnetic cores for each of the 100 channels.
- Highly Versatile—can be modified to accommodate most applications which require additional features.

The Chalk River "Kicksorter" is designed to span random pulses of various amplitudes and shapes, sort them according to amplitude into 100 channels, and store a record of the counted pulses in a magnetic core memory. This computer, with its magnetic core memory and versatile data display system, makes it possible to observe the pulse amplitude spectrum as it accumulates or after it has accumulated.

In addition to its wide use in gamma spectroscopy, the "kicksorter" has many applications in medical research, neutron time-of-flight studies, radioactive fallout studies, shielding studies, oil well and uranium logging, neutron activation analyses, measuring of radioactivity in humans, and other areas.

The analyzer is designed so that information accumulated may be displayed or read out in various ways. Data may be observed on the oscilloscope, or information already accumulated in the memory core may be displayed on the screen, plotted on a strip chart recorder, or printed out in decimal form on an automatic printer.

For additional information, wire or write to:

Bendix International

DIVISION OF THE BENDIX CORPORATION
205 East 42nd Street
New York 17, N. Y., U.S.A.
Cable Address: "Bendixint"

Sales Representative for Great Britain

NUCLEAR ENTERPRISES (G.B.) LTD.

BANKHEAD MEDWAY, SIGHTHILL,
EDINBURGH 11, SCOTLAND

SALES AND SERVICE AVAILABLE THROUGHOUT THE WORLD

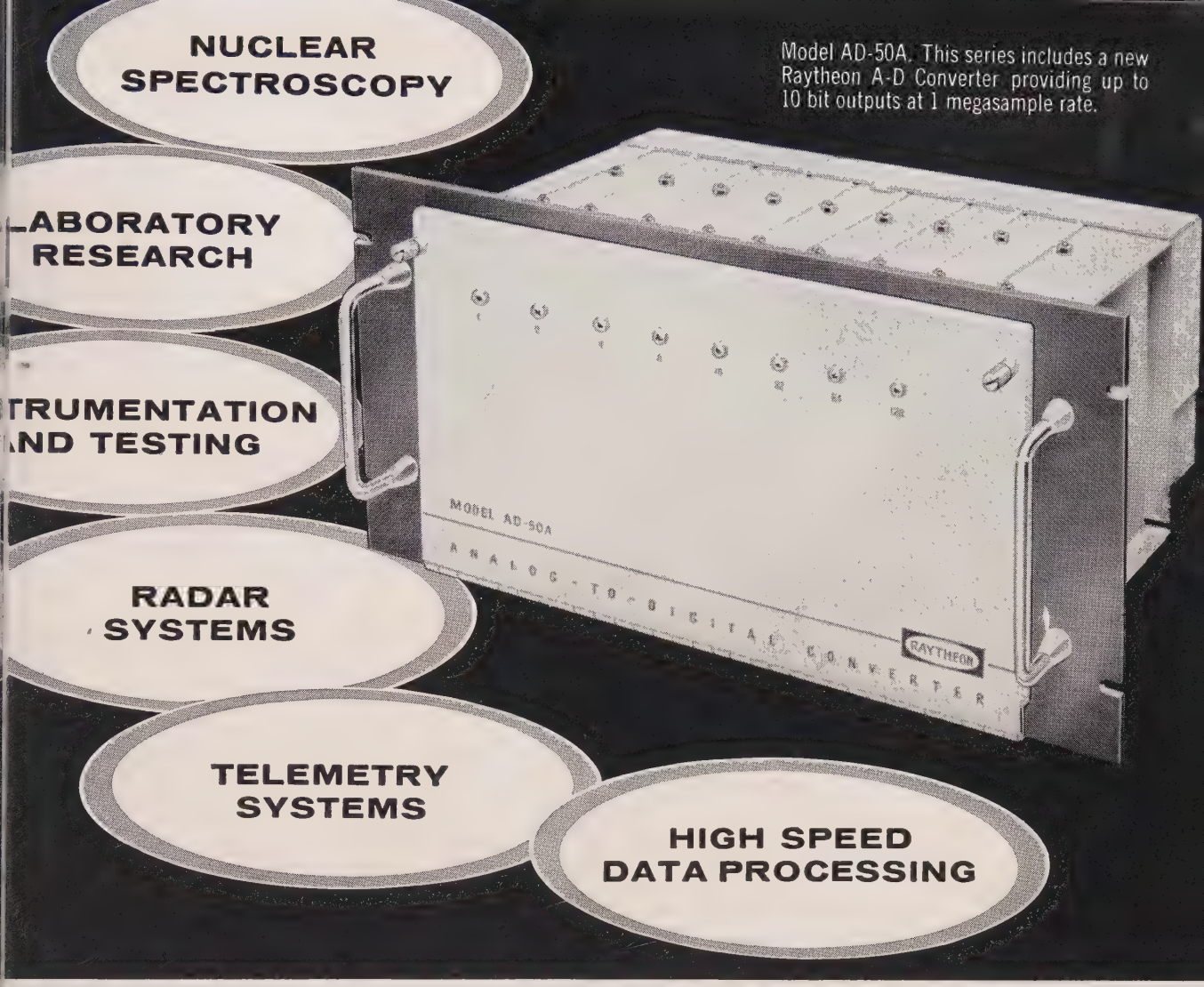

'THEON'S NEW A-D CONVERTER: UP TO 5.0 x 10^6 INDEPENDENT 8 BIT WORDS PER SECOND!

han any other available, Raytheon Analog-Digital er's 25-nanosecond aperture time allows digitizing s less than ½-microsecond in width. With multi-input, its applications encompass any product or requiring digitized analog voltages in continuous mittent form.

he size of an office typewriter, Model AD-50A is integrated with established systems: its flexible de-ows acceptance of variable input as well as wide ns in output format and logic. Its almost unlimited applications offer industry, government and the military a basic, solid state tool that revolutionizes the present state of the art.

All of its outputs are usable, every readout is valid, and it can be operating in your system in less than 90 days.

'THEON

'THEON COMPANY

MAIL COUPON TODAY FOR BROCHURE

Raytheon Company, Dept. 31, Lexington 73, Massachusetts NI
Attention: M. B. Curran

Please mail me Specifications on:

☐ Model AD-50A 8 Bit Converter
☐ New 10 Bit, 1 megasample Converter

I'm interested in possible applications to the following type system(s):

_____

_____

_____

_____

*Name & Title*_____

*Company*_____

*Address*_____

*City & State*_____

STANDARD FUNCTIONNAL UNITS . . .

FRENCH ATOMIC ENERGY COMMISSION SYSTEM

. . . master-key to nuclear instrumentation

Standard functional units are assembled in cabinets in order to be used as complete assemblies : scales for counting, amplitude selectors, ratemeters, etc...

REGISTER UNIT TYPE TND.1
Function :
counting (registering)
Dekatron divider

TIMER UNIT (SLOW RESPONSE)
TYPE TAL.2

Intended for automatic pre-set counting

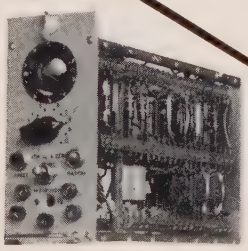

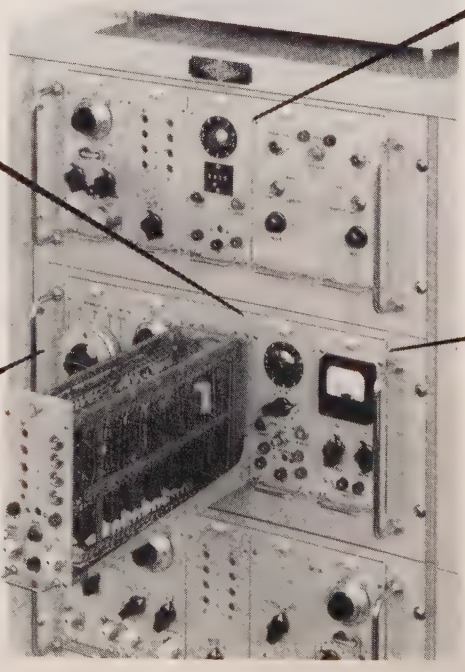

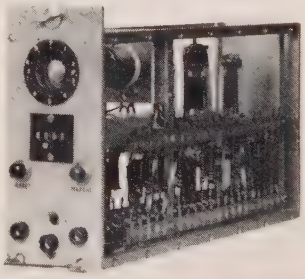

VERY HIGH TENSION UNIT

RATEMETER TYPE TIS.1
supplies a tension or a current proportionnal to the number of counts received

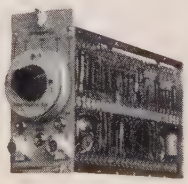

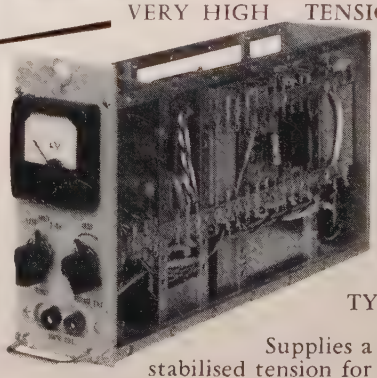

TYPE THT.

Supplies a very high stabilised tension for detectors pre-amplifier

ELA

L'ÉLECTRONIQUE APPLIQUÉE

96/100, rue Maurice Arnoux • MONTROUGE • ALE 45-20, 83-20
25, rue du Docteur Finlay • PARIS 15e • TÉL. SÉGUR 14-75

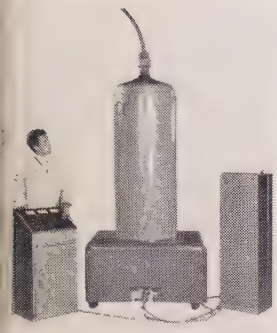

600 kV Generator

Research Centres and Industry alike find the modern, polished solution to the problem of continued high voltage in the

SAMES ELECTROSTATIC GENERATOR

Electrostatic Painting with the STATRON

HIGH VOLTAGE GENERATORS

* 50 kV to 600 kV
* 20W to 3 kW
* Positive or negative polarity
* Medium or high stability

for

* Electrostatic precipitation
* Electrical testing
* Electronic optics
* X-rays
* Nuclear Physics, etc.

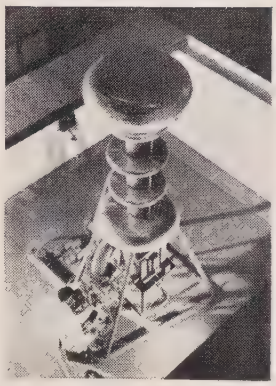

Vertical 600 kV
Accelerator at the Centre d'Etudes Nucléaires de Grenoble

ELECTROSTATIC PAINTING

The STATRON is a portable equipment for electrostatic painting, featuring

* 90 kV voltage
* Complete safety, owing to use of electrostatic generator.
* Paint output: 15 litres/hour
* Supply: 110 or 220 V, single phase.
* Consumption: 110 Watts

PARTICLE ACCELERATORS

Type	Acceleration Voltage	Particles Accelerated	Application
J	150 kV	ions	Neutron Generator by D/T or D/D reaction
L	300 kV	ions	
S	600 kV	ions or electrons	All applications

SOCIETE ANONYME DE MACHINES ELECTROSTATIQUES

21, RUE JEAN MACÉ, P.O. BOX 150, TEL: 44.77.64 GRENOBLE, FRANCE

REPRESENTATIVES

GENERATORS AND ACCELERATORS

Austria: AUSTRONIK, Salzburg – Belgium: CENTRONICS, Brussels – Chinese People's Republic: Cie OLIVIER, Paris – Denmark: DANSK SCIENTA, Copenhagen – Great Britain: MILES HIVOLT LTD., Shoreham by Sea – Italy: SECI, Milan – Netherlands: PROJECTO, Amsterdam – Norway: LEHMKUHL, Oslo – Portugal: A.G.M.E., Lisbon – Spain: CRESA, Barcelona – Sweden: SCIENTA SCANDIA, Gothenburg – Switzerland: OMNIRAY, Zurich – Western Germany: DR. NAMUR, Darmstadt – Bulgaria, Czechoslovakia, Eastern Germany, Hungary, Poland, Rumania, U.S.S.R.: CIFAL, Paris.

ELECTROSTATIC PAINTING EQUIPMENT

Algeria: FAMPA, Algiers – Austria: PETER PETERSEN, Vienna – Belgium: DURMECO, Brussels – Chinese People's Republic: Cie OLIVIER, Paris – Denmark: DANSK SCIENTA, Copenhagen – Eire: HODGES & SONS, Dublin – Great Britain: AEROSTYLE LTD., London – Italy: TRASMETAL, Milan – Netherlands: STUURMAN, Wormerveer – Norway: LEHMKUHL, Oslo – Portugal, RAMADA, Ovar – Spain: INSTITUTO ELECTROQUIMICO, Barcelona – Sweden: SCIENTA SCANDIA, Gothenburg – Switzerland: REGSA, Lausanne – Western Germany: A. WIRTH, Reutlingen – Bulgaria, Czechoslovakia, Eastern Germany, Hungary, Poland, Rumania, U.S.S.R.: CIFAL, Paris.

High Voltage Engineering Corporation . . .

"Charged Particles"

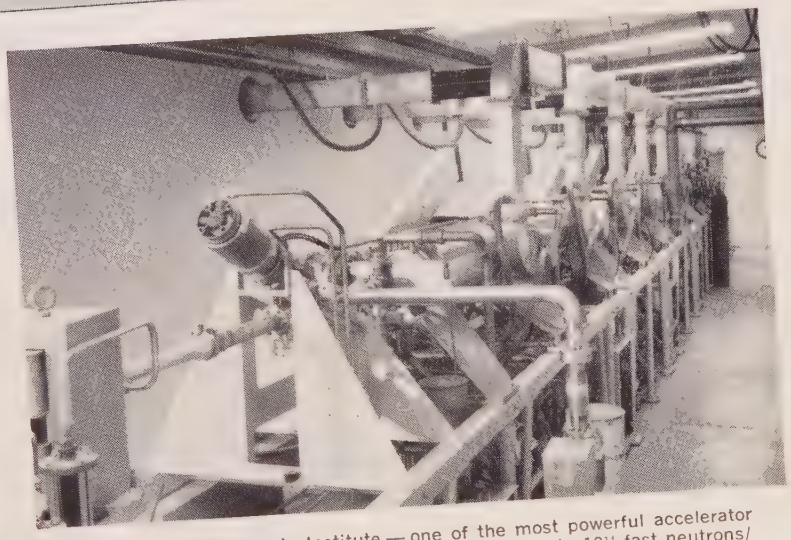

Rensselaer Polytechnic Institute — one of the most powerful accelerator neutron sources ever built, this linac will yield up to 10^{11} fast neutrons/sec, or a thermal flux of 10^{12} neutrons/sec/cm^2, with peak energy at 77 Mev, and peak pulse current of 800 ma. Primarily for neutron-time-of-flight and nuclear reactor research, the accelerator will also aid RPI's solid-state and radiation effect studies.

High Energy Linacs

Today's rapid advances in particle accelerator technology are particularly illustrated by the microwave linear electron accelerator (linac). Spurred by experimental requirements for more intense bursts of high-energy electrons and neutrons contained within precise limits of time and space, High Voltage Engineering and Applied Radiation Corporation have sustained intensive development of linacs. The result has been consistent improvement in linac reliability, and a series of record-breaking machines for research.

Two research linacs of considerable sophistication are now being installed at Yale University and Rensselaer Polytechnic Institute physics departments. The Yale machine is a five-section L-band accelerator, producing 28 kw of average radiation power and peak energies of 77 Mev. It will be used in a broad physical research program with emphasis on nuclear cross-section investigations. RPI's accelerator is an unusually powerful neutron physics research tool.

The accelerators of the near-future are exemplified by the machine now being built for the U.S. National Bureau of Standards. This linac, designed to performance specified by the NBS, will produce electron beam peak energies up to 150 Mev. Its 40 kw power output at 100 Mev will be greater than any previously obtained from a linear accelerator and about 100,000 times that obtainable from existing NBS high energy accelerators.

Availability of the intense high energy electron beam — and of secondary radiations such as x-rays, positrons and neutrons — opens up new research areas for NBS scientists. The linac will be used in low temperature chemistry, solid state physics, metallurgical studies, neutron activation analysis, nuclear alignment studies and determination of radiation standards.

Machines of such power were not available previously, and provide the experimenter with many intriguing opportunities.

Applied Radiation

As a powerful source of ionizing radiation, the linac is also a prime candidate for industrial radiation programs where electron penetration above 3 Mev is required. For example, most of the surgical sutures used today (made by Ethicon, Inc., a division of Johnson & Johnson) are electron-beam sterilized in aluminum-foil packages by industrial linacs operating on a two-shift production basis.

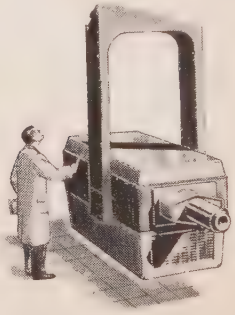

Development at High Voltage Engineering and ARCO has led to compact microwave electron accelerators for x-ray inspection and deep-x-ray therapy. High energy x-ray linacs can radiograph through two feet of steel or non-destructively inspect our biggest solid fuel rocket engines. Medical x-ray linacs provide the radiologist with a new precision therapy tool for treating deep-seated malignancies.

If you see the possibilities for accelerators in your research program or have a challenging radiation application, we'd be pleased to receive your inquiry.

High Voltage Engineering Corporation

Burlington, Massachusetts, U.S.A.

•

Applied Radiation Corporation

•

High Voltage Engineering (Europa) N.V

HVEC arco

NUCLEAR INSTRUMENTS AND METHODS 12 (1961) 1–10; NORTH-HOLLAND PUBLISHING CO.

TEST ROUTINES AND MONITORING FOR A LARGE COUNTER EXPERIMENT†

STANLEY C. BAKER††, QUENTIN A. KERNS, FREDERICK A. KIRSTEN,
DICK A. MACK and THOMAS A. NUNAMAKER

Lawrence Radiation Laboratory, University of California, Berkeley, California

Received 15 February 1961

Some recent multichannel scintillation-counter experiments are so complex that the use of test routines and fault monitoring becomes essential. In a recent experiment, it was desired to initially align the system, provide continuous calibration during the experiment, and rapidly locate the cause of threshold drift or catastrophic failure. A test and monitoring system was devised in which synthesized pulses are injected into several points of the system, and the operation is automatically compared with the desired response. If the system performance does not agree within prescribed limits, an alarm sounds. Through a program that varies the amplitude of the test signal, one can check coincidence-circuit threshold and feed-through characteristics. By programming delay between input pulses, the resolving time can be measured.

Several novel monitoring devices have been developed which allow one to assess the display of a large volume of information at a glance. One unit for reading time delays involves the use of a cathode-ray-tube raster display, another unit for reading binary information employs a transistor-driven incandescent lamp panel.

1. Introduction

With recent expansion in the complexity of nuclear counter experiments, it has become desirable to automate not only the acquisition of the experimental data but also the methods of checking the counting system for proper performance. In a recent pion-scattering experiment, a number of error-checking techniques were employed to (a) facilitate initial alignment of the equipment during setup, (b) maintain a check on the threshold amplitude levels of the discriminator units during running, and (c) detect faulty operation in the overall system[1]). A block diagram showing how the errorchecking units apply to the system is shown in fig. 1.

Some error-detection schemes are directly applicable to the signals generated by a nuclear event. In general, however, it is more desirable to inject light or electrical test pulses at an appropriate point in the system to simulate the variables normally encountered in operation. An example of the former method, in which the signal does its own checking, is the use of the redundancy parity-bit check in the paper-tape punching units in this experiment as well as in many computers. In the latter type of test routine, simulated signals are programmed both in amplitude and time of occurrence to verify the limits of reliable operation.

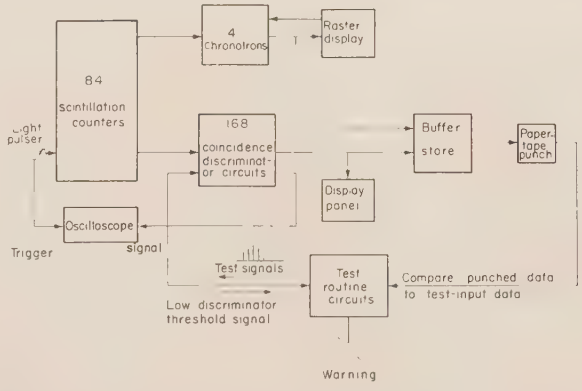

Fig. 1. Block diagram of data-acquisition system emphasizing error-checking circuits.

This paper describes checking methods that were employed in a recent experiment along with plans for a more complete checking program in a future run.

† This work was done under the auspices of the U.S. Atomic Energy Commission.

†† Present address: Cubic Corporation, San Diego, California.

1) S. C. Baker, F. A. Kirsten, D. A. Mack and C. Wiegand, Nucl. Instr. and Meth. 12 (1961) 11.

2. Error Detection

Before considering the particular devices used, it would be well to discuss our requirements for an error-detecting system. The following design criteria were incorporated into this experiment whenever practical:

a. The test program must simulate as nearly as possible the actual response to a desired nuclear event in a background of undesired events. Test signals should have the same range in rise time, duration, and amplitude as those expected from the nuclear interaction. One can simulate the response to random events by testing at repetition rates higher and lower than the maximum encountered in actual operation and with signal amplitudes greater and less than those produced by a correct event.

b. The system response to one desired event out of a background of as many as 100000 or more unwanted events per acceleration period should be evaluated.

c. The test routine must detract as little as possible from the normal running of the experiment. How often tests are made must be a compromise between shortened running time and the loss from possible catastrophic failures occurring between infrequent test periods.

d. Error-detection circuits must be of the highest reliability to insure proper test-routine results.

e. Error detection should localize the trouble to a particular area. Then operation can be restored usually by simply exchanging a functional unit with a spare. If operation is still not restored, a technician must then resort to point-by-point circuit tracing.

f. It is helpful if the test routine is capable of marginal checking to detect incipient failures. It is also desirable to differentiate between the response of a circuit that is out of adjustment (*e.g.*, a drift in voltage-threshold level) and one that is completely inoperative.

g. The test routine must be as straightforward as possible, and the results easily and rapidly interpreted. Time is often of the essence for restoring the experiment to normal operation.

h. Error-correcting circuits should be considered where feasible.

3. Coincidence-Discriminator Test Routine

3.1. GENERAL DISCUSSION

An automatic testing and checkout unit for the coincidence portion of the data-acquisition system was designed to utilize a ramp pulser as a test-signal source. The purpose of this test is (a) to check the amplitude threshold of each of the 168 discriminator units, (b) to test for cross-talk between coincidence-discriminator units, (c) to check the operation of the core store and associated circuits, and (d) verify the operation of the tapepunch driving circuits. This test routine was applied to the system by interrupting normal operation after 128 Bevatron acceleration periods and using the interval of two Bevatron beam times for testing. Simulated phototube pulses from the ramp generator were applied to the even-numbered coincidence-discriminator circuits during the first of these two Bevatron beam times, and to the odd-numbered circuits during the second. A group of about 30 simulated phototube pulses was generated during each ramp; they ranged in amplitude from 80% to 110% of the previously determined threshold level of each discriminator. The discriminators were required to maintain signal thresholds within $\pm$ 10%; thus any discriminator which triggered during the 80 to 90% portion of the ramp had drifted outside the specified range. If any of them produced an output during the 80 to 90% interval, the ramp was terminated at the 90% level, the number of the misbehaving coincidence-discriminator was indicated on a light panel, and an alarm sounded. If no outputs were detected by the 90% level, the ramp was continued up to the 110% level where it terminated. By this time, all even- (or odd-) numbered channels should have triggered. The test "event" was then stored, and the process repeated nine more times, filling the core store. The results were then punched out onto paper tape as is done for normal events. During the punching process, a part of the test-routine circuitry sampled the voltages across the tape-punch magnets. The purpose of this was to verify that the proper channels were being punched. A missing signal in one channel

indicated a failure in some part of the system. Accordingly, an alarm sounded. The presence of cross-talk between channels was also detected during the punching by nothing whether any even-numbered channels triggered when only odd-numbered ones should be present and vice versa.

The method of generating the ramp is shown in fig. 3 and some of the waveforms in fig. 4. When a gate is applied, the charging voltage is allowed to rise to the 80% level. The bootstrap charging circuit causes the voltage to change linearly. When the 110% level is reached, a blocking oscillator

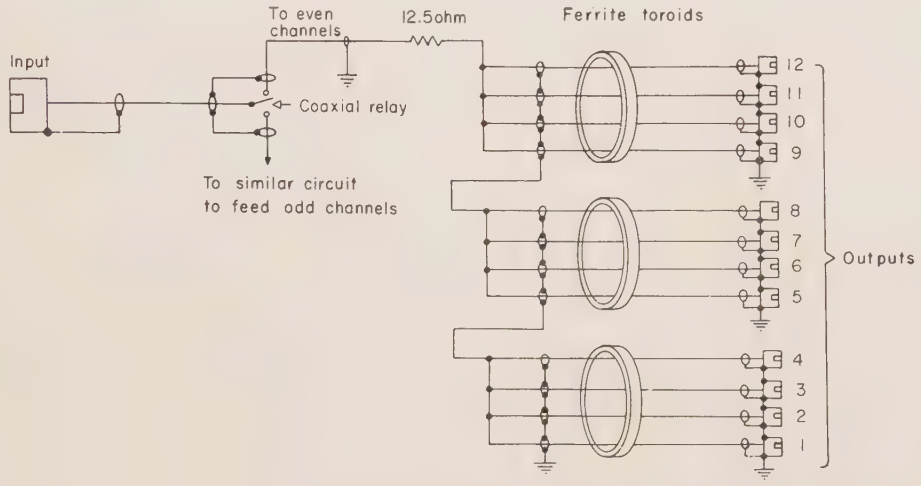

Fig. 2. Schematic diagram of test pulse distributor. All cables are miniature 50-ohm coaxial. Each group of four cables makes four turns around a toroid.

3.2. RAMP PULSER

The ramp pulser generated bursts of simulated phototube pulses having a rise-time of about 3 nsec and a decay time of about 10 nsec. During each burst of about 30 msec duration, the amplitude of the pulses varied linearly with time from 80 to 110% of a nominal amplitude.

A mercury-relay capsule was chosen as a pulse-generating element capable of producing signals of accurately controlled amplitude and of sufficiently high energy to be split into groups of 84 signals. With such a pulse generator, the ramp envelope is generated simply by applying a similarly shaped charging-voltage waveform to a small capacitor. The capacitor is periodically discharged by the vibrating relay contacts into a 25-ohm-impedance shaping network. The pulses from the shaping network simulate normal phototube pulse response. They are then split into two 50-ohm outputs which feed two pulse distributors. The pulse distributors further split the pulse 12 ways as shown in fig. 2, for distribution to groups of 5 coincidence discriminators each.

triggers and produces a signal that turns off the gate.

3.3. DISPLAY PANEL

The display panel has a two-fold use. It provides an easy method for the observation of experimental data during the running of the experiment and facilitates error checking during test periods. The panel consists of an array of incandescent lights arranged in the same spatial pattern as the scintillation counters in the experiment; there is one light for each coincidence-discriminator unit. While the data-acquisition system is capable of storing ten different events per Bevatron beam burst, the eye has difficulty in remembering more than one event in an internal of a few seconds; thus it was decided to display only the first event in any beam burst. This is accomplished by a gated flip-flop driving each light circuit.

A light-gate generator normally holds all of the flip-flop gates so that they cannot receive a pulse. Just before the accelerator beam, this gate is opened so that each flip-flop may receive a pulse

from its respective coincidence-discriminator circuit. When the first event is detected by the system, the light-gate generator is turned off for the duration of the Bevatron beam period. In this manner, only the first event pattern in each beam burst is stored on the light panel. The display flip-flops are reset at the beginning of the next Bevatron acceleration cycle. The light bulbs (General Electric No. 344) glow brightly at 12 V and draw about 20 mA. They glow very dimly at 5 V and draw about 9 mA. An emitter-follower stage which couples the flip-flop to the light bulb was designed so that when the flip-flop is on, the light bulbs draw 20 mA, and when the flip-flop is off, the light bulbs draw 9 mA. Thus both the binary 0 and 1 state can be distinguished from an open circuit or a defective bulb.

The lights are essential in determining the threshold of the coincidence-discriminator circuit and in checking the operation of the whole system. The system is constructed so that it is easy to program a known test pattern into each coincidence-discriminator circuit through a test-pulse input. By comparing the light-display panel with the punched-tape record, one can determine if a system malfunction occurred in circuits of the coincidence discriminators or after them. That is, if the display panel indicated the correct pattern but the punched tape did not, the trouble was in the core memory or read-out circuits.

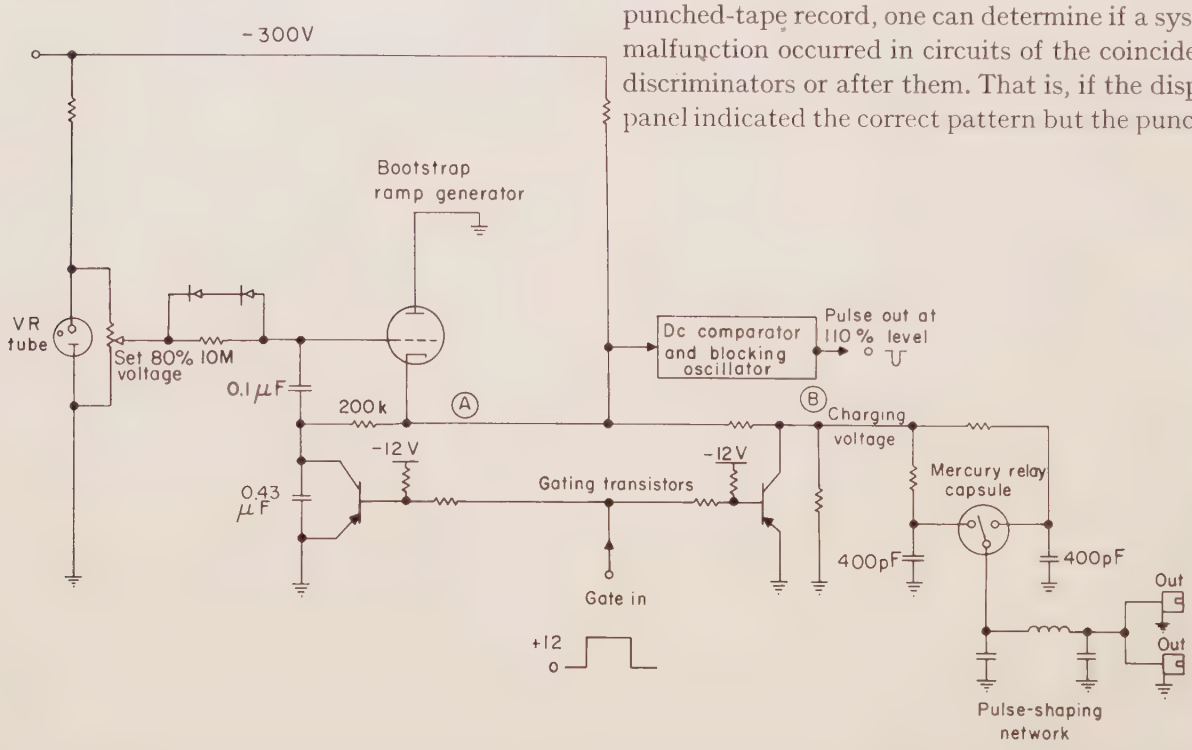

Fig. 3. Simplified schematic diagram of ramp pulser. The wave forms for A and B are shown in fig. 4. The mercury delay capsule vibrates at 400 cps.

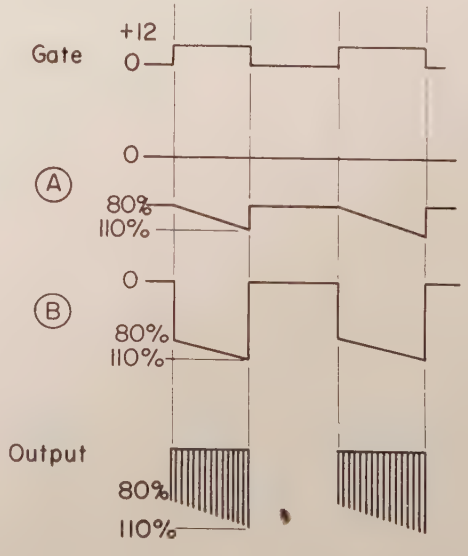

Fig. 4. Wave forms of the ramp generator.

4. Chronotron Test Circuits

4.1. GENERAL DISCUSSION

The test-pulse generator and cathode-ray-tube (CRT) display was designed to check the operation of the chronotron under simulated operating conditions[2]). Simulated phototube pulses are sent to the chronotron, where their time delay is measured. The measured time delay is read back to the CRT sends two simulated phototube pulses to the chronotron at the start of the horizontal sweep. At the end of the horizontal sweep, the reset-pulse generator sends a reset pulse to the chronotron. By programming the interval between the two pulses of the pair, one is able to check all possible delay combinations of each chronotron and present these on one raster.

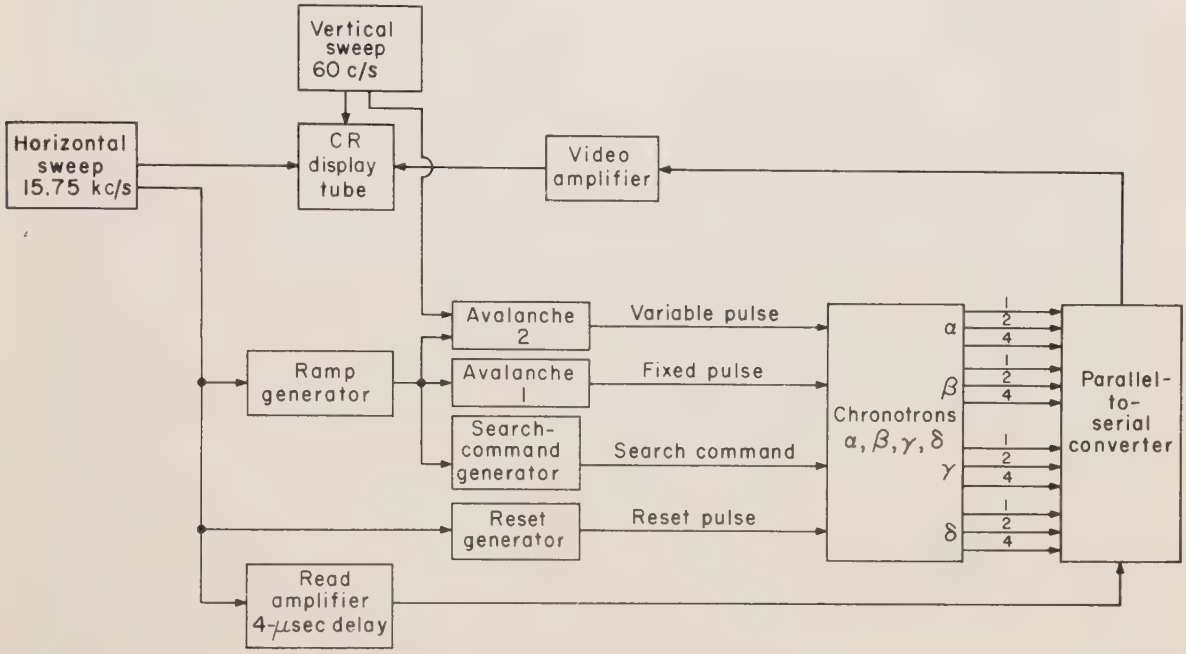

Fig. 5. Block diagram of chronotron test routine.

raster, where the display patterns for all four chronotrons may be observed simultaneoulsy and compared. A block dagram of the test circuits is shown in fig. 5. Knowing the correct patterns, an observer can quickly discern whether or not a chronotron is operating properly. If it is not, the changes in the raster pattern quickly help localize the trouble.

The display tube uses the horizontal and vertical sweep circuits of a standard television set. The display is a binary-coded signal shown in the form of a bar graph. The vertical oscillator runs at the 60-cycle line frequency, while the horizontal oscillator free runs at about 15.75 kc/s. A pulse-pair generator and reset-pulse generator are slaved to the horizontal oscillator. The pulse-pair generator

The test routine is gated on whenever the data-acquisition system is not in operation. For this experiment, the test routine was off for a few tenths of a second out of each 6 sec, so there was a nearly continuous display.

The pulse-pair generator uses 2N501 transistors operated in the avalanche mode to generate two simulated phototube pulses. The time delay between the two pulses is controlled by firing one unit (avalanche No. 1) at a fixed time with respect to the horizontal sweep, and firing the other (avalanche No. 2) with a ramp generated at the beginning of the horizontal sweep plus some fraction of the vertical sweep voltage. The fraction of

[2]) A. Bjerke, Q. Kerns and T. A. Nunamaker, Nucl. Instr. and Meth. **12** (1961) 25.

Fig. 6. Display of binary-coded test signals of all four chronotrons. Left to right are chronotrons, α, β, γ and δ. Time increases from top to bottom.

the vertical sweep voltage depends upon the time interval that it is desired to test and display. Thus the relative timing between these two pulses is varied as a function of the vertical sweep with time increasing from top to bottom of the CRT display.

At the end of the horizontal sweep, the reset generator sends a reset pulse to the chronotrons, thereby resetting them for the next pair of test pulses.

4.2. CHRONOTRON TEST CYCLE

At the beginning of the horizontal sweep, the pulse-pair generator sends two simulated phototube pulses to all four chronotrons, along with a search command signal that starts the chronotrons. The chronotron measures the time delay between the two test pulses and reads out into a parallel-to-serial converter; its operation is described below. The readout of the parallel-to-serial converter is actuated by the readout pulse generated about 5 μsec after the beginning of the horizontal sweep. This readout pulse reads all the chronotron outputs into a type-HH-2000 delay line. The chronotron signals thus arrive at the CRT video amplifier in serial fashion, where they are amplified to brighten the video display. The proper test display is shown in fig. 6, where all four chronotrons are being checked together and are displaying all possible time-delay combinations simultaneously. In actual operation not envolving a test routine, a chronotron obviously measures only one interval per nuclear event. The display is in binary form; 1, 2, and 4 being read from left to right from each of the four chronotrons. At the top of the display, all chronotrons are reading out from time interval one, while at the bottom of the display, all chronotrons are reading from interval seven. Time is calibrated in vertical steps and marked on the screen so that any timing error shows immediately as a vertical shift in a portion of the pattern. The display not only tells when there is an error, but also tells its magnitude and location in a particular time interval. It is possible to observe any 60-cycle effects in the chronotron by changing the phase of the 60-cycle vertical sweep. If there are line-frequency effects present, these will produce a shift in the display as the phase of the vertical sweep is changed. This is useful for checking against 60-cycle effects in the chronotrons.

Figure 7 shows the display of fig 6, with the vertical time scale expanded. A 1-nsec delay has been introduced intentionally into the second (β) channel in order to give a time calibration for the picture. The jitter of the display is within 0.1 nsec. as can be seen from the photo. This is seen more easily by observing the display in operation for a few minutes. This jitter is the sum of the jitter in the pulse-pair generator and in the chronotron.

If desired, events can be read directly from the chronotron on a 21-in. oscilloscope by using the parallel-to-serial converter. In this case, the CRT is swept in the vertical direction by a 0.1-sec ramp that is triggered whenever the Bevatron is pulsed. The horizontal sweep of the CRT is triggered for each chronotron event, and the video signal is controlled by the parallel-to-serial converter. The resulting display is a series of dots along each horizontal sweep in accordance with the binary readout of each of the four chronotrons.

By means of switches in the parallel-to-serial converter, the decimal output of any one chronotron can be displayed along with its binary output. This feature is useful for pin-pointing any malfunction; by inspection of the decimal display, one can tell which chronotron channels are operating properly and which ones are not. For example, if the decimal display is correct and the binary display is not, the trouble must be in the binary storage rather than in the chronotron itself. The flexibility of this type of monitoring has made it possible to keep the chronotron operating properly with very little down time, since trouble normally can be spotted and corrected before it becomes serious.

4.3. PARALLEL-TO-SERIAL CONVERTER

The binary outputs of the four chronotrons appear as dc levels at the inputs to the parallel-to-serial converter, as shown in fig. 8. When the amplifier gates of the converter are pulsed by a read signal, a 1-μsec pulse is sent down the HH-2000 delay line only if there is a chronotron input. Because each chronotron is tapped into the delay line at a different point, its output is a serial representation of the chronotron inputs.

Fig. 7. Expanded display of chronotron binary-coded test signals showing 1-nsec delay in channel β.

The read-gate amplifiers are 2N501 transistors with their collectors tied to the center conductor of the HH-2000 line through a diode. The diodes are necessary to prevent pulses on the line from forward biasing the 2N501 transistor and thus shorting

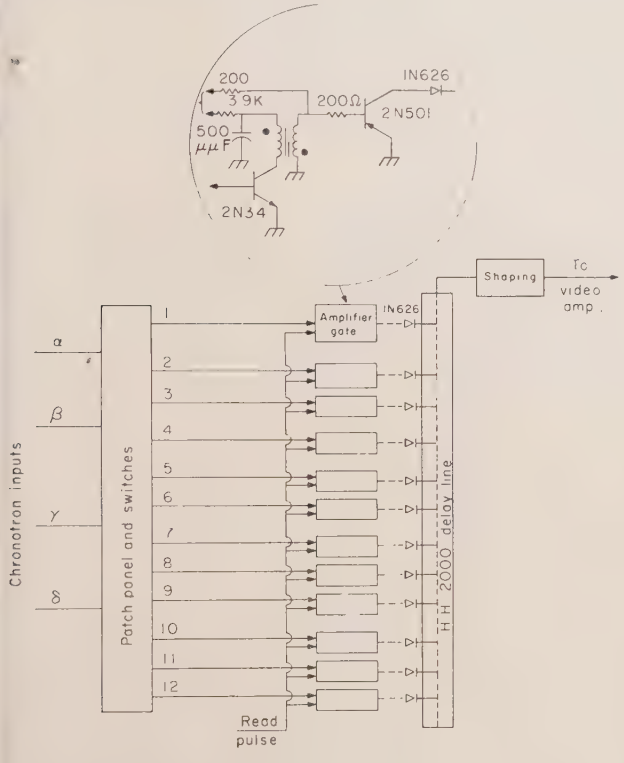

Fig. 8.
Block diagram of chronotron parallel-to-serial converter.

out the line. Collector voltage for all transistors is supplied from the center conductor of the delay line. When the amplifier is pulsed, the transistor saturates, which shorts the line for about 1 μsec, and thus puts a positive pulse on the line equal to the collector voltage of the transistor. To compensate for the pulse-height attenuation of the delay line, a higher collector voltage is used at the far end of the delay line than at the output end of the line by establishing a dc voltage gradient along the line with a dc current through the line. Without compensation, the pulse-height variation was about 3:1; with compensation, the variation was reduced to about 3:4. This first-order compensation was sufficient to produce a well-standardized video output after going through a simple shaping circuit.

4.4. SWITCHING

To increase the flexibility of the converter, all inputs are brought in through patch panels and switches. This makes it possible to arrange the display in any desired manner. The most useful displays used were (a) all four chronotron binary outputs, and (b) the display of the decimal outputs of a single chronotron along with its binary display. The binary display of all four outputs provides a check on the whole chronotron system, while the display of the decimal plus binary outputs affords a check on the internal operation of each chronotron.

4.5. PULSE-PAIR GENERATOR

The pulse-pair generator is a conventional avalanche pulse generator using 2N501 transistors. Each avalanche unit is driven by a blocking oscillator which is in turn driven by a ramp generated at the beginning of each horizontal sweep. In order to time the variable pulse, a portion of the 60-cycle vertical sweep is added to its ramp. This varies the timing between the two avalanche pulses as a function of the vertical-sweep position.

The output of the avalanche transistors is taken from the collector through a 10-$\mu\mu$F capacitor to a 50-ohm output cable and has an amplitude of about 5 V. When using 2N501 transistors in the avalanche mode, we have found that reliable operation is possible only for light loads.

5. Conclusions

The methods described here, while quite elementary, have given us confidence in the system and, when faults did occur, allowed rapid location and correction. Several improvements are planned for use in the fault location system of a future scattering experiment. It is desirable to have the initial error-checking procedure include the entire chain of counting equipment from detector to output-data unit; that is, test signals injected at the detectors should produce a known set of output signals.

Programmed light pulses illuminating scintillation or Čerenkov detectors should generate the correct coincidence-system response. This information would then be placed in the buffer-store unit and recorded on magnetic tape. Should the magnetic tape record not correspond to the expected

output response, then the experimental equipment would be divided into several logical blocks to localize the circuit malfunction. These divisions include the scintillation detectors and gate-forming circuits, the coincidence and chronotron circuits, the core storage, and the magnetic tape transport. Work is under way to provide a more complete errorchecking system.

Acknowledgements

We wish to thank Messrs. Lee Wagner, William Flood, and Cordon R. Kerns for the circuit design and construction of the parallel-to-serial converter, as well as Mr. Robert Reynolds for the mechanical design. Mr. Thomas Clark donated and modified the television set used for the monitor.

NUCLEAR INSTRUMENTS AND METHODS 12 (1961) 11–19; NORTH-HOLLAND PUBLISHING CO.

AN ELECTRONIC DATA-ACQUISITION SYSTEM FOR USE WITH A COMPLEX NUCLEAR PHYSICS EXPERIMENT†

STANLEY C. BAKER††, FREDERICK A. KIRSTEN, DICK A. MACK, and CLYDE WIEGAND

Lawrence Radiation Laboratory, University of California, Berkeley, California

Received 15 February 1961

An electronic data-acquisition system is used with a nuclear physics experiment of such complexity that data processing required a high-speed computer. The system acquires data from 168 signal channels of scintillation counters and four channels of chronotron circuits. It has the capacity to store 10 events during the 0.1-sec-long Bevatron beam pulse. The storage time for the information from each event, consisting of 168 bits from the counters plus 12 bits from the chronotrons, is 40 μsec. In the interval between beam pulses, the stored information is punched onto paper tape in a form suitable for computer input.

This report describes the over-all characteristics and operation of the system. The specific parts of the system and techniques for semi-automatic testing are given in the companion reports.

1. Introduction

Several high-energy physics experiments have recently been proposed which would require the acquisition and processing of data in amounts that are very large compared to previously performed counter experiments. The electronic data-processing techniques now available make experiments of this type entirely feasible. This report describes a data-acquisition system which has been used in a scattering experiment of such complexity that previously used methods of data handling were quite inadequate[1]).

The rate at which humans can process data is vastly lower than that of electronic apparatus. The design philosophy we followed, therefore, was to use electronic data channels wherever the rate of data flow would be slowed by the use of any human operations such as recording, selection, or interpretation of data. In the system described herein, this required an all-electronic channel from the phototube through the output of the computer. The personnel involved were thereby freed of the tedious tasks, and, aside from supervising the operation of the electronic "slave", could devote their time to studying the results of the experiments.

This new system performed several functions: It partially analyzed the data to select potentially useful nuclear events; it "de-randomized" the useful data by storing the information from randomly occurring events in an orderly fashion; and it prepared a paper-tape record of the data in a format suitable for entry into an IBM-704 computer. The results of the experiment were known as soon as the computer had processed the tape.

We believe that the electronic complexity and "untouched-by-human-hands" aspects of the data processing is novel enough and of sufficient interest to warrant the detailed description of the system given in this and five other reports[2–6]). This report reviews the general aspects of electronic instrumentation. Discussions of some specific components of the system are given in the other reports.

† This work was done under the auspices of the U.S. Atomic Energy Commission.

†† Present address: Cubic Corporation, San Diego, California.

[1]) Clyde Wiegand, "Handling of Counter Data", presented at the International Conference on High Energy Physics Instrumentation, Berkeley, California, September 1960; Lawrence Radiation Laboratory Report UCRL-9343 (in press).

[2]) Stanley C. Baker, Nucl. Instr. and Meth. **12** (1961) 20.

[3]) A. E. Bjerke, Q. A. Kerns and T. A. Nunamaker, Nucl. Instr. and Meth. **12** (1961) 25.

[4]) F. Evans and F. A. Kirsten, Nucl. Instr. and Meth. **12** (1961) 39.

[5]) Q. A. Kerns and G. C. Cox, Nucl. Instr. and Meth. **12** (1961) 32.

[6]) S. C. Baker, Q. A. Kerns, F. A. Kirsten, D. A. Mack and T. A. Nunamaker, Nucl. Instr. and Meth. **12** (1961) 1.

2. Description of the Experiment

The purpose of the experiment was to make measurements on pion-pion scattering. A beam of 1 to 2 BeV/c π mesons from the Bevatron was focused upon a liquid-hydrogen target. About one in 10^6 of the pions in the beam collided with a proton in such a way as to produce a second pion and a low-energy neutron. These three particles emerged from the target and were detected by a large array of scintillators. The array was composed of 84 separate elements fitted together to form a π steradian section of a sphere 5 ft in radius centered upon the target. The array intercepted all particles emitted in the angular interval from 4 to 60 deg with respect to the beam. One 6810A or 7046 multiplier phototube was coupled to each scintillator element. Thus the coordinates of the three particles were roughly measured by noting which of the 84 phototubes generated an output. The energy of the neutron was determined by measuring the time difference between the occurrence of the prompt-pion phototube signals and the later neutron signal. With this information, the computer made calculations regarding the kinematics of the event, separating the physically possible events from the false "events" composed of background signals.

3. Electronics

The electronic system can be described logically and functionally as being composed of four sections:

1. The "fast-logic" system separated the signals of the potentially useful events from the background.

2. The coordinate and time-separation detector measured the space and velocity coordinates of the particles in the potentially useful events.

3. The "buffer store" stored the selected events and at a later time punched them on to paper tape. This section included the control circuitry.

4. Auxiliary equipment, including an individual-event visual monitoring system and test circuitry, afforded examination and testing of the operation of the system.

Sections 1 and 2 are made up, in general, of standard pieces of counting equipment of wide applicability but arranged into a system especially tailored for this experiment. Section 3, the buffer store, is designed to be useful in many other experiments in its present form. The over-all block diagram is shown in fig. 1.

An important and difficult aspect of the electronic instrumentation was the selection of potentially useful events (hereafter called simply events) from

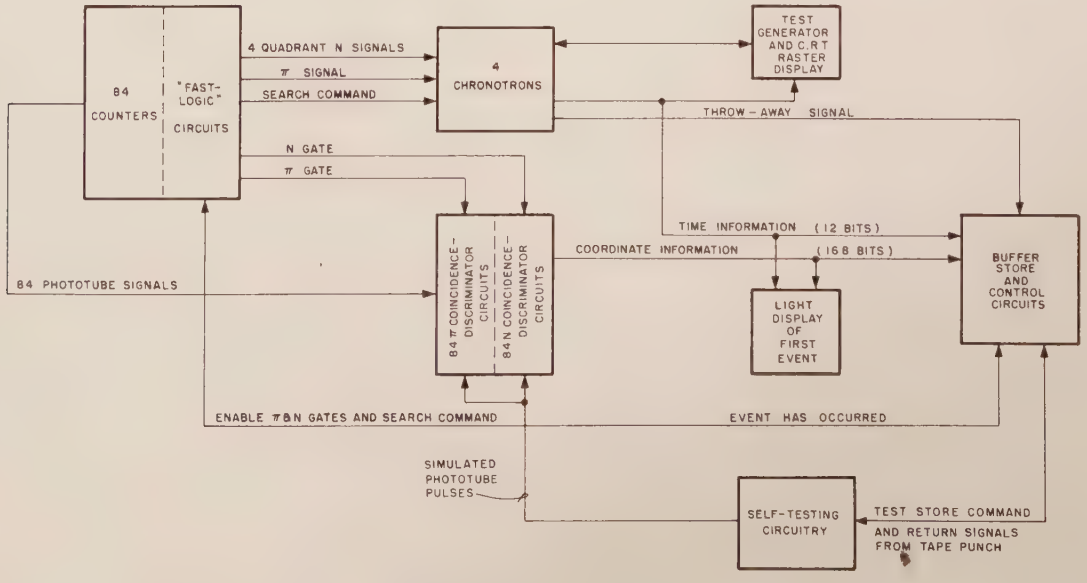

Fig. 1. Over-all block diagram.

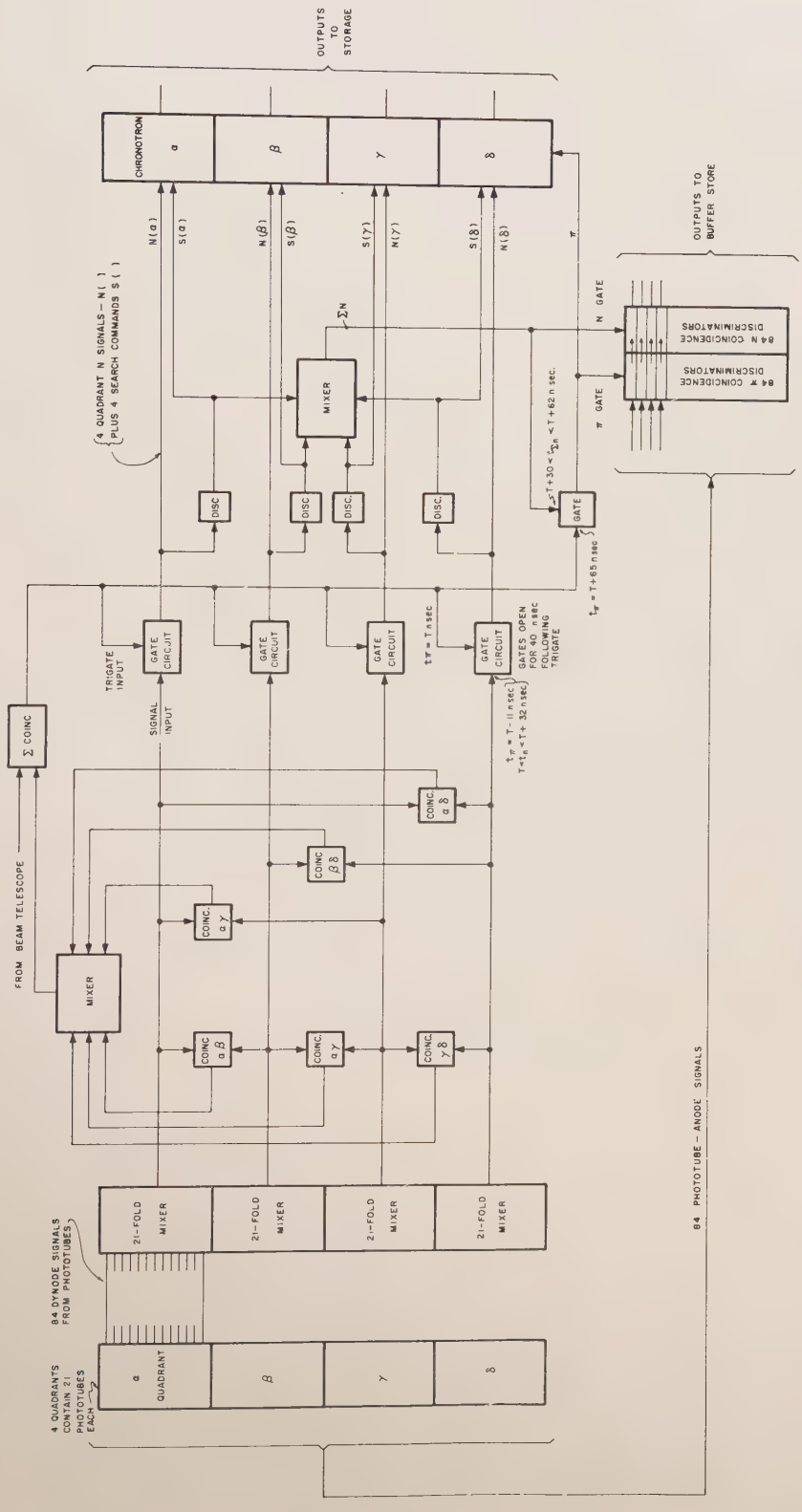

Fig. 2. Block diagram emphasizing fast-logic portion of system.

the background of unwanted interactions. The events are potentially useful until accepted or rejected by the computer. The planning of this part of the system requires a certain amount of judgment. Making the selection too restrictive may result in an undesirably small percentage of useful events in the data. This is expensive in data storage capacity and in computer time to select them from the background.

For this experiment an event was defined as one in which at least two pion-like phototube pulses and one neutron-like pulse were detected, the pions being required to be in separate quadrants of the dish. Pion-like pulses were those that had the proper amplitude and were originated by the phototube 5 nsec after a beam particle interacted in the target (prompt pulse). A neutron-like pulse was one that had the proper amplitude and occurred from 11 to 43 nsec following the two (or more) pion pulses. The pion-like pulses and the neutron-like pulses are hereinafter referred to as π pulses and N pulses, respectively.

The selection of events was performed by the fast-logic portion of the system. It completed the logical operations involved in the selection in about 200 nsec, and signaled the following circuitry when an event was detected. Figure 2 is a simplified block diagram emphasizing this portion of the system.

As shown in the block diagram, the 21 phototube dynode signals from each of four quadrants of the dish (α, β, γ, and δ) were summed in a 21-fold mixer to obtain four composite quadrant signals. The four quadrant signals were fed to 6 two-fold coincidence circuits to form all possible combinations of signals from two quadrants. An output from any one of the six coincidence circuits indicated that particles had simultaneously entered two quadrants of the dish. The six outputs were mixed and applied in coincidence with a signal from a counter telescope in the beam. There was a beam-telescope signal whenever a beam particle was deflected by the hydrogen target. An output from the Σ coincidence circuit indicated that the requirement of two pion pulses had been met.

To determine if a neutron-like pulse was present at the proper time, the output of the Σ coincidence circuit was used to open four gates simultaneously. The open time of each gate was fixed by a delay line to be 50 nsec following a "trigate" (GATE TRIgger) command. It will be noted that the same pion signals that originated the trigate also arrived at the inputs of the gate circuits. However, as indiated on the block diagram, the transit time of the signal from the phototube dynodes to the trigate input is T nsec, whereas the transit time from phototube to gate input is only (T-11) nsecs. Thus, provided the pion signal lasts for less than 11 nsec, only the N signals (if any) plus inevitable background pulses would pass through the gates. The gate outputs are labelled N(α), N(β), *etc.* They are summed in a mixer circuit and the summation applied to a fifth gate as another trigate. The signal input to this gate is the Σ coincidence output. The output of this circuit—the "π-gate" signal—thus appears only if both the π and N signals occur with the proper time relationship.

The coordinates of the particles of an event, *i.e.*, the code number of the scintillator through which it passed, are determined and temporarily stored by 168 coincidence-discriminator circuits[3]).

The anode of each of the 84 phototubes is connected to the inputs of two coincidence-discriminator circuits. The purpose of one is to detect π signals, the other, N signals. Therefore, one set of 84 coincidence-discriminator circuits receives as a second input the π gate singal generated by the fast-logic section. The other set gets the N gate. When an event occurs, the 84 π coincidence-discriminator circuits search for a π signal, and 11 nsec later the 84 N circuits search for an N signal. Any coincidence-discriminator that receives a sufficiently large input from a phototube in coincidence with its gate sets a flip-flop circuit, which retains the information until it can be stored in the buffer store.

The time separation of the π and N signals is measured by four chronotron circuits, one for each quadrant of the "dish"[4]). It was feared that the background signal from combining 84 phototubes into one chronotron input would give too high an accidental rate. By employing four chronotrons, the computer could discard N signals coming from the wrong quadrant.

The chronotron inputs from the fast-logic block

onsist of the four neutron-quadrant signals—
(α), N(β), N(α), N(δ)—and one (common) π
gnal. For an event of the proper type, only one
uadrant signal was generated, and the chronotron
ieasured the time difference between this quadrant
gnal and the π signal when commanded to do so
y the search command.

As shown in fig. 1, the input of the fast-logic
lock marked "enable π and N gates and search
ommand" enables or inhibits the generation of π
nd N gates and a search command according to its
oltage. Thus the control block can control the ac-
eptance of events for storage. Specifically, the
ates are disabled between Bevatron beam times,
nd also during the time an event is being stored.

The interrelation of the other blocks on the
iagram can be understood better by following the
equence of operation after an event. First the, fast-
ogic block will have detected the occurrence of
vent. It will generate a 20-nsec π gate pulse im-
iediately followed by an N gate pulse of the same
ength. These gates are timed to arrive at the coin-
idence-discriminator circuits at the same time as
ie π and N signals from the phototube anodes
espectively. Note that the π and N coincidence
iscriminators receive the same signals from the
hototubes; they rely on the timing of the gates
o separate the π's from the N's. Those coincidence
iscriminator circuits that have received phototube
ignals while the gates are present will have trig-
ered their discriminators and set their flip-flops.
he flip-flops then perform a temporary storing
ction until the event can be placed in the core
torage.

Simultaneously, signals are applied to the chro-
otron inputs. Since the velocity of both π's is very
lose to that of light, they strike the counters
imultaneously, and their occurrence can be
eralded by a single pulse—the "π signal". From
1 to 43 nsec later, a pulse arrives on one of the
uadrant N-signal lines corresponding to the
uadrant of the phototube array in which the
eutron landed. The chronotron measures the time
ifference and sorts it into one of seven serial "time
oxes", the narrowest being about 3 and the widest
bout 7 nsec. The output of the chronotron is
igitized into a 3-bit binary code for each of the
four channels. The code for the appropriate quadrant contains the number of the "time box" that corresponds to the particular event. The codes for the other three quadrants contain all zeros. As with the discriminators, the values of the codes are temporarily stored by flip-flops.

The occurrence of the π and N gates also sends an "event-has-occurred" pulse to the control circuits. This pulse in turn disables the fast gates so that no more events can be accepted until storage of the present event is complete. The control circuits initiate the routine necessary to record in the core storage the 168 bits of coordinate and 12 bits of chronotron information. The storage process takes 40 μsec. The control circuits then reset the temporary-storage flip-flops in both the discriminators and the chronotrons, and then again enable the π and N gates to start the search for the next event. This process will be repeated either until the core store has reached its capacity of 10 events or until terminated by the end of the Bevatron beam time.

Following the end of the accelerator beam time, the control block signals the buffer store to read out the stored information including the Bevatron pulse number, onto the paper tape. The punching process occupies most of the $5\frac{1}{4}$ sec between beam pulses.

As described above, the gate-forming circuitry in the fast-circuitry block was designed to select for storing only those groups of signals that had some of the characteristics of the events that we wished to record. It was expected that about one beam particle in 10^6 would form a desired event; thus the selection problem was quite severe. During the course of the experiment it was found that, owing to this high background rate, an undesirably large proportion of "events" that passed preliminary examinations by the "fast-logic" circuitry were obviously not of the desired type. Some of these contained many more than the two π signals and one N signal of the interaction of interest. These nonuseful events consumed core storage capacity needed for potentially useful events. Therefore, a "throw-away" inspection block was added. Its function was to take a second look at the event while it was in the temporary flip-flop storage before being placed in the cores. If the event had

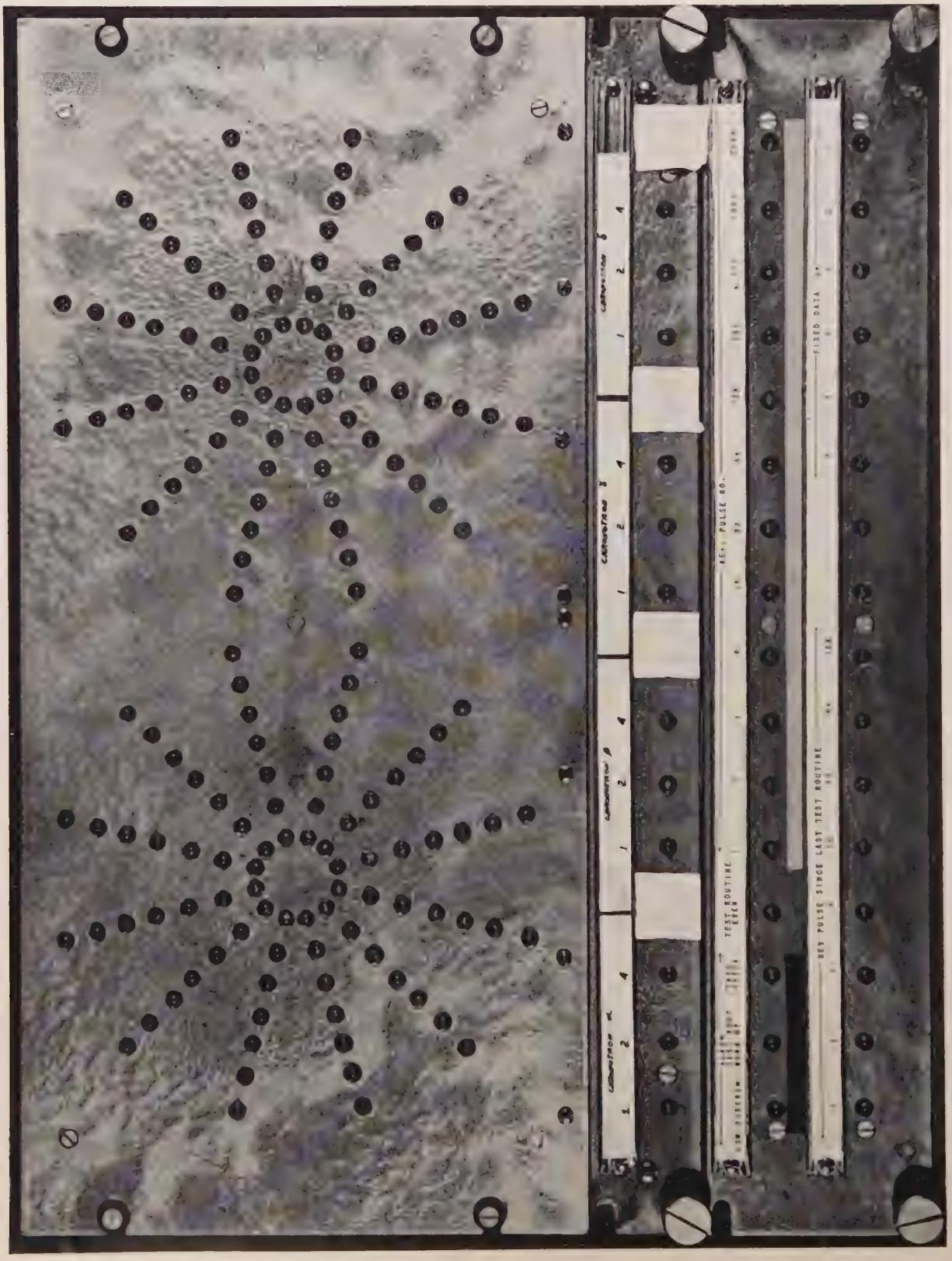

Fig. 3. Light display panel.

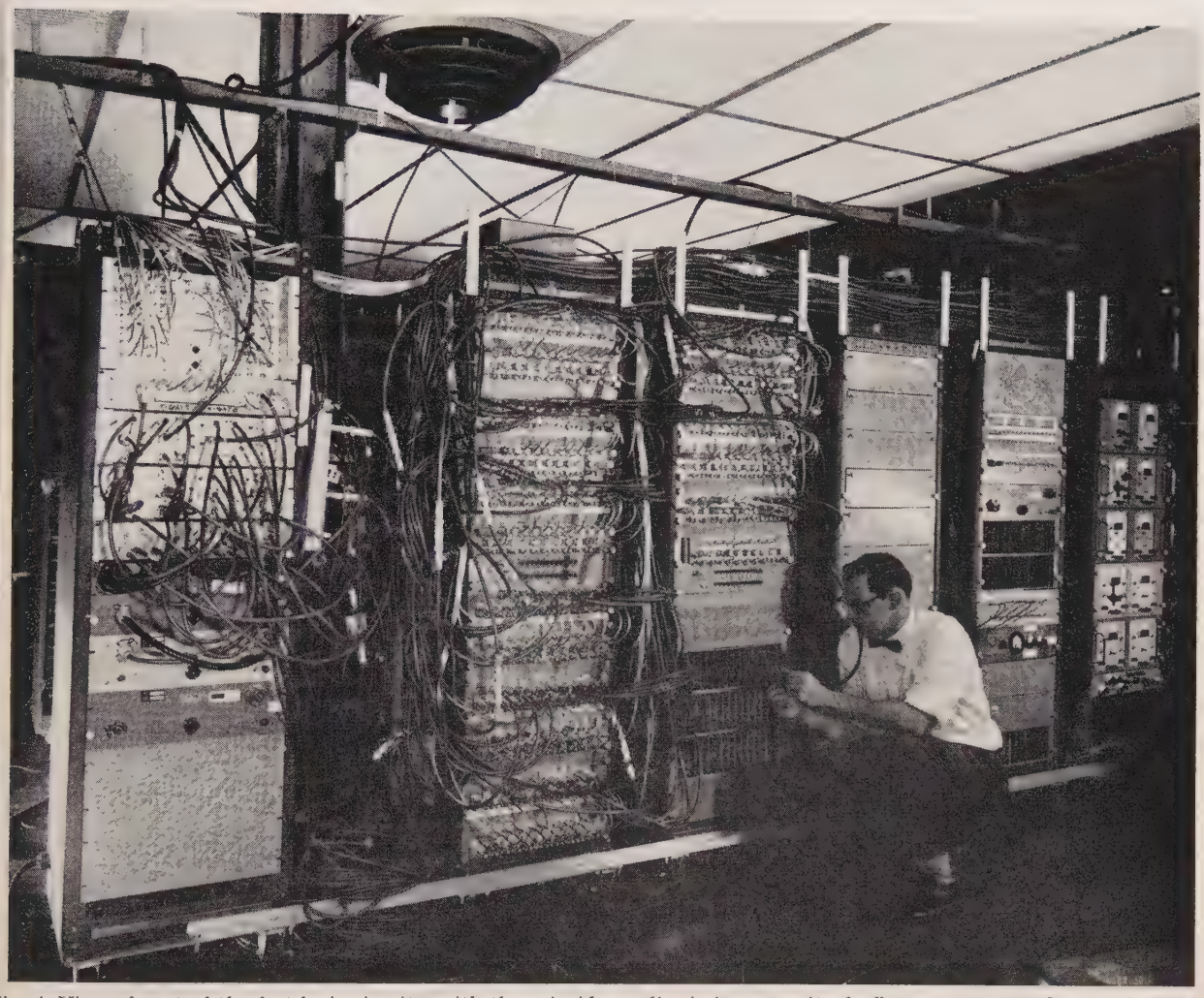

Fig. 4. View of part of the fast-logic circuits, with the coincidence-discriminator units, buffer store, test and control circuits and power supplies.

certain characteristics that obviously made it useless (e.g. chronotron signals in more than one quadrant), the throw-away block would signal this information to the control circuits, thereby inhibiting the "store" command, and causing the temporary storage flip-flops to be reset and allowing the π and N gates to be generated once more. The throw-away cycle consumed 10 μsec.

During an experiment, and especially during the tune-up phase, it is convenient to have displays of the information being gathered or processed by the system. These should be arranged so that the displayed information is quickly absorbed by the observer. Easily recognized patterns are important. In this system, a panel with 180 miniature light bulbs was used for this purpose. The panel contained one bulb for each of the 168 discriminators and 12 bulbs for the chronotrons. As shown in fig. 3, the bulbs for the discriminators were laid out in the same patterns as the actual scintillator elements. Appropriate circuits were employed to cause the light panel to display the information stored for only the first event of each Bevatron pulse[6]), i.e., to indicate which of the coincidence discriminators and chronotrons received pulses during the first event. A glance at the panel immediately indicated the geometrical and time relationship of the particles in that event. The light display panel was also useful in testing the system.

With systems of this complexity involving

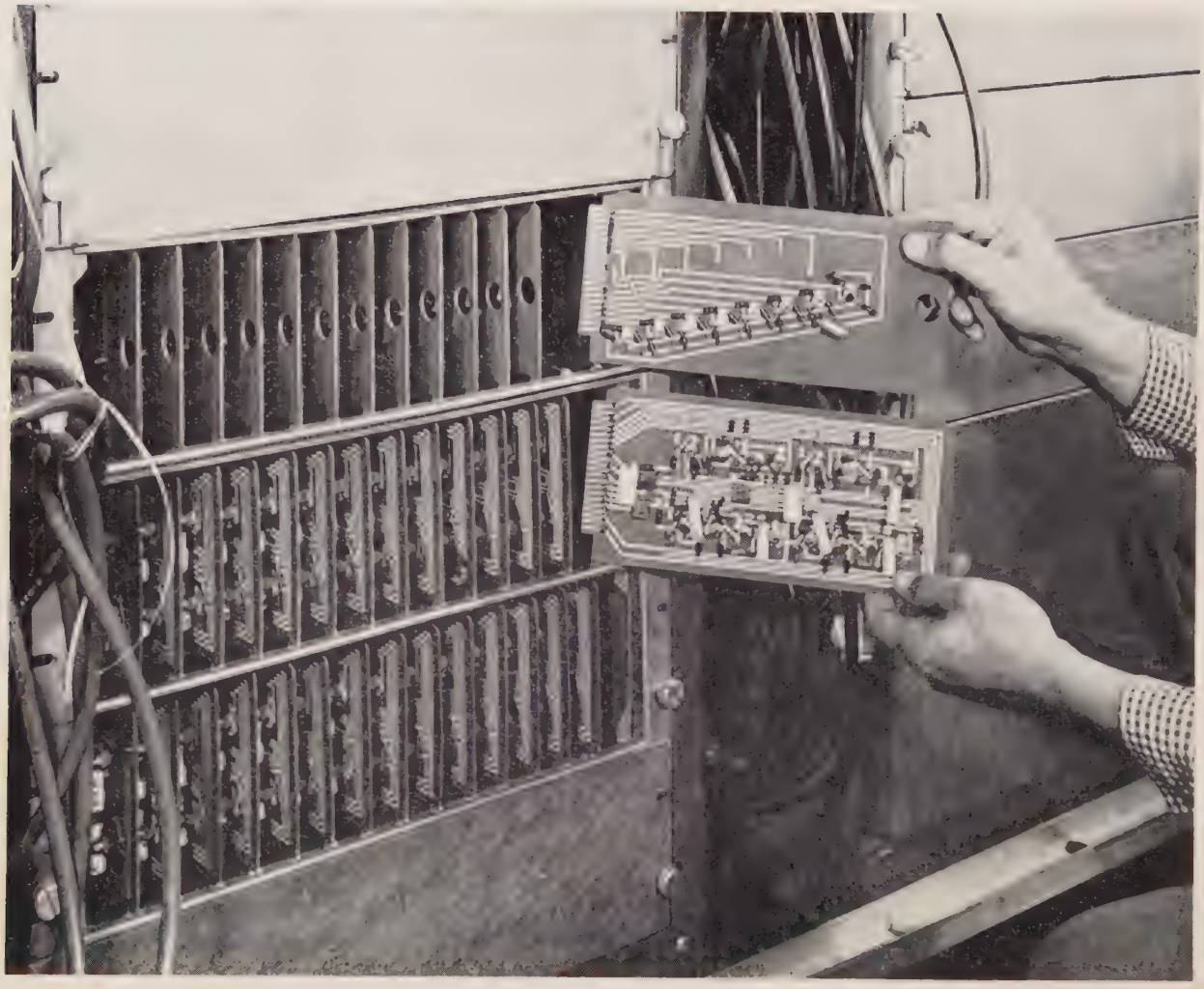

Fig. 5. Typical printed-circuit boards about to be inserted into bins.

hundreds of individual circuits and thousands of transistors, means must be provide for quick and easy checking of the operation. In the present system, this was carried out in several ways. On the circuit level, test jigs were made for several of the standard circuit boards, which were used in large numbers. In these jigs, simulated operating signals were applied to check the performance of the circuits. As an example of system-level checks, a test pulser applied simulated phototube pulses simultaneously to either half (84) of the 168 coincidence-discriminator circuits. Together with the light display, this pulser afforded a quick check of the range of sensitivities of the discriminators of these circuits. The results of this test could also be punched out on the paper tape and automatically checked to insure that all coincidence discriminators had the same sensitivity within $\pm$ 10% and that the buffer store and paper-tape punch were operating correctly. An automatic system for checking the timing accuracy of the chronotrons was also used. It displayed in a single pattern on a cathode-ray-tube screen the complete time characteristics of all four chronotrons. These tests are described in more detail in the companion papers.

4. General

The physical characteristics of part of the system are visible in fig. 4. Standard 19-in.-width relay

racks were used, and they were numbered 1 through 6 from left to right. Rack 1 contained part of the fast-logic circuitry. Rack 2 and the upper half of Rack 3 contained the 168 coincidence-discriminator circuits. The lower half of Rack 3 contained circuits that couple the outputs of the coincidence circuits to both the buffer store and the light panel. Rack 4 contained the buffer store. The light read-out panel was at the top of Rack 5, with the control and test circuitry below; Rack 6 contained the power supplies.

In general the circuits used in the system were built in a modular style. This modular feature is visible in fig. 5, which shows samples of two groups of transistor printed-circuit boards. Each board contained several identical circuits. The boards were contained in bins having a capacity of 14 boards each. The three bins visible in the photograph contained 52 boards of two types of circuits. Several identical circuits were grouped on each printed board whenever possible in this system. It was usually possible to rectify the effects of trouble on a particular board by replacing it with a pretested spare board. System "down-time" was greatly reduced in this way.

Approximately four-thousand transistors were used in this system. The operational time to date has been too short to obtain good figures for the reliability of the transistors and circuits. However, since the usual circuit defects were remedied, the results have been gratifying. As an example, the buffer store, which uses about 2000 transistors, operated 24 hr a day for 1 month without a circuit or transistor failure.

NUCLEAR INSTRUMENTS AND METHODS 12 (1961) 20–24; NORTH-HOLLAND PUBLISHING CO.

A TRANSISTOR COINCIDENCE-DISCRIMINATOR CIRCUIT FOR 10^{-8}-SECOND PULSES†

STANLEY C. BAKER††

Lawrence Radiation Laboratory, University of California, Berkeley, California

Received 15 February 1961

A transistor coincidence-discriminator circuit of better than 10^{-8}-sec resolution and 0.25-V sensitivity has been designed for use where large numbers of such circuits are required in a single system. The experience gained in operating 168 units in a physics experiment, and the methods developed for testing the sensitivity and resolution of the circuits during both initial checkout and operation in the experiment show the approach used to circuit design to be highly feasible.

1. Introduction

For several years, multiple-counter experiments have been performed at this Laboratory using two-fold coincidence circuits in which each channel receives pulses from a scintillation counter and a common gate pulse. The gate pulse, usually generated by a counter system, indicates the passage of a particle with a particular time of flight or momentum. Thus all coincidence channels are sampled for the gate period whenever the desired event is detected.

A pulse-amplitude discriminator follows the coincidence circuit to accurately determine which events produce signals above a predetermined threshold level and should be recorded. To relax the bandwidth requirements of the system after a coincidence has been detected, a memory circuit is employed to preserve the response of each event until further logical operations are completed.

Multiple-diode coincidence circuits whose outputs are appropriately delayed and mixed for display on an oscilloscope have been used in numerous experiments[1]). A permanent record is then made on photographic film for later analysis.

When a 168-channel system was proposed, it became evident that the experimental data should be acquired and preserved in a form suitable for immediate entry into a computer[2]). The coincidence-discriminator circuit described here was developed

† This work was done under the auspices of the U.S. Atomic Energy Commission.

†† Now at Cubic Corporation, San Diego, California.

[1]) See, for example, fig. 5 of C. A. Coombes, B. Cork, W. Galbraith, G. R. Lambertson, and W. A. Wenzel, Phys. Rev. 112 (1958) 1303.

[2]) S. C. Baker, F. A. Kirsten, D. A. Mack and C. E. Wiegand, Nucl. Instr. and Meth. 12 (1961) 11.

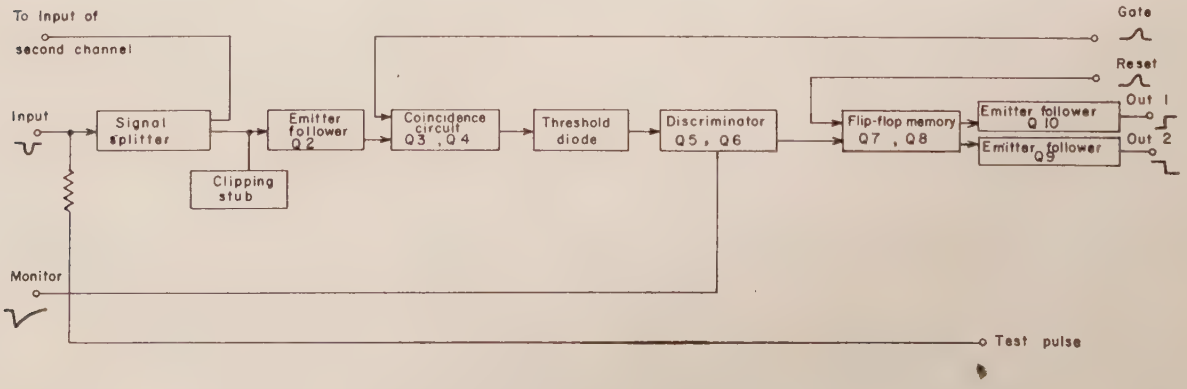

Fig. 1. Block diagram of the coincidence-discriminator circuit.

to accept pulses directly from multiplier phototubes without preamplification and to store the coincidence patterns electrically instead of photographically.

Development specifications for the unit are the following: The minimum input-amplitude sensitivity must be 0.25 V into an impedance of 125 ohms, but 10 V signals must not cause adverse effects. The memory must accept information at a rate of at least a 100 kc/s; however, 10 V noncoinciding pulses at either the phototube or gate inputs occurring with a frequency of 10 Mc/s must not cause accidental output signals. The time resolution of the coincidence circuit should be 5 nsec or less. The unit must operate satisfactorily up to an ambient temperature of 55°C. Since more than one coincidence circuit would be operated from each phototube signal, a means of operating units in parallel should be provided. The output of the coincidence-circuit portion of the unit must be monitored without affecting the operation of the remainder of the unit.

2. Circuit Description

At the time of development, the most economically feasible transistors with a sufficient gain-bandwidth product (i.e. $f_T > 100$ Mc/s) were PNP types. A diffused base, mesa unit, type 2N1143, was selected for use in the fast circuits. It has a minimum gain-bandwidth product (f_T) of 250 Mc/s at a collector potential of 10 V at 10 mA. Using PNP transistors meant that coincidence-circuit limiters had to receive positive base signals to cut off their collector currents.

A block diagram of the coincidence discriminator that was developed is shown in fig. 1, and the schematic circuit diagram in fig. 2.

The minimum acceptable input signal turned out to be 100 mV, which gave an adequate margin in sensitivity over the specified value of 250 mV. A phase-splitting stage, transistor Q1, was used to provide isolation between the portion of the signal fed to the coincidence circuit and that part which might be used to drive another unit or a phototube-signal monitor. For proper operation, the monitor jack is terminated in an impedance of 125 ohms. The input stage Q1 inverts negative phototube

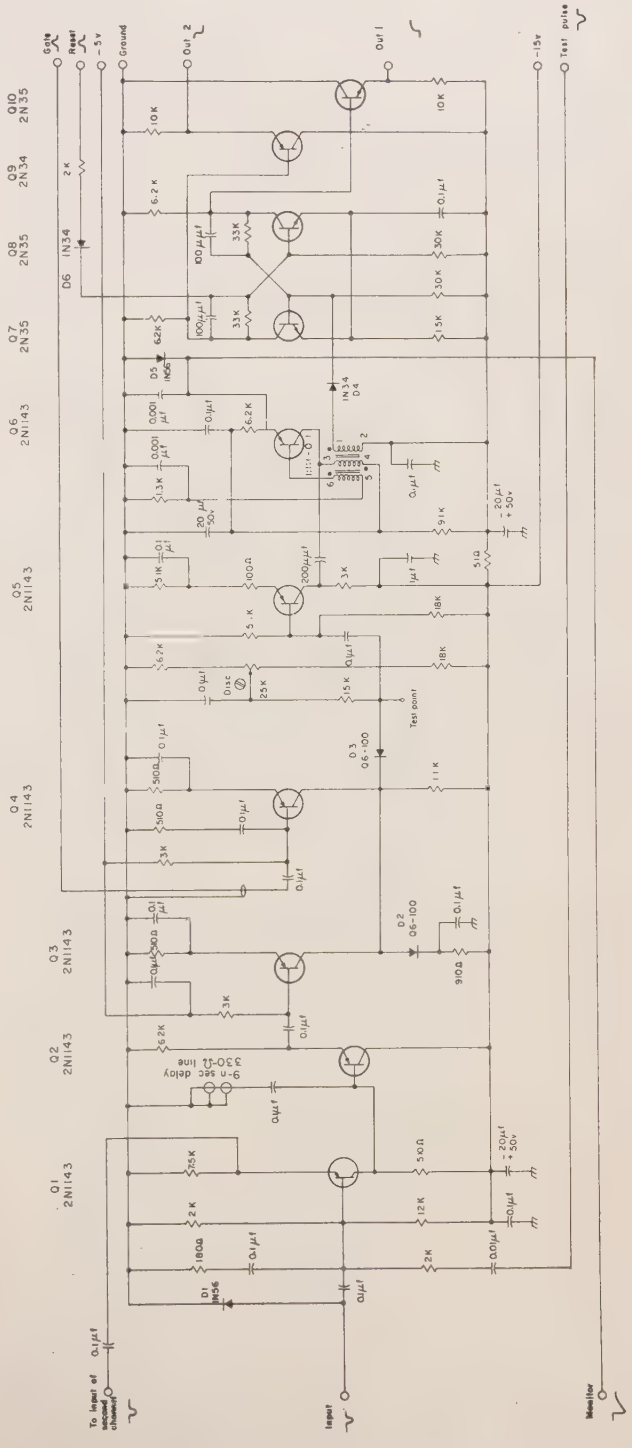

Fig. 2.
Schematic diagram of the coincidence-discriminator circuit.

signals in order to apply positive pulses to the coincidence limiters.

Since the pulse length of phototube signals may vary considerably a 9-nsec, 330-ohm, coaxial clipping stub was employed in the collector circuit of Q1 to limit this length to 18 nsec. The collector emitter follower drives five grounded-emitter amplifiers in parallel. The gain is 0.5 for each channel loaded with 125 ohms. It provides a positive output signal 0.5 V in amplitude and 20 nsec long.

A Garwin coincidence circuit was selected[3]). Diode D2 is the one normally associated with the

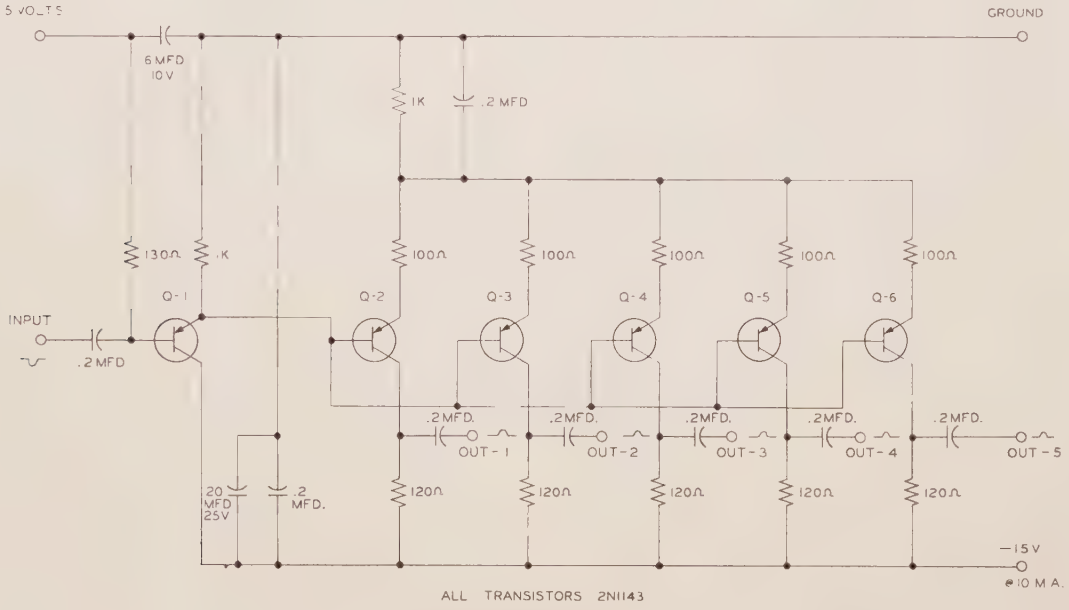

Fig. 3. Schematic diagram of the five-channel driver unit.

load resistance in parallel with the input impedance of transistor Q2 provides a termination for the clipping stub. The use of Q2 as an emitter follower provided a better impedance match for the clipping line than that afforded by feeding the clipped signal directly to limiter Q3.

The gate pulse, which is applied in common to each coincidence unit, is externally shaped to a specified height and width. Careful design was required in the gate distribution system to drive two groups of 84 coincidence units with a minimum delay and pulse lengthening. Distribution was made by first splitting the gate into three channels driven by a complementary PNP-NPN emitter follower. Each of these channels is then multiplied into six more channels in another emitter-follower unit. These channels are finally separated into five more to provide the gate signals to drive each coincidence unit.

A schematic circuit diagram of the last 5-channel gate driver is shown in fig. 3. A type 2N1143 Garwin circuit; it draws 55% of the combined collector currents of limiters Q3 and Q4. Both transistors Q3 and Q4 must be cut off before D2 unclamps and allows an output signal. The output is directed to an amplitude-discriminating diode D3. The coincidence ratio (doubles-to-singles) is approximately 10/1.

Several other coincidence circuits were investigated, but this one proved to be best suited to our needs. In other circuits degenerating resistors in the emitters of the limiters caused the input impedance to be much higher and allowed a better termination for a transmission line than could be obtained with the circuit actually employed. This, however, increased the pulse height needed for limiting. Decreased sensitivity was undesirable, while matching impedances was not a great problem, and so unbypassed emitter resistors were not used.

[3]) R. L. Garwin, Rev. Sci. Instr. **24** (1953) 618.

To obtain more output signal, the circuit of fig. 4 was tried, in an attempt to get a good coincidence ratio without sacrificing half the output current, as is done with the Garwin clamp diode. When one transistor in fig. 4 cuts off, the other side assumes the whole current; when both sides are cut off, the

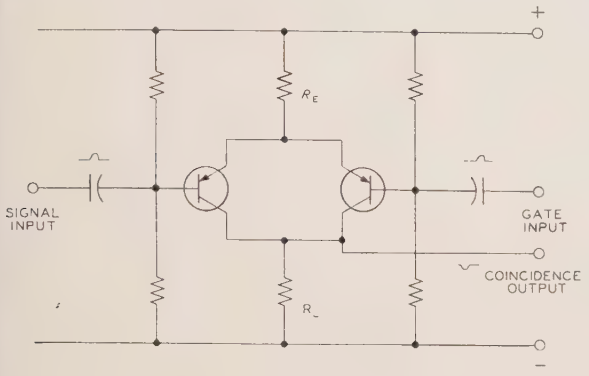

Fig. 4. Alternate coincidence circuit.

whole bias current is available as a pulse in the output. This worked well and provided the same resolution time as the Garwin circuit, but again the loss of sensitivity was too disadvantageous. This loss is, of course, due to the presence of the emitter resistor.

Amplifier Q5 and blocking oscillator Q6 serve to convert signals with an amplitude greater than the threshold bias on diode D3 into a 4-V, 0.8-μsec pulse. A blocking oscillator was chosen to generate this pulse, because it needs only one transistor and possesses a very sensitive triggering action. When biased beyond cut off, it exhibits good threshold stability. The pulse produced has a very stable width, and operation is good over a wide range of temperature.

To make sure that transients produced by the blocking oscillator did not feed back into the sensitive portion of the circuit, the power supplied to the trigger circuit had to be well-bypassed.

The capacitance loading by the memory flip-flop Q7 and Q8 reduces the input sensitivity of the blocking oscillator. Diode D4 provides some isolation for the blocking oscillator during its regenerative period.

Memory for coincident events is provided by an Eccles-Jordan bistable circuit. Two output connections are buffered by emitter followers Q9 and Q10.

Fig. 5. Coincidence discriminator unit.

The flip-flop is reset by a positive pulse applied to diode D6 after the necessary logic functions have been completed by the rest of the readout system.

Each unit was constructed on a glass-epoxy-laminate, printed-circuit board measuring 3 by $10\frac{1}{2}$ in. A photograph of this unit is shown in fig. 5. Ten coincidence-discriminator units and two gate-circuit driver boards were plugged into a frame measuring $3\frac{1}{2}$-in. high by 19 in. wide. Phototube-signal and coincidence-monitor connections were made to a front panel on each unit; all other cont nections were made through connections at herear of the board.

During initial line-up as well as during the running of multichannel experiments it was desired to check the operation of the unit—especially the threshold sensitivity[4]). A test signal (introduced in parallel with the phototube input and in time coincidence with a test gate pulse) provided a means of making this measurement. A pulser was constructed to allow test signals to be introduced in this manner by either a single pulse or at a 800 cps rate. The pulses were shaped to resemble the actual phototube signals.

3. Operation

The amplitude threshold of the coincidence-discriminator circuit was found to be a strong function of the dc supply voltages. The — 5 V bias potential had to be kept within 0.1% to keep the threshold variation within 1%. The sensitivity to the — 15-volt supply line was not as great; it had to be maintained within 1% to hold the threshold within 1%. These voltages were monitored by a 2% full-scale recorder during operation.

The drift of the threshold level with time was quite acceptable. At the Bevatron without temperature control during a normal 8-h period, four or five of the 168 units would drive outside of a $\pm$ 5% range. This was measured by the checking system previously mentioned[4]). It was a simple matter to periodically readjust the threshold levels of these units that had drifted outside the prescribed range.

During the early part of the experiment, approximately 12 transistors were burned out in the input amplifier Q1. It was found that switching on the high voltage for the phototubes caused a large positive transient on the signal line. A protective diode, D1, is now placed across the input circuit.

Acknowledgements

The circuit and package design was done in cooperation with H. G. Jackson. Stuart Wright checked and maintained each circuit both before and during operation.

[4]) S. C. Baker, Q. A. Kerns, F. A. Kirsten, D. A. Mack and T. A. Nunamaker, Nucl. Instr. and Meth. **12** (1961) 1.

NUCLEAR INSTRUMENTS AND METHODS 12 (1961) 25–31; NORTH-HOLLAND PUBLISHING CO.

A SOLID-STATE CHRONOTRON FOR DIGITIZING TIME DELAYS†

ARTHUR E. BJERKE, QUENTIN A. KERNS and THOMAS A. NUNAMAKER

Lawrence Radiation Laboratory, University of California, Berkeley, California

Received 15 February 1961

This solid-state chronotron measures the relative time delay between two shaped photomultiplier pulses, and quantizes this time delay into seven time intervals with widths of 3 to 7 nsec. These intervals represent the difference in time of flight of two particles in a large scattering experiment, and may be varied at will by changing front panel cables. The quantized time delay is then stored in a buffer storage until readout, at which time the system is recycled. Because the chronotron was used with a system having a 40-μsec cycle time, a maximum repetition rate of 100 kc/s was selected. However, this rate could be increased considerably if necessary.

The time intervals are formed by splitting the two shaped photomultiplier signals into parallel diode coincidence circuits, with the time delay of each coincidence circuit set for the center of its respective time interval. Since the coincidence circuits are identical, both the position and width of each time interval are determined only by the delay cables. Thus the coincidence circuit with the greatest output voltage indicates the correct time interval. To detect this voltage the stretched output of each coincidence circuit has a common ramp voltage added to it, and together these signals begin driving a bank of blocking oscillators. As soon as one blocking oscillator triggers, all others are disabled and the blocking oscillator that triggered sets up its binary coded number in the buffer storage. As the ramp generator always insures that one blocking oscillator triggers there is never a hole between time intervals, even if the edges of the intervals drift, because when one interval expands its neighbors will contract.

Long-term stability of the time interval centers is a few tenths of a nanosecond, and the 24-hr stability of the edges of the intervals is $\pm$ 0.5 nsec. With the aid of a TV monitor used in checking the system, the chronotron can be held within the above limits indefinitely by simple daily adjustments.

1. Introduction

The solid-state chronotron described here is designed to measure the time interval between two photomultiplier signals[1]). This interval represents the difference in time of flight of pions and neutrons in a large scattering experiment[2]).

The chronotron quantizes time into seven time intervals which vary in duration from 2.9 to 7.2 nsec, as shown in fig. 1. It also stores the binary-coded numbers of the time intervals in a flip-flop-buffer storage. For the time measurement described here, all phototube signals could have been superimposed onto two signal lines. However, because of the noise contribution of the large number of photomultipliers used in the experiment, it was felt safer to employ four separate chronotron channels.

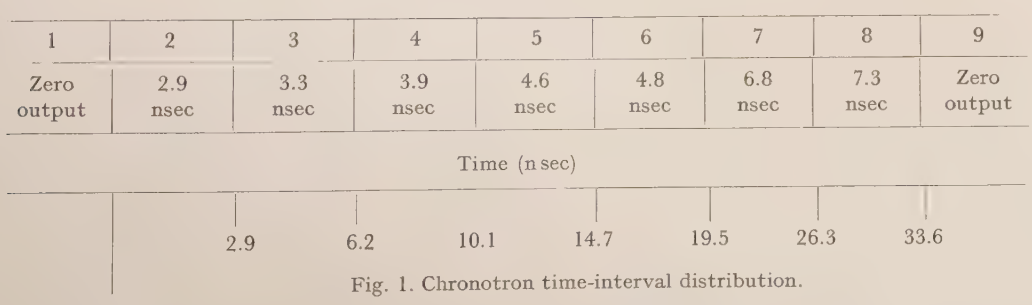

Fig. 1. Chronotron time-interval distribution.

Since all the chrontrons are identical, this discussion will be limited to only one unit. Figure 2 is

† This work was done under the auspices of the U.S. Atomic Energy Commission.

[1]) I. A. D. Lewis and F. H. Wells, "The Chronotron Timing Unit", in *Millimicrosecond Pulse Techniques* (McGraw-Hill Publishing Co., New York, N.Y., 1954) pp. 269–271.

[2]) S. C. Baker, F. A. Kirsten, D. A. Mack and C. Wiegand, Nucl. Instr. and Meth. 12 (1961) 11.

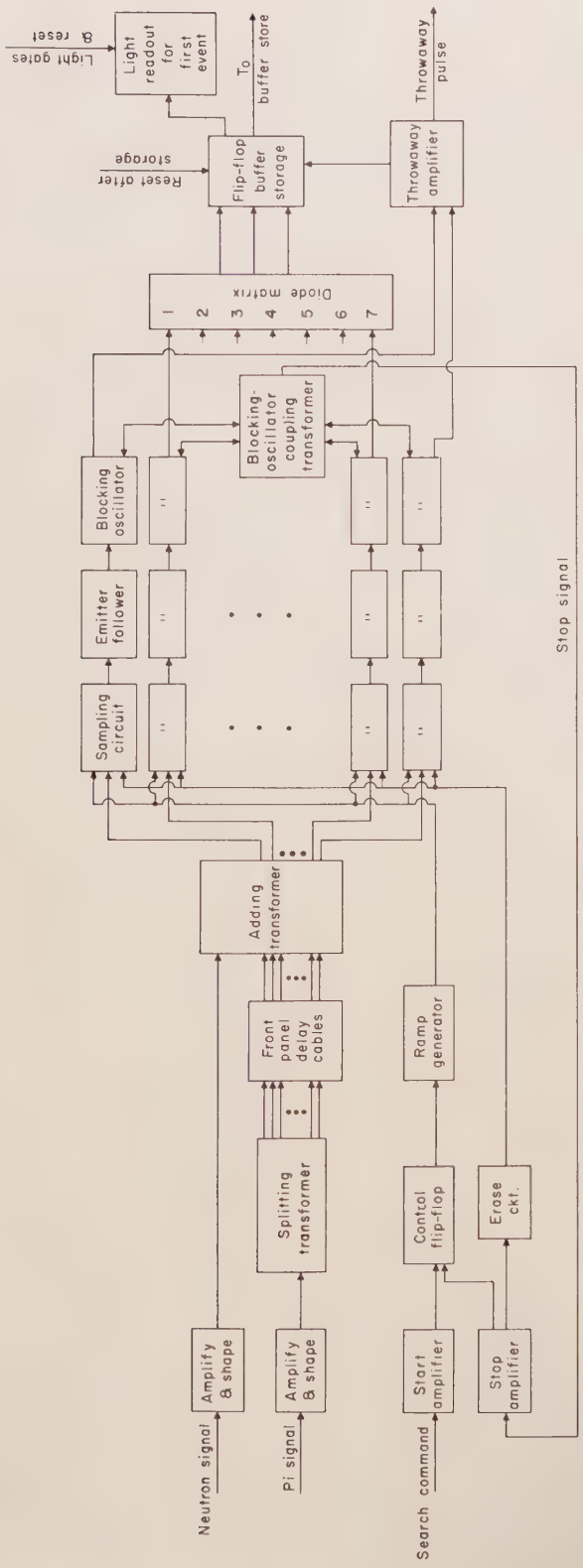

Fig. 2. Chronotron block diagram.

a block diagram of the chronotron; fig. 3 shows the sampling and detection circuits. Figure 4 shows all four chronotrons mounted together, along with their monitoring and power-supply panels. An individual chronotron is also shown in figs. 5 and 6. A provision for monitoring has been used with the chronotron, and has proven very necessary[3]). With the amount of equipment used, monitoring is needed in setting up the equipment initially as well as in checking each channel once the equipment is operating.

The time intervals are formed by splitting the two photomultiplier signals (called π for pion, and N for neutron) into parallel diode coincidence circuits, with the time delay of each circuit set for the center of its respective time interval. Since the coincidence circuits are identical, both the position and width of each time interval are determined only by the delay cables associated with that channel. Thus the coincidence circuit with the greatest output voltage indicates the correct time interval. In order to detect this, the stretched output of each coincidence circuit has a common ramp voltage added to it, and together these signals drive a bank of blocking oscillators. As soon as one blocking oscillator triggers, all others are disabled, and the blocking oscillator that triggered sets up its channel number in the flip-flop buffer storage. Because the ramp generator always insures that one blocking oscillator triggers, there is never a hole between time intervals even if the edges of the intervals drift; when one interval expands, its neighbors contract. If the ramp generator is not started, none of the blocking oscillators triggers, since the outputs of the coincidence circuits alone are less than the blocking-oscillator bias. If the ramp generator is fired in the absence of N and π signals, the most sensitive blocking oscillator will fire. For this reason the end blocking oscillator—numbers 1 and 9—are made slightly more sensitive than the others. Thus if the ramp is started in the absence of any signal, a zero is read out.

Long-term stability of the time-interval centers is a few tenths nanosecond, and the 24-hr stability of the edges of the intervals is $\pm$ 0.5 nsec. With the

[3]) S. C. Baker, Q. A. Kerns, F. A. Kirsten, D. A. Mack and T. A. Nunamaker, Nucl. Instr. and Meth. **12** (1961) 1.

id of a raster-type cathode-ray-tube display used n checking the system[3]), the chronotron can be held ithin the above limits indefinitely by simple daily djustments.

signals. The channel with the largest sampled charge corresponds to the best coincidence, and thus represents the correct time interval. To detect this channel, a bank of identically biased blocking

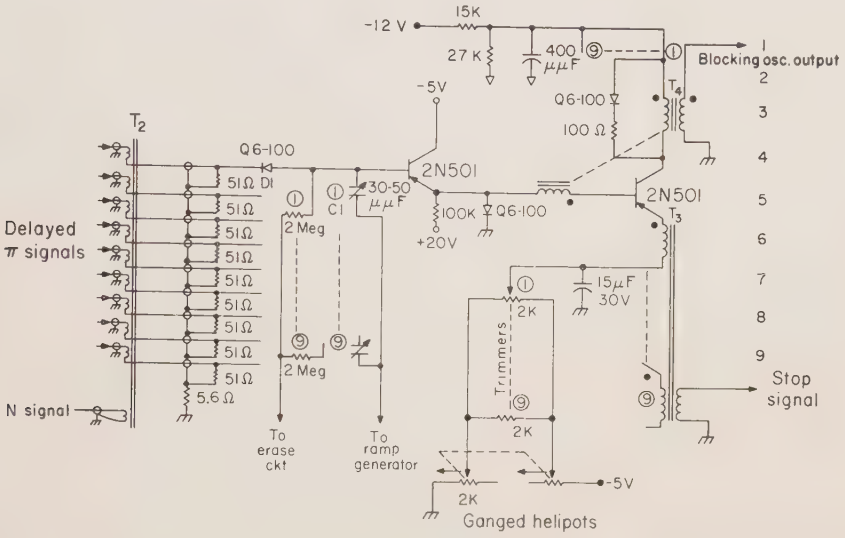

Fig. 3. Chronotron sampling and blocking-oscillator circuits.

. Circuit Operation

The N and π phototube signals are amplified and haped by Hewlett-Packard 460A and B distributed mplifiers. The shaped pulses have symmetrical ave shapes with a half width of about 6 nsec and ery little amplitude fluctuation. The output of the amplifying and shaping circuits is fed into a plitting transformer where it is split into nine dentical outputs. These outputs are then delayed elative to one another by the center-to-center time eparation of each chronotron interval. The delay ables are made accessible from the front panel to acilitate changing the width of the time intervals. Nine channels are necessary to form seven time oxes, the extra two channels being necessary to ive good time definition to the beginning of the rst time box and the end of the seventh time box. fter being delayed, the π signal passes through an dding transformer (T2 of fig. 3), where the N gnal is added. The sum of these two signals is then pplied to a Qutronics Q6-100 diode that samples he pulse through a sampling capacitance C_1 of g. 3), thus leaving a charge on the sampling capa- itor that is proportional to the sum of the two oscillators is driven toward firing by a ramp voltage applied to the low side of the sampling capacitor (C_1). The channel with the largest signal triggers its blocking oscillator first and disables all other blocking oscillators before they can trigger. This disabling is accomplished mainly by coupling all the blocking-oscillator emitters through a common-emitter transformer (T3 of fig. 3). Therefore the firing of any one increases the reverse cut-off bias on the other blocking oscillators, thus preventing them from triggering.

The ramp is turned off by a stop signal taken from the common-emitter transformer (T3) of the blocking oscillator. This signal also starts an erase circuit that discharges each sampling capacitor, with a 10-μamp discharge current lasting for 10 μsec.

The decimal outputs of the blocking oscillators are fed through a diode matrix to a flip-flop buffer storage. Here the channel number is stored in binary form and is eventually read into the core storage. Alternatively, the blocking-oscillator outputs may be connected to the throw-away amplifier, which immediately resets the whole system.

3. Splitting and Adding Transformers

The splitting transformer (T1) for the π signal has a 50-ohm input impedance and a 5.6-ohm output impedance (*i.e.*, nine parallel 50-ohm Sub-Minax coaxial outputs). The transformer has a bifilar winding on a Ferroxcube type-102 core. There are four parallel primary windings and eight parallel secondary windings. Parallel windings are used in order to reduce the leakage inductance of the transformer. The measured rise time of this transformer is 1.2 nsec.

The π and N signals are added by means of the adding transformer (T2) placed as close as physically possible to the sampling diodes. The N signal is brought in on a 50-ohm coaxial and connected to a 6-turn winding on the type-102 core. The nine 50-ohm coaxial cables which contain the delayed π signals are bundled together and wound with two turns on the core. Each cable is terminated in a 51-ohm resistor, and its center conductor fastened to the Q6-100 sampling diode (D1 in fig. 3). The shields of these nine cables are tied together on the sampling diode side of the core and grounded through a 5.6-ohm resistor. This resistor terminates the incoming N signal, which then appears across the outer conductor of the nine cables and ground. The signal at the input of the sampling diodes (D1) to ground is the sum of the π and N signals.

4. Sampling Circuit and Buffer Amplifier

The sampling diodes are selected to insure that all nine circuits have similar sampling characteristics. First the diodes are selected for a reverse impedance of at least 1 meg, which gives leakage currents (I_d) of 1 μamp or less. Next the junction capacitance (C_d) and the forward conductance are measured. From this data, nine similar diodes are selected for each chronotron. The C/I decay time constant of the sampling circuits must be kept large with respect to the time necessary to trigger a blocking oscillator. (Here C, the total sampling capacitance, is equal to C_1 plus C_d and the input capacitance of the emitter follower. The total leakage current, I, is due to the reverse leakage of the sampling diode, I_d, plus the base current of the emitter follower, I_b.) With the circuit used, the decay-time constant was of the order of 16 μsec. To keep this time-constant high the base current (I_b) of the 2N501 emitter followers is kept to less than 2

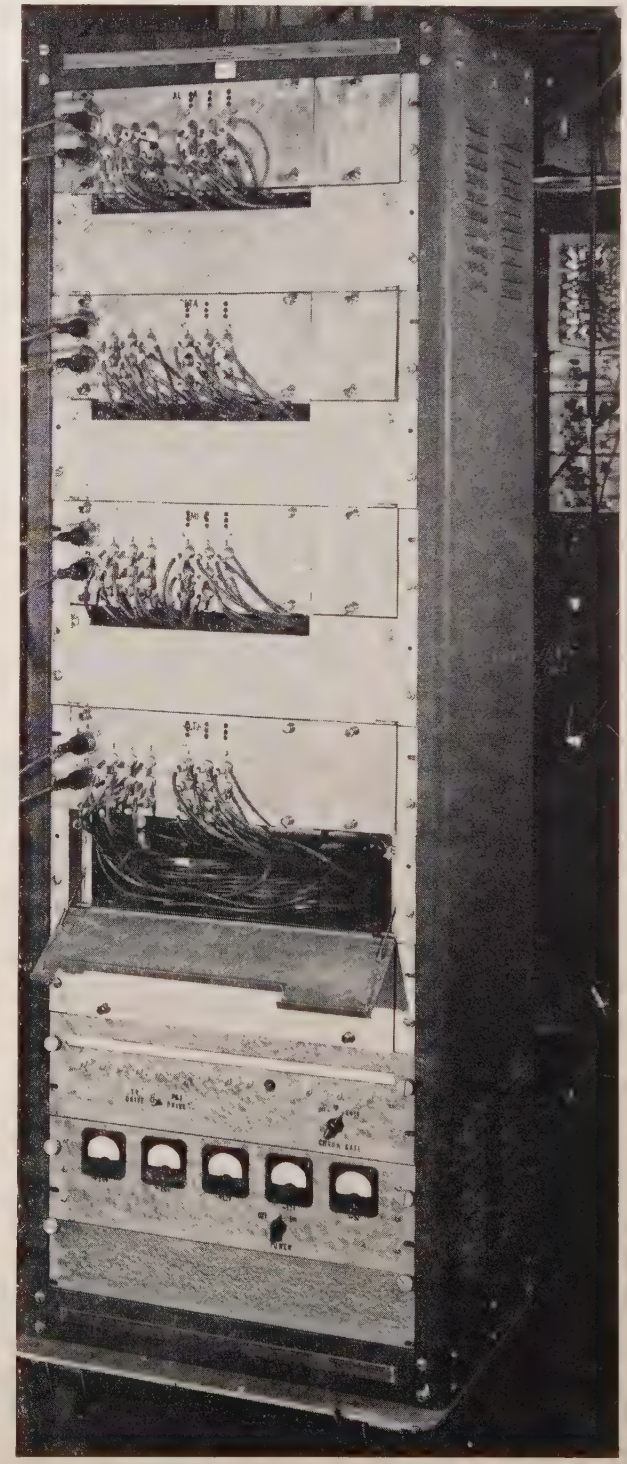

Fig. 4. Chronotron rack showing four chronotrons.

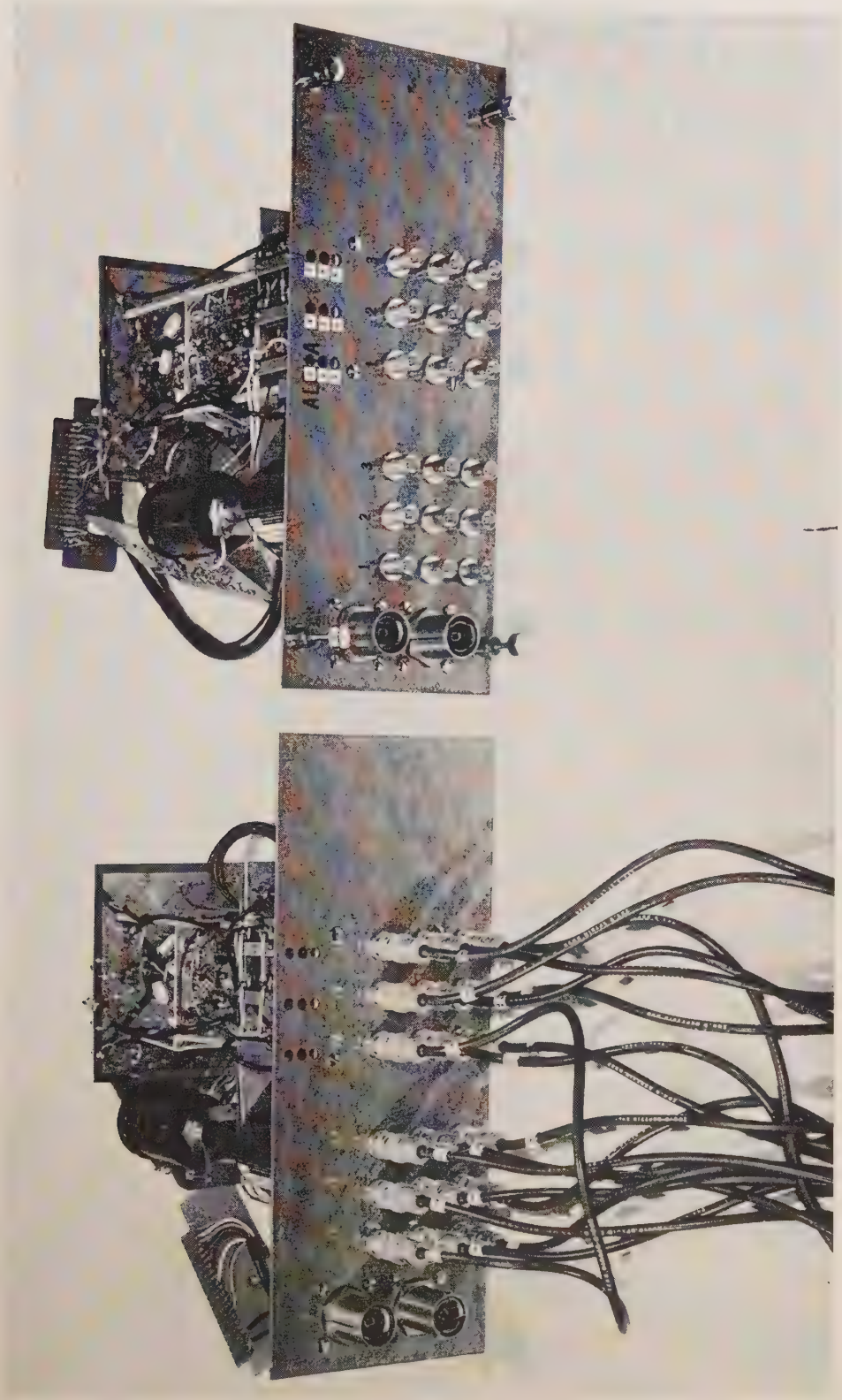

Fig. 5. Front view of two chronotrons showing one unit with delay cables and another without.

μamp by using high-beta transistors with low collector leakage current. The nine emitter-follower transistors for each chronotron are selected to have similar base currents, thus keeping all delay time constants similar. The final adjustment of the delay time constant is made by trimming the sampling capacitance (C_1). The process of selection described here may seem overly restrictive, but we have found that the number of rejected components has been very small, because components that cannot be used in one part of the circuit usually can be used in another part of the circuit.

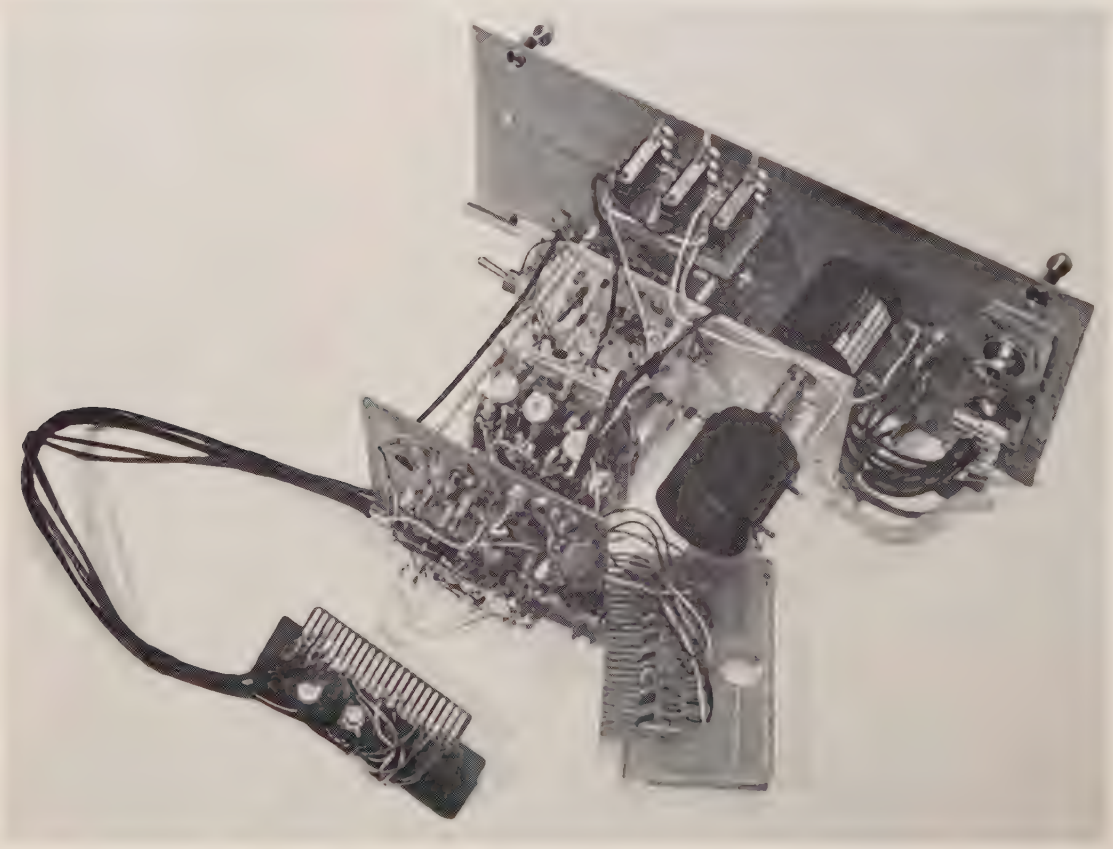

Fig. 6. Top view of chronotron.

5. Blocking Oscillators

The blocking oscillators (see fig. 3) are biased in a cut-off condition, and their emitters are all coupled together through the emitter-coupling transformer (T3). When the ramp is applied, all blocking oscillators are driven toward conduction; the channel with the largest signal will trigger its blocking oscillator first. As soon as the first blocking oscillator triggers, all others are prevented from triggering by the action of the emitter-coupling transformer (T3), which increases the cut-off bias of all the other blocking oscillators as soon as any one has triggered. A stop signal is taken from the emitter-coupling transformer, which immediately reverses the ramp (this further insures that no other blocking oscillators will fire). In addition, the blocking oscillators have a common power supply to the collector (*i.e.*, the simple RC network shown in fig. 3) which stores only enough charge to support the firing of one blocking oscillator. By using these various precautions we have obviated trouble from double firing.

The blocking-oscillator transformer (T4) is wound bifilar on a type-102 Ferroxcube core, with a three-turn base winding, a 12-turn collector

winding, and a six-turn output winding. The emitter-coupling transformer (T3) is also on a type-102 core. The blocking oscillator works into an impedance of about 50 ohms through this transformer. Type-2N501 transistors are used for the blocking oscillator and are selected for a minimum beta of 30. We have found that the majority of the transistors that can not be used in the emitter follower can be used as blocking-oscillator transistors. The firing voltage of the blocking oscillators was made adjustable by means of a varying dc potential at the ground side of the emitter coupling transformer (T3). Rise time of the blocking oscillator was 12 nsec, and the equivalent noise referred to the base of the transistors was 1.5 mV.

6. Readout and Control Circuits

The outputs of the blocking oscillators are fed directly to a diode matrix with a binary 1, 2, 4 readout. The diode matrix drives a bank of three flip-flops that serve as the buffer storage between the chronotron and the core storage of the system[4]). Once the core storage has accepted the output of the chronotron, a reset signal is generated which resets the chronotron flip-flops. At this point the chronotron is ready to accept a new input.

The chronotron ramp signal is normally initiated by an external search command. When this command is not available, the chronotron may be started directly from the N signal by taking this signal from the adding transformer T2.

7. Operating History

Four chronotrons were built and installed to measure time of flight in a large scattering experiment[2]). The time intervals for this experiment ranged from 3 to 7 nsec and are shown in detail in fig. 1. A rastertype cathode-ray-tube display was used to monitor the chronotron intervals during the experimental dead time[3]); in operation with the Bevatron, monitoring was almost continuous.

During the experiment, the 24-hr stability of the edges of the time intervals was within $\pm$ 0.5 nsec. To correct for this shift, the chronotron was adjusted daily, thereby operating within these limits during the entire experiment. Short-term stability of the time intervals was within a few tenths of a nanosecond.

Acknowledgements

Many thanks are due the people who helped make this chronotron possible. In particular Mr. Robert F. Reynolds handled the mechanical design and construction. Messrs. Lee J. Wagner, William S. Flood, and E. Thomas Clark, contributed their time and ideas.

[4]) Frank Evans and Frederick A. Kirsten, Nucl. Instr. and Meth. **12** (1961) 39.

NUCLEAR INSTRUMENTS AND METHODS 12 (1961) 32–38; NORTH-HOLLAND PUBLISHING CO.

A TRIGGERED NANOSECOND LIGHT SOURCE†

QUENTIN A. KERNS and GERALD C. COX

Lawrence Radiation Laboratory, University of California, Berkeley, California

Received 15 February 1961

A nanosecond light source based on a corona discharge started by field emission has been developed for attachment to scintillation counters.

These individual light sources, placed to illuminate each phototube and fired by a pulse generator through splitting transformers and cable delays, have facilitated the coincidence timing of an array of photomultiplier detectors. Pulse generation, a pulse-splitting transformer, light-source construction, and timing properties, as well as spectral intensity are discussed. An optical attenuator designed for the source is described.

1. Introduction

The coincidence timing of an array of photomultiplier detectors has been facilitated by use of a light-pulse generation system for simulating nuclear events. The system consists of a pulse generator, pulse-splitting transformers, cable delays, and individual light sources placed to illuminate each phototube.

Figure 1 illustrates the arrangement. It is desired to simulate an event by producing a pattern of light pulses in appropriate time sequence at the various phototubes. For example, consider the hypothetical pattern, shown in fig. 2, of an event in which simultaneous pulses illuminate Phototubes 1 and 3, whereas Phototubes 2 and 4 receive pulses with

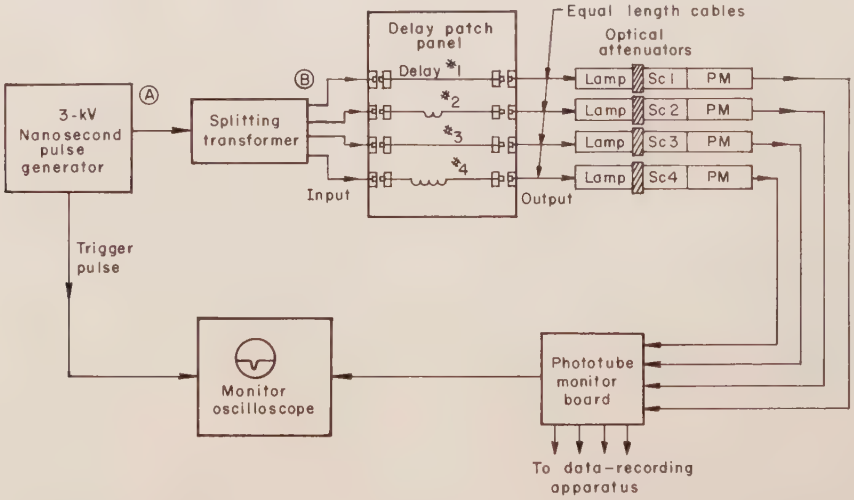

Fig. 1. Corona lamp simulation of a nuclear event.

Fig. 2. Illustrative pattern of pulses.

† This work was done under the auspices of the U.S. Atomic Energy Commission.

relative delays of 2 and 18.5 nsec. As a matter of convenience, the time delays to and from the patchboard shown in fig. 1 can be equalized; in such a case, to set up the pattern in fig. 2, one would insert a minimum-delay patch cable in Channels 1 and 3, (e.g., 2 nsec), and in Channels 2 and 4 delays of 2 and 18.5 nsec plus the minimum (thus, 4 and 20.5 nsec).

It is clear that the time jitter of any one of the pulses relative to the pattern must be minimized. The pulse-generating system secures timing accuracy by generating a single high-level pulse and distributing it to the lamps via splitting transformers and coaxial lines. Thus the voltage pulse pattern at the lamps is inherently jitter-free. The recurrence rate of the pattern, on the other hand, need not be precise. Usually, the patterns are generated during beam-off intervals. When the pulse generator is switched on, the pattern recurs at a rate of about 100 pulses/sec.

Trigger pulses, noted in fig. 1, are derived by transformer coupling from the high-level pulse and are useful in starting oscilloscope sweeps in advance of the phototube signals and as fiducial marks along the sweep. Delay in the signal cables and in the phototube (approx. 50 nsec) is usually sufficient to allow for sweep-starting time.

2. Pulse Generator

The electrical pulses are generated by switching a charged coaxial cable into an output transmission line of matched impedance (51 ohms). A mercury capsule† in a constant-impedance oil-filled enclosure is the switch. Figure 3 shows typical current-voltage characteristics for such a switch prior to electrical breakdown. Polarity has little effect on the current-voltage characteristic. A simplified schematic diagram of the pulse generator is shown in fig. 4.

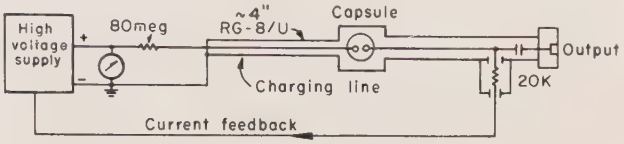

Fig. 4. 3 kV nanosecond pulse generator simplified schematic.

The capsule relay contact is not vibrated to produce contact closure. Instead, the voltage on the charging cable periodically rises to the breakdown

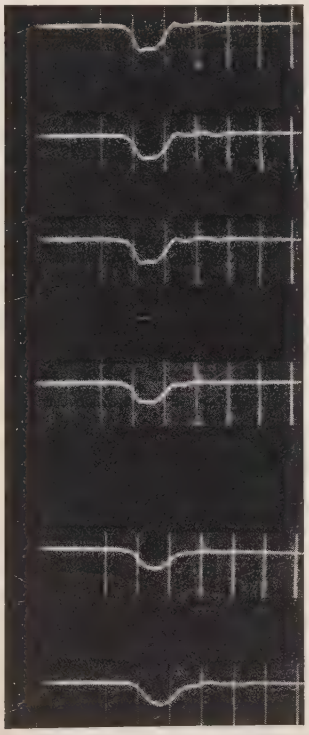

(a) The 3000-V pulse output from the generator.

(b) One of the four 1500-V outputs from the splitting transformer.

(c) A 3000-V generator pulse after passing through 22 ft. of RG-8/U.

(d) Pulse (a) after passing through 76 ft. of RG-8/U. Amplitude is about 2400-V. The amplitude loss is 20%.

(e) Pulse (a) after it passes through 55 ft of RG-55/U. The amplitude loss is 25%.

(f) Pulse (a) after passing through two splitting transformers cascaded, plus 55 ft of RG-55/U. Amplitude is 540-V. With no loss the amplitude would have been 750-V.

Fig. 5. Wave shapes for some combinations of generator, transformers and cables.

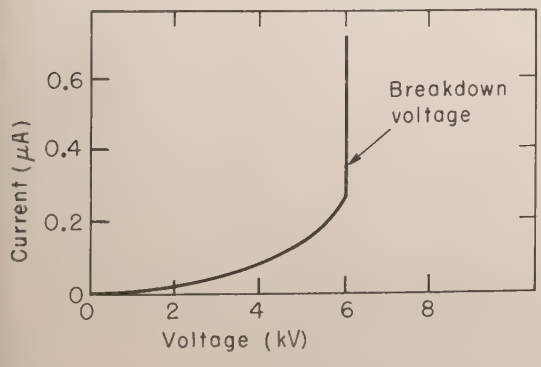

Fig. 3.
Typical current-voltage curve characteristic for mercury capsule.

† The capsules used were obtained from the Western Electric, 275-C, and from C. P. Clare and Company, HG-1003 mercury-wetted contact relays. A few capsules have relatively high leakage currents. These are not used in the pulse generator, but may be adequate for other uses.

potential and a spark occurs. Pulses that have the shape shown at (a) in fig. 5 are produced at about 100 pulses/sec.

After several hours of operation, it is desirable to redistribute mercury on the contact surfaces; a coil is provided to vibrate the relay contacts for the purpose. The high-voltage supply and current-regulation circuitry is all solid state, with a power consumption from the 60-cycle supply of 4.8 watts. Sixteen generators of the 3X5403 type (fig. 6) have been built for the application discussed here.

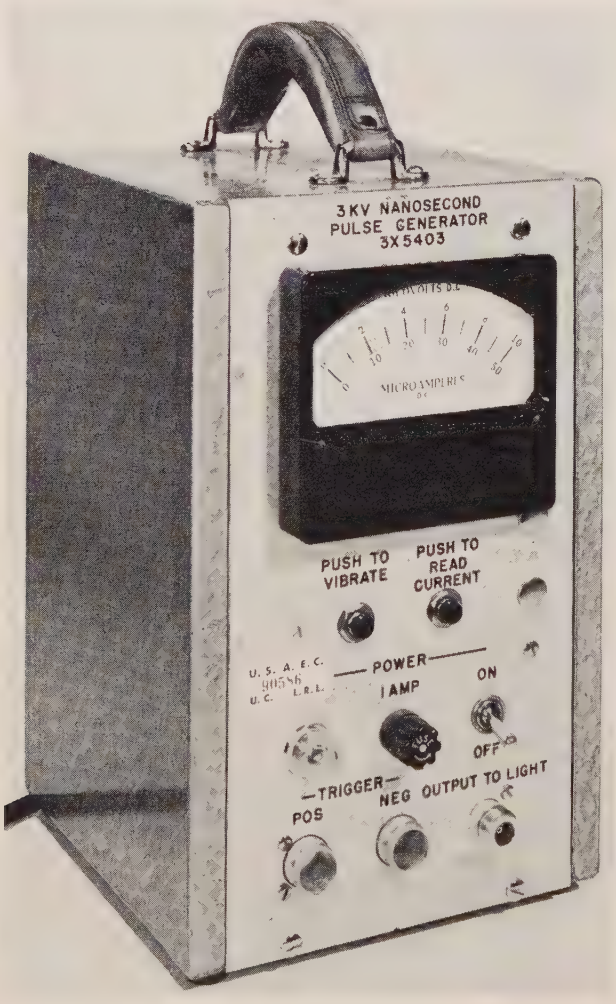

Fig. 6. 3 kV nanosecond pulse generator.

3. Splitting Transformers

The input and output impedances of the splitting transformer are 51 ohms. Four equal and synchronous outputs are provided at just half the input voltage. Thus, one transformer can feed four others to produce sixteen identical signals at $\frac{1}{4}$ the voltage level of the primary pulse generator. The rise time of the transformers is adequate for an additional cascade, from which there would be 64 output channels available at $\frac{1}{8}$ the generator voltage. There is some loss in rise time and amplitude in the transformers, but it is less than the loss in cables that are used to delay and distribute the pulses. The transformer is constructed of four equal lengths (1.6 nsec) of miniature 51-ohm coaxial cable (RG-174/U). The series-parallel connection of the four cables may be seen in the photograph of the transformer, fig. 7. Two of the four cables have a voltage pulse along the shield length, and are wound on a ferroxcube 102 toroid 1-in. in diameter to raise the impedance of this shunt path. A pulse-inverting transformer of similar construction has been used also with some of the light sources.

Figure 5 shows the wave shapes for some combinations of generators, transformers, and cables. RG-9/U cable has been used for moderate delay, RG-55/U for short delay or patch cables. Styroflex cable of 1-in. diameter has been used for 150-nsec delay, and would be satisfactory for delay up to a microsecond. GR-type 874 connectors, or type N connectors, are used with the RG-9/U cable, and BNC connectors with the RG-55/U cable. The generator, transformer, and cabling system have been maintained in coaxial configuration throughout in order to keep spurious radiation from other circuitry. (RG9/U and RG55/U are the double-shielded versions of RG8/Uand RG58/U.

4. Corona Lamps

The lamp construction has been based on the idea of securing a corona discharge at the tip of a tungsten wire touching a dielectric. Glass has been successfully used for the dielectric, resulting in the construction shown in fig. 8.

The 2-nsec voltage pulse is applied to the tungsten wire. If the electric field is sufficiently high, field-emitted electrons initiate the corona discharge which is the source of light. Negative polarity on the wire gives a lower threshold voltage than positive polarity, and less amplitude fluctuation at a given voltage.

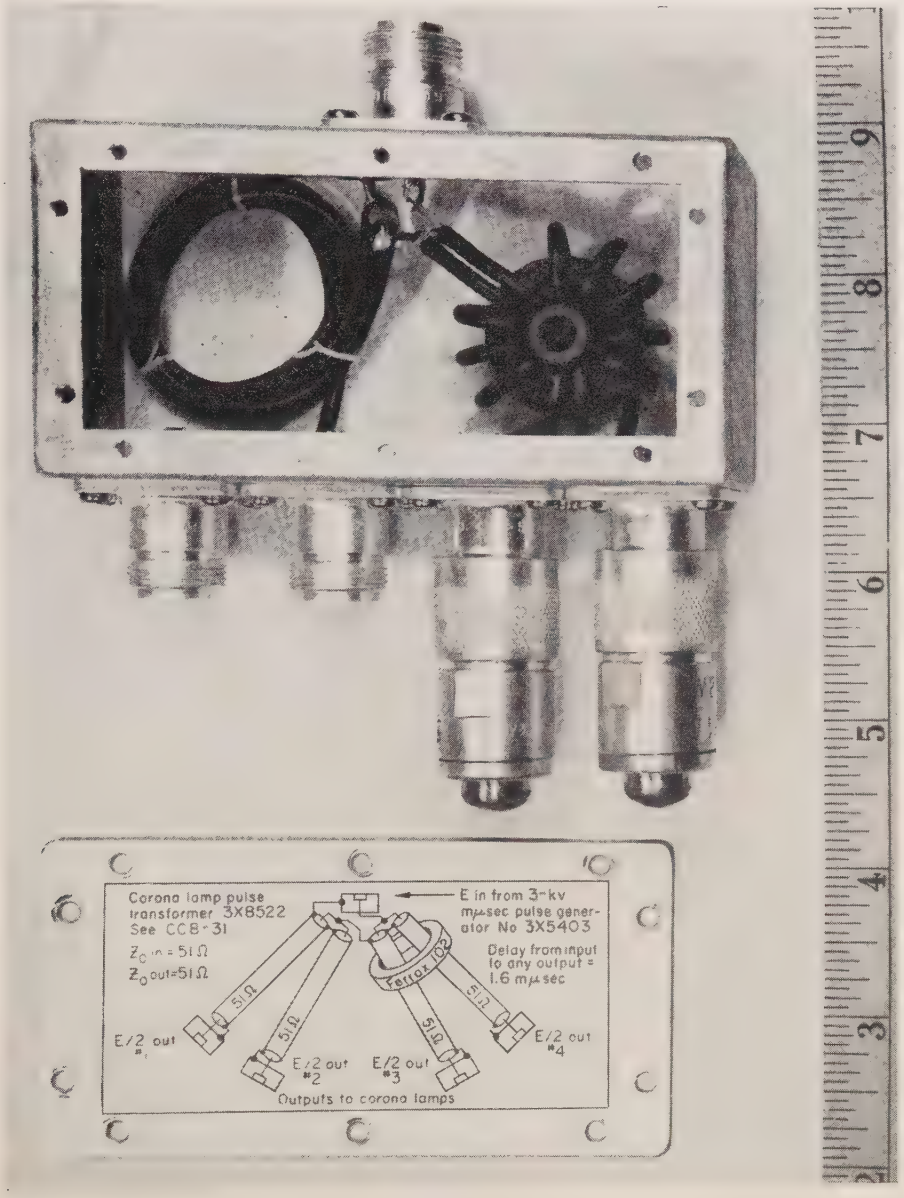
Corona lamp pulse transformer 3X8522 See CC8-31
$Z_{0\,in}$ = 51 Ω
$Z_{0\,out}$=51 Ω
E in from 3-kv mμsec pulse generator No 3X5403
Delay from input to any output = 1.6 mμsec
Teflon tape
51Ω
E/2 out #1
E/2 out #2
E/2 out #3
E/2 out #4
Outputs to corona lamps

Fig. 7. Pulse splitting transformer.

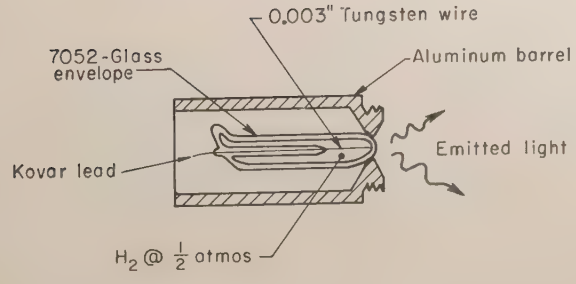

Fig. 8. Corona lamp. (Cutaway view.)

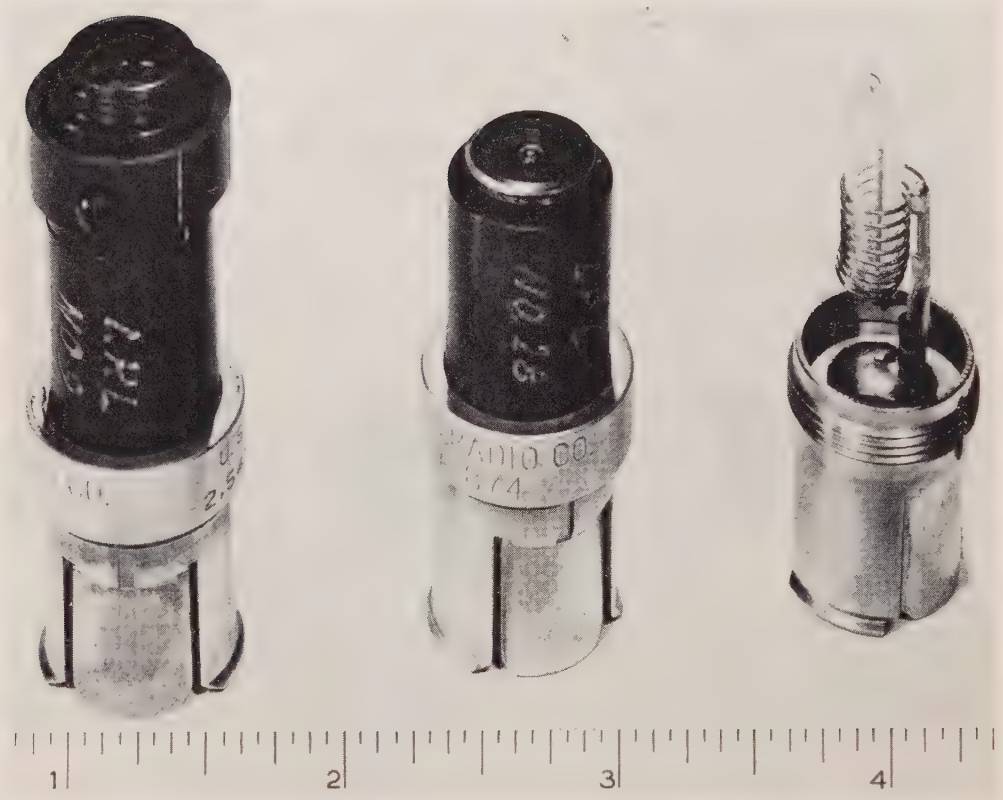

Fig. 9. Photograph of corona lamps. Lamp on the left has the adjustable polaroid attenuator attached.

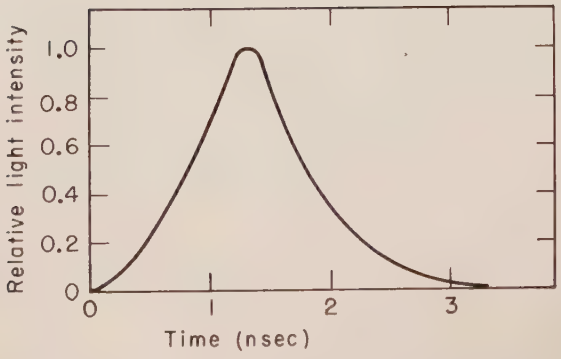

Fig. 10. Corona lamp light-pulse shape.

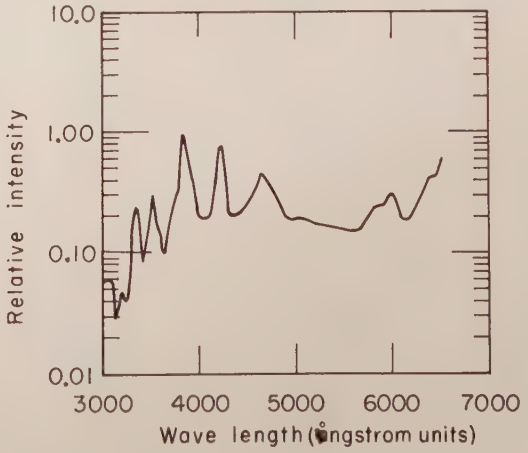

Fig. 11. Corona lamp spectrum.

The light-pulse wave shape has been measured in detail† for a lamp similar to the one shown in fig. 9, but pressurized to 1 atm hydrogen and driven directly from the 3 kv pulse on a terminated 50-ohm line. Figure 10 shows the result. The width at half maximum is about 1 nsec. It should be noted, however, that the light pulse could be somewhat shorter than 1 nsec because of time-resolution limitations in the sampling phototube.

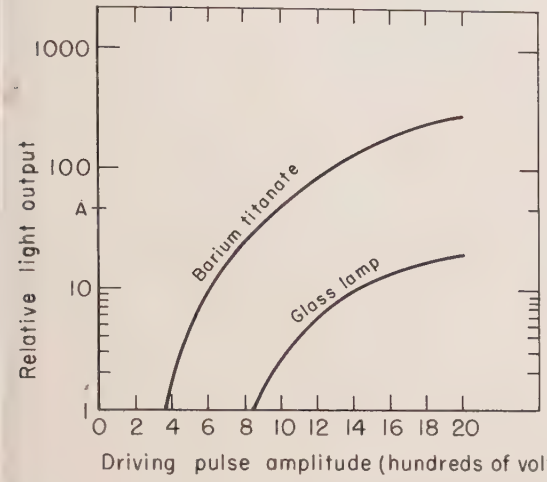

Fig. 12. Light intensity as a function of pulse voltage Point A represents 5000 photoelectrons, $6\frac{1}{2}$ in. from a 2-in. phototube.

† The method of measuring the light pulse shape by using a gated 1P21 phototube has been described by F. A. Kirsten, Fast Pulse Techniques in Nuclear Counting, UCRL-8706, February 12, 1959, p. 2, part 1 and 2.

The optical spectrum has been examined with a Bausch & Lomb diffraction grating spectrometer set to a slit width of approximately 100 Å, and viewed by an AMPEREX 56 AVP phototube. Figure 11 shows the spectrum obtained, after correction for phototube response, grating and mirror efficiency, and solid angle. The light appears blue to the dark-adapted eye.

It was desirable to reduce the operating voltage of production lamps. Two measures were taken. First, the pressure was set at $\frac{1}{2}$ atm (lower pressures lengthen the light pulse). Second, a small inductance coil was placed in series with the lamp, almost doubling the available voltage. The coil may be seen in fig. 9, which also shows the 51-ohm terminating resistor shunting the input connector. The effect of the coil on the light pulse length is small; however, the pulse can be lengthened by adding still more inductance. Recently, we have

Fig. 13. A barium titanate lamp without the outer glass envelope. The scale is graduated in centimeters.

made a lamp design using barium titanate as the dielectric, anticipating a lower operating voltage because of the higher dielectric constant of the titanate.

Figure 12 shows light intensity as a function of pulse voltage for the glass corona lamp and also for the barium titanate design. The barium titanate unit is viewed from the tungsten wire side. It is shown in fig. 13. To date, life tests on the barium titanate units have been limited to 150 hours at 100 pulses/sec. The operation for this time is stable with an amplitude jitter less than 10%. The envelope contains hydrogen at a pressure of $\frac{1}{2}$ atm. A lower pressure gives more light output and good amplitude stability but lenghtens the decay time of the light.

Decay times of 15 to 30 nsec have been observed at millimeter pressures. Under high vacuum, the light output is impracticably small. Further work is in progress with the titanate lamp.

5. Optical Attenuator

A variable optical attenuator is shown attached to one of the Corona lamps in fig. 9. It provides an adjustment of the light amplitude without disturbing any of the electrical settings.

An adjusting ring moves an inner Polaroid film with respect to the outer Polaroid film and lamp, with stops at maximum and minimum attenuation. Indexing lines are spaced to give attenuation steps of two, up to an attenuation factor of 64. The maximum attenuation is greater than 100 times minimum attenuation.

Mechanical strains in the polarizing films must be avoided, as they give rise to double refraction. Satisfactory results have been achieved with a glue of Epoxy resin W 820 plus an air-dry DTA catalyst†. Fixed optical attenuators have been used, as well as electrical attenuators such as the General Radio No. 874-G3—which, however, should not be used at the 3-kV level, though it may be used at the lamp.

Circuit schematic diagrams, fabrication drawings, and accessory drawings are available. They are listed on Lawrence Radiation Laboratory Drawing No. 4X1091.

Acknowledgement

We wish to thank Mr. Bob Reynolds for the mechanical design of the lamp holders and the optical attenuators, Mr. Harry Powell for the lamp construction, and Mr. Lee Wagner and Dr. Yahia El Hakim, who obtained the data for figs. 12 and 11, respectively.

† Diethylenetriamine from Shell Chemical Company.

NUCLEAR INSTRUMENTS AND METHODS **12** (1961) 39–42; NORTH-HOLLAND PUBLISHING CO.

AN 1800-BIT BUFFER STORE AND READOUT SYSTEM†

FRANK EVANS and FREDERICK A. KIRSTEN

Lawrence Radiation Laboratory, University of California, Berkeley, California

Received 15 February 1961

The logical design and organization of an 1800-bit buffer store for use with nuclear physics experiments is described. The heart of the system is an 1800-bit magnetic core memory, which stores up to 10 events, each event consisting of 180 parallel bits of input information. The storage time per event is 40 μsec. Upon command the buffer store transfers the information out of the core memory, six parallel bits at a time, onto punched paper tape.

The buffer store uses transistorized circuits of modular design, constructed on printed boards, and interconnected by taper-pin wiring.

1. Introduction

In a complex experiment where it is necessary to transfer coordinate and time information from a nuclear event into a low-speed record, e.g. punched paper tape, a buffer store is usually interposed. This comparatively small store temporarily holds binary data from particle detectors, coincidence circuits, *etc.*, preparatory to unloading in a uniform sequence. The data for each event is often presented simultaneously over many channels, and each event occurs randomly in time. The effect of the buffer store, then, is to average the acquisition rate with respect to the permanent tape record.

In the following discussion, we shall describe a system employed in Bevatron experiments having a large number of detectors. The buffer consists of magnetic-core memory elements, including the drive and control circuits. The end product is punched paper tape.

2. Magnetic-Core Planes

The store is made up of six planes, each containing a 10-by-30 array of toroidal cores. The magnetic material is a ferrite having a nearly square hysteresis loop with the two residual flux states representing the binary numbers 0 and 1. Part of a plane is shown in fig. 1. Each core is linked with two read wires, two write wires, and one sense wire. Coincident current pulses of equal magnitude on the two read wires threading a given core will return the residual flux to the 0 state. These currents are adjusted so that the magnetomotive force contributed by a pulse on one read wire is not great enough to reverse the flux. At the end of a read cycle all cores are in the 0 state.

Similarly, during the write cycle, binary 1's are entered by supplying two coincident currents of the polarity opposite to the read pulses at the selected core location.

The sense winding shown links all memory elements in the plane. A voltage pulse is induced on this wire whenever the flux in the core is reversed. The sense winding output is gated only during the read interval.

For the write mode, the 30 vertical write wires in each array–180 in all–are connected separately. These correspond to the 180 binary input channels in this experiment. Of these channels, 168 contain coordinate data and the other 12 contain time information. In the horizontal direction, the wires are connected in series through all six planes. These ten circuits then are called event-write lines, each one of them containing one core from every data channel. The buffer store has a capacity of ten events, each with 180 descriptive bits.

The paper tape has seven levels. The first six are reserved for binary data, the seventh for odd parity write-in. The store then is unloaded in groups of six-bit characters. In the read mode the store is wired so that each core plane is unloaded into one tape level—one bit per character. The

† This work was done under the auspices of the U.S. Atomic Energy Commission.

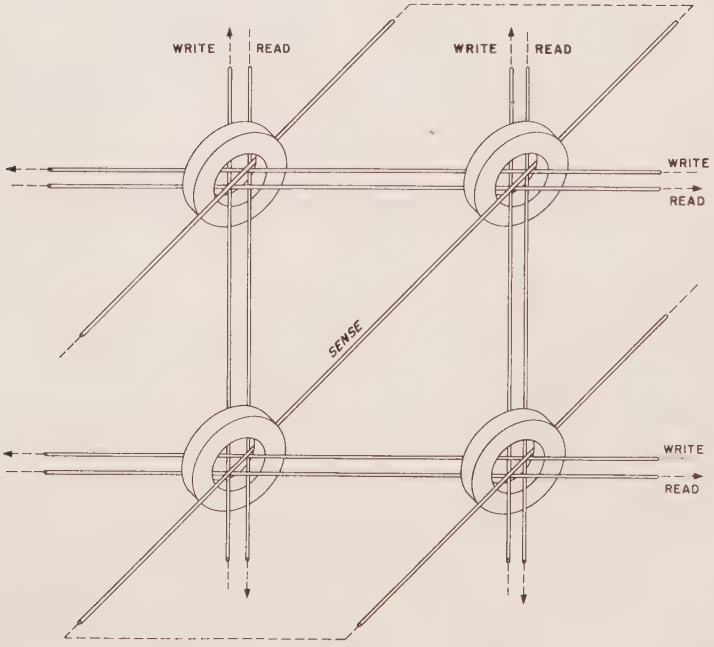

Fig. 1. Part of core plane.

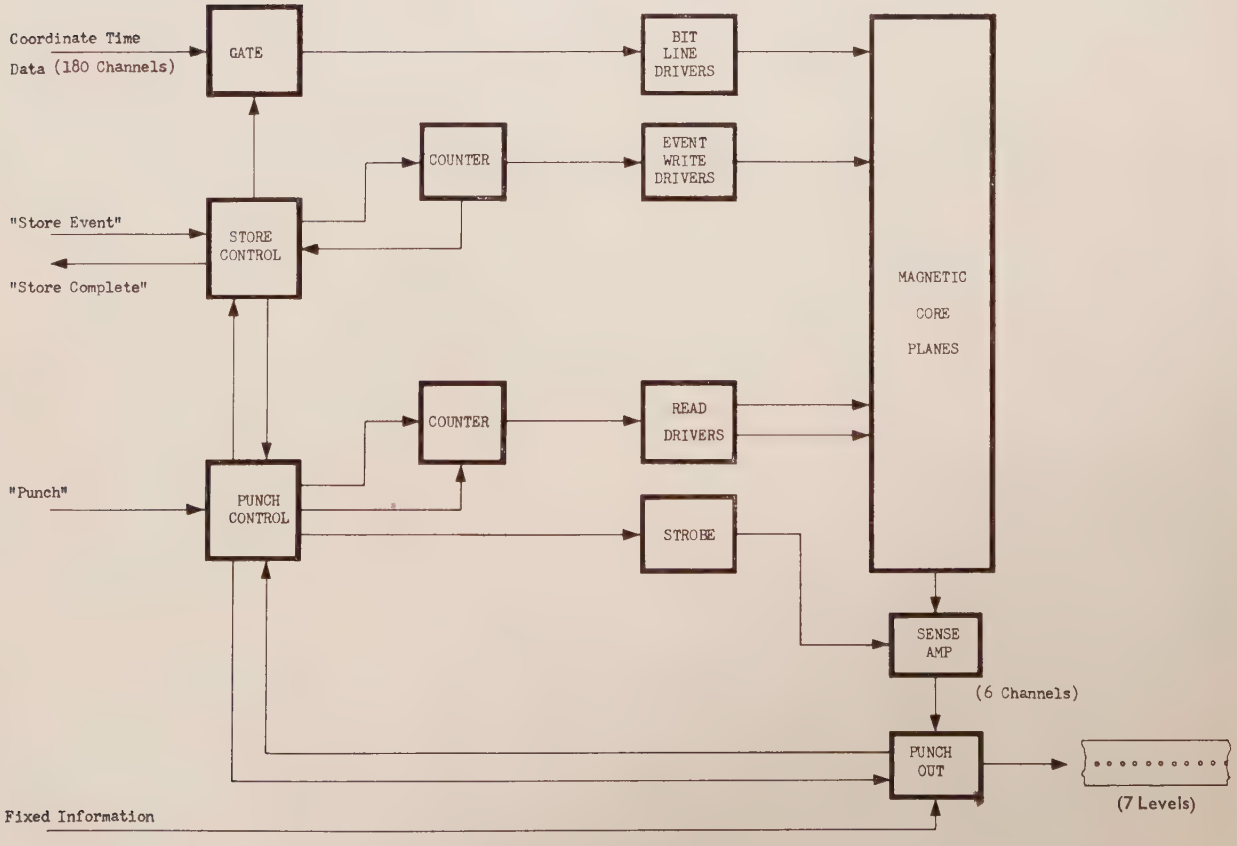

Fig. 2. Functional diagram of the buffer store.

sequence of reading out is from top to bottom, with the events appearing on tape in the order of occurrence.

3. Functional Arrangement

The functional diagram of the circuitry used with the core store is shown in fig. 2. When an event is detected, a STORE EVENT command is fed into the store control, which in turn opens the gates on the 180 data channels. The gate outputs are fed into corresponding bit line drivers, which can be triggered by binary 1's but not by 0's. A counter advances with each event, and the event-write lines of the core store are energized in sequence.

Some events will not be stored. The store control will not open the data gates if (a) a previous event is being stored at the same time, (b) the contents of the store are being read out, or (c) the store is already filled to ten events. In the first case, an event following within less than 40 μsec (the total storing time) will be lost. The store control also puts out a store-complete signal, which indicates that an event has been stored and that there are less than ten events in store.

A PUNCH command starts the sequence that unloads the entire store onto paper tape. This is done at 60 characters per second, the maximum rate of the Teletype punch. The first three characters are fixed information including the Bevatron-pulse serial number. These are followed by one space, then 300 characters representing event data. The total readout time is approximately 5 sec. In Bevatron experiments, this permits unloading the store between beam pulses. If less than ten events are stored between beam pulses, only those portions that are filled will be read out. The punch-out time will be correspondingly less.

The read selectors shown in fig. 2 select the core locations to be interrogated. With each tape character, the punch control advances the counter, which in turn operates the read selectors. Sense amplifiers detect the presence of 1's as pulses and fill the corresponding registers in the punch-out circuits.

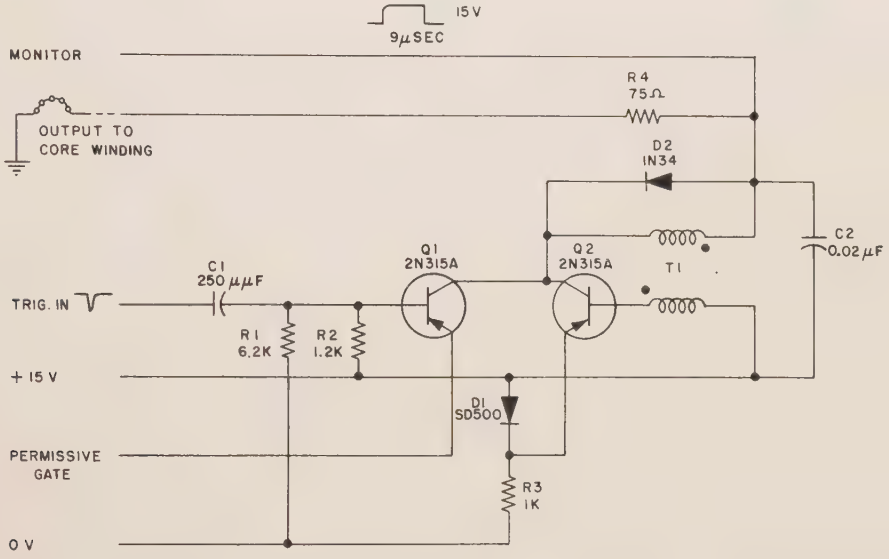

Fig. 3. Schematic diagram of the core driver.

4. Circuitry

The store control, punch control, and part of the punch-out consist of logic circuits, *i.e.*, flip-flops, one-shot multivibrators, "and" gates, "or" gates, and inverters. These are made up as standard transistor boards with two or more circuits per board.

The cores require 380 mA to reverse flux. A coincident current pulse of 190 mA is supplied by a

blocking-oscillator circuit shown in fig. 3. The voltage across D1 normally biases off Q_2. When the trigger appears as shown, the collectors start toward + 15 V, current flows to the base of Q_2 from T_1, and Q_2 becomes regenerative. Unless the permissive gate appears on Q_1, Q_2 will not be triggered. Resistor R_4 limits the current into the cores, and capacitor C_2 limits the pulse rise time to prevent capacitive feed-through to the sense winding. The voltage backswing is prevented from exceeding the rating on the 2N315A by D2.

Pulses appearing at the sense windings are coincident with the leading edge of the read current pulses, and are about 20 mV in amplitude for a binary 1, and 3 mV for a disturbed 1. The sense amplifier shown in fig. 4 amplifies these pulses discriminating against those with amplitudes of 3 mV and less. The base of Q_1 and collector of Q_2 are grounded, thus amplifying pulses of either polarity. Transformer T2 and diodes D1 and D2 form a pulse rectifier, which in turn supplies only negative pulses to the noninverting amplifier Q_3 and Q_4. Actually, Q_3 is slightly below cutoff, and consequently discriminates against small pulses. A low impedance output is furnished by Q_5. The overall gain is about 1000. with the output limiting at — 15 V.

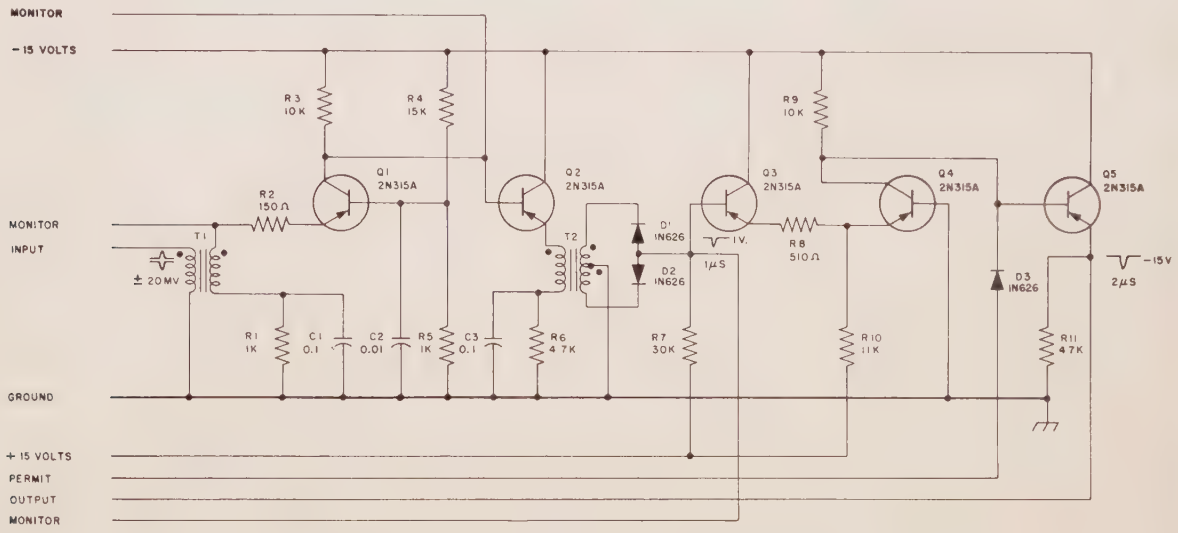

Fig. 4. Schematic diagram of the sense amplifier.

5. Conclusions

The buffer is adequate for many experiments. Practically all of the events recorded to date have had very few binary ones in the 180 data channels. As a result, many more events could be stored in the same core planes, if the input data were coded.

Acknowledgement

The authors wish to thank Messrs. D. A. Mack and J. A. G. Russell for their stimulating discussions and criticism during this development.

NUCLEAR INSTRUMENTS AND METHODS **12** (1961) 43–59; NORTH-HOLLAND PUBLISHING CO.

A MULTIFOLD COINCIDENCE-VETO CIRCUIT USING TRANSISTORS†

ARPAD BARNA††, J. HOWARD MARSHALL and MATTHEW SANDS

California Institute of Technology, Pasadena, California

Received 16 February 1961

A versatile coincidence-anticoincidence circuit in the 50 nsec time range is described capable of being used with large number of counters. Basic considerations with detailed circuits, operation and performance are given.

1. Introduction

This paper describes a coincidence anticoincidence circuit designed primarily for use with counter telescopes at the CalTech 1.5 GeV electron synchrotron. It has been used successfully to set amplitude windows on pulses from counters in counter telescopes containing up to nine counters. In such counter telescopes this circuit allows the precise determination of dE/dx, range, and particle type. Since the absolute stability of the circuit is better than 2 percent, narrow windows and stringent requirements on pulse heights are possible. The resolving time of the fourfold coincidence circuit is 40 nsec, that of the four fold veto circuit is 75 nsec. Secondary operations are possible in the 0.5 μsec time range.

Because of its high complexity, the circuit is constructed using transistors. This reduces the size and power consumption and greatly increases the reliability and freedom from maintenance encountered in vacuum tube circuits.

The circuits are built on plug-in boards with a large degree of versatility in the wiring between boards. This allows the system to be programmed in many different ways.

The input can be driven from the output of a fast coincidence circuit or directly from a photomultiplier tube without the need for a preamplifier.

Fig. 1 shows the basic block diagram of the system.

The amplifier (fig. 2) has a maximum gain of 250.

The triggering levels of the discriminators are adjustable from 1 to 10 volts. The outputs are 50 nsec wide negative pulses with 15 nsec risetime and 6 volt amplitude.

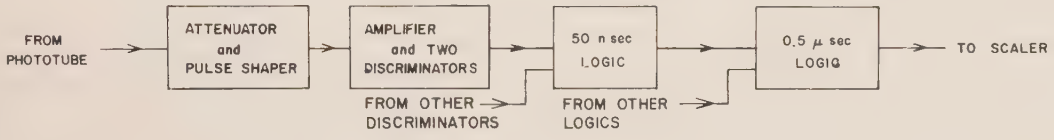

Fig. 1. Simplified block diagram.

The 50 nsec logic (fig. 3) has 4 pairs of inputs. Coincidence and veto can be selected between two of a pair, with a possibility for redundancy to check proper operation. Both vetoed and non-vetoed outputs are available. The pulse shape is critically damped to 0.5 μsec width with 2 volts negative amplitude.

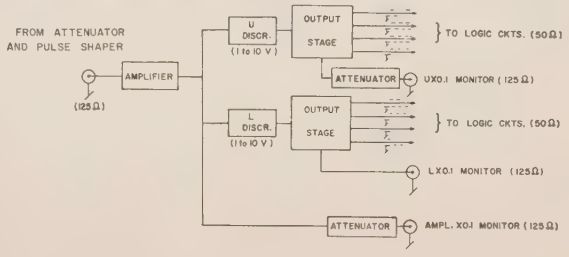

Fig. 2. Amplifier and discriminator.

The 0.5μsec logic (fig. 4) provides secondary coincidence and vetoes between outputs of 50 nsec or 0.5μsec logic circuits.

† This work was supported in part by the U.S. Atomic Energy Commission.

†† Presently at Ransom Systems. San Pedro, Calif.

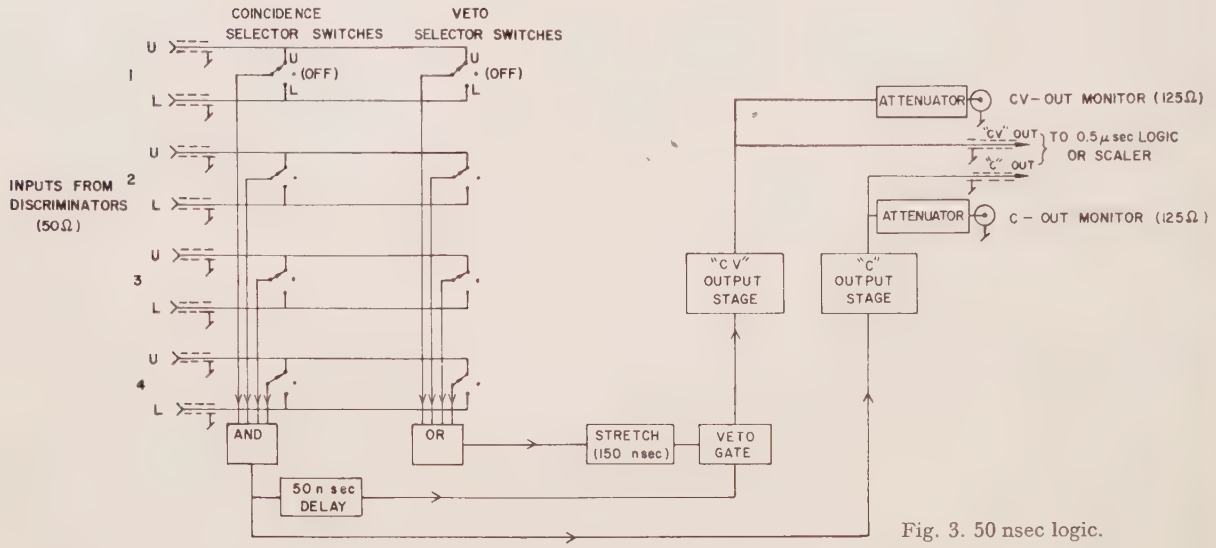

Fig. 3. 50 nsec logic.

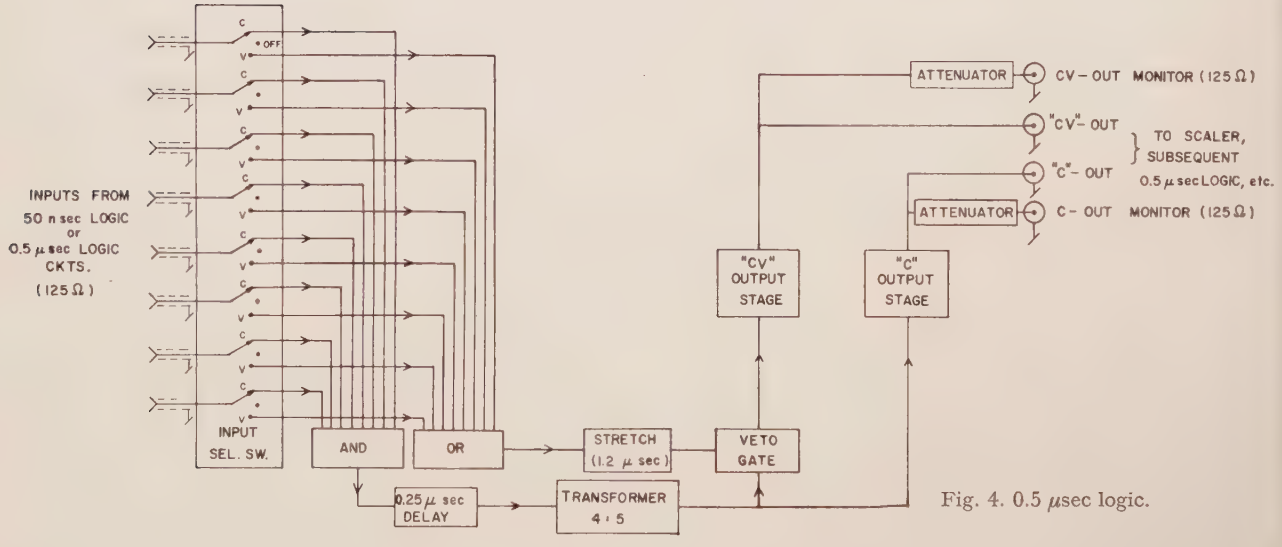

Fig. 4. 0.5 μsec logic.

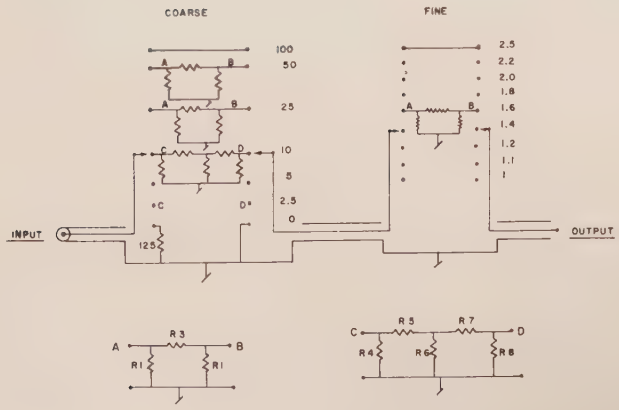

Fig. 5. Attenuator.

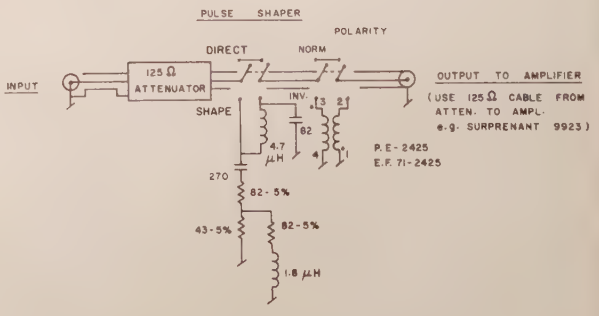

Fig. 6. Inverter and shaper.

2. Circuits

2.1. ATTENUATOR (fig. 5)

The attenuator consists of 125 ohm π networks with a maximum attenuation of 100, attainable in 12 percent (1 db) steps.

A coarse and a fine attenuator are provided. For attenuation larger than 10, double π networks are used for better transient response.

The values of the resistors are shown in table 1.

2.2. PULSE SHAPER AND INVERTER (fig. 6)

The pulse shaping circuit is an RLC combination.

When the output is loaded by 125 ohms, the input has a resistive impedance of 125 ohms, and the output current in response to an input $i_{IN} = Q\,\delta(t)$ is

$$i_{out} = \frac{Q}{2\tau}\,\frac{t}{\tau}\,\exp\left(-\frac{t}{\tau}\right).$$

This response has $T_R = 0.56\,\tau$, $T_{\frac{1}{2}} = 2.4\,\tau$ and

TABLE 1

Switch position	R_1	R_3	R_4	R_5	R_6	R_7	R_8
Coarse							
100	∞	0					
50	375-P	95-P					
25	210-P*	235-P					
10			300-P	125-P	120-P	250-P	200-P
5			190-P	300-P	100-P	235-P	200-P
2.5			172-P	385-P	85-P	385-P	172-P
Fine							
2.5	∞	0					
2.2	2.2 k	15					
2.0	1.1 k-5 %	30-P					
1.8	750-5 %	43-5 %					
1.6	560-5 %	62-5 %					
1.4	440-P	77.5-P					
1.2	375-P	95-P					
1.1	330-P	110-P					
1	292-P	130-P					

* -P denotes one percent resistor.

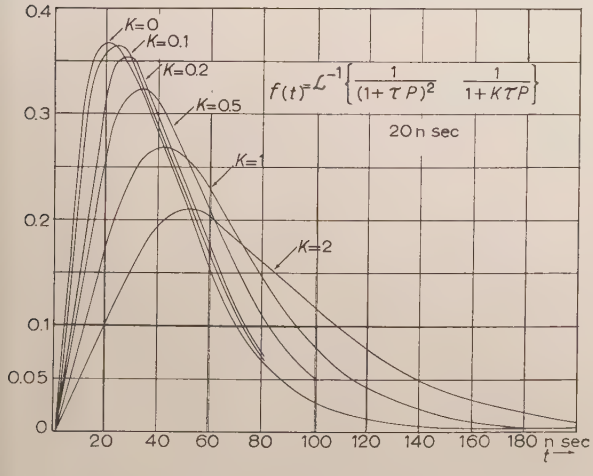

Fig. 7.
Output of the pulse shaper for different values of K.

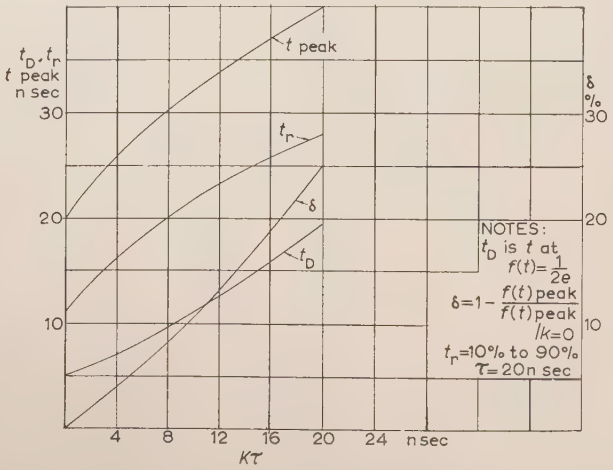

Fig. 8.
Pulse shaper delay, rise time and amplitude loss as function of KT.

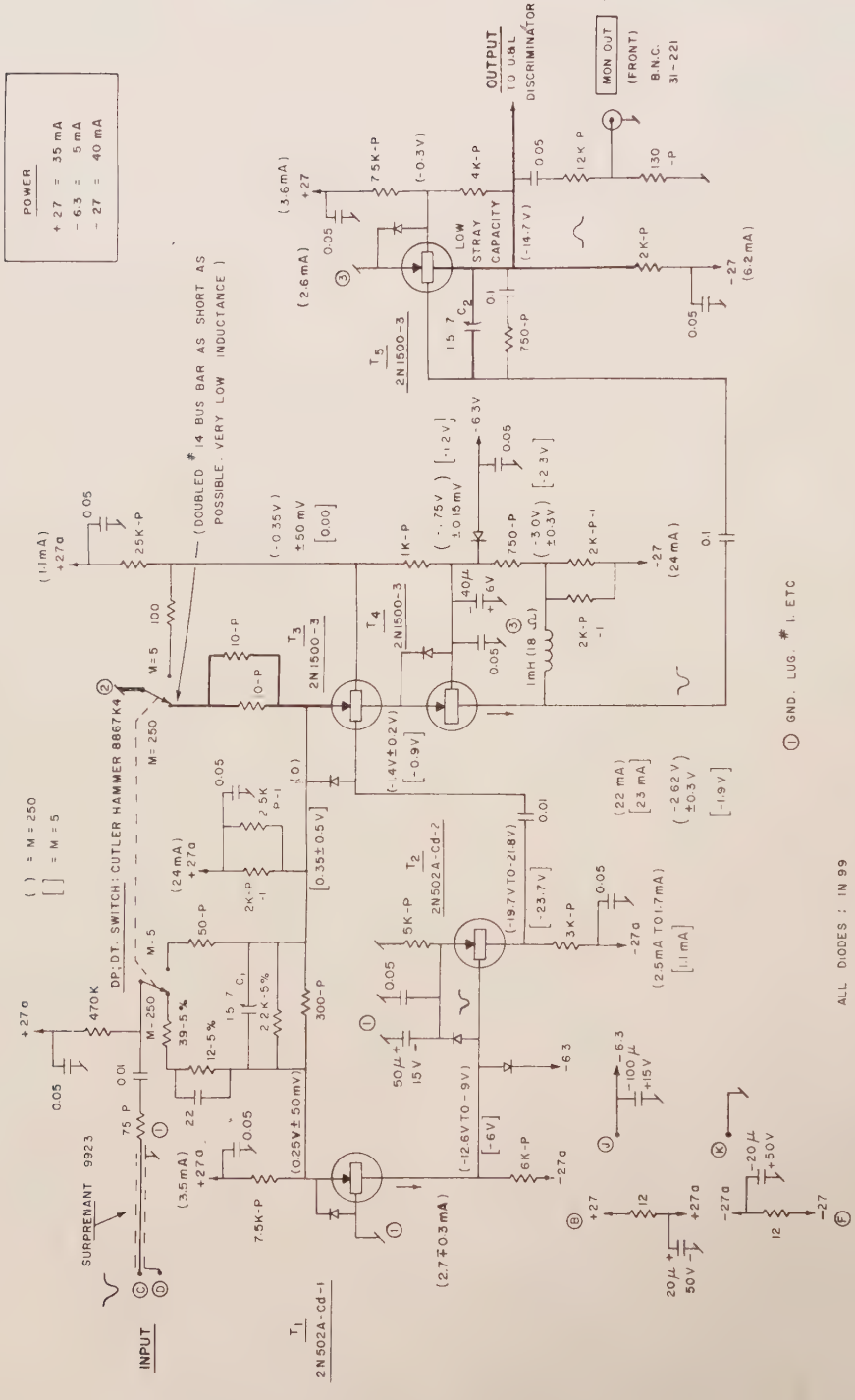

Fig. 9. Amplifier.

$_{max} = \tau$. For this circuit $\tau = 20$ nsec. The curves f fig. 7 give the response of the 50 nsec shaper to n input pulse with an exponential decay time onstant of $k\tau$; similarly for a circuit with a δ unction response of $e^{-t/k\tau}$, they give the output for 50 nsec shaper pulse.

The curves of fig. 8 are derived from fig. 7 and how the dependence of the delay, rise time and mplitude loss on the exponential time constant.

Since the amplifier rise time is not stabilized by eedback, it is not desirable for the output ampli- ude to be strongly dependent on the amplifier rise ime. The curves in figs. 7 and 8 with $k = 0.25$ $k\tau = 5$ nsec) approximately give the effect of the mplifier rise time (10 percent to 90 percent ≈ 11 nsec) on the pulse shape. For this use the mplitude loss at the peak is about 5 percent, and hus ± 20 percent variations in amplifier rise time vill produce a ± 1 percent effect on the peak mplitude.

The finite risetime also causes timing jitter for ifferent input pulse heights. For $k\tau = 5$ nsec $T_R = 11$ nsec) the peak of the pulse occurs at 7 nsec, limiting the timing jitter to a maximum of 7 nsec. For the same reason wide input pulses hould not be used with the shaper. Photomulti- lier tube pulses with a half-width of about 10 nsec orrespond to a k of approximately 0.3, and thus roduce an acceptable response. For 10 nsec wide nput pulses, maximum timing jitter on the output f the discriminator was found to be 30 nsec. This mits the coincidence resolving time to longer than 0 nsec.

The inverter consists of a 1:1 pulse transformer PE-2425). The transformer can be switched in or ut of the signal path. For a 125 ohm load, it has a nsec rise time and 3 percent droop at 50 nsec.

3. AMPLIFIER (fig. 9)

The amplifier consists of two stages, with a total ain of 250. For large input signals the first stage an be bypassed and the output stage, which has a ain of 5, can be used alone. The transient response adjusted so that, with an input pulse with a 12 sec rise time, the rise time of the output pulse is ypically 17 nsec for a gain of 250, 15 nsec for a gain f 5; with overshoots and ringing less than 5 percent.

The absolute value of the gain is within ± 5 percent of the nominal value, and the linearity is better than ± 1 percent for output pulse heights < 10 V. The input impedance is 125 ohms ± 5 percent. The output impedance < 15 ohms; the maximum duty cycle is 10 percent. The temperature drift of the amplification is less than ± 1 percent for a temperature change of ± 10°C.

The operation is as follows:

First stage:

With the amplification switch in the 250 position, T_1, T_2 and T_3 form a current feedback amplifier with a feedback current gain of 50. T_2 and T_3 each give a current gain of β (see ref.[1])). T_1 isolates the output from the input, preventing back interaction and, since it is a grounded base stage, it has a current gain of α. The emitter of T_2 is capacitively grounded, making it a grounded emitter stage for signals. The coupling capacitor 0.01 μF from the collector of T_2 to the base of T_3 is chosen to give a closed loop decay time constant greater than 100 μsec. The signal emitter current of T_3 then divides between the 5 Ω to ground and the 264 Ω back to the emitter of T_1. Thus, the open loop gain is $M_0 = \alpha_1\beta_2\beta_3 = 1200$ and the feedback gain:

$$M_f = \frac{R_F}{R_L}\frac{1}{1 + \frac{R_F}{R_L}\frac{1}{M_0}} = 50$$

where R_F = resistor from e_1 to e_3 = 264 Ω and R_L is the resistor from e_3 to ground (5 Ω). This gives a feedback factor $F = M_0/M_f = 24$ and an input impedance to the emitter of T_1 of $r_e/F \approx 0.2$ Ω for times longer than 20 nsec. Thus, for the total input impedance one has $R_{IN} = 120$ Ω, and the long time response is determined by the 0.01 μF capacitor at the input. Capacitor C_1 is set for optimum transient response. The rise time can be estimated.

$$T_{R1} \cong \frac{2.2\tau_0\sqrt{\beta_2^2 + \beta_3^2}}{\sqrt{F_1}} = 11 \text{ nsec}$$

where $\tau_0 = \tau\beta/\beta = 0.5$ nsec, $\tau\beta$ is the β time constant.

With the amplification switch in the 5 position, the signal is fed into the emitter of T_3 whose base

[1]) Symbols and equivalent circuits are discussed in: A. Barna, J. H. Marshall and M. Sands, Nucl. Instr. and Meth. 7 (1960) 124.

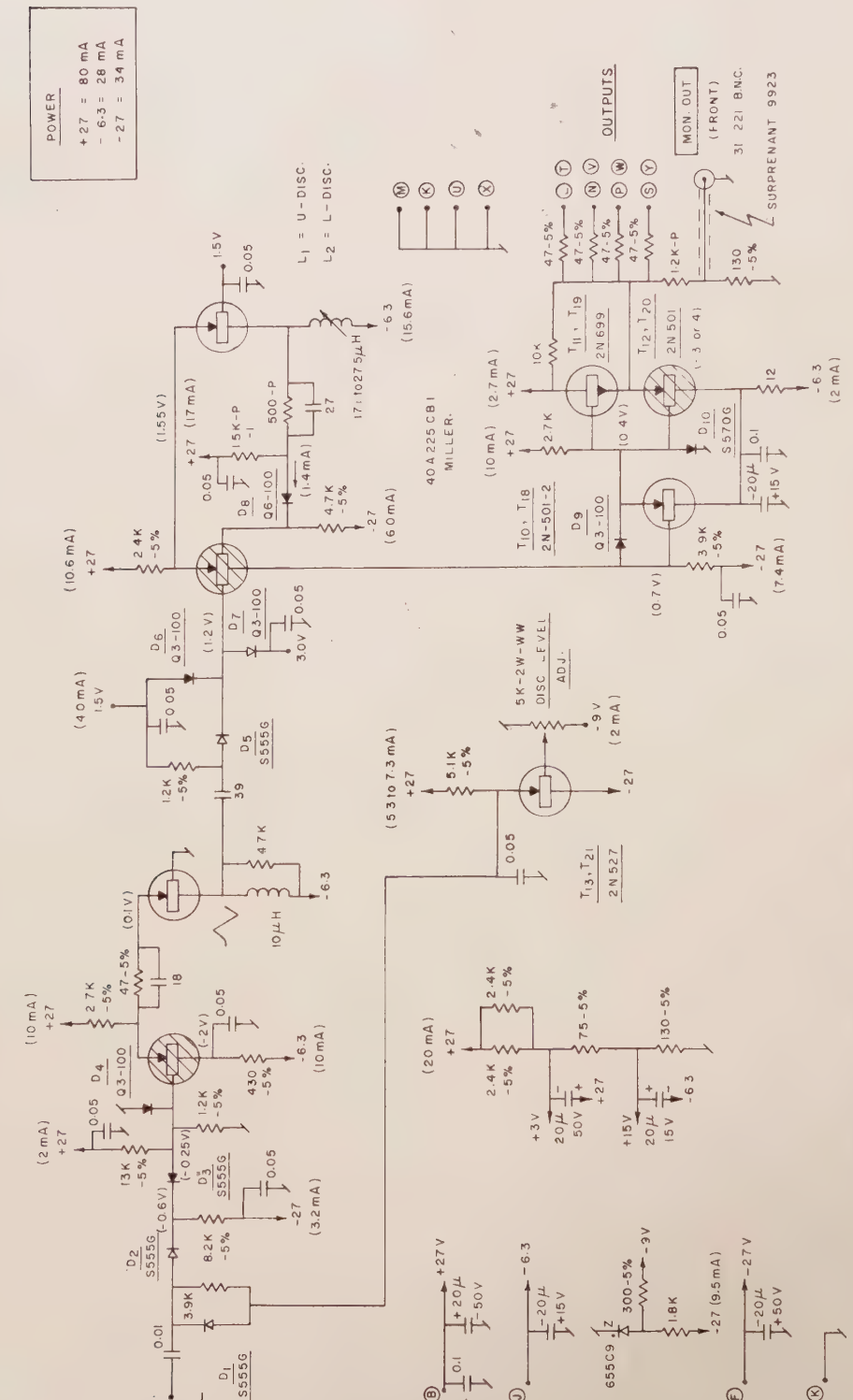

Fig. 10. Discriminator.

has now been grounded to eliminate T_1 and T_2 from the loop. The 5 Ω resistor is disconnected from ground to prevents its loading the input. T_3 then has a current gain of α_3 which is nearly 1 ($\approx$ 98 percent) and an input impedance of the order of 1 Ω.

Second Stage

T_4 acts as an isolation stage between the first stage and T_5, and it presents a low impedance to the collector of T_3 and a high impedance to the base of T_5. It has a current gain of α_4 ($\approx$ 98 percent).

T_5 is a single transistor feedback stage with an open loop current gain of β_5 and a feedback transfer impedance R_T given by:

$$R_T \approx R_F \left[\frac{1}{1 + \frac{R_F}{\beta_5 R_L}} \right]$$

R_F = feedback resistor from collector to base = 630 Ω;

R_L = load impedance from collector to ground $\approx$ 500 Ω (includes two discriminators).

$$R_T \approx \frac{630}{1.017} = 625\ \Omega\ .$$

The feedback factor F is given by:

$$F = \frac{\beta_5 R_L}{R_F} \cong 60\ .$$

This gives an output impedance of:

$$R_{out} \approx \frac{R_F}{\beta_5} = 8.5\ \Omega\ .$$

Capacitor C_2 has a similar function as C_1.

The output impedance of T_5 actually looks inductive with an inductance in series with $R_{F/\beta}$ of $R_F \tau_0$ where

$$\tau_0 \approx \tau_{\beta/\beta} \quad \text{and} \quad \tau_\beta = \beta\text{-rise time constant}\ .$$

$$\tau_0 \approx 0.5\ \text{nsec}\ .$$

This inductance will cause ringing if the stray capacity on the collector of T_5 is in excess of about 5 pF.

For signals small enough so that T_5 operates linearly, the rise time of the second stage can be estimated as being:

$$T_{R_2} \approx 2.2\ R_F(C_c + C_2)$$

where C_c = collector to base capacity of the transistor T_5.

For $C_c + C_2 = 5$ pF: $T_{R_2} \approx 7$ nsec.

The DC currents through T_1 and T_2 are stabilized with emitter resistors. The emitter of T_2 is by-passed to ground capacitively so as to make it a grounded emitter stage for fast signals. The current through T_5 is stabilized by D.C. feedback from the collector to the base.

With the amplification switch in the 250 position, the current and dissipation of T_3 and T_4 are stabilized by D.C. feedback from the collector of T_4 to the base of T_3. The voltage of the base of T_4 is determined by a voltage dividing chain from the collector of T_4 to the base of T_3. The emitter of T_3 is essentially grounded through the 5 Ω resistor. In the amplification = 5 position, the current is stabilized by the 2k and 2.5k resistors in the emitter of T_3. The D.C. feedback is disconnected by grounding the base of T_3. The base voltage of T_4 is derived from a voltage divider chain as before.

All diodes (IN99) in the amplifier are protective.

2.4. DISCRIMINATOR (fig. 10)

The discriminator has a minimum useful input range of 1 to 10 volts with a linearity better than 0.1 V. The change in triggering level for constant amplitude pulses having widths of 20 ns and 200 ns is $<$ 10 mV; for widths of 20 ns and 10 ns it is $<$ 0.15 V. The change is triggering level, for a pulse arriving more than 150 nsec after the preceding one, is less than 0.1 V, for 100 nsec less than 0.75 V. The temperature dependence of the triggering level is $<$ 5 mV/°C. The maximum continuous duty cycle is 10 percent.

The output pulse height is $-$ 6.5 V $\pm$ 10 percent with 50 nsec pulse width and less than 15 nsec rise and fall times. The disciriminator consists of a window amplifier, whose output current is differentiated and used to trigger a univibrator, which drives the output stage.

The operation of the circuit is as follows:

Window Amplifier

Transistors T_6 and T_7 form a long tail pair which, combined with the input diodes (D_1, D_2, D_3, D_4)

form a window amplifier. A current of 3 mA is stabilized through D_3 by a resistor (8.2k) to -27 V. This current comes partly from D_4 and partly from resistors. D_2 is back biased by a voltage derived from an emitter follower (T_{13}). In case of high repetition rates, D_1 recovers the input capacitor (0.01) μF), the discharge current flowing into the low impedance seen at the emitter of T_{13}. The 1 mA current through D_4 pulls the base of T_6 about $\frac{1}{4}$ V negative, thus guaranteeing that the 10 mA current stabilized through the resistor (2.7k) to $+$ 27V all flows through T_6, leaving T_7 cut off.

The window amplifier starts to give an output when the input voltage becomes sufficiently positive, so that there is about 1 mA current flowing in D_2, causing D_4 to cut off. The maximum current of the window amplifier is 10 mA when the signal cuts off T_6. Larger positive inputs cause D_2 to draw the entire 3.2 mA of the 8.2 k resistor, cutting of D_3 and disconnecting T_6 from the input. The base of T_6 goes to $+$ 2.2 V and its emitter is at about $+$ 0.7 V, safely cutting off T_6 without exceeding its maximum base-emitter back voltages of 2 V.

Temperature drifts in the emitter-base voltage of T_6 and T_7 tend to cancel each other, since the univibrator triggers at about 5 mA out of the 10 mA total current of window amplifier. This condition of equality is independent of the emitter-base voltage drop for indentical transistors. Similarly, the voltage drifts of D_2 and D_3 tend to cancel each other, since they oppose each other. The principal temperature drift comes from T_{13} whose emitter base voltage drifts at about the rate of 2 mV/1°C. For a temperature swing of $\pm$ 10°C, this yields $\pm$ 20 mV.

The 47 Ω, 18 pF RC circuit between the emitters of T_6 and T_7 produces negative feedback, decreasing the rise time at the expense of transfer impedance according to the law:

$T_R R_T = 2.2\tau_0(R_s + 2R_b)$

$R_T = V_{in}/i_{out}$ = transfer impedance

R_s = source impedance including forward resistance of D_2 and D_3

R_b = base spreading resistance of the 2N501

T_R = 10 percent to 90 percent rise time

$\tau_0 = \tau_\beta/\beta = 0.8$ nsec.

The circuit used has a transfer impedance of about 70 Ω and $T_R \approx 10$ nsec. The fast rise time is necessary to reduce the pulse width dependence of the triggering level.

Pulse Shaper

The output of the window amplifier is shaped by the 10 μH choke and the 39 pF capacitor. Diode D_5 is normally slightly conducting and a low impedance path exists through D_5 and D_6 to A.C. ground. Under these conditions the LC circuit is undamped and has a sinusoidal response with a period of 70–80 nsec. When the signal current through the 39 pF condenser reverses sign, it cuts off D_5, leaving an impedance of 1.2 k to ground, which is large enough to overdamp the response of the LC circuit, causing it to decay exponentially back to its D.C. level. Also, diode D_5 disconnects the trigger pulse from the univibrator after 35 nsec, allowing the univibrator's pulse width to be independent of the input pulse width even for long input pulses.

The damping of the pulse shaper response is critically dependent on stray capacity across the 10 μH choke. In order to reduce this effect, the choke is by-passed by 4.7 k, providing additional damping.

Univibrator

Transistors T_8 and T_9 form a long tail pair with positive feedback from the collector of T_9 to the base of T_8, making a univibrator. A current of 4.6 mA is drawn through D_6 causing T_8 to conduct all of the 10.6 mA with T_9 cut off. D_8 is conducting a current of about 1 mA.

The circuit triggers when a trigger pulse greater than 4.6 mA unhooks D_6 and causes current to flow in T_9. For short times the 20 μH presents a large impedance, and all of T_9's current flows back to the base of T_8. This positive feedback continues to increase the current of T_9 until T_8 cuts off. The base of T_8 is clamped by D_7 and a low impedance path exists from the 500 Ω resistor to A.C. ground through D_7 and D_8. The 20 μH choke, 500 Ω resistor, and 27 pF condenser form a critically damped network causing the current through D_7 to decrease with time. After about 22 nsec, the current through D_7 reaches zero, causing it to unhook, leaving about

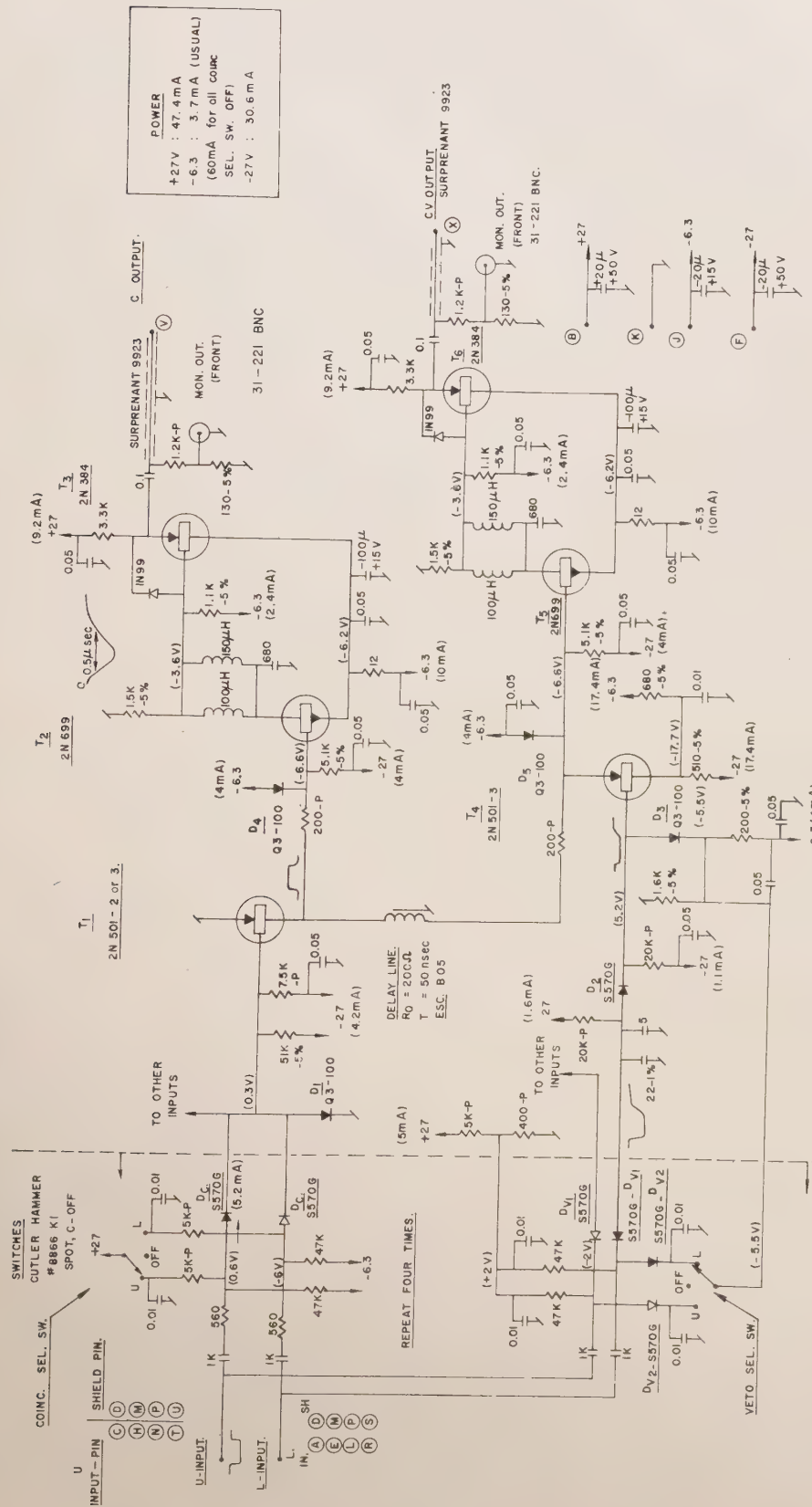

Fig. 11. 50n sec logic

1.2 k impedance to ground. The 20 μH choke continues discharging through this impedance for another 5 nsec, at the end of which time D_6 starts conducting and T_8 starts taking current from T_9. Thus, the circuit starts to trigger back in about 27 nsec. Since the circuit has a rise and fall time of about 10 nsec, this gives a total width at half maximum current (i.e. 5 mA) of:

$$T_{\frac{1}{2}} = \tfrac{1}{2}(10 + 10) + 27 = 37 \text{ nsec}.$$

After the circuit triggers back, D_8 unhooks the choke (20 μH) recovers through a 2 k resistance and disconnects all but about 1 mA of its current from the biasing diode D_7. The higher impedance causes the choke to recover faster, and the fact that its current is no longer flowing in D_7 allows the circuit to be immediately retriggered. After 100 nsec the choke is recovered and D_8 starts conducting again and the univibrator operates normally. For a trigger pulse less than 100 nsec after the first triggering pulse, the circuit will retrigger, but its pulse width is too short, due to residual current still flowing in the choke.

Output Stage

Transistor T_{10} is normally cut off by the forward voltage drop of D_9 with its emitter clamped at 0.4 V by D_{10}. When the univibrator is triggered, the 10.6 mA from the collector of T_8 is turned off, causing the base of T_{10} to be pulled to -27 V through the 3.9 k resistor. This unhooks D_{10} and the emitter follows the base toward -27 V and stops at -6.1 V when the transistor (T_{10}) saturates. The fact that T_{10} saturates causes its storage time to be added to the half width of the output pulse. The storage time is specified as 13 nsec for the 2N501, resulting in:

$$T_{\frac{1}{2}\,\text{output}} = 37 + 13 = 50 \text{ nsec}.$$

The rise time can be estimated as follows, for times short compared to $\tau_\beta = 40$ nsec.

$$T_R \approx \tau_0 \sqrt[3]{\frac{6CV}{I_0\tau_0}} = 11 \text{ nsec}$$

where C = load capacity (370 pF for four logic circuits and connecting cable).

V = output voltage (6.5 V)

I_0 = input current (7 mA)

$\tau_0 = \tau_\beta/\beta = 0.8$ nsec.

If one includes a 10 nsec rise time for the input current:

$$T_R \approx \sqrt{(11)^2 + (10)^2} = 15 \text{ nsec}.$$

2.5. 50 nsec LOGIC (fig. 11)

The logic is a fourfold coincidence circuit with four veto inputs. There are two outputs, one for coincidence with veto and the other for coincidence without veto. The coincidence resolving time is 37 $\pm$ 5 nsec, the veto resolving time is 50 to 75 nsec, both defined as half width of the delay curve at half height.

The output pulse is a critically damped -2.2 V $\pm$ 15 percent pulse with a width of 0.4 to 0.5 μsec at half height and the peak at 0.2 μsec. The output for vetoed coincidence is typically $\pm$ 20 mV. The maximum continuous ounting rate is 1 Mc/s. The output impedance is < 20 ohms, and the output should not be loaded by more capacity than 300 pF.

The operation of the circuit is as follows:

Coincidence circuit

The coincidence circuit is primarily an "And" circuit requiring the presence of certain pre-selected inputs in order to get an output.

The transistor T_1 is cut off by the forward voltage drop of D_1(Q 3-100). The D.C. current in D_1 is determined by the coincidence selector switch and the 4.2 mA drawn through resistors (7.5 k-P, 51 k-5 percent) to -27 V. Whenever a coincidence selector switch is in either a "U" or an "L" position (i.e. not off), it causes 5.2 mA to flow from + 27 V through the coincidence control diode (D_c-S570G). Of the total current flowing through the eight D_c diodes, all but 4.2 mA normally flows through D_1. Thus, there can be from 1 mA (for only one coincidence selector switch not off) to 16.6 mA (for no switches off) flowing in this diode. In the case where all switches are off, the 4.2 mA pulls T_1 into saturation.

When a D_c diode is connected to + 27 V through 5 k by the coincidence selector switch, thus conducting 5.2 mA, it can be cut off by a negative signal which will absorb its 5.2 mA. The cathode of the D_c diodes (i.e. base of T_1) shifts only about 0.6 V from D_1, conducting 17 mA to T_1 saturated. Thus

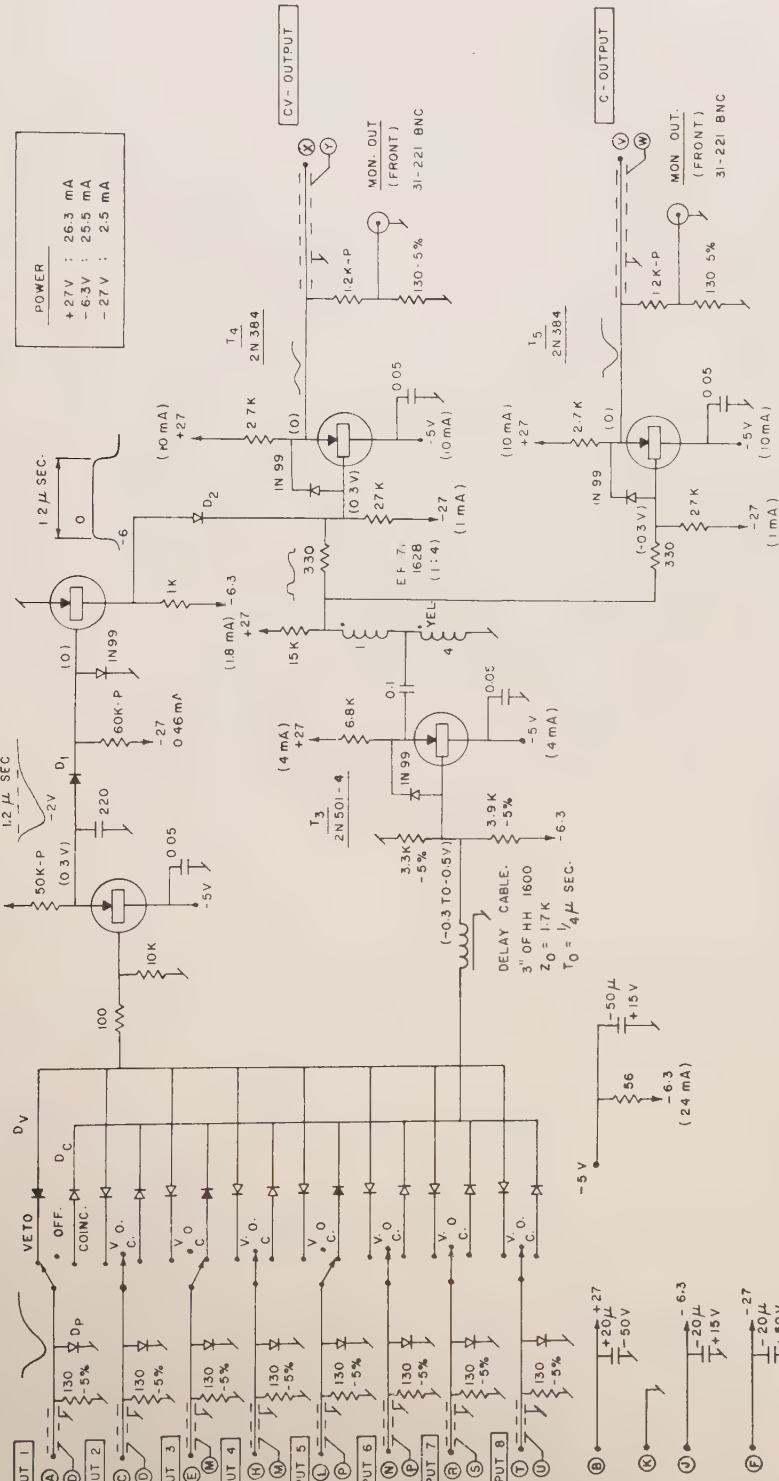

Fig. 12. 0.5 μsec logic.

the required voltage at the input to cut off a D_c diode is approximately 560 $\Omega \times 5.2$ mA = 3 V. When a D_c diode is not connected to + 27 V through 5 k by the coincidence selector switch, its anode is pulled to — 6 V by a resistor (57 k) to — 6.3 V. Thus, any negative signals at its anode have little effect on the base of T_1. (It would take a positive stray signal of + 6 V to turn the diode on.)

To turn on T_1, D_1 must cut off and the 4.2 mA current then pulls T_1 into saturation. This can happen only if all the D_c diode currents are simultaneously zero. This means that one gets an output only if there are simultaneous signals of at least — 3 V on all inputs which are connected to + 27 V through 5 k by their coincidence selector switches. Thus, one has provision for making one to four-fold coincidence, depending on the setting of the coincidence selector switches.

When T_1 saturates, it sends a current of 30 mA toward the base of T_2, cutting off D_4 and saturating T_2. T_1 also sends a 30 mA current through the 50 nsec delay line toward the base of T_5, unhooking D_5 and saturating T_5 if there is no veto.

Veto Circuit (T_4)

The veto circuit is primarily an "Or" circuit which vetos one of the outputs of the coincidence circuit when any of certain preselected inputs are present.

When no inputs are present, D_2 and D_3 are normally conducting, holding the base of T_4 at — 5.2 V and thus cutting it off. If D_2 should become cut off, the 1.1 mA flowing through the resistor (20 k) to — 27 V then pulls T_4 into conduction, causing about 50 mA to flow through D_5 and its cathode to drop to about — 6.9 V. If a coincidence current pulse of 30 mA arrives, it cannot unhook D_5 and thus T_5 does not turn on. The (low) impedance of the voltage divider in the collector of T_4 is chosen so that the D.C. saturation current of T_4 is greater than 30 mA, preventing a loss of veto from pile-up on the collector of T_4.

When the veto selector switch connects the cathode of one of the D_{V_2} diodes to — 5.5 V, this pulls the cathode of the D_{V_1} diode connected to it to — 5.2 V and turns this diode slightly on. If a negative pulse is applied to the cathode of such a conducting D_{V^1}, then the diode conducts harder, pulling the condenser (27 pF) on the anode of D_2 down to nearly the input voltage. This unhooks D_2 and starts the veto procedure. When the input signal returns to zero, the anode of D_{V_1} is held at about — 11 V for a — 6 V input signal, while the cathode goes back to — 5.2 V. Thus, D_{V_1} cuts off and the 27 pF starts to decay exponentially to + 27 V with a time constant given by 20 k $\times$ 27 pF = 540 nsec. When the anode voltage of D_2 has reached — 6.9 V, D_2 starts conducting again, unclamping T_1 and ending the veto. The diode D_{V_2} presents a low impedance path for positive signals and thus recovers the input 1 k condenser for pile-up at high counting rates.

When the cathode of a D_{V_2} diode is left open by the veto selector switch, then its anode is pulled to + 2 V, thus cutting off the D_{V_1} connected to this input. This blocks input pulses up to — 7 V from operating the veto circuit.

Output Circuit ($T_2T_3T_5T_6$)

The purpose of the output circuit is to convert the short, fast rise pulse from the output of the coincidence circuit (collector of T_1) into a longer, slow rise output pulse useful for driving scalers or the 0.5 μsec logic.

The part of the circuit containing T_2 and T_3 is identical with the part of the circuit containing T_5 and T_6 except for the veto transistor T_4. If there is no veto, the outputs of the two parts are the same, and if a veto is present, T_3 gives the same output as if no veto were present, but T_6 gives no output.

Normally T_2 and T_5 are cut off by the forward voltages of D_4 and D_5 respectively. These diodes draw 4 mA determined by resistors (5.1 k) to — 27 V. In the collectors of T_2 and T_5 are pulse shaping networks which convert a short voltage pulse into an output of the form

$$V(t) = V_0 \frac{t}{\tau} \exp\left(-\frac{t}{\tau}\right)$$

where τ = 200 nsec. T_3 and T_6 are emitter followers to prevent load impedances as low as 100 Ω from interfering with the pulse shaping network. The narrow voltage pulse to drive this network is manufactured by saturating T_2 and T_5 with the current coming from the saturation of T_1 at coincidence. As the width of the pulse at the collector of

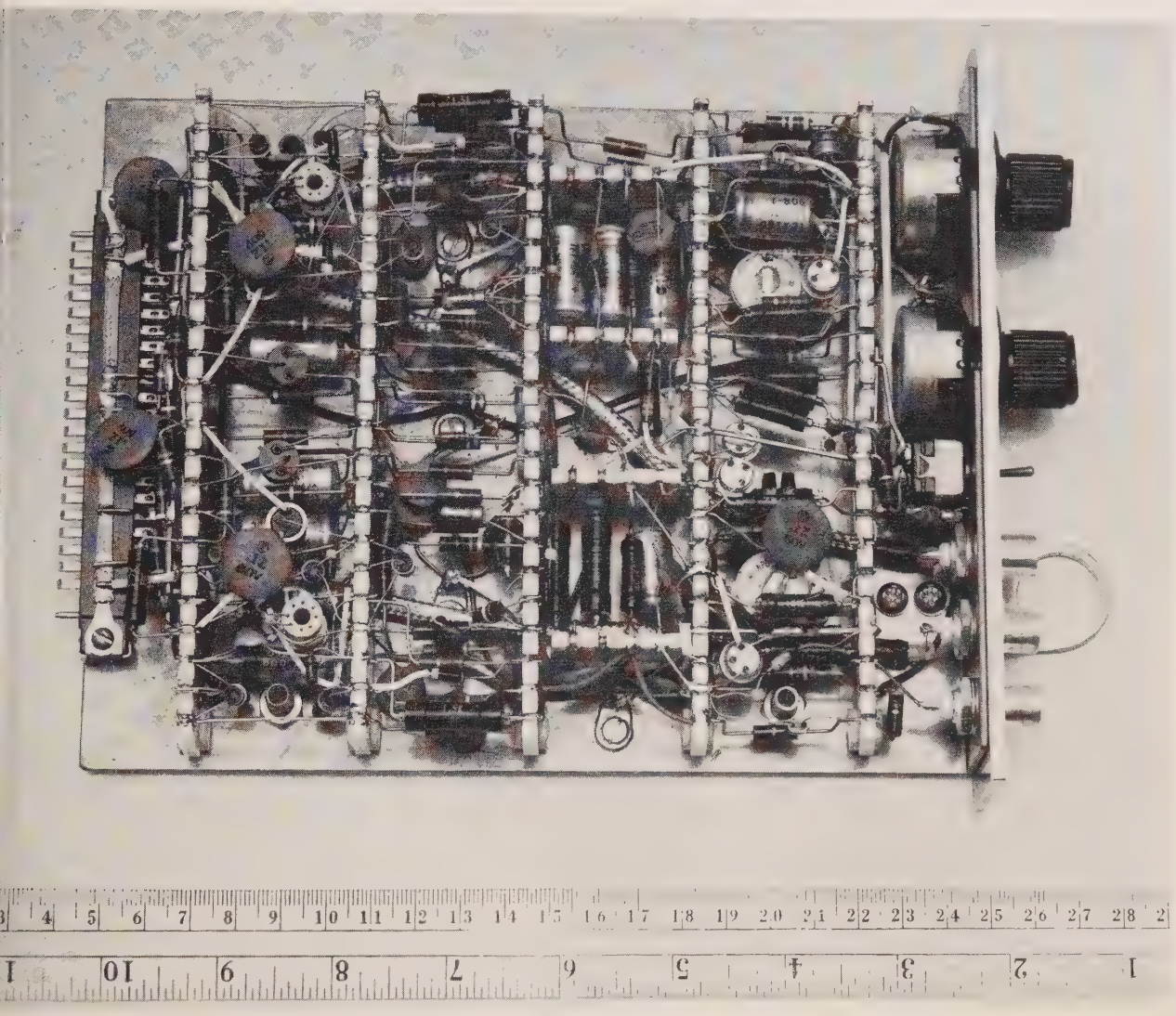

Fig. 13. Photograph of a unit consisting of an amplifier and two discriminators.

T_1 changes from 10 nsec to 20 nsec, the output pulse amplitude changes from 0.2 V to 2 V.

The pulse arriving at the vetoed coincidence output is delayed 50 nsec by a lumped constant 200 Ω delay line. This more nearly centers the coincidence pulse in the stretched veto pulse if both the coincidence and veto inputs occur simultaneously. (A 40 nsec delay line would have provided a more perfect centering, but none was commercially available.) The cable is nearly terminated on the base of T_5 by a 200 Ω series resistor. The voltage on the base of T_5 changes by about 0.5 V causing a 10 percent reflection. By the time the reflection reaches the collector of T_1, the coincidence is over and the 200 Ω resistor to the base of T_2 prevents further reflections.

2.6. 0.5μsec LOGIC (fig. 12)

The coincidence resolving time is 0.25 to 0.5 μsec with a veto resolving time of 0.5 to 1 μsec. The output at coincidence follows the smallest input within $\pm$ 10 percent with a vetoed coincidence output of less than $\pm$ 0.1 V. The maximum continuous counting rate is 1 Mc/s. The output has an impedance of $<$ 20 ohms, capable of driving capacities up to 300 pF.

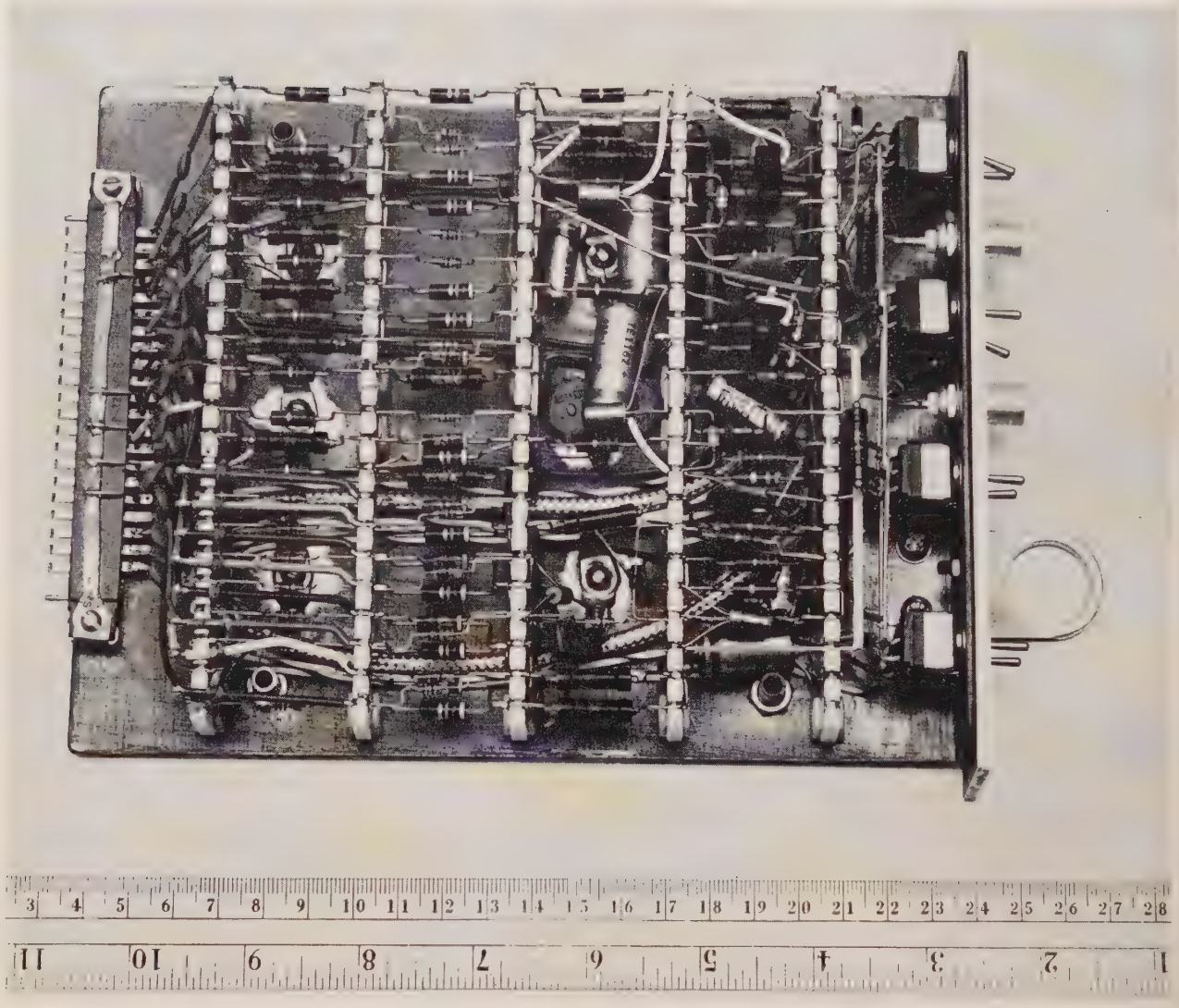

Fig. 14. Photograph of the 50 nsec logic (shield removed).

The operation is the following:

Coincidence Circuit

The coincidence circuit is a diode "And" circuit with Input Switches to determine which inputs are in coincidence.

When one of these switches is in the "C" position, it connects the particular input to the base of T_3 (2N 501-4) through D_c and a $\frac{1}{4}$ μsec delay cable. Unless all of the D_c diodes are unhooked, either by a negative input pulse or through the Input Selector Switch being in the "V" or "off" position, the base of T_3 is near ground. If all D_c diodes are unhooked, then the base of T_3 moves to the voltage of the least negative input or to -3 V, whichever is less negative.

Transistor T_3 is an emitter follower and drives the 1:4 transformer (EF71-1628) which is connected as an auto transformer giving a 25 percent voltage increase. The purpose of this transformer is to make up voltage losses in the emitter followers and thus give nearly unit gain from the input to the output at coincidence. This makes it possible to cascade slow logic circuits.

The $\frac{1}{4}$ μsec delay cable (HH 1600) delays the coincidence inputs with respect to the veto inputs

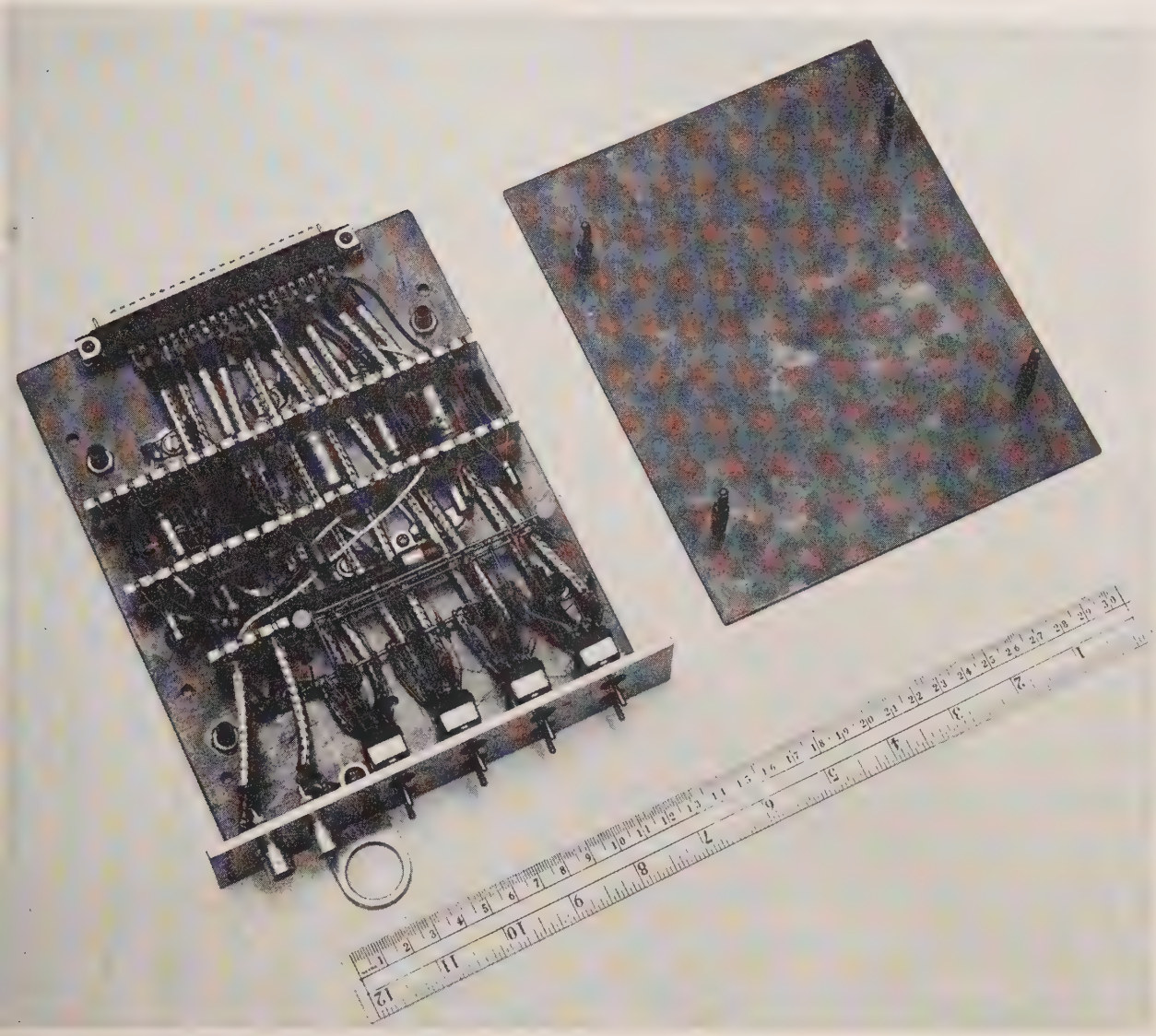

Fig. 15. Photograph of the 0.5 μsec logic and the shield.

o that the veto pulse will overlap the coincidence ulse. The delay line is terminated in 1.7 k at the ase of T_3.

The diodes D_p on the input are to recover the apacitors coupling the outputs of the Logic hassis. This prevents large D.C. drifts on the input t high counting rates. The IN99 diodes from mitter to base of the transistors are all protective.

eto Circuit (T_1, T_2)

The veto circuit is a diode "Or" circuit with the nput switches determining which inputs can veto.

When one of these switches is in the "V" position, negative pulses on its input will pass through diode D_V(IN270) and reach the base of T_1. This charges the stretching capacitor (220 pF) which holds D_1 (IN270) unhooked for 1 μsec after charging. When D_1 is unhooked, the $\frac{1}{2}$ mA flowing in the 60 k resistor pulls T_2 (2N384) into saturation, raising its collector voltage from — 6.3 V to zero. This makes D_2 (IN270) ready to conduct and prevent the passage of negative signals to the base of T_4(2N384). Thus, the output of T_4 is vetoed by the low impedance of the saturated transistor T_2.

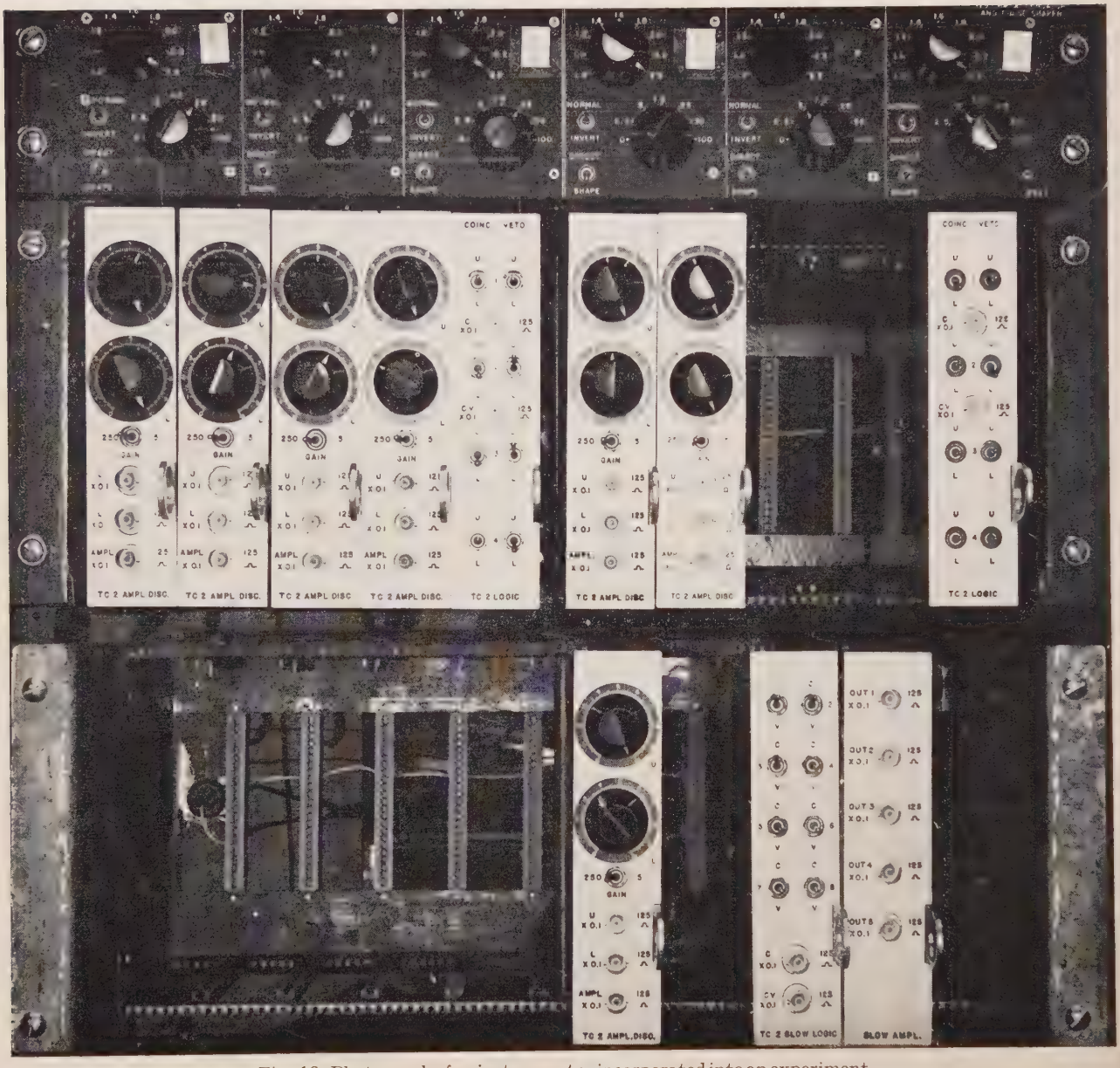

Fig. 16. Photograph of an instrument as incorporated into an experiment

Output Stages (T_4, T_5)

Both the coincidence output stage (T_5) and the vetoed coincidence output stage (T_4) are emitter followers. They are both connected to the transformer (EF71-1628) by 330 Ω resistors, and the bases are pulled negative by $\frac{1}{3}$ V so as to give nearly zero output D.C. voltage.

The vetoed coincidence output stage is coupled by 330 Ω to the transformer so that the delay line termination will not be significantly changed by the low impedance seen at the base of T_4 when a veto is present. For the same reason T_3 was chosen to be a high beta transistor ($\beta > 100$). The 300 Ω was used in the coincidence output stage so that the two output impedances would be the same when no veto was present.

The collectors of all the emitter followers are decoupled from the -6.3 V supply by 56 Ω and 20 μF to prevent pickup form pulse loading of the supply.

3. Construction

The circuits are built on 16 cm × 20 cm copper plates, having 4 cm × 17.5 cm front panels. Ten of these units plug into a 17.8 cm × 45 cm rack. Signals as well as power lines connect through the rear connector. The monitor coax connectors and the controls are mounted on the front panel. Components are mounted on ceramic terminal strips with coaxial cables and D.C. wires underneath. Care has been taken to keep grounds short. Interconnections between the discriminators and 50 μsec logic circuits use 50 ohm cable with taper pins; other signal wires 125 ohm cable. It was found necessary to provide low inductance grounds to each chassis in a sliding contact built into the mounting channel.

Extreme care has to be taken to provide reliable power lines (+ 27 V, — 27 V, — 6.3 V), since the absence of any of them may cause serious damage to the circuit. A safety interlock circuit has been used to ensure simultaneous shorting of all lines, if one fails.

Fig. 13 shows the unit of an amplifier and two discriminators. The first stage of the amplifier is located at the upper front part, the second stage under it, the two discriminators in the rear part.

Fig. 14 shows the 50 nsec logic. The coincidence and veto diodes are located in the rear and the 50 nsec lumped constant delay line at the upper front part. Six attenuators, pulse shapers and inverters are mounted on a 9 cm panel (fig. 16).

4. Performance

The circuit has been used successfully to identify protons and pions in a six counter telescope at the CalTech synchrotron (fig. 16). At the present time this telescope has been expanded to nine counters with dE/dx windows set by this circuit aiding in the detection of 150 MeV K^+ mesons. Plans are being made to make a further expansion of the telescope to 20 to 25 counters and detect higher energy K^+. Experience in the past has shown the circuit to have the high degree of stability and reliability required for such multi-counter experiments demanding narrow amplitude windows.

Appendix

TRANSISTOR SELECTION

In the design of these circuits it was sometimes necessary to use transistors with selected betas. The betas of the 2N501's and 2N1500's were selected at $V_{ce} = -3$ V and $I_b = -0.01$ mA into the following groups:

2N1500–1, 2N501–1	$15 < \beta < 35$
2N1500–2, 2N501–2	$35 < \beta < 50$
2N1500–3, 2N501–3	$50 < \beta < 100$
2N1500–4, 2N501–4	$\beta > 100$

The 2N501's and 2N1500's of the same β class are electrically interchangable. Experience has shown the 2N1500 to be a more reliable transistor than the 2N501, and thus recently all circuits are built using 2N1500's instead of 2N501's.

The 2N502A's have also been β-selected at $V_{ce} = -10$ V, $I_b = -0.05$ mA into the following groups:

2N502A-1	$15 < \beta < 25$
2N502A–2	$25 < \beta < 44$
2N502A–3	$44 < \beta < 100$
2N502A–4	$100 < \beta < 200$

In fig. 9, 2N502A–Cd–1 and 2N502A–Cd–2 are specified. The Cd refers to a 2N502A with cadmium junctions which at the time of the design of the circuit had to be specified. At present all 2N502A transistors made by the Philco Corporation use cadmium, and it is no longer necessary to specifically request it.

NUCLEAR INSTRUMENTS AND METHODS 12 (1961) 60–66; NORTH-HOLLAND PUBLISHING CO.

THICK JUNCTION RADIATION DETECTORS MADE BY ION DRIFT

JACK H. ELLIOTT

Lawrence Radiation Laboratory, University of California, Berkeley, California

Received 11 March 1961

Lithium-drifted detectors with depletion thicknesses up to 3.38 mm, capable of stopping 24-MeV protons and 96-MeV α particles, have been produced. To the degree of accuracy of the experiment, the output pulse amplitude was linearly proportional to the energy absorbed in the detector, showing that the charge produced was collected with 100 % efficiency. 47.6-MeV cyclotron-produced α particles were resolved to 0.9 % full width at half-maximum. Most if not all of this width is attributed to beam energy spread. Details of production of these detectors are described.

1. Introduction

Solid-state radiation detectors have proven advantageous for short-range ionizing particles[1,2]) because of their high energy resolution. To the degree of accuracy of existing experiments, the output pulse amplitude is proportional to the energy lost by the particle, independent of its charge, mass, and velocity.

The method to be described employs the ion-drift technique of E.M. Pell[3]) to extend the depletion region (sensitive region) in p–n junctions, and thereby increase the usefulness of these detectors to include longer-range particles.

Two parameters that affect the depletion thickness W are the resistivity ρ of the silicon and the reverse bias voltage V, where

$$W \propto (\rho V)^{\frac{1}{2}} . \qquad (1)$$

The maximum voltage that can be applied to the junction depends on several variables. Avalanche breakdown in either the bulk material or the junction edge may be the limiting factor or, under other circumstances, noise due to surface or bulk leakage currents may set the limit[4]).

On examination of eq. (1) it is seen that high-resistivity material is required to obtain thick depletion layers at a reasonable bias voltage. Material exhibiting greater than 10000 ohm-cm resistivity is difficult to obtain and suffers change of resistivity or even of type[5]) during high-temperature processing (e.g., diffusion). By applying the ion drift method, essentially intrinsic (high-ρ) silicon can be produced in a p–n junction made from low-resistivity starting material.

2. Principles of the Ion-Drift Method

E. M. Pell has described the ion-drift principle in detail; the description given here is brief. The method depends on the tendency of ionized donors or acceptors to drift in the electric field existing in the depletion layer of a junction when the junction is reverse-biased. It may be seen that the general result of such drift is a tendency to create an intrinsic semiconductor layer in the junction region in which donor and acceptor impurities almost exactly compensate. With most types of impurity, diffusion masks the ion-drift effect; but with lithium, there is a temperature range (100 to 400°C) in which ion-drift effects can be made predominant.

To demonstrate the effect, consider a block of p-type silicon into which lithium (a donor impurity) has been diffused from one face. Figure 1 shows a donor-acceptor profile after this initial diffusion. If the resulting n–p junction is reverse-biased and the temperature raised to 150°C for a short time, the donor-acceptor profile is as shown in fig. 2. Lithium ions (positive charge) have been trans-

[1]) M. L. Halbert and J. L. Blankenship, Nucl. Instr. and Meth. 8 (1960) 106.

[2]) S. S. Friedland, J. W. Mayer and J. S. Wiggins, Nucleonics No. 2, (1960) 54.

[3]) E. M. Pell, J. Appl. Phys. 31 (1960) 291.

[4]) F. S. Goulding and W. L. Hansen, Nucl. Instr. and Meth. 12 (1961) to be published.

[5]) W. L. Hansen (Lawrence Radiation Laboratory) private communication.

ferred from the Li-excess side of the junction to the Li-deficient side, owing to this drift in the electric field that exists in the junction region.

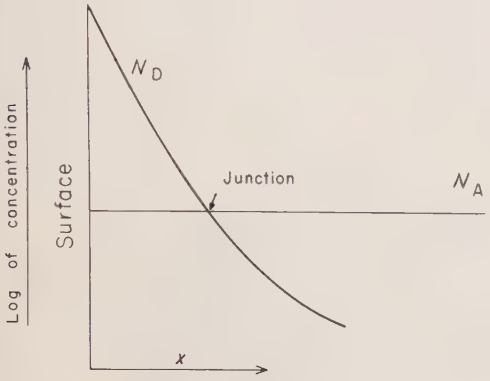

Fig. 1. Concentration profile of donor N_D and acceptor N_A impurities in a diffused junction diode.

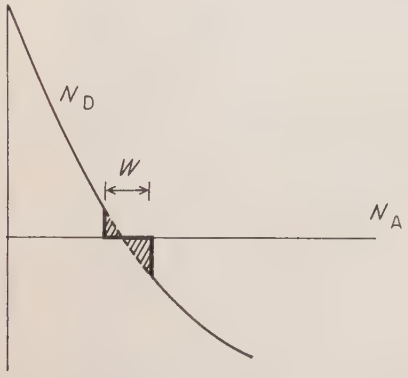

Fig. 2. Concentration profile after a period of drift.

Pell[3]) has shown that W^2 is proportional to the time of drift at constant voltage and temperature. The drift field must be sufficiently large so that diffusion rate is negligible compared with drift rate.

3. Preparation of Li-Drifted Detectors

3.1. DISCUSSION OF METHOD

Drift rate is proportional to temperature and voltage[3]). The maximum temperature is determined by the temperature at which the starting material becomes intrinsic and the junction is lost[6]). Lower-resistivity heavily doped p-type material allows higher drift temperatures. Therefore, the amount of lithium transferable at the higher temperatures with low-ρ material is greater than can be transferred in high-ρ material, but the amount of Li needed to compensate the amounts of p-type impurity is also greater in the low-ρ silicon. A qualitative study of starting material, judged from the drift rate of 0.47-ohm-cm (ref.[4])) and 2000 ohm-cm (ref.[7])) p-type silicon and the allowed operating temperatures, led to the choice of 100 ohm-cm material.

Severe pitting of the surface into which the lithium is diffused prompted use of a p^+ impurity coating on the opposite side of the silicon wafer, and led to the resolution to drift the Li ions all the way to this back coating so that it could be used as the particle-entry side.

3.2. PREPARATION OF THE SILICON

Wafers with surfaces parallel to the (111) plane were cut from the silicon ingot[8]) containing the p-type impurities (approx. 100 ohm-cm). Thicknesses ranged from 50 mils[9]) upwards. The surfaces were lapped with 1950-mesh Al_2O_3 grinding com-

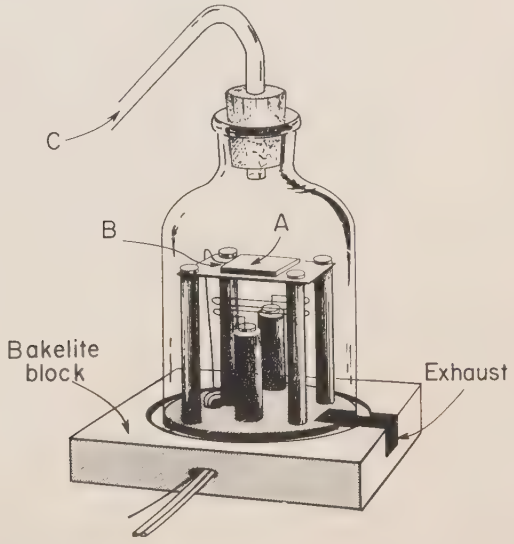

Fig. 3. Diffusion furnace. A carbon holder A for the slice is shown supported above the heating element. The thermocouple junction fits into a hole B, drilled in the carbon plate. Helium flow C and the bell jar exclude oxygen while diffusing.

[6]) F. J. Morin and J. P. Maita, Phys. Rev. **96** (1954) 28, fig. 13.

[7]) E. M. Pell (General Electric Research Laboratory, Schenectady) private communication.

[8]) Electronic Chemicals Div., Merck and Co.

[9]) 1 mil = 0.001 in. = 2.54×10^{-3} cm.

pound to a smooth finish. The wafers were then washed in synthetic detergent and thoroughly rinsed with methanol[10]), trichlorethylene[10]), methanol, and deionized water. One face of the slice was etched with a solution of 1 part hydrofluoric[10]) and 10 parts nitric acid for 5 minutes and then with a slower etch (1 part HF, 20 parts HNO_3) for 10 min to remove damage due to lapping. Following

3.3. DIFFUSION

A suspension of lithium in oil[11]) was painted with a small glass rod on the surface opposite the Al side and the slice was heated in the diffusion oven (fig. 3) to 250 to 300°C to drive off the mineral oil. A dry helium gas flow into the oven excluded oxygen. Once the mineral oil had been removed, the temperature of the slice was raised to 450°C for

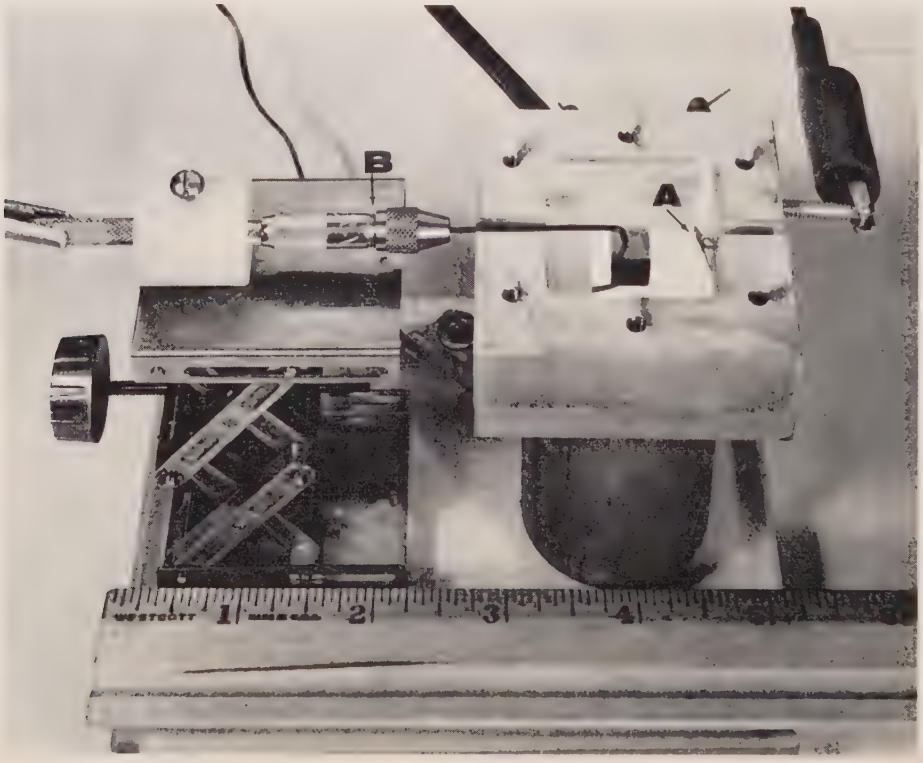

Fig. 4. Drift oven, shown with its cover removed. The heating element is in a cavity cut in the lower portion of the silver-plated brass block. A indicates the thermocouple lead. B indicates the steel spring wire probe and holder.

thorough rinsing in methanol, trichloroethylene, methanol, and deionized water and drying with a jet of dry nitrogen, a 500-Å-thick coating of aluminum metal was immediately vaporized, in vacuum, onto the etched surface. The aluminum was then alloyed into the silicon by placing the slice in a furmace at 650°C for 2 min. In the following 3 min the slice was slowly removed from the furnace. Nitrogen flow through the furnace tube excluded oxygen during the alloying. This completed the p^+ surface through which particles are allowed to enter the sensitive region of the detector. Most slices were then cut to an area of 0.3 × 0.3 inch. approximately 60 seconds and then cooled. This produced a junction approx 20 mils in from the lithium side. When the slice had cooled below 80°C it was dropped into water to remove the excess lithium on the surface. After the slice was washed as described earlier (prior to etching the surface), picein wax in trichloroethylene was painted on the two faces and dried under a heat lamp. The edges

[10]) Electronic Grade, Baker and Adamson.

[11]) Available from Lithium Corporation of America Inc.: 30% lithium, 69% mineral oil, and 1% oleic acid.

[12]) Joseph Evans, Fundamental Principles of Transistors (D. Van Nostrand Co., Princeton, N.J. and New York, 1958) Ch. 2.

vere then etched for 2 min in hydrofluoric and nitric acids (1:3). The Picein was removed by vashing with trichloroethylene followed by metha-nol and deionized water. Dry compressed nitrogen vas then used to blow the water off (to prevent most of the water from drying on the slice), thus maintaining maximum purity.

3.4. ION DRIFT

The Li-junction diode was placed Li face up in the drift oven shown in fig. 4. A voltage supply, a relay, and a Boonton Q Meter, to measure capacity, were connected in series. The temperature was raised and the increase in the depletion width, W, was observed by measuring the capacity. For a parallel-plate capacitor,

$$C = \frac{4\pi A}{\varkappa W} . \qquad (2)$$

Here A is the area of the junction and $\varkappa$ is the dielectric constant for silicon (12 at room temperature).

The drifting of the Li-junction diodes was usually begun with 300 volts at 150°C. Generation current[12] increased as W grew, finally reaching a value where thermal runaway occurred. A current-sensitive relay protected the detector from damage by switching off the heater element and the applied

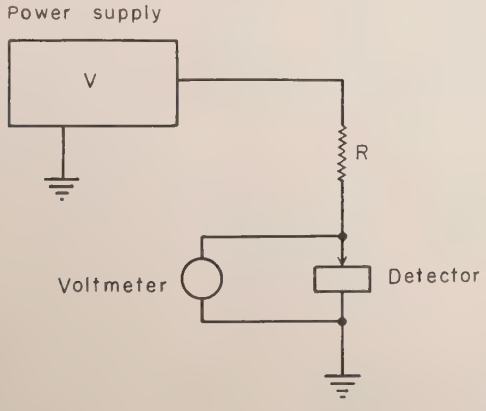

Fig. 5. Schematic drawing of the power-limited voltage supply. The value of R is chosen to limit the amount of power that can be dissipated in the detector.

voltage. To continue the drift either the operating temperature or voltage was reduced, resulting in a slower drift rate. Thermal runaway continued to drive the drift-rate parameters to lower values as W grew. Drift rates were determined for 100-ohm-cm silicon starting material by the above procedure; they are discussed below.

A technique that maintained the fastest drift rate at any time for a given operating temperature made use of high starting voltages and a resistor which

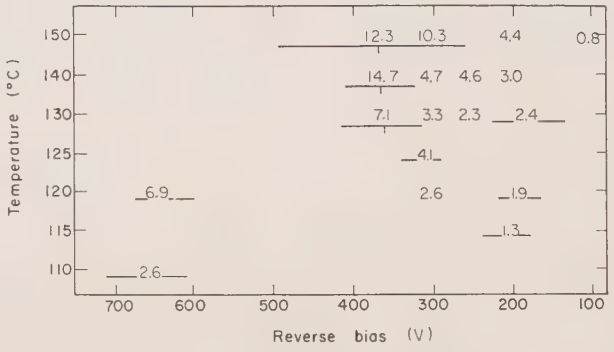

Fig. 6. Rate of junction growth (mils²/minute).

limited the maximum amount of power that could be expended in the crystal (fig. 5). By determining the current and voltage across the slice at the point of thermal runaway the power input became known ($P = iV$). The value of the resistor was then chosen so that at all values of leakage current the maximum power to the slice was just below the thermal runaway point. The drift then started at a

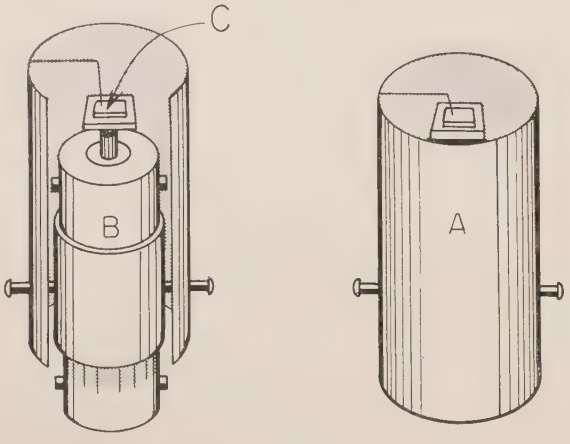

Fig. 7. Detector holder. Cylinder A with a spring contact soldered at the opening fits over a BNC cable-to-cable connector B. An ohmic platform soldered to a BNC cable pin supports the detector C.

high voltage, and with increased W the conduction in the diode increased, causing a gradual decrease in the amount of voltage across the diode. When the

voltage dropped below 200 V it was usually advantageous to lower the temperature, permitting an increase in voltage.

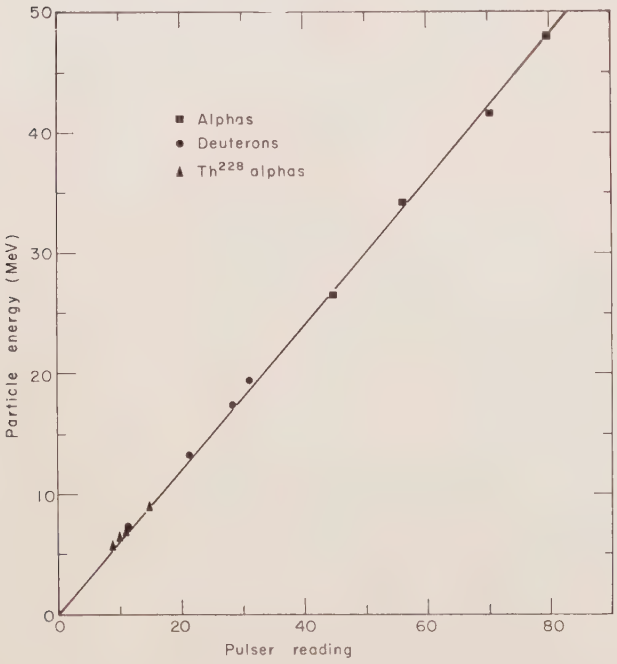

Fig. 8. Particle energy *vs* pulse amplitude.

mate and serve as a guide in adjusting operating parameters. As W becomes larger for a given pair of parameters the field decreases, and the rate decreases somewhat, probably owing to diffusion competition. Lines under the rates obtained by using the limiting resistor indicate the voltage range over the period during which the rate was measured.

The depletion thicknesses of two crystals were extended to about 130 mils. Both required almost 80 hours drift time, ending with a final drift temperature of 115°C.

3.6. DETECTOR PERFORMANCE

The Li-drifted detectors were mounted in the holder shown in fig. 7. The p^+ side was contacted with steel spring wire which provides tension to hold the crystal in place.

A preamplifier designed for use with junction detectors of the conventional type (i.e., thin depletion layers)[4]) was used along with a linear amplifier and a 100-channel pulse-height analyzer. A calibrated pulser signal was fed into the preamplifier input to test the stability of the system.

Energy measurements were made with helium ions and deuterons from the Crocker Laboratory

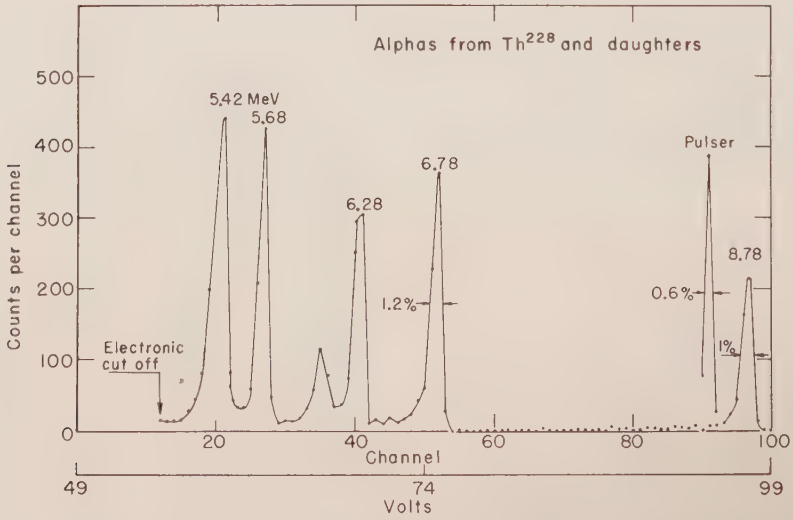

Fig. 9. Spectrum of Th^{228} and daughter alpha particles.

3.5. EXPERIMENTAL DATA

Rates of W growth in units of mils^2/min were determined for 100 ohm-cm Si at various voltages and temperatures (fig. 6). These rates are approxi-

60-inch cyclotron, elastically scattered through 15 deg from a 0.0001-in. gold foil in a 36-in. scattering chamber[13]). Particles were degraded to various

[13]) B. G. Harvey and J. Cerny, Phys. Rev. **120** (1960) 2162

nergies by aluminum absorbers. Alpha particles om a Th^{228} source were also measured. The count- g system was designed for nuclear reaction ex- erimental use, and therefore did not require that onnections between detector and preamplifier be hort. Four feet of cable was used to connect the etector to the preamplifier and 75 feet of cable onnected the preamplifier to the counting area.

Confirmation that linearity is obtained with the using deuterons from the reaction $Li^6(\alpha, d)B^8$, a cutoff at a deuteron energy of 32.8 MeV was found for the detector in fig. 10. The sensitive thickness of 133 mils was found from the range-energy relationship for deuterons in silicon. This thickness agrees with the less accurate determination by capacity measurement (1.8 ± 0.1 picofarads). This detector would therefore be capable of stopping 24-MeV protons and 96-MeV α particles.

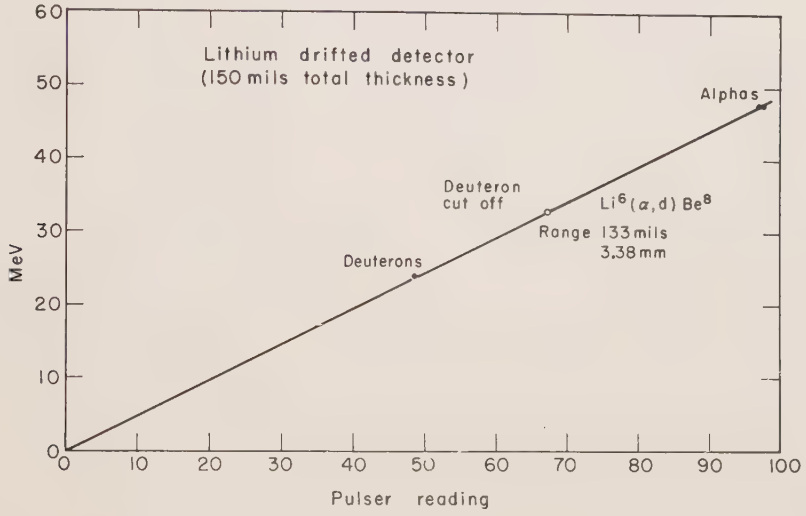

ig. 10. Particle energy *vs.* pulse amplitude for the 133-mil detector. The 32.8-MeV cutoff for deuterons from the $Li^6(\alpha,d)B^8$ reaction determines the sensitive thickness.

nicker Li-drifted detectors is shown in fig. 8. leasurements were made at 60 v reverse bias, iving a W of 57 mils. This detector was fully epleted to 80 mils thickness when 150 V bias was pplied.

Figure 9 shows the spectrum of Th^{228} and daugh- er α particles. Maximum resolution obtained for ne 8.78-MeV energy group was 0.93%, which is omparable to the performance of the conventional hosphorus-diffused silicon detectors currently sed with this electronic system.

A check on linearity of a much thicker detector 33 mils = 3.38 mm) is shown in fig. 10. When a pectrum of particles, some having ranges in Si nger than W, falls onto the detector, a pulse- eight (energy) cutoff of pulses coming from the etector is observed. This cutoff energy cor- sponds to the energy deposited by a particle that ust stopped in the sensitive depth. Particles of reater or less energy produce smaller pulses. By

Resolution obtained for the 47.6-MeV α particles was 0.9% full width at half-maximum. It is not a measure of the detector's ultimate energy resolution, since prior to this measurement the cyclotron beam spread had been estimated to be up to 0.8% in energy[14]).

Figure 11 shows that the 80-mil Li-drifted detector resolves the K- and L-conversion peaks from the spectrum of Cs^{137}.

Large changes in the depletion layer thickness, measured by capacity, have been encountered after 1 month's storage. When reverse bias was applied for a few hours at room temperature the thickness increased. Repeating the particle-method determination of thickness for the 133-mil detector shown in fig. 10 confirmed the original thickness. These

[14]) Walter John, Jr., Systematics of Excitation Functions with Application to Lead (Thesis), University of California Radiation Laboratory Report UCRL-3093, August 4, 1955 (unpublished).

results indicate that storage with reverse bias is desirable.

4. Concluding Remarks

Preparation of thick large-area Li-drifted detectors requires much longer times when the technique described above is used, since leakage current, caused by thermal generation of charge carriers and dependent upon the volume of the depletion region, forces the use of lower temperatures and voltages. With larger inexpensive drift ovens, many junctions can be drifted at one time.

The lifetime of the minority charge carriers sets a limit on the thickness at which a detector will remain linear and not lose charge owing to recombination. This limit has not been reached at a thickness of 133 mils, as evidenced by the data above.

Acknowledgements

The author wishes to express his appreciation to E. M. Pell for his invaluable guidance and discussions, as well as to F. S. Goulding, W. L. Hansen, B. G. Harvey, L. Schifferle and E. Woo for their many helpful discussions and their cooperation. The author also would like to thank the crew of the Crocker Laboratory 60-inch cyclotron for assistance.

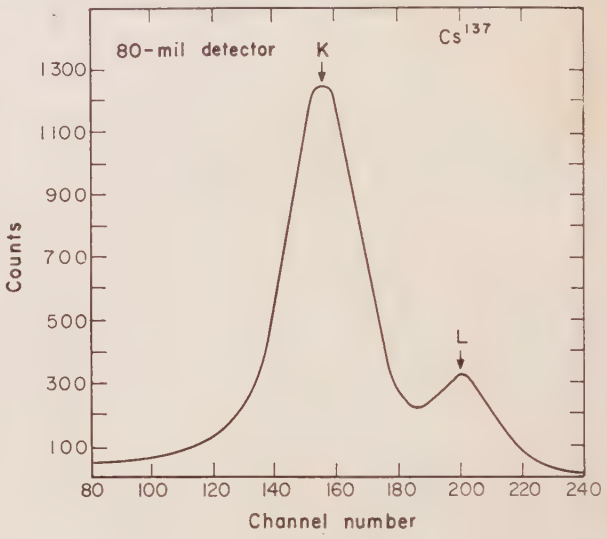

Fig. 11. K- and L-conversion peaks from the decay of Cs^{137}.

This work was done under the auspices of the U.S. Atomic Energy Commission.

UCLEAR INSTRUMENTS AND METHODS 12 (1961) 67–74; NORTH-HOLLAND PUBLISHING CO.

OBSERVATIONS ON THE RESPONSE OF TWO p-n JUNCTION DIODES TO PROTONS

J. BENVENISTE, R. BOOTH and A. C. MITCHELL

Lawrence Radiation Laboratory, University of California, Livermore, California

Received 16 February 1961

ie response of two silicon p–n junction diodes has been meas-ed for protons up to 13.3 MeV. In one case the dependence of pletion layer thickness with bias voltage was found to be $T \propto V^{0.46}$. The observed resolution, made up of contributions from crystal noise, beam width, and scatterer thickness, was about 1%for 9-MeV protons.

Introduction

This report is concerned with observations made n the response of silicon p–n junction diodes to rotons of various energies up to 13.3 MeV. Data re presented for two diodes† made from 10000 m-cm material. The thickness of these wafers is out 30 mils or 170 mg/cm². The first has an active ea which is roughly circular and about 5 mm in ameter. This is referred to as the "normal" tector since the particles were incident along a ne normal to the front face. The second is rather uare and about 1 cm on a side. This unit was ounted so that the incident protons made an ngle of 60° with the normal to the front face. Thus e depletion layer was expected to appear twice as ick to these particles as it would if the particles ad entered normally. Because of the way in which was used, this detector is referred to as the lant detector." A $\frac{1}{8}$-in. collimator before each tector selected a central portion of the active ea to eliminate edge effects.

Experimental Arrangement

The experiment was performed in our remotely erated 40-in. scattering chamber. The scattering ometry is schematically represented in fig. 1. efore entering the scattering chamber, the beam as collimated to $\frac{1}{8}$ in. and further cleaned up with ti-scattering slits. The spread in scattering angle ie to the finite size of the beam where it strikes e scatterer is expected to be less than 0.2 degree.

† These units were made available to us through the courtesy Dr. J. Mayer of the Hughes Aircraft Co.

The collimator and scattering chamber are carefully aligned along the beam as is the detector when rotated to the zero-degree position. The position of

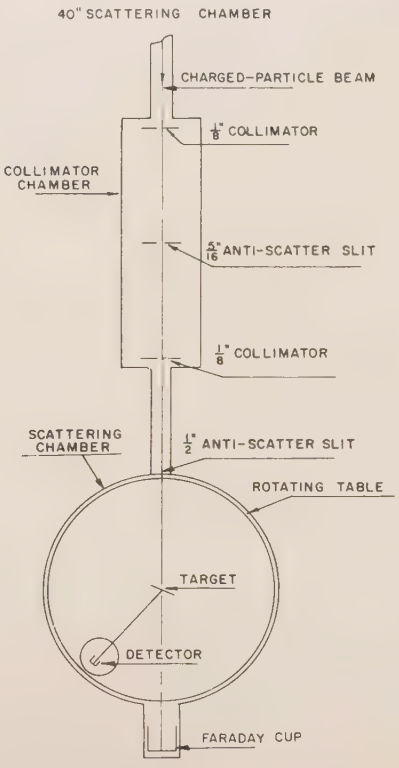

Fig. 1. Schematic representation of scattering geometry.

each component is true to within 10 mils of the beam line. This contributes an error of only 0.03 degree to the measured scattering angle. The precision of the remote indicator of detector position is $\pm$ 0.1 degree.

The beam energy is determined by measuring the range of the protons in aluminum. With the application of the range-energy relations, the precision of the energy measurement is expected to be 0.5%. We find, for the bombarding energy at the center of the scatterer, 13.3 MeV.

A special preamplifier (fig. 2a) was constructed to operate in the scattering chamber. The rest of the electronics included a good linear amplifier and a 256-channel analyzer. The block diagram appears in fig. 2b.

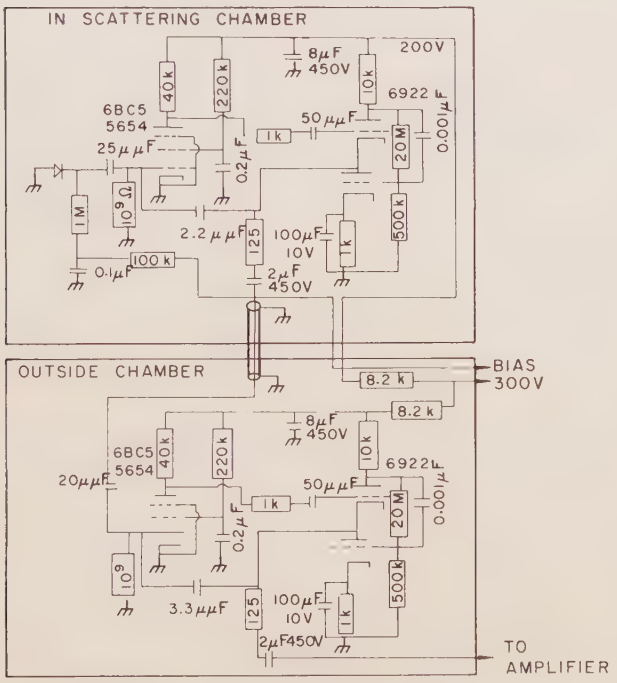

Fig. 2a. Preamplifier circuit.

3. Proton Response

The response was determined by observing protons scattered elastically and inelastically from a thin (1 mg/cm²) Mylar foil. The energy of the various proton groups observed was determined from the kinematics of scattering from hydrogen and the several levels in C^{12} and O^{16}. These are the dots of Figs. 3a–3d and 4a–4e. In each case corrections were made for energy loss in the scatterer and the linearity characteristic of the multichannel analyzer.

The triangles represent α-particle data from a Cm^{242} source. That they land on the same straight line as for protons indicates that the output from these junction diodes is a function only of the energy deposited in the depletion layer, not the nature of the particle.

In each case the response curve is seen to be quite linear up to the break point. Beyond this point, data for the falling portion of the curve are contributed by higher-energy protons. That their output pulses are low is just due to the fact that their range is larger than the depletion layer thickness. The dashed portion of each curve was, therefore,

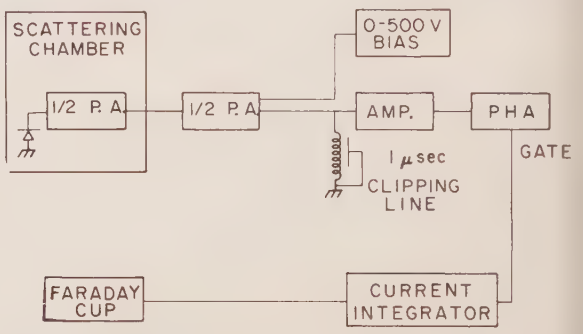

Fig. 2b. Block diagram of detector electronics.

derived in the following way: For the most penetrating particles the amount of energy deposited in the depletion layer was determined from a comparison of the pulse-height response with that of a lower-energy proton. Then with the use of range-energy curves for aluminum (these are considered to be sufficiently close to silicon to require no corrections), the thickness of material in which the high-energy protons will deposit the observed amount of energy is calculated assuming no scattering. This is taken to be the depletion layer thickness. The rest of the dashed curve is derived by calculating the energy that would be lost by a proton of energy E_p in a layer of this thickness.

Extending this curve back till it intersects the straight line yields a sort of idealized response curve—one which would be expected if the depletion layer had well-defined boundaries and if the detected particle did not scatter. It should be expected that where multiple scattering effects are most important (e.g., where the particle range is not much greater than the depletion layer thickness as calculated above) the depletion layer will

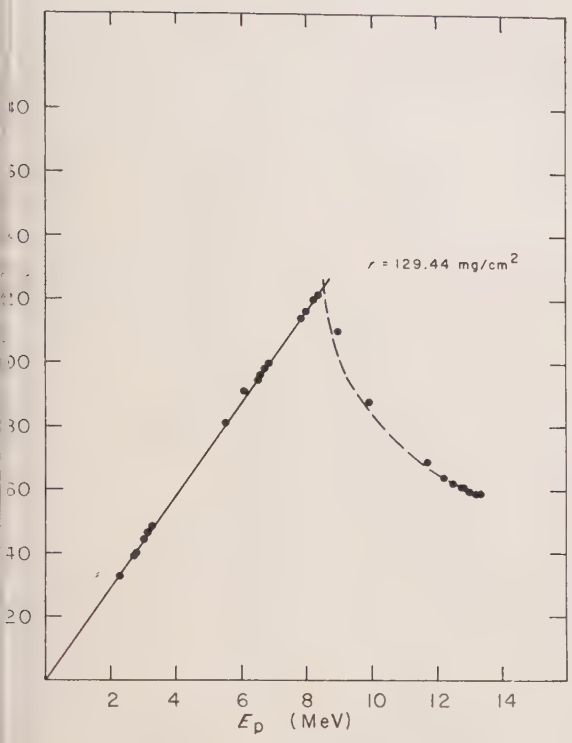

ig. 3a. Response curve for "normal" detector for 150-V bias.

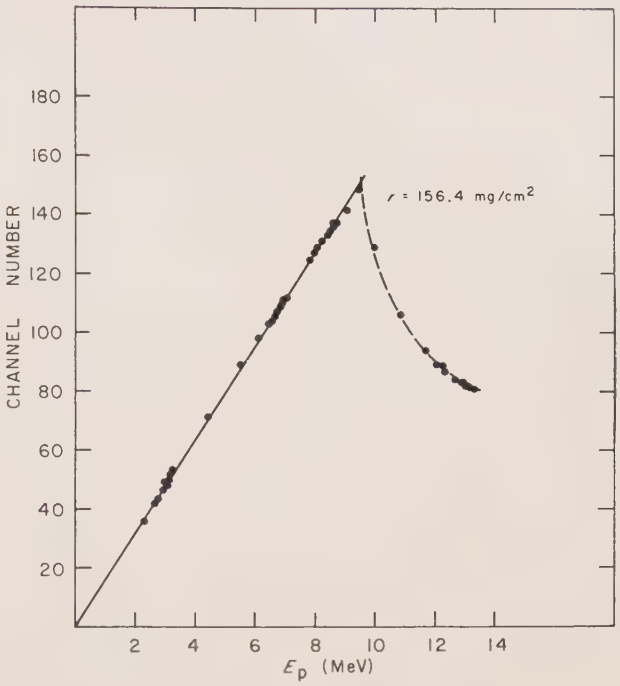

Fig. 3b. Response curve for "normal" detector for 250-V bias.

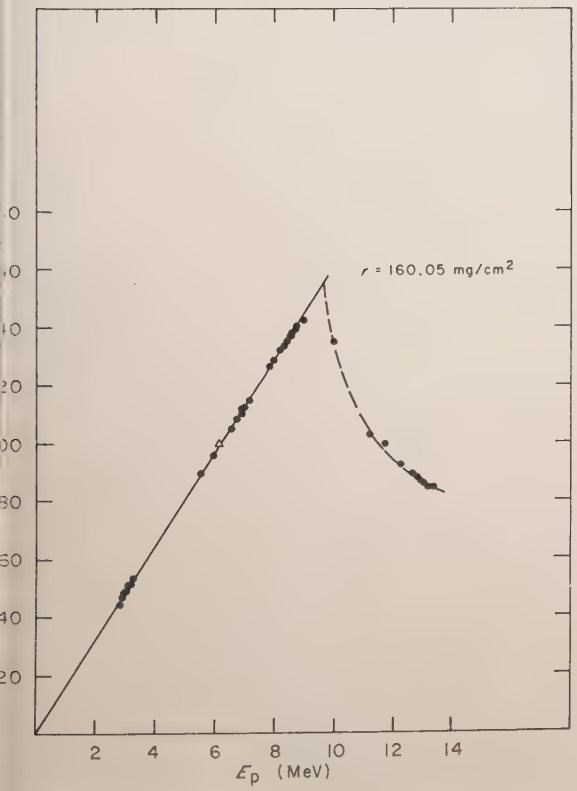

ig. 3c. Response curve for "normal" detector for 300-V bias.

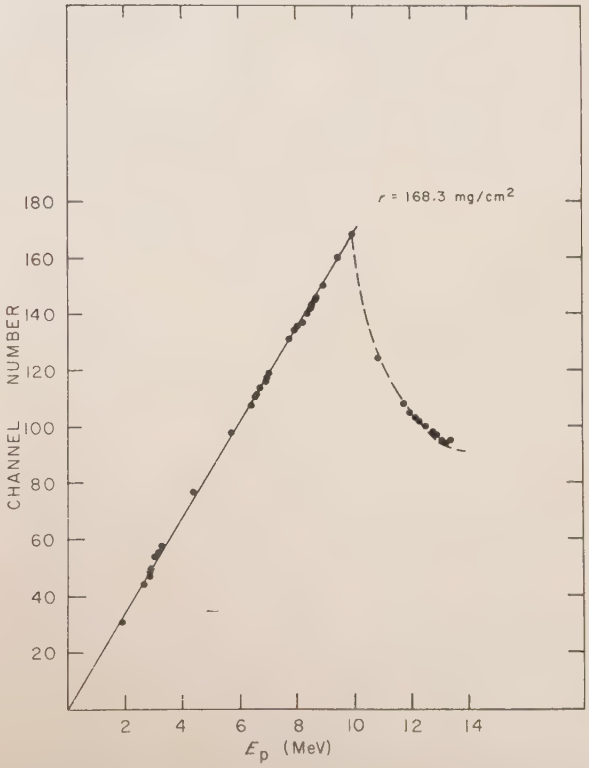

Fig. 3d. Response curve for "normal" detector for 400-V bias.

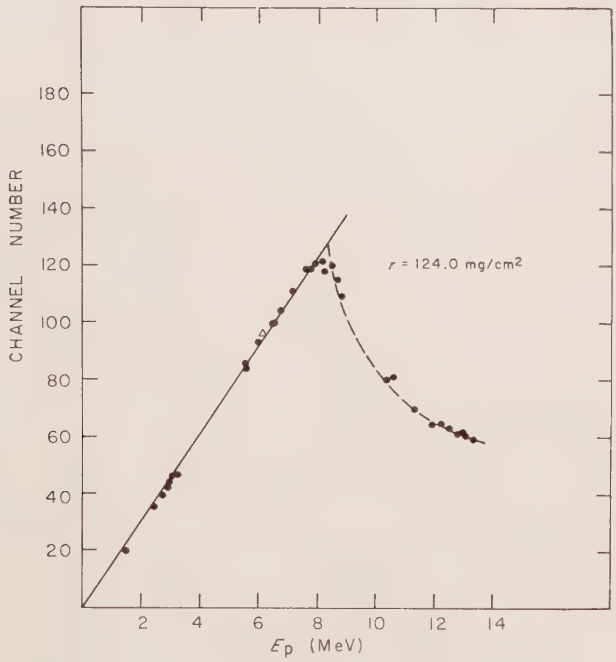

Fig. 4a. Response curve for "slant" detector for 50-V bias.

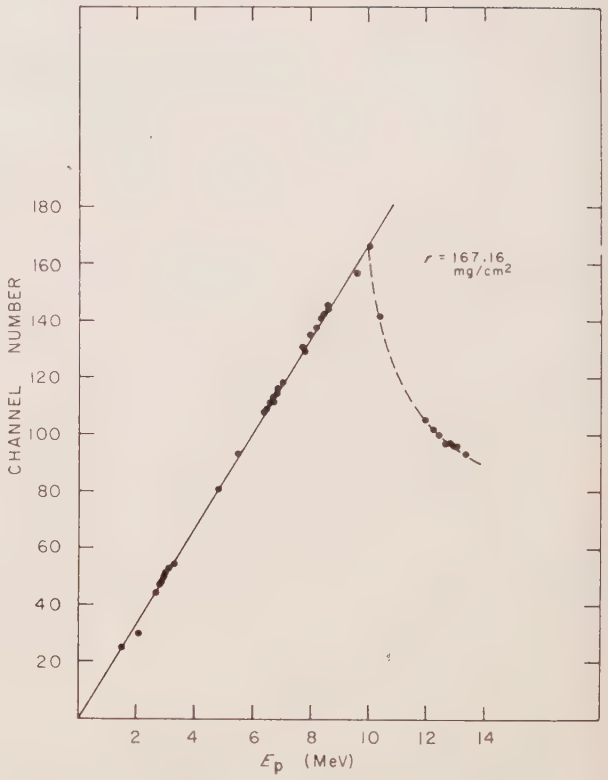

Fig. 4b. Response curve for "slant" detector for 100-V bias.

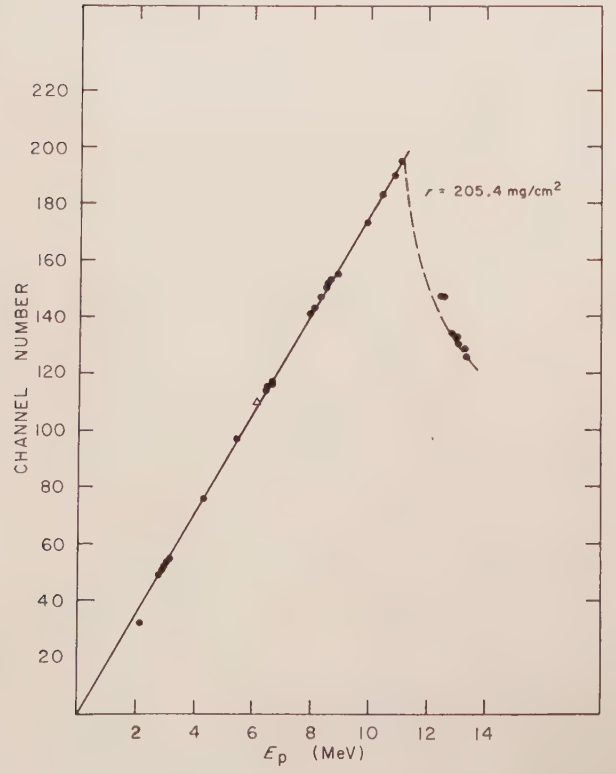

Fig. 4c. Response curve for "slant" detector for 150-V bias.

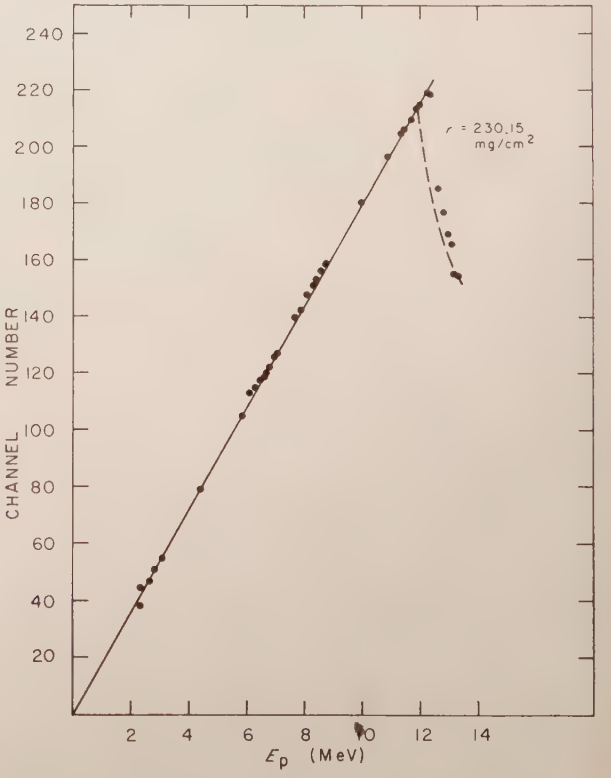

Fig. 4d. Response curve for "slant" detector for 200-V bias.

pear somewhat thicker and thus exhibit a slight unding off of the break point. It should also be pected that the behavior of the response curve ar the break point would be effected by the time

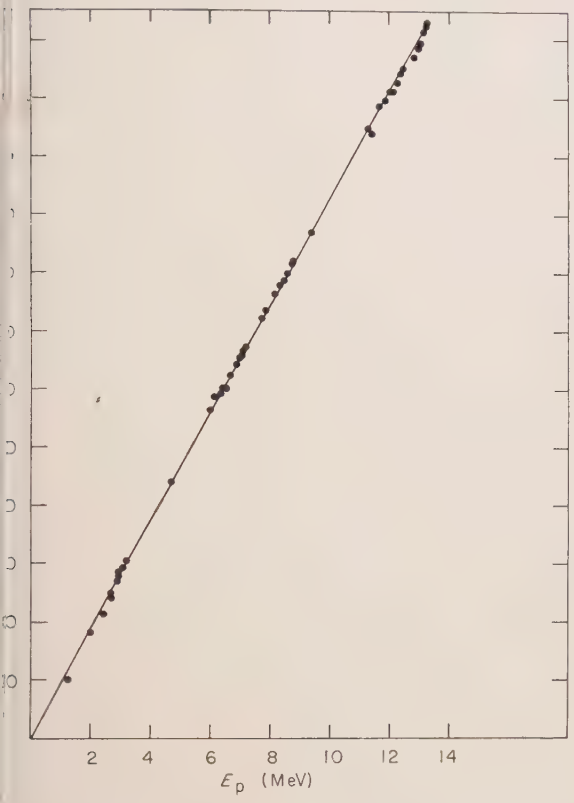

ig. 4e. Response curve for "slant" detector for 270-V bias.

evoted to the collection of electrons and holes. What we have observed therefore is closely related o the 1-μsec clipping line used at the input to our mplifier.

Calculations of depletion layer thickness were nade for several values of bias voltage and the nformation is summarized in fig. 5. For the slant etector the data are consistent with a power-law elation between depletion layer thickness and bias oltage:

$$T \approx V^{0.46}.$$

or the normal detector it appears that the deple- on layer thickness soon became comparable to the nickness of the silicon wafer (≈ 170 mg/cm^2) so nat strong deviations from a simple power-law elation were apparent.

Figure 6 shows a typical spectrum of protons scattered from the Mylar foil and observed in the normal detector. The highest energy group is due to scattering from hydrogen. Its unusual breadth is due to the finite acceptance angle of the detector, and the strong angular dependence of the scattered proton energy. The next lower peak is due to protons inelastically scattered from the 4.43-MeV level of C^{12}. The large broad peak just below this is due to elastically scattered particles from C^{12} plus some contribution from O^{16}. The position of this peak is understood in terms of the fact that these more penetrating particles deposit only a portion of their energy in the depletion layer. The large breadth is due to multiple scattering of the detected particle in the depletion layer. This phenomenon was more completely investigated and reported in an earlier article.†

Figure 7 shows the Mylar spectrum as observed in the slant detector. Here the elastic peaks for C^{12} and O^{16} have taken their rightful place at the top of the spectrum because the effective depletion layer thickness is now sufficiently large to absorb completely the proton energy.

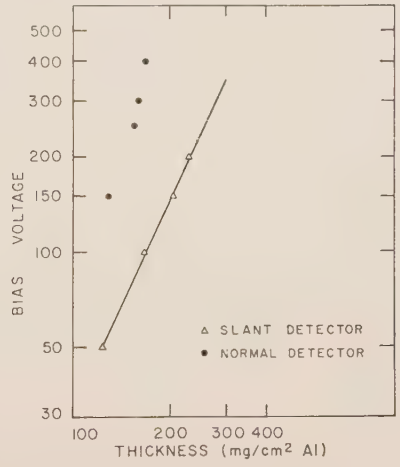

Fig. 5. Summary of depletion layer thickness measurements at several bias voltages.

Slightly higher-energy protons (e.g., those scattered from Au) continue to show the linearity of the slant detector's response; however, the pulse distribution suffers considerably as is seen in fig. 8.

† Article No. NuPh-148, obtainable on request to the P-Division office, Mrs. D. Hine.

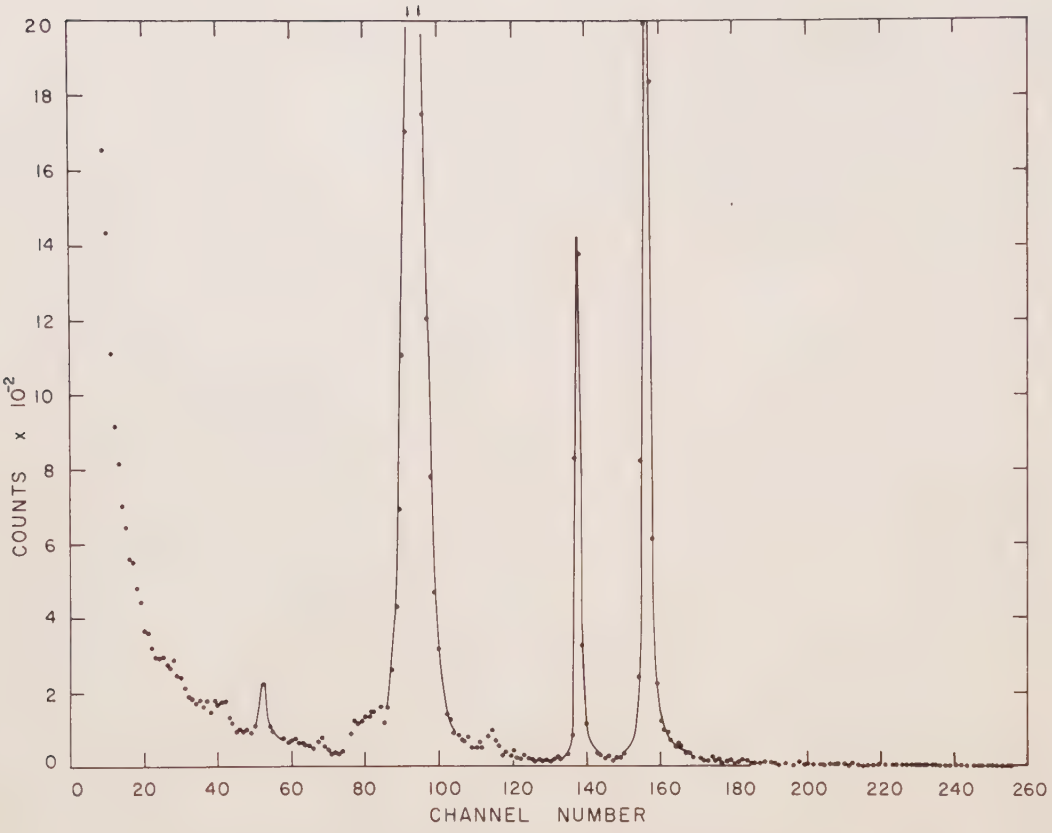

Fig. 6. "Normal" detector spectrum of protons scattered from Mylar foil at 32.6°.

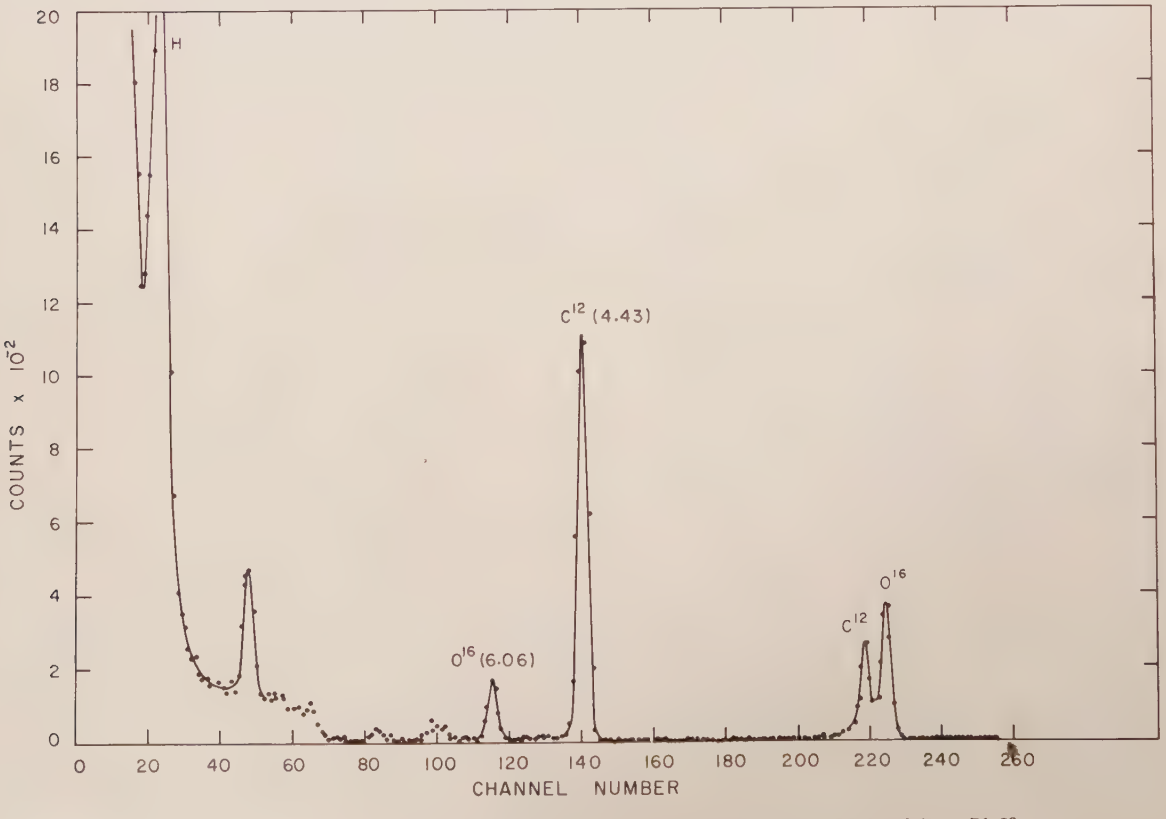

Fig. 7. "Slant" detector spectrum of protons scattered from Mylar foil at 71.6°.

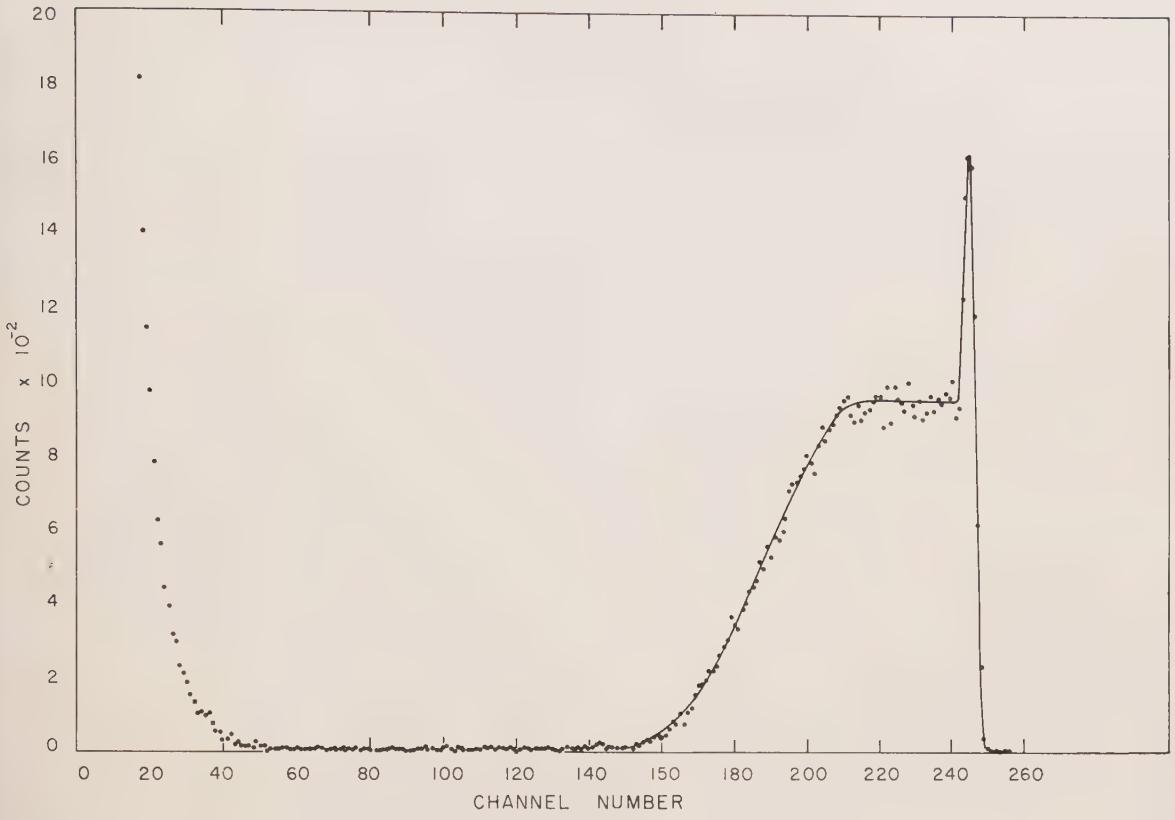

Fig. 8. "Slant" detector spectrum of protons scattered from Au foil at 67°.

The large low-energy tail may be understood in terms of multiple scattering of the incident protons in such a way as to leave the depletion layer prematurely. This is schematically represented in fig. 9.

4. Resolution

The observed resolution (fig. 10) is made up of several contributions. These include the statistical spread in the number of electrons and holes produced, noise in the silicon crystal and preamplifier, the finite energy spread of the beam, and the thickness of the scatterer. If, for simplicity, we assume that the resultant of these several contributions may be derived by taking the square root of the sum of the squares, then we may write for the observed resolution squared:

$$R^2 = \frac{1}{E^2}\left[aE + n^2 + b^2 + c^2E^{-1.36} \right].$$

The last term in the bracket is the foil thickness term. Its form comes from the assumption that the rate of energy loss of the incident particle in the detector material may be written as a power law:

$$\frac{\mathrm{d}E}{\mathrm{d}x} \approx E^{-0.68}.$$

This form is closely true for $E \gtrsim 5$ MeV where this contribution becomes important.

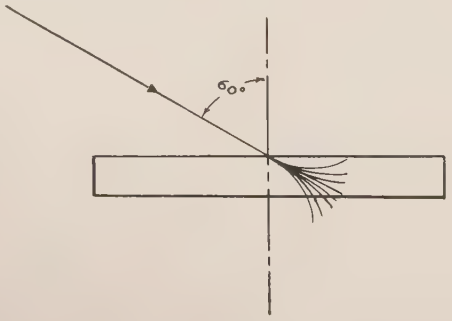

Fig. 9. Schematic representation of multiple scattering of protons in slant detector.

In fitting the expression for R^2 to our observations we simplify matters by taking $a = 0$, since we expect the statistical contribution to the spread to be quite small compared with the other contributions. Subsequent analysis yields.

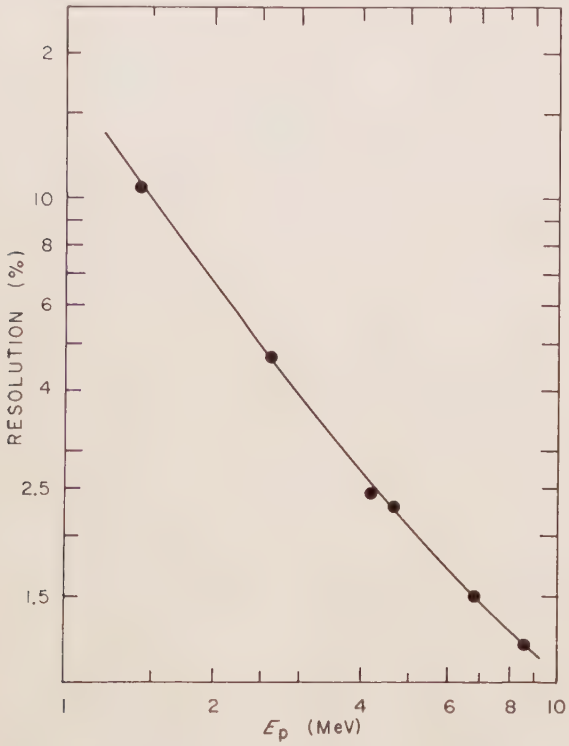

Fig. 10. Observed resolution versus incident particle energy.

$$n^2 + b^2 = 0.917 \times 10^{-2}$$

and

$$c^2 = 2.62 \times 10^{-2}$$

when energy is expressed in MeV. These numbers are in reasonable agreement with what we expect from independent considerations. Our observations on noise showed that preamplifier noise amounted to about 20 keV while silicon-crystal noise was roughly 40 keV. Thus we find for the energy spread of the beam entering our scattering chamber,

$$b = 83 \text{ keV} .$$

5. Conclusion

We have measured a depletion layer thickness equal to the range of a 9.5-MeV proton. Since this depletion layer is essentially as thick as the silicon wafer, it is not clear that we have gauged the full potential of the 10 000 ohm-cm material. The slanting technique increases the effective depletion layer thickness as expected. However, multiple scattering of the most energetic incident particles distorts the pulse-height distribution so that the full effective depletion layer thickness is not useful.

The energy dependence of the observed resolution has been explained in terms of crystal noise, beam width, and scatterer thickness. The contribution of crystal noise to the observed resolution amounts to 0.5% at 9 MeV.

NUCLEAR INSTRUMENTS AND METHODS 12 (1961) 75–102; NORTH-HOLLAND PUBLISHING CO.

MTR PHASED CHOPPER VELOCITY SELECTOR†

R. M. BRUGGER and J. E. EVANS

Phillips Petroleum Company, Atomic Energy Division, Idaho Falls, Idaho

Received 17 February 1961

The Materials Testing Reactor (MTR) velocity selector consists of a pair of Fermi-type phased choppers and a pair of rotating collimators. The four rotors are driven at identical speeds up to 5225 rpm by four hysteresis synchronous motors. With the appropriate angular phase difference established between the choppers and the collimators, bursts of monoenergetic neutrons are selected from the MTR's Maxwellian flux. Phase instability broadens the initial neutron burst by only 12 %, as demonstrated by actual measurements of time distributions. The monochromatic neutrons produced by the selector are used in measuring inelastic scattering cross sections by means of time-of-flight equipment. Intensities per time channel are sufficient to give reasonable statistics in a 24 hour run. Wavelength resolutions between 2 % and 8 % are realized. The paper describes the layout and characteristics of the velocity selector in detail, and discusses problems associated with backgrounds and time and intensity calibrations. Inelastic scattering data taken on samples of methane gas and on a beryllium single crystal are displayed and analyzed to show the counting rates and background levels achieved with the selector, and to demonstrate the versatility possessed by this type of monochromator.

1. Introduction

The phased chopper velocity selector described in this paper has been built at the Materials Testing Reactor and put into operation measuring the molecular and solid state properties of matter by observing inelastically scattered slow neutrons. Its mechanical properties and operating characteristics are described in sufficient detail to allow other experimenters in the field to evaluate the advantages and disadvantages of such a phased chopper velocity selector and to construct a similar machine if they so desire. Examples of data are shown to help in these evaluations.

The inelastic scattering of thermal neutrons has been shown to be a powerful tool in studying the forces between molecules or other groups of atoms[1,2]). The results of these experiments allow physical properties of the gaseous, liquid, and solid states to be investigated. For each of these states the experimental requirements are similar, but the physical properties are markedly different and the interpretations include many phases of solid state physics and molecular physics.

Despite the valuable information to be gained, inelastic scattering measurements have been attempted only in the last few years because of the high intensities and low backgrounds required. The measurements are the equivalent of triple scattering measurements (for example, the triple axis spectrometer method[3])), and it is only with the most intense sources of thermal neutrons now available that sufficient counting rates can be obtained. While different experimental arrangements are being used[4]), the basic requirements are identical; an intense source of monoenergetic neutrons in the thermal range, and a method of determining the energy and the angle of scattering of the neutrons after scattering.

The primary objective of the inelastic scattering measurements being made at the MTR is to obtain the differential scattering cross section, both as a function of scattering angle and neutron energy after scattering, for samples of reactor moderator

† Work done under the auspices of the U.S. Atomic Energy Commission.

[1]) Proceedings of the International Atomic Energy Agency Symposium on the "Inelastic Scattering of Neutrons in Solids and Liquids", Vienna, Austria October 11–14, 1960, to be published.

[2]) L. S. Kothari and K. S. Singwi, "Interaction of Thermal Neutrons With Solids", Solid State Physics **8** (Academic Press, 1959) pp. 110–192.

[3]) B. N. Brockhouse, "Methods of Neutron Spectrometery", See ref.[1]).

[4]) Session II, "Methods of Neutron Spectrometery", See ref.[1]).

and reflector materials. These measurements will be extended over ranges of initial neutron energies and sample temperatures. From these measurements, reactor physicists should be able to develop a better understanding of neutron transport and energy

Fig. 1, a cutaway drawing of the MTR neutron velocity selector, is helpful in visualizing the basic principles of operation of the equipment. A beam of neutrons from the reactor is chopped by chopper A into bursts of polyenergetic neutrons. As these

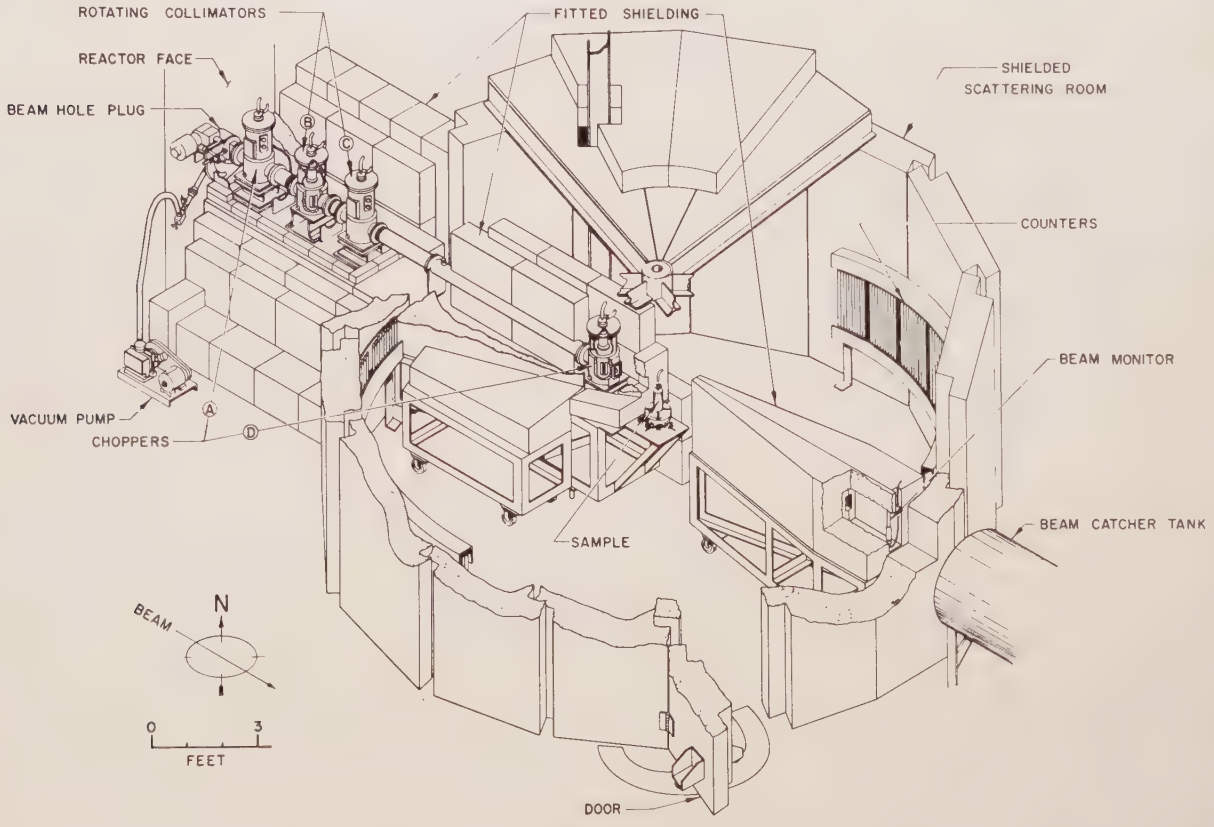

Fig. 1. A cutaway drawing of the MTR velocity selector. The distances between the centers of the rotors are: A to B = 0.498 m, A to C = 1.029 m, A to D = 3.437 m. The distance from D to the sample is 0.500 m and the distance from the sample to the center wires of the detectors is 2.00 m.

exchange near thermal energies. The data will also be available for actual calculations of reactor fluxes. Of the different types of experimental arrangements that are being used to measure inelastic scattering, a modification of the phased rotor super chopper[5]) seems best suited for measuring the desired differential cross sections with intermediate resolution, $\Delta\lambda/\lambda$ between 1 and 10%. For each initial neutron energy and sample temperature, the machine is capable of measuring simultaneously the energy and angular dependence of the scattered neutrons over a wide range of energies and azimuthal angles.

travel down the flight tube, they spread in time and distance as a result of their varying energies. Chopper D is spinning at exactly the same speed as chopper A, and its relative angular position, called

[5]) P. A. Egelstaff, "The Phase Control of Rotors at High Spinning Speeds", Proceedings of Conference on Peaceful Uses of Atomic Energy, Geneva 1956, Record of Proceedings of Session 15A, pp. 119–220. For later developments see R. D. Lowde, "The Principles of Mechanical Neutron-Velocity Selection", J. Nuc. Energy **11** (1960) 69–80);

Egelstaff, Hay, Holt, Raffle and Pickles, "The Phase Control of Rotors at High Spinning Speeds", Journal of the Institution of Electrical Engineers (13–1–1961); and P. A. Egelstaff and S. J. Cocking, "A Four-Rotor Thermal Neutron Analyzer", See ref.[1]).

the rotor phase†, lags behind that of A by a predetermined angle. Thus, chopper D passes only neutrons of one narrow energy group, that is, neutrons arriving at chopper D when it is "open". The first requirement for making inelastic scattering measurements, a source of monoenergetic neutrons, is thus attained.

Since the monoenergetic neutrons produced by the velocity selector are already in bursts, they are ideally suited to time-of-flight measurements. Thus, the second condition, that of determining the energy of the neutrons after scattering, is possible. The neutrons of essentially one energy strike the sample placed after chopper D, and some gain and some lose energy during the scattering process. The time of flight of those neutrons scattered into groups of detectors placed in a horizontal plane at up to 15 angular positions around the sample are recorded by a multichannel time sorter. This equipment in conjunction with the MTR fulfills the needs for successfully performing inelastic scattering measurements. The small detector in the beam is a beam monitor used to determine the flux when absolute cross sections are measured and to determine the time distribution when monitoring the rotor phase stability. The intermediate rotors are rotating collimators which are needed to suppress fast neutron background.

In selecting the different parameters for the velocity selector, many factors were considered. Since intensity is one of the primary limiting factors, the beam was made as large as possible with the existing beam hole available. Floor space and intensity set an upper limit on the flight paths to be used, and resolution indicated a lower limit. The design of the choppers was dictated by the strength of the materials used and the rotational speeds that could be obtained. Once the rotational speed had been selected, the chopper foil spacing, which determines the burst width, was selected so that the loss of resolution $\Delta\lambda/\lambda$ due to burst width is in the 1 to 10% range. The number of scattering angles and the number of time channels per angle were selected so that the uncertainties they contribute are of the same magnitude as the errors introduced by the previously selected parameters. Since the problem of intensity vs. background and the problem of the phasing of several choppers were predicted to be major hurdles, one overriding consideration was that no single component should be an extensive development job in itself, and that commercial components or previously proved components should be used wherever possible.

To describe the MTR velocity selector, this paper is divided into three major sections. The first discusses the mechanical and electrical components, i.e. beam hole collimation plug, choppers, motors, shielding, etc. The second section discusses the operating characteristics of the velocity selector, i.e. rotor phasing, counting rates, backgrounds, etc. The final section discusses representative results that illustrate the advantages and disadvantages of a velocity selector of this type.

2. Experimental Equipment

2.1. NEUTRON BEAM FACILITY

The MTR beam hole available for the program of inelastic scattering of slow neutrons is HG-6 [6]). This 6-in. diameter hole penetrates the external shield and the graphite region of the reactor and leads up to the 5-ft-diameter reactor tank. Between the end of this hole and a corner of the slab-shaped fuel core there is at least a 14-in. thickness of reflector beryllium, and 1 in. of aluminum in the reactor tank wall. Indium foil flux measurements at the outer wall of the reactor shielding, with the 2 by 4 in. collimation plug described in the next paragraph in place, gave a sub-Cd flux of 1.4×10^8 neutrons/cm^{2}sec at a reactor power of 40-megawatts. Under the assumption of isotropic flux this corresponds to a sub-Cd source flux of 0.8×10^{13} neutrons·cm^{2}sec at the reactor tank wall. The Cd-ratio for a $1/v$ detector was 170.

A beam hole collimation plug was built to control the neutron and gamma beams from this hole. A longitudinal section of the 199-in.-long collimation

† In describing a phased chopper velocity selector, the word "phase" is used in several senses. Therefore, in this paper the term "rotor phase" designates the instantaneous angular position of one rotor with respect to a second, while the term "electrical phase" refers to the phase relation between the several sources of the sinusoidal power supplied to the motors. The word phase is also used with respect to the oscillator (3-phase) and to the motors (4-pole, 2-phase) in the usual sense.

[6]) J. R. Huffman, Nucleonics **12**, no. 4 (1954) 20.

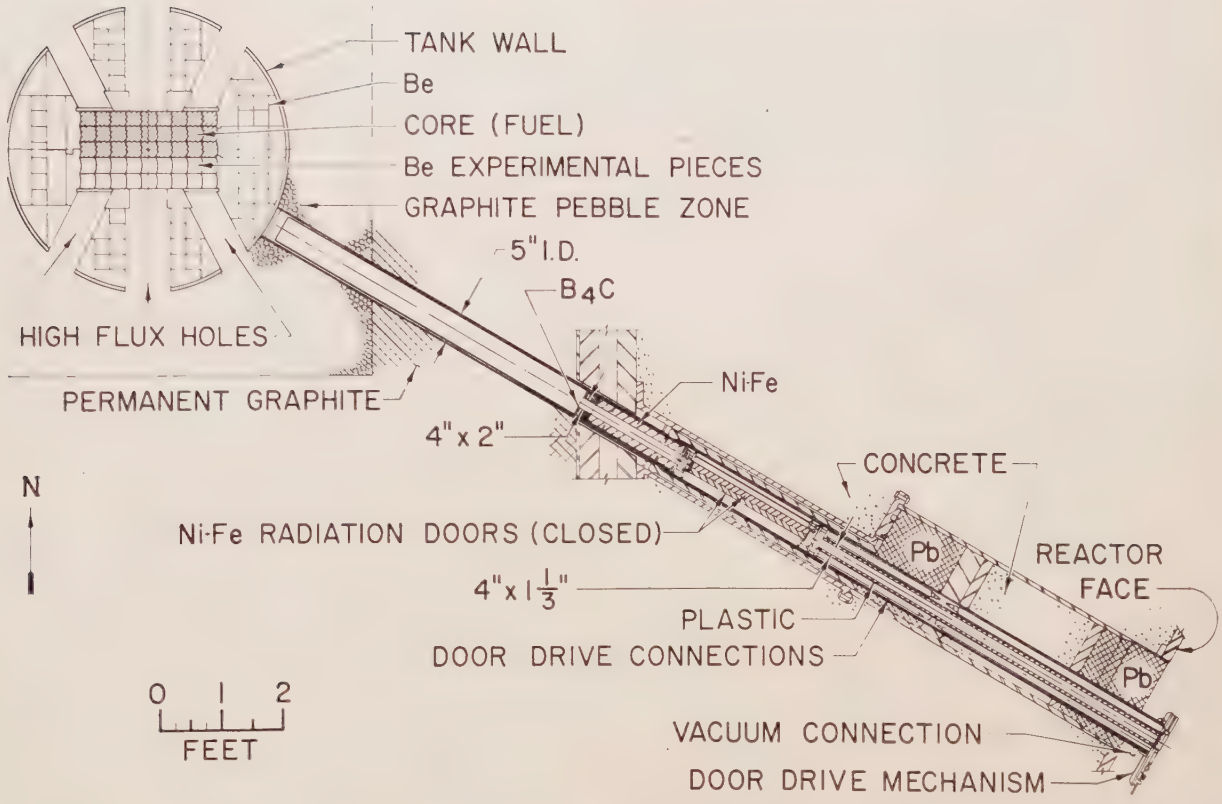

Fig. 2. The HG-6 beam hole, the collimation plug and the core of the MTR.

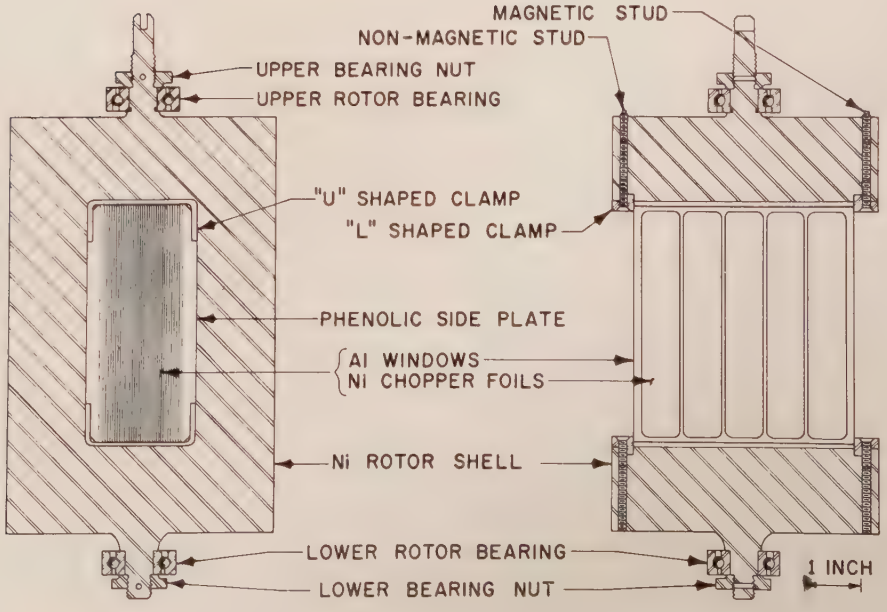

Fig. 3. Sections at 90° of a velocity selector chopper.

plug is shown in fig. 2. The tip section is a 5-in.-i.d. Al tube. The beam is first collimated by 3 in. of B_4C to a 2-in.-wide by 4-in.-high area 67.75 in. from the tip, which limits neutron activation of the rest of the plug, and 20 in. of 50–50 nickel-iron. Next come the radiation doors which consist of two 23.5-in. pieces of nickel-iron which can be moved symmetrically by a rack and pinion and mechanical linkage system to a fully opened width of 2 in. These radiation doors are operated remotely by a motor drive system. Nickel-iron was selected as a collimating material because of the relatively high gamma and neutron attentuation factors of both materials and because the extremely low neutron cross section regions in one material are covered by the high cross section regions in the other material. The butt end of the plug which is 81.75 in. long is filled with concrete except for the 2 × 4-in. beam channel. Plastic inserts in the butt end of the plug further limit the beam to a width of 1.33 in. to correspond to the openings in the choppers now being used.

The plug is evacuated to eliminate a 25% neutron loss due to air scattering and to prevent corrosion of the plug due to oxides of nitrogen formed by the gamma-ray fields if air is present. With the reactor at 40 MW the gamma-ray intensity in the beam is greater than 25 r/h when the radiation door is open and 10 to 30 mr/h when the door is closed. With the door closed the neutron beam is well below recommended personnel exposure limits.

2.2. ROTORS

The high resolution mechanical shutters of the MTR velocity selector are two Fermi-type slow choppers[7]), each consisting of alternating nickel and aluminum laminae in a rotor shell. For these to be effective choppers, each must pass a high percentage of the desired energy neutrons when the chopper is open and must scatter or absorb almost all neutrons of all energies when the chopper is closed. The choppers must also open and close in a small enough time interval so that the time uncertainty, and thus the velocity or wavelength uncertainty, is relatively small.

In this paper a distinction is made between: 1. rotor shells which have no inserts, 2. rotating collimators which are rotor shells with simple inserts used to control fast background, and 3. choppers which are rotor shells with nickel plus aluminum insert assemblies. The last are the ones that chop the thermal neutron beam into bursts so that time-of-flight measurements can be made. The word rotor is used when it is not necessary to distinguish between these three.

The standard rotor shells have the physical shape shown in fig. 3. They are 4.75 in. in diameter and 7.37 in. high with shafts at each end for the bearings. A hole 2 in. wide by 4.37 in. high is cut perpendicular to the axis through the center of the shells for passage of the beam. These shells, which weigh 28 lbs, are constructed of Duranickel R (94% Ni, 0.25% Fe, 0.25% Mn, 0.05% Cu, 0.16% C, 0.40% Si, 0.005% S, 4.3% Al) because this material has high strength properties.

The construction of these rotor shells is a precision machining job. After ultrasonic inspection of the Duranickel bars and the rejection of any areas with flaws, the shells are rough-machined, and then heat-treated for added strength. The heat treatment increases the hardness to greater than Rockwell 30C. The tolerances maintained in the final machining are 0.0002 in. All surfaces are polished to a 32-μin. finish and inside corners are left with a radius of curvature of 0.125 in. to avoid cracks starting at these points. To produce a rotor timing pulse in a magnetic pickup, 0.125-in.-diameter studs of magnetic material are mounted in the top of the rotor shell, near the periphery and centered over the ends of the beam pass hole. If only one timing pulse per revolution is needed, a non-magnetic stud having the same weight replaces the magnetic stud in one hole to preserve rotor balance. The shafts at each end of the rotor shells are 0.5 in. in diameter with threaded ends for a nut to hold the inner bearing race. A hole is provided for a nylon safety pin to secure the nut. At the top and bottom of each side of the beam pass hole in the rotor shells, 0.25 by 0.25 in. grooves are cut on chords 2 in. from the axis of the rotor shell. "L" shaped blocks or clamps, fitted into these grooves and held with two bolts each, are used to hold any inserts placed in the rotor shell. These "L" shaped clamps are precision machined from heat hardened steel.

[7]) Fermi, Marshall and Marshall, Phys. Rev. 72 (1947) 193.

To convert a rotor shell to a thermal neutron chopper, a sandwich of aluminum and nickel laminae is inserted into the shell with the plane of the sheets parallel to the beam pass hole. The nickel sheets, 0.010 in. thick by 4.25 in. high by 4 in. wide with 0.0005-in. cadmium plating on each side, are the chopping sides of the rotating slits. To keep these nickel sheets in their proper location, 0.032-in. aluminum grids, which act as windows for the neutrons, are inserted between the nickel sheets. To make these windows more effective, five holes 4.125 in. high by 0.700 in. wide are cut in each aluminum spacer leaving a 0.125-in. rib on each edge and four 0.062-in. ribs between. These ribs are parallel to the rotor axis. Since these thin ribs have little strength perpendicular to their length to withstand the centrifugal forces, each aluminum grid is bonded to a neighboring nickel sheet by an epoxy resin compound. After testing several bonding materials, a material[8]) was found that adhered satisfactorily to the cadmium. Because the resin has a high scattering cross section, each nickel sheet plus aluminum grid subassembly is carefully scraped to remove any hydrogenous material from the sides of the aluminum ribs through which the neutrons must pass.

Thirty of these nickel sheet plus aluminum grid subassemblies are stacked into a sandwich about 1.3 in. thick with no bonding between the subassemblies. This set of foils is clamped between two 0.3-in.-thick pieces of phenolic which are held at top and bottom by "U" shaped aluminum clamps. This structure is machined to size and press fit into the rotor shells to form a chopper. The insert of foils is held from slipping by the "L" shaped clamps at the top and bottom of each beam pass hole of the rotor shell. The effective beam pass area is 4 in. high by 1.3 in. wide, and the effective chopping radius for the center slit is 2 in.

The rotating collimators, which provide additional control of the fast neutron background, are assembled from the rotor shells by adding the side pieces of phenolic without the sandwich of foils. The phenolic pieces are held by the "U" shaped clamps and are confined in the rotor by the "L" shaped clamps. The 4-in.-high by 1.3-in.-wide hole allows the transmission of the thermal neutrons that arrive at the rotating collimators at the desired time.

A high strength alloy, Duranickel R, was selected for the rotor shells because it has a relatively high macroscopic neutron cross section in the energy region of the reactor spectrum that makes the main contribution to the fast neutron background. Since nickel does not become highly radioactive from thermal neutron capture, the first chopper of the velocity selector has a surface radiation level of only 20 mr/h after over two years of use.

The cross section of nickel has several S wave resonances in the keV region near which the cross section is markedly low. These act as energy sensitive windows transmitting more neutrons of those energies. It would be desirable to have 25–50% of iron in the rotor shell material so that the iron cross section will blind these windows. However, no high strength iron-nickel alloys were available at the time construction was started. To compensate partially for the low cross section at these nickel-windows, phenolic (specific gravity 1.35, with the following composition in weight percent: C 63.95%, H 6.59%, O 27.02%, N 1.27%) is used as the foil clamps. It was selected after crude transmission measurements, which were sensitive to the fast neutron background, showed phenolic to be more effective than equal thicknesses of iron, aluminum, nickel, or lead and as effective as beryllium.

The thickness of the nickel plates of the choppers is a compromise between true intensity and background intensity. The thicker the nickel, the smaller the area of the aluminum windows and hence the smaller the thermal neutron transmission when the choppers are open. The thinner the nickel plates the less scattering material is in the beam when the choppers are closed, and the higher the backgrounds. Most thermal neutron chopper designers set the scattering foil thickness equal to or less than the window width[9]). The 0.010-in.-thick nickel sheets and 0.032-in. aluminum windows were selected to give a neutron transmission efficiency of

[8]) Bond Master Adhesive, Rubber and Asbestos Corporation, Bloomfield, New Jersey.

[9]) L. F. Curtiss, "Introduction to Neutron Physics" (Van Nostrand, Princeton, New Jersey 1959) pp. 197-208;
D. J. Hughes, "Pile Neutron Research" (Addison-Wesley, Cambridge, Mass. 1953) pp. 243–249.

up to 75% while still introducing an appreciable amount of nickel into the beam when the choppers are closed. The strength of the nickel plates is important too. The 0.010-in. nickel plates have enough rigidity so that most of the aluminum window material can be removed without serious misalignment. The aluminum ribs have to be spaced every 0.700 in. to limit the bending of the outer nickel plate to 0.002 in. due to centrifugal forces at 6000 rpm. The thickness of the aluminum spacers was selected to give burst half-widths of about 30 μsec measured at the detectors when the choppers are spinning at 6000 rpm.

At first it was specified that each rotor must be dynamically and statically balanced to 0.0002 in.-oz, in order to prevent wear of bearings and to help in phase stability. Since neither of the first two choppers tested needed correction, later choppers have not been balanced and no troublesome effects have been noticed.

The choppers were designed to withstand all forces up to speeds of 18 000 rpm, which should allow safe operation up to 15 000 rpm. To realize the design limit, the surfaces of the rotors have a 32-μin. finish with no scratches, the nickel alloy of the rotors have a hardness of Rockwell 30C, and the density of the insert foil assembly is less than 2.3 g/cm^3 since all the force of the foil assembly is carried by the sides of the rotor shells. The most likely place for a break to occur in a rotor shell during high speed operation is from the corner of the beam pass hole to the side of the rotor.

The rotor shells were tested by spinning them at speeds up to 16000 rpm for periods of several hours. To date the choppers have been tested at speeds up to 7 000 rpm. A potential danger point in the chopper is the loosening of a nickel-aluminum bond and the tearing loose of an aluminum rib. No indication of this happening has been noticed on the two choppers that have run at 4 720 rpm for over a year.

2.3. ROTOR AND MOTOR HOUSINGS

Each rotor is mounted in a separate housing as shown in fig. 4. A hole for a rotor which allows 0.030-in. peripheral clearance for the rotor was machined in a solid piece of stainless steel 8.81 in. high by 9.19 in. in diameter. A rectangular hole 4.12 in. high by 2 in. wide was cut perpendicular to the rotor axis through the 2.19-in. walls for the passage of the beam. A bearing seat was cut at the bottom of the rotor housing to support the lower rotor bearing. Plates with O-ring seals complete the vacuum seal at the bottom of the rotor housing and allow access to the lower bearing so the nut or the outer bearing race clamp may be removed.

A motor housing made from 0.25-in. wall iron tubing is added to the top of the large rotor housing. A shoulder provides for precise alignment and an O-ring assures a vacuum seal. The upper rotor bearing sits in the motor housing with a wavy spring applying a small amount of pressure to the upper bearing. The motor housings are pinned for alignment and are bolted to the rotor housing by six bolts. The top of the motor housing is sealed by an O-ring both at the outer edge and around the motor cooling tower.

Each of the four rotors has a separate motor which is bolted to a cross member of the motor housing. The cross member has shoulders for motor alignment. A flexible coupling[10]), designed so that little strain is put on the shafts if they are not perfectly aligned, is used to connect the motor to the rotor. While these couplings are classed as non-backlash couplings, a torque of 1 in.-lb introduces a deflection between the ends of the coupling of 1 minute of arc. The top plates of the motors are machined flat, except for aligning shoulders, and cooling towers are bolted to the tops of the motors and extend through the top plates of the motor housings. These cooling towers are designed to carry about 0.3 gal/min of water down the center pipes over the top plates of the motors and back through the outer pipes.

The rotor housings are each mounted to the tables by heavy iron, adjustable legs. The three housings nearest the reactor are mounted on one table and the housing nearest the sample is mounted on another table (see fig. 1). The tables are constructed of 2-in. angle iron with a 0.5-in.-thick iron top. Cross bracing is added so these tables will be stable bases for the rotor housings and can carry several tons of shielding.

[10]) N. 12725, style CC flexible coupling, Thomas Flexible Coupling Co., Warren, Penn.

Sections of 5-in.-i.d. iron pipe connect the rotor housings and provide an evacuated path for the neutron beam. The pipe sections are joined to the rotor housings through large flanges with O-ring seals. To allow for alignment, flexible couplings and bellows are placed at strategic points along the connecting pipes. The rotor housing nearest the reactor is joined to the beam hole plug with a flange sealed by $\frac{1}{8}$-in. cork. This cork allows a seal even though the two joining faces are not parallel at this point. Appropriate valves for evacuation and bleeding air into the system are located in one section of the pipe.

For convenience, the chopper nearest the reactor is designated as A, the rotating collimators as B and C, and the final chopper as D. The distances A to B, A to C, and A to D are 0.49, 1.029, and 3.437 meters respectively. All distances are measured from the rotor axes.

The rotor housings are constructed with 2.19-in.-thick walls as a safety measure. Calculations show that these walls should be thick enough to contain the pieces of a rotor if it breaks through the axis. As an added safety feature, the space between a rotor and its housing is only 0.030 in. If the rotor yields before breaking it will rub the sides of the housing and quickly decelerate. Another advantage of this small spacing is that when a motor housing is removed and the rotor is resting in only the bottom bearing it cannot tip sideways and bend the bottom shaft. Since the heavy rotor housings are solidly fastened to the table, they are solid mounts for the rotors and allow only a minimum amount of vibration.

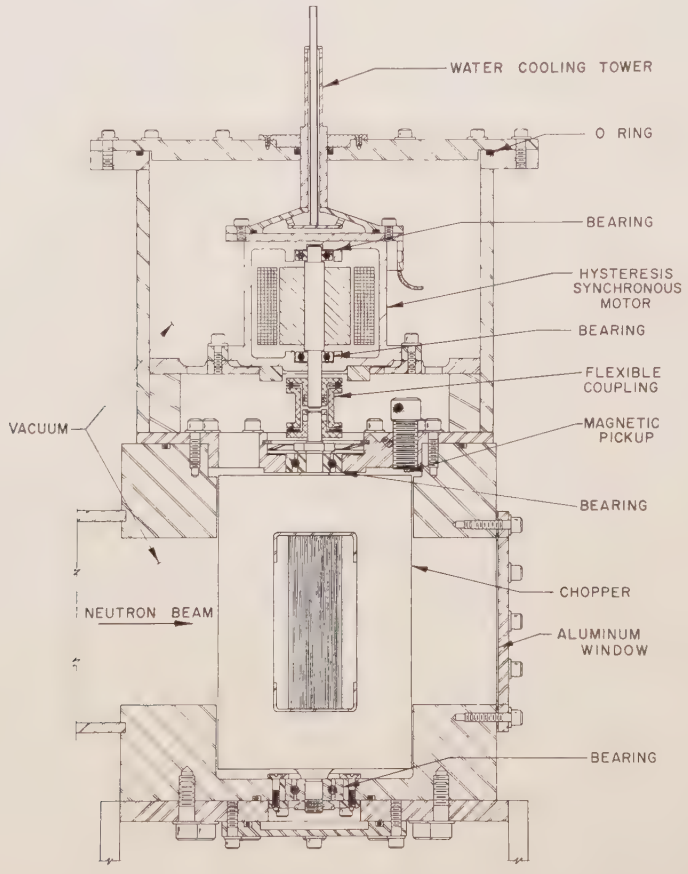

Fig. 4. Chopper D motor, motor housing and rotor housing. The beam passes into the air through the aluminum window on the right hand side.

The motors and rotors are carefully aligned about a common vertical axis. All pieces that contribute to this alignment are carefully machined to 0.0005-in. tolerance and reference shoulders and the bearing seats are cut to the same precision. Even with these precautions it was felt that special flexible couplings are needed so that lateral pressure would not be exerted on either of the two rotor bearings or on the two motor bearings. The careful alignment is needed to remove as much of the drag due to the flexing of the flexible coupling as possible.

The evacuated volume extends from the tip of the beam hole plug to the out board side of the rotor housing nearest the sample. This insures that no neutrons in the beam are lost by air scattering until they have passed through the velocity selector. Since air scattering of thermal neutrons is about 5% per meter and the evacuated beam path is 8.6 meters long, a sizeable savings of neutrons is realized. Air drag on the spinning rotors is eliminated also. For the rotating collimators, which have the large open holes in the center, air drag can be appreciable at atmospheric pressure.

Since the rotors spin in a vacuum, the motors are also placed in the vacuum chamber. This eliminates the need for dynamic O-ring seals or oil seals, both of which can give exasperating troubles and introduce drag. All leads are electrically insulated since the motors are brushless. The bottoms of the motors sit on heavy frames and dissipate heat by conduction while the tops of the motors are cooled by the 0.3 gal/min water flow.

Two types of bearings for the rotors have been used in the MTR velocity selector. The medium precision[11]) thrust bearings with 5-mm diameter balls and 1.687-in. outer race are sealed with the lubricant packed by the manufacturer. The velocity selector has been operated at 2100 rpm and 5000 rpm for several months with these bearings without observing troublesome effects. The second type of bearing, the high precision bearings[12]) which have the same dimensions as the others, are not sealed. Before being used they are carefully cleaned with acetone and alcohol and then packed with high temperature grease[13]). These thrust bearings have also been used at 5000 rpm for periods of months with good results.

Both types of bearings are stiff when first put into operation. This causes a noticeable drag on the rotors until the bearings have been run in for several days. Since they operate in a vacuum, the grease tends to be pushed out of the bearings during evacuation, but the amount of grease left provides adequate lubrication .No rotor bearings have gotten noticeably hot nor has the grease hardened in the vacuum. The bearings have lasted from one month to many months before being replaced. They are replaced if they feel, sound rough, or if the phase jitter (see § 3.2) of a particular rotor is greater than usual. The velocity selector has run at 5000 rpm for periods of 4–5 months without replacing bearings. Because of the superior rating by the manufacturer, the high precision bearings are being used at the present time.

Since the motors are under-powered for driving the 35-lb choppers, it is necessary to eliminate as much of the drag as possible. The initial running-in period of the bearings is a help in lessening the bearing drag. The operation of the rotors in a vacuum eliminates the air drag while the special type flexible coupling allows little drag from lateral forces because of small misalignments of the motors and rotors. Care is taken that the springs holding the upper rotor bearings are just snug and do not exert much downward force on the rotors. The flexible coupling must not be depressed or a downward force is exerted on the rotor by the motor. Lately the outer races of the bottom rotor bearings have not been clamped, thus allowing the bearings to seek their own horizontal alignment.

2.4. SHIELDING

Even with the highest flux reactors and elaborate experimental equipment, the counting rates of inelastic scattering experiments are low. To make the effects of inelastic scattering appear above the background that is always present, the quantity and quality of shielding is important. Fig. 1 shows most of the shielding that is around the MTR velocity selector.

[11]) SKF 6301–ZZ-5 bearing, SKF Industries Inc., Philadelphia, Penn.

[12]) 3MM301WI bearing, Fafnir Bearing Company, New Britain, Conn.

[13]) Density M6 Lubriko grease, Master Lubricants Co., Philadelphia, Penn.

A scattering room is centered about the sample position with a minimum radius of 92 in. The walls of this room are formed from steel cans 6.5 ft. high by 4 ft. wide by one ft. thick. These cans have stepped edges which overlap. The cans have 0.25-in.-thick steel walls and are filled with a 30–70 weight percent mixture of boric acid and paraffin. The ceiling consists of two layers of similar cans 6 in. thick. A door at one side of the room allows easy access. This shielding presents 12 in. of paraffin plus boric acid to all neutrons trying to enter from the top and sides. The shielding room is completed by the 3 ft. thick concrete reactor buildings floor.

To contain the neutrons scattered by the different rotors of the velocity selector, smaller metal cans filled with the boric acid and paraffin mixture are fitted around the velocity selector from the reactor wall out to the sample position. Another shield confines the beam after the sample to prevent most air scattered neutrons from reaching the counters. All surfaces of the scattering room shielding and the faces of the velocity selector shielding that are visible to the detectors are covered with 0.020 in. of cadmium. In a few places that are difficult to shield, asbestos bags filled with pellets of paraffin and boric acid are used. Shielding of different shapes and materials (mainly plastic and paraffin) are put inside the 5-in. diameter pipes connecting the rotor housings to help collimate the beam. For certain experiments 0.020-in. cadmium is used to guide the beam from the shielding near the last rotor to the sample and from the sample to the next piece of shielding. This cadmium further reduces the number of air scattered thermal neutrons that reach the detectors.

The BF_3 neutron detectors are surrounded by a 0.5-in.-thick layer of powdered B_4C in flat aluminum cans except for an adjustable opening facing the scattering sample. Since the BF_3 proportional counters that are used with the MTR velocity selector are not sensitive to gammas, only enough gamma shielding is used so that the area near the velocity selector is safe for personnel. Most of this gamma background is due to scattering of the reactor gamma beam by the first rotor or from the (n,γ) reactions in the first rotor. A 2-in. lead shield is placed around the first and second rotors. The gamma intensity at the sample position when the reactor is at 40 MW, the beam doors are open, and the rotors are spinning at 4720 rpm is about 1 r/h while the field near the last rotor outside the beam is about 2 mr/h. The beam is absorbed in the catcher tank placed outside the scattering room.

There are several sources of neutron background that affect the inelastic scattering experiment. Since thermal neutrons are easily controlled by a 0.020-in. layer of cadmium, the sources of epicadmium or fast neutrons give the major difficulty. Several experiments near the velocity selector bring beams from the core of the reactor through the reactor shielding wall, and these introduce a background of high energy neutrons into the velocity selector experiments. Whenever possible, these sources are shielded at the source with paraffin filled boxes or magnetite brick. However, a flux of fast neutrons still persists. The scattering room with 1-ft thick walls was built to suppress this background in the detectors.

The other major source of neutron background is the beam used with the velocity selector. The thermal neutrons are easily absorbed or scattered by the first chopper. The fast neutrons in this beam scatter from the rotors; most from the first chopper but some from each of the other rotors. The fitted shielding is placed around the velocity selector to thermalize and absorb these neutrons.

Paraffin plus boric acid is used as the principle shielding because of its high content of hydrogen which moderates the fast neutrons and because of its high boron content which absorbs the thermalized neutrons. The paraffin mixture is contained in metal cans for ease of handling and to limit the fire hazard. The B_4C shielding is placed near the counters so that a large amount of absorber of the same type as is in the detectors is present to capture fast neutrons.

2.5. NEUTRON DETECTORS

The individual neutron counters used with the MTR neutron velocity selector are commercial BF_3 proportional counters[14]). The aluminum cathodes of these counters are 1-in. o.d. with 0.031-in.-thick

[14]) Reuter-Stokes Company, Cleveland, Ohio.

walls. The anodes are polished 0.006-in. tungsten (wolfram) wires with active lengths of 18 or 20 in. The counters are filled to 167 cm pressure with 96% enriched $B^{10}F_3$ gas. Their average efficiency is about 40% for 0.025-eV neutrons traveling perpendicular to the axis.

The counters are mounted in the B_4C shielded counter rack with their center wires vertical and at two meters from the sample position. The two counter racks, each covering 90° of scattering angles, are constructed so that counters can be moved to most angles in the horizontal plane around the sample. Provision is made for a second layer of counters 1.98 meters from the sample if additional counters are needed for future experiments. One rack is placed on one side of the beam to cover a forward quadrant and the second rack is placed on the other side of the beam to cover a backward quadrant. The two counter racks cover scattering angles from 10° to 164° with a few degrees overlap at 90°.

Several counters, usually ten, are connected in parallel to form a single angle detector. The shells are at ground potential and the center wires are at + 7000 volts, supplied by a 10000-volt power supply[15]). The signals from each set of detectors are fed to a separate preamplifier and amplifier, then to one angle input of the 4096-channel time sorter. The amplifier is biased to accept all pulses initiated by neutrons and to exclude all pulses initiated by gamma rays. The amplifier gain and bias is checked at least once a week to detect any drift or malfunction.

The beam monitor is a 4-in. active length BF_3 counter similar to the previously mentioned ones. It is mounted vertically in the beam with cadmium shielding all but a 0.125-in. diameter hole in the front. It is placed in the beam 2 meters from the sample. The signals from this beam monitor are fed to one section of the time analyzer so that both flux and velocity selector resolution, including phase stability, can be recorded.

Boron trifluoride counters were selected because they were commercially available, and they have a relatively high efficiency of a known character for thermal neutrons, good stability, and good gamma discrimination. The good gamma discrimination allows the problem of gamma shielding to be ignored except for the personnel hazard. The effects these counters have on resolution and backgrounds will be discussed in later sections.

2.6. 4096-CHANNEL TIME ANALYZER

The 4096-channel time analyzer is a transistorized magnetic core storage time sorter constructed by the Instrument Development Group at the MTR specifically for the inelastic scattering experiment[16]). The analyzer can be operated as a single 4096-channel analyzer, two 2048-channel analyzers, four 1024-channel analyzers, eight 512-channel analyzers or as sixteen 256-channel analyzers. The channel widths may be set at 2.5, 5, 10, 20, 40, 80 or 160 μsec. Initial delays, the time between the triggering pulse and the activation of the first time channel, can be varied in steps of 40 μsec from 2.2 μsec to 64000 μsec. If the analyzer is operated as four 1024-channel analyzers for example, each must have the same initial delay and channel width. The analyzer can be operated manually or controlled by preset time or preset monitor count. The total number of counts per channel that can be stored is 2^{16} and the dead-time is 2.5 μsec.

The counting rate vs. time channel data from the cores are presented in three ways: 1. on an oscilloscope display, 2. on a strip chart record, and 3. on punched IBM cards. The first two are used for visual inspection while the latter is used for accurate processing of the data. A data run may be momentarily stopped at any time for visual inspection of the data with the oscilloscope. On each card, eight data words plus the initial delay, channel width and mode of operation are punched. Thus the data are in convenient form for IBM machine computation.

2.7. MOTORS AND ELECTRICAL DRIVING NETWORK

The MTR velocity selector has four rotors each driven by a separate hysteresis synchronous 2-phase 4-pole motor[17]). These motors are rated at

[15]) Model 410A power supply, John Fluke Company, Portland, Oregon.

[16]) Frank Petree, "Proceedings of the 1959 Biennial National Nuclear Instrumentation Symposium", Idaho Falls, Idaho, pp. 81–84.

[17]) Ford Instrument Co., Long Island City, New York.

1800 rpm and $\frac{1}{35}$ horse power when driven two phase from a 60-cps 110-volt supply. Each motor has its own bearings of the standard sealed lubricant type.

These motors, which were originally purchased to test whether hysteresis synchronous motors would hold phase position accurately relative to the applied electrical field, have proved so successful, even though underpowered, that they are being used as the driving system of the MTR velocity selector. The velocity selector has been run at speeds between 1500 rpm and 5225 rpm with these motors with good phase stability. When power at 240 volts and 174 cps is applied the motors accelerate the 35-lb choppers from the stopped position to a full speed of 5225 rpm in about three minutes. Some trouble was encountered at the highest voltages with electrical breakdown of the insulation in the motors. The pressure around the motors is 50 μ.

Fig. 5 shows the electronic driving network for the velocity selector. A precision three-phase variable frequency oscillator[18]) is set to the desired operating frequency. One phase is fed directly to a 200-watt power amplifier[19]) and then to a motor. The three phases are mixed by a control transformer[20]) so that the single phase output can be adjusted to any electrical phase position with respect to the single bypassed phase. This adjustable phase is amplified by another 200-watt power amplifier before going to the other winding of the motor. The control transformer is adjusted so that the electrical phase is about 90° at the desired frequency. The oscillator is an audio range Miller RF circuit with automatic gain controls. It delivers three-phase sinusoidal output between 10 and 1000 cycles/sec and 0 to 10 volts RMS. The amplifiers are class B push-pull negative feed back high fidelity audio amplifiers with a maximum output of 200 watts.

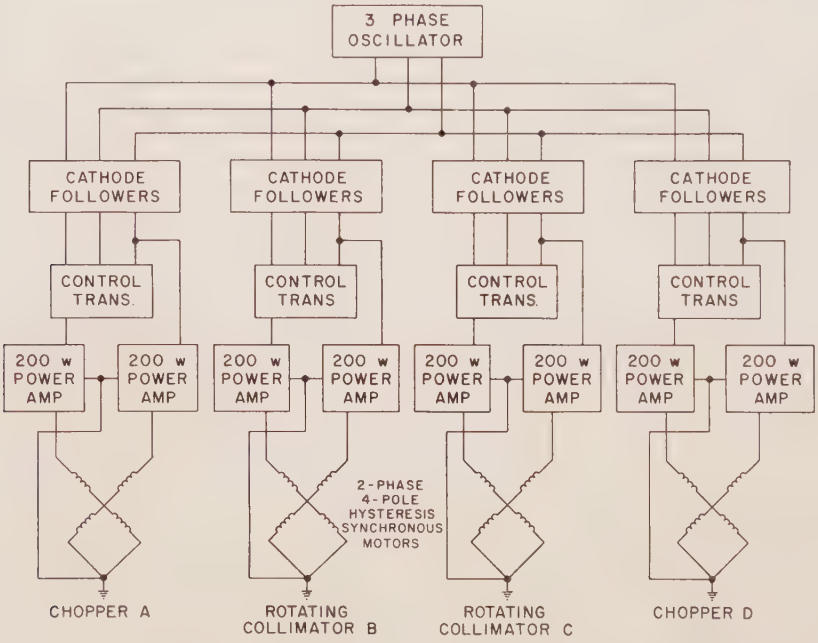

Fig. 5. Electronic driving network for the four motors of the MTR velocity selector.

2.8. AUXILIARY ELECTRONIC EQUIPMENT

A high gain magnetic pickup[21]) is used with each rotor to deliver a timing signal. The height of this

[18]) Model No. 603 oscillator, Genisco Inc., Los Angeles, California.

[19]) Model M1 200 AB amplifier, McIntosh Co., Binghamton, New York.

[20]) Type 18CT 6a control transformer, Norden-Ketay Corp., New York, New York.

[21]) Model 3030 transducer, Electro Products Lab, Inc., Chicago, Illinois.

pickup above the magnetic stud of each rotor (about 0.125 in.) is adjusted to give a pulse that rises to + 15 volts in 100 μsec, drops to — 15 volts almost linearly in 100 μsec and then returns to zero in 100 μsec. The point in time where this linear portion crosses zero voltage (the crossover) is the zero for the timing signals. If the gap is too small, an inflection step is observed near the crossover. If the gap is large, a small pulse with no inflection step is observed.

This signal is fed to a pulse shaping circuit that delivers a pulse 20 volts high, 1 μsec wide with a 0.1-μsec rise that is used to trigger the time analyzer and to set the phase position of each rotor. This 1-μsec-wide signal appears a few μsec before the crossover of the magnetic pickup signal. This time difference is included in the time calibration discussed in § 3.3. This system has been reliable and stable.

Several safety circuits are incorporated into the velocity selector. If the temperature of the motors, as measured by a thermocouple in the top plate of each motor, rises above 100°F the power to the motors is removed and the data input to the time analyzer is stopped. This protects against loss of water flow and hot motor bearings. If the speed changes by more than $\pm$ 10% because of a bad bearing or rotor unbalance both the motor and data input to the time analyzer are stopped.

2.9. SAMPLE CHANGER

A simple two-position sample changer is used to cycle a sample and a blank into the beam. Samples vary with the material to be studied but generally are less than 0.125 in. thick (except for gases) and cover the full 4 × 1.3-in. beam. A desirable thickness is such that about 10–15% of the neutrons are scattered. This allows a sufficient counting rate but limits multiple scattering in the sample. The sample holder and other supports are carefully covered with cadmium to limit scattering by these. The usual mode of operation is to take scattering data for 10 minutes with the sample in the beam, then to measure the background for 10 minutes with the blank in the beam, repeating this cycle many times. The data from the detectors are stored in different halves of the time analyzer for sample and blank. By cycling in short intervals long period drifts in the electronic circuits and the changes in reactor flux are averaged.

3. Operation

3.1. VELOCITY SELECTING ACTION

Tolk and Brugger[22]) have calculated the burst shapes or time distributions to be expected from two phased choppers spaced a given distance apart. These calculations are good representations of the action of the MTR velocity selector and are more convenient to use to demonstrate the velocity selecting action than experimentally obtained bursts. The neutron burst in time immediately after the first chopper has a full width at the base about equal to the slit width times the period of the chopper divided by 2π times the chopping radius. The intensity distribution in this burst is almost a triangle in time and contains neutrons with a wide range of velocities. Immediately before the second chopper these neutrons have spread out in time to assume a shape similar to a Maxwellian, however, this Maxwellian is suppressed in certain regions due to the coarse velocity selecting action of a single chopper. In these calculations the $1/E$ tail of the reactor spectrum is not considered.

After the second chopper a triangular burst is again produced, but this burst contains neutrons of only a small velocity range which depends upon the rotor phase of the two choppers and the distance between them. At some distance from the last chopper, i.e. at the beam monitor, the burst has broadened in time due to the difference in velocities of the neutrons in the burst; but, the neutrons are still in bursts with a relatively narrow half-width in time. When the neutrons in these bursts are scattered by a sample it is possible to observe at the detectors whether neutrons have been removed from the burst to another position in time. Thus the neutron energy change caused by scattering in the sample can be measured.

A single chopper acts like a coarse velocity selector because of the finite time required for the neutrons to pass through the chopper. The path of the neutrons through the chopper in the chopper

[22]) N. H. Tolk and R. M. Brugger, Nucl. Instr. and Meth. 8 (1960) 203.

reference frame is an Archimedes spiral but it has been shown that the arc of a circle is a close approximation for the choppers considered in this paper[22]). To maximize the transmission of neutrons

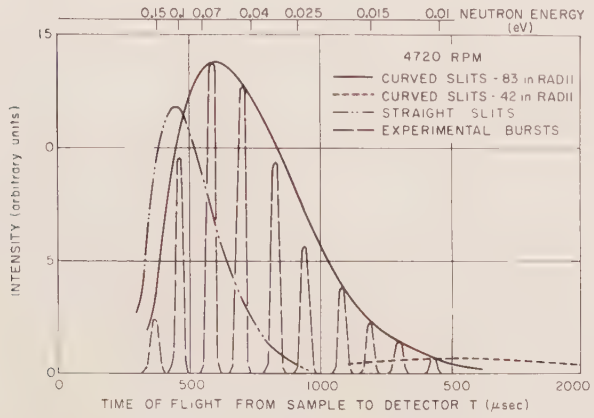
0.15 0.1 0.07 0.04 0.025 0.015 0.01 NEUTRON ENERGY (eV)
4720 RPM
CURVED SLITS - 83 in RADII
CURVED SLITS - 42 in RADII
STRAIGHT SLITS
EXPERIMENTAL BURSTS
INTENSITY (arbitrary units)
TIME OF FLIGHT FROM SAMPLE TO DETECTOR T (μsec)

Fig. 6. The envelope of the calculated peak burst intensities (one burst per revolution) for choppers having straight slits, and choppers having circular slits with radii of curvature of 83.3 in. and 42.1 in. The rotational speed is 4720 rpm, the distance between choppers is 3.437 meters and the point of observation is 2.500 m after the last chopper. Experimentally obtained bursts for the choppers with 83.3-in. slit radii are also shown.

of the desired velocity v_0 it is necessary to have choppers with circular slits such that $2\omega\rho = v_0$ where ω is the angular velocity of the slits and ρ is the radius of curvature of the slits. As the neutron velocity becomes greater or less than v_0, the transmission probability becomes progressively less until velocity limits are reached beyond which no neutrons will pass. To give high transmission over the velocity range of interest at rotor speeds up to 6000 rpm, sets of choppers with straight slits and with curved slits with radii of curvature of 83.3 in. and 42.1 in. have been made for the MTR velocity selector. The curved slits are made as described in § 2.2 except that phenolic side pieces are cut with the desired radius of curvature. The nickel foil plus aluminum grid subassemblies are then pressed between these side pieces and assume the desired shape. Once the shielding is removed, about one hour is required to interchange one pair of choppers for another pair.

Fig. 6 shows the envelope of the calculated burst shapes for these three sets of choppers operating at 4720 rpm and with a distance of 3.437 m between choppers. Since two bursts per revolution are obtained with the straight slit choppers, these give better counting rates down to an energy of 0.06 eV. The set with 83-in. radii is best between neutron

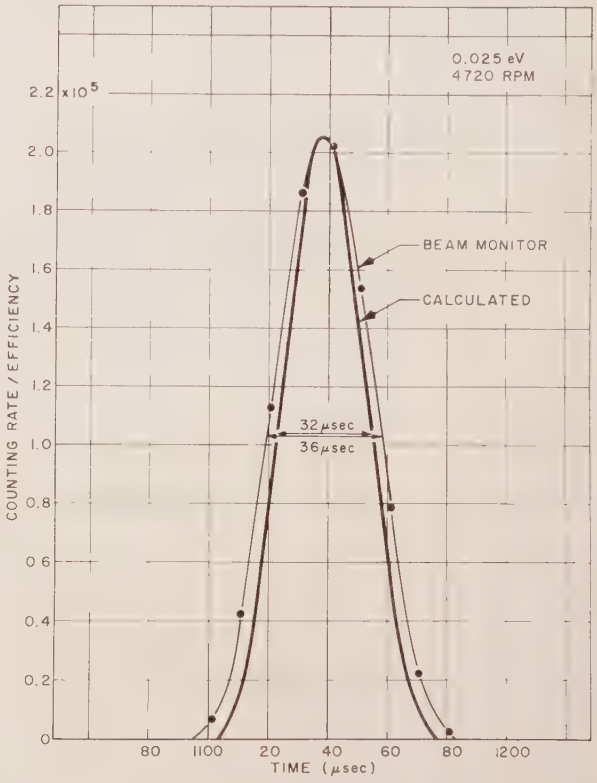

Fig. 7. A calculated burst shape and an experimental burst shape. The calculated curve has been normalized to the experimental burst at the peak of the experimental curve. The choppers with 83-in. radii of curvature slits had a distance A to D = 3.437 m and D to detector = 2.500 m.

energies of 0.06 eV and 0.01 eV while the set with 42-in. radii is best at smaller energies. If the angular velocity is changed the transmissions change. Included in fig. 6 are experimentally obtained bursts for the 83-in. radius of curvature rotors. A temperature of the Maxwellian distribution of 125°C was needed for agreement; this high temperature is attributed to diffusion hardening of the source flux.

Fig. 7 shows a typical burst shape obtained with the beam monitor in a 22-h run with a rotor phase difference of 1570 μsec. The solid points are the data obtained with 10-μsec channels corrected for detector efficiency while the heavy curve is one

calculated to correspond to this case. The experimental curve is broader by 4 μsec than the calculated curve due to phase jitter. However, the shape is preserved verifying the predicted shape (sin $A/A)^2$ where $A = \pi t/2\tau$ (ref.[22])) between $\pm 2\tau$ where τ is the half-width at 0.405 maximum.

To bring the rotors of the velocity selector up to operating speed, the 3-phase oscillator is first set to the desired frequency and power is applied to the motors. The electrical phase is adjusted to 90° between the two phases for each motor by the differential control transformers. Since the motors are of the hysteresis type, they lock in synchronism at arbitrary points and their relative rotor phase position must be rotated to give the desired rotor phase so that bursts of neutrons of the desired energy are produced. The relative times of the signals from the magnetic pickups of each rotor are observed by both an oscilloscope and electronic counter[23]). This electronic counter scales the pulses produced by a crystal controlled oscillator between a start signal (the signal from rotor A) and a stop signal (the signal from rotor B, C or D). The relative rotor phase is measured in microseconds which is easily related to velocity, since both the oscilloscope and electronic counter read in time directly. At a speed of 4720 rpm, an angular rotation of one degree is equal to 35.3 μsec.

Using the magnetic pickup time signal from chopper A as a time base, the other rotors are shifted to the desired rotor phase by the control transformers. For coarse adjustments, the 90° electrical phase between legs of one motor are shifted until the motor starts to shift out of synchronization. When the rotor slips to the desired rotor phase, the electrical phase between legs is returned to 90° and the motor stops shifting. Small adjustments of the rotor phase up to $\pm$ 200 μsec ($\pm$ 6°) are made by changing the electrical phase slightly away from 90°. An electrical phase of less than 90° reduces the rotor phase while an electrical phase of more than 90° increases it. Within the $\pm$ 200 μsec ($\pm$ 6°) the motors hold in synchronization. In this way all rotors can be set to the desired rotor phase in a few minutes. Once the rotor phases are set they hold for a period of days.

[23]) Model 524C electronic counter, Hewlett Packard Co., Palo Alto, California.

3.2. PHASE STABILITY

The variation of rotor phase between two rotors is called, in this paper, the rotor phase jitter. For a system of phased choppers to act as a velocity selector, this phase jitter must be small enough so that the broadening of the burst due to the rotor phase jitter is a small fraction of the total burst width. The rotor phase jitter between two rotors, choppers A and D, observed as the time between signals from the two rotors measured by the electronic counter every three seconds for a period of about three hours, is shown in fig. 8. The half-width at half-maximum of this curve is about $\pm$ 8 μsec ($\pm$ 0.23°). If one convolutes this curve with a calculated curve similar to that of fig. 7 a reasonable fit to the experimental points is obtained. Since the rotor phase jitter broadens the burst width by only about 4 μsec (0.11°) or about 12%, the phasing as accomplished with the present motors and electronic drive system is quite satsisfactory for a phased chopper velocity selector.

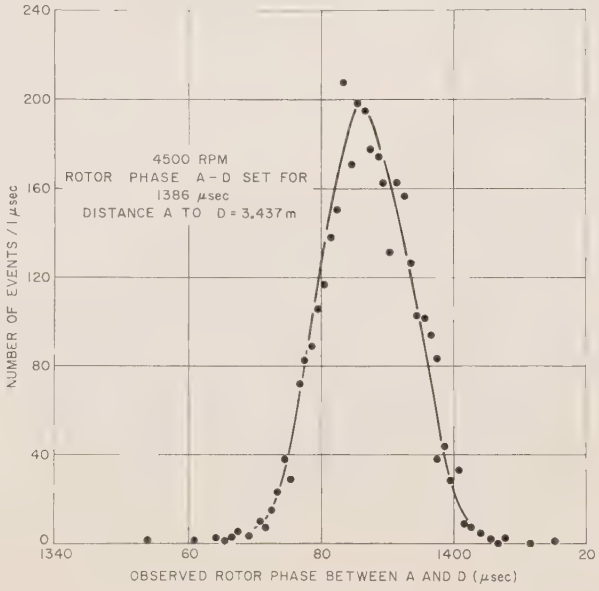

Fig. 8. The distribution of the rotor phase jitter between choppers A and D measured every three seconds with an electronic counter.

Fig. 9 shows a distribution of the period of the

oscillator as recorded 43 times a minute using the electronic counter. The distribution has two peaks and a width of about 1.4 μsec. Fig. 10 shows how these variations occur in sequence. Since the signal

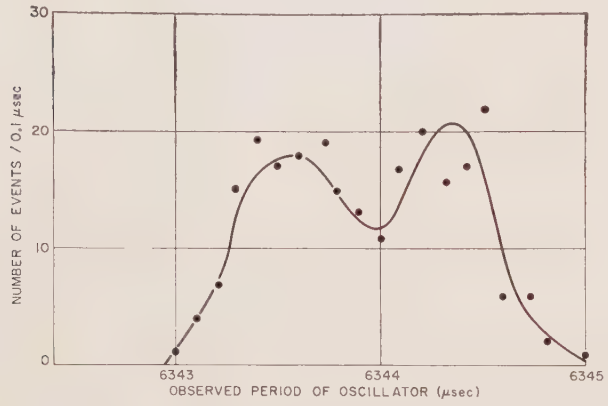

Fig. 9. The distribution of the period of the oscillator measured 43 times a minute with an electronic counter.

to the electronic counter is from the pulse shaping circuit (§ 2.8) the fluctuations can be due to period changes, magnitude changes, or ripple.

Fig. 11 shows a distribution of the periods of chopper A as measured with the electronic counter

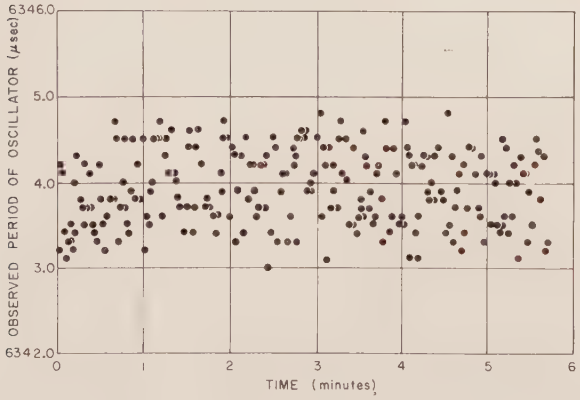

Fig. 10. Time sequence of measured periods of the oscillator corresponding to fig. 9.

43 times a minute. This distribution is assymmetric, being peaked at longer times, and has a full-width at halfheight of 1 μsec. Fig. 12 shows the time sequence of these period measurements. In this case, a definite pattern is present showing periods of about 20 sec with additional longer and shorter periods.

The magnitude of the phase jitter is independent of the rotational velocity of the rotors over the regions observed, that is 1500 to 5225 rpm. At times when the rotor phase jitter has been larger,

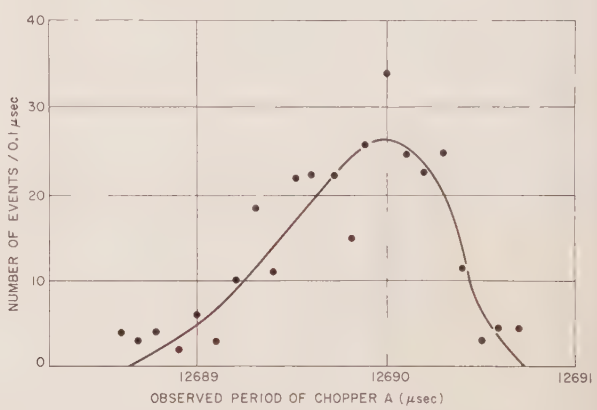

Fig. 11. The distribution of the period of chopper A measured 43 times a minute with an electronic counter.

the cause has been traced to 1. worn bearings in either the motors or the rotors, 2. excessive drag resulting from such effects as a tight spring on the upper rotor bearing, a compressed flexible coupling between motor and rotor, or excessive bearing

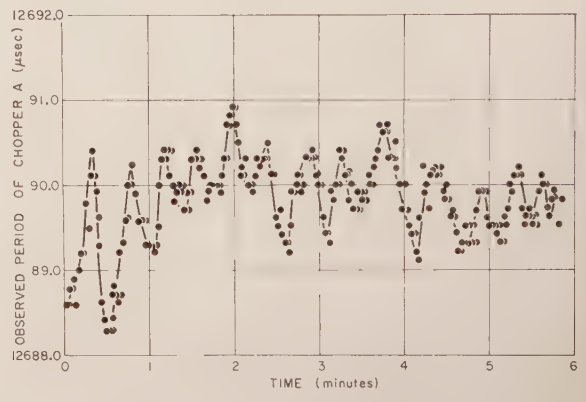

Fig. 12. Time sequence of measured periods of chopper A corresponding to fig. 11.

thrust pressures caused by too many shims behind the motor bearings, 3. malfunction of the power amplifiers, or 4. instability of the oscillator frequency.

The limited stability of the oscillator is the primary cause of the rotor phase jitter. Experience has shown that the phase jitter is independent of

rotor speed and that a slight increase in the magnitude of the period jitter of the oscillator is immediately evident in the rotor phase jitter. The oscillator jitter is fed to each rotor, and is damped and filtered to some extent by the response of the heavy rotors. The very fast fluctuations are too fast for the rotors and motors to follow while the very slow fluctuation (several minutes) are followed uniformly by all rotors. The fluctuations with intermediate periods are not followed in exactly the same way be each rotor, because of the slightly different properties of the motors and rotors. The heavy rotors tend to limit the phase jitter by their inertial damping action. Some of the small differences between rotors are 1. the weights, especially between choppers and rotating collimators, 2. the moments of inertia, 3. the electrical coupling in the motors, and 4. the drag introduced through bearings, flexible coupling, etc. The drag is probably the major cause of nonuniform response between two choppers, a nonuniform drag being more offensive than a uniform drag. In the design and construction of the velocity selector it was predicted that friction and drag would be the major causes of phase jitter. Thus the design minimized the sources of drag as much as possible. It was surprising that the stability of the oscillator and associated electronics are usually the limiting factors. It was also unexpected that standard commercial hysteresis motors would perform so well. It is only when a bearing is very bad or that obvious sources of drag are present, that eliminating the drag has improved the rotor phase jitter.

3.3. TIME CALIBRATIONS

The purposes of the velocity selector is to select and measure energies of neutrons by selecting and measuring times and distances. To calibrate the instrument against external standards, all pertinent distances are measured to 0.016 in. To determine if any time delays exist between the time the rotors open and the time the signals from the pulse shaping circuit that triggers the analyzer arrive at the analyzer, the gamma bursts from each chopper were observed with the time analyzer. These gamma bursts are observed when the bias on the amplifier of the beam monitor is lowered. They represent the time of alignment of the entire chopper foil assembly with the beam and not that for single slits. A time delay of 46 μsec is present because of a delay of 50 μsec due to the LC circuit of the magnetic pickup and attached cable and because of an advance of 4 μsec due to the one-μsec-wide pulse from the pulse shaping circuit occurring before the crossover of the magnetic pickup signal.

With these measurements of delay and the known distances, it is possible to make accurate energy measurements. As a consistency check a single beryllium crystal was placed at the sample position and the Bragg neutrons were observed at different angles. Rocking curves were measured by varying the initial energy (changing the rotor phase) and by varying the crystal angle. When the correct distances, times, angles, delays, and lattice spacings are used, consistency to 1–2 μsec is obtained. See § 3.4, fig. 14 for experimentally measured burst widths and flight times. This method of calibration not only checks the timing signals, distances, and angles but also checks the time standard (the pulsed crystal oscillator of the 4096-channel analyzer), the readout of the time analyzer, and the energy calculation section of the program used to process the data.

3.4. RESOLUTION

The resolution of the velocity selector is variable for each angle, initial neutron energy, and final neutron energy. Involved in these considerations are the angular and energy uncertainty of neutrons both in the initial beam and in the scattered beams. These different parts will be discussed qualitatively with several examples for illustration.

The angular divergence of the initial beam is determined by the size of inserts in chopper D and the size of the nickel-iron collimator in front of the beam door in the collimation plug. The aperture of the nickel-iron collimator is 4 × 2 in., that of the foil assembly of the last chopper is 4 × 1.3 in. and they are about 6.4 meters apart. Thus, the horizontal divergence is less than 0.3° while the vertical divergence is less than 0.8°.

The angular divergences of the scattered beams are greater, being defined principally by the width and height of the detector assemblies. The 10 by

18-in. detector assemblies at 2 meters from the sample subtend angles of 7.2° in the horizontal plane and 13° in the vertical plane. Near 90° the vertical angle is not as critical as the horizontal angle since for most samples the scattering is axially symmetric. However, for scattering angles near 0 and 180° these 10 × 18-in. counter assemblies subtend a somewhat larger scattering or polar angle.

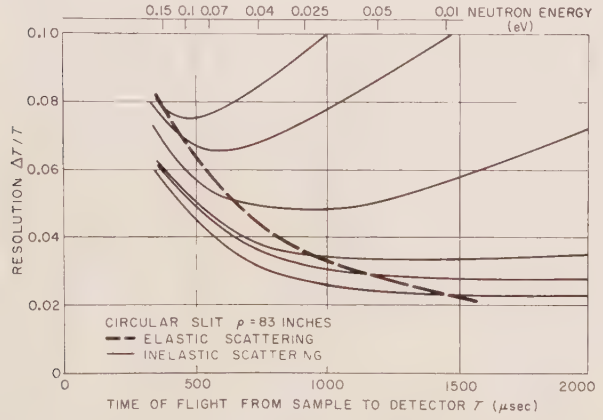

Fig. 13. The resolution of the velocity selector defined as the width of the burst measured at the detectors divided by the time of flight from the sample to the detector. The dashed line represents the resolution of the initial beam (elastic scattering) and the solid lines show the resolution for inelastic scattering.

Since the time distribution of the initial burst is usually symmetrical, the time resolution $\Delta T/T$ can be stated as the full-width at half-maximum of the burst ΔT measured at the detectors, divided by the time T for the neutrons to travel from the samples to the detectors. This distance is used because it is the distance over which the neutrons are actually timed if they change energy. To include both the time uncertainties and the velocity uncertainties the burst width must be measured at the detectors.

The time resolution $\Delta T/T$ has been determined for several cases of both elastic and inelastic scattering by means of the calculated burst shapes[22]). The results are shown in fig. 13. The dashed line is for elastic scattering and agrees with the line having an equation of $\Delta T/T = a/T$ only at times corresponding to velocities where $2\omega\rho = v_0$. At other times the coarse velocity selecting action narrows the burst.

The width of the burst for elastic scattering is attributed to two parts. One part is due to the uncertainty in time when the neutrons passed the center of the choppers and the second part is due to the uncertainty of velocities of the neutrons when they pass the chopper. For inelastic scattering, assuming that the neutrons receive or give up a discrete amount of energy, a discrete change in velocity components occurs but the uncertainty due to the time that the neutrons pass the center of the chopper remains constant. The solid curves of fig. 13 are obtained by adding discrete velocities to the velocity components of the bursts and remeasuring the widths.

The resolution for energy change, solid curves, in the scattering process can be fit with the curve $\Delta T/T = (aT^2 + b)/T$. Since the bursts are represented by $[\ (\sin A)/A\ ]^2$ where $A = \pi t/2\tau$ and the widths can be predicted by the above equations, the information for resolution broadening theoretical data is available.

Other uncertainties are present in the measurements because of the finite size of the apparatus. The beam at the scattering sample is 1.3 in. wide so that some distance uncertainties, that can be expressed as time uncertainties, are present. These depend on the shape and orientation of the sample. When a flat sample is mounted so that the normal to the sample bisects a forward quadrant of detectors, the neutrons scattered from the two edges of the sample have different flight paths. As an example, consider the counters at 90°. The difference in the two extreme flight paths is 2 × 1.3 in.; thus $\Delta D/D = \Delta T/T$, ≈ 3.3%. For inelastic scattering a more detailed analysis has to be made depending upon the magnitude of the energy gain or loss.

Other distance uncertainties result from the finite size of the counters. The 1 in. thickness of the counters introduces an extreme uncertainty in the flight path of $\Delta T/T = 1.3\%$. The 18-in. length of the counters introduces an extreme uncertainty of 0.2%. The distance actually used in making time calculations is from the center of the sample to a point on the center wire of the central counter of the detector assembly 4.5 in. below the horizontal central plane.

The above mentioned values are extremes and

the measured uncertainties are not as large. Fig. 14 shows the plot of the full-width at half-height of the bursts vs. scattering angle for neutrons scattered from a 0.062-in. sample of vanadium placed with its normal passing through the 45° detector. On the same figure are given the differences between the times predicted by the rotor phase and distances, and the measured times that the peak intensity was actually observed. Zero degrees represents the non-

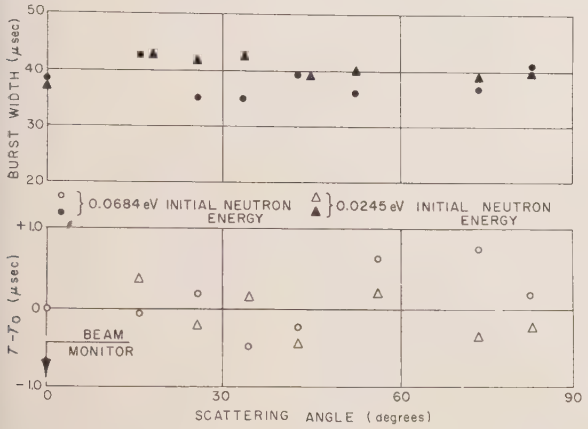

Fig. 14. The full burst width at half-maximum (solid points) and the difference between the predicted and the observed times of the peak intensities of the bursts (open points) as observed at the seven angles for scattering from a vanadium sample. T is observed time and T_0 is predicted time.

scattered beam as measured by the beam monitor. Time uncertainties and burst broadening due to the above mentioned distance uncertainties are seen to be small.

3.5. INTENSITY CALIBRATION

In some velocity selector measurements it is desirable to measure absolute intensities to obtain absolute cross sections. To reach this goal the relative intensities of the initial and scattered beams are determined as follows; the velocity selector is set to deliver bursts of 0.025 eV neutrons and a flux map both in time and space is made with the beam monitor of the beam at the sample position. Fig. 15 shows distributions along horizontal and vertical center lines of the intensities of the beam that are obtained by integrating the measured bursts over time. The total intensity of the beam at the sample position is obtained by integrating over all horizontal and vertical distributions.

An interesting observation from these measurements is that a definite time shift is noted when the time for peak intensity is compared with its position of observation in the horizontal plane. These are the open points of fig. 15. The time at the center of the beam is almost exactly that predicted by the rotor phase setting while the left side (looking along the beam away from the reactor) is several microseconds early and the right side is several micro-

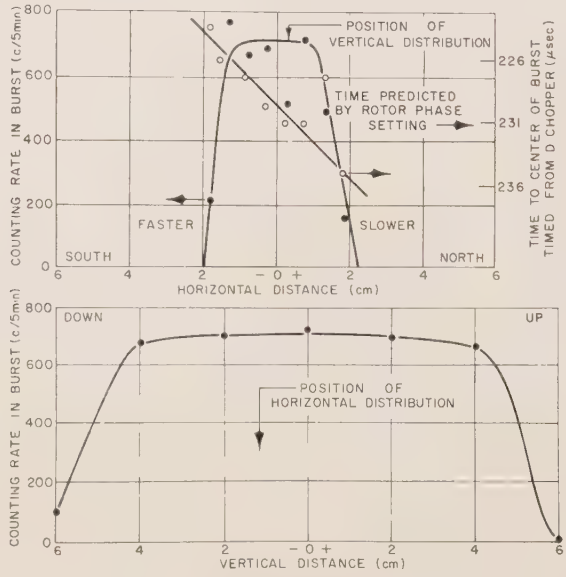

Fig. 15. A horizontal and a vertical distribution of the counting rates (solid points) at the sample position. The open points and straight line show how the time of peak intensity changes from one side of the beam to the other.

seconds late. The choppers rotate clockwise as observed from above and the major part of this time difference is due to the sweep of the beam across the sample.

The horizontal angular divergence of the beam passing through the velocity selector is about 0.3°. The divergence of a single slit of a chopper is the slit width divided by the chopping diameter or 0.8°. Even though the choppers have the poorer collimation and they open and allow the beam to shine with full brilliance for a short time and then close, the small time sweep mentioned in the preceding paragraph is observed. For maximum intensity and minimum time uncertainty, the chopper producing full brilliance is preferable to the chopper sampling the source and sweeping the intensity across the beam.

The next step in the intensity calibration is a comparison of the counting rate of the beam monitor at the sample position and at the normal operating position two meters beyond the sample. Then the counting rate of each bank of counters is compared to the counting rate of the beam monitor with a radium beryllium source imbedded in polyethylene placed 1.5 meters away from the face of the detectors. A source is used so that the effect of the full area of the detectors is measured and not just one small part. The assumption is made that the flux from the source is nearly Maxwellian and that both types of counters are relatively thin. With this relative measurement of the efficiencies of the detectors, each detector and the beam monitor is given a figure of merit at one energy and its calculated efficiency, normalized through the figure of merit, is used in the data computation program. The errors introduced by the assumptions that the counters are thin and that the source flux is Maxwellian are smaller at the present time than those arising from counting statistics. See § 4.1 for a consistency check of this method.

3.6. INTENSITIES

The problem of the intensities delivered by the velocity selector can best be understood by considering the fluxes at different points along the beam. As a particular example consider the choppers with 83-in. radius of curvature slits spinning at 4720 rpm with 1571 μsec rotor phase between A and D choppers spaced 3.437 meters apart. At the tip of the beam hole the flux is about 0.8×10^{13} thermal neutrons/cm^{2}sec. Only 1.4×10^8 n/cm^{2}sec exit in the beam from the 1.3×4-in. beam hole at the face of the reactor. The rest are sacrificed to obtain a beam. Chopper A, because of its duty cycle and coarse velocity selector action, excludes all but about 0.1% of the thermal neutrons in order to produce bursts. This leaves about 1.4×10^5 n/cm^{2}sec. In producing bursts of neutrons having only a small range of velocities, chopper D transmits about 1100 n/cm^{2}sec or less than 0.8% of the neutrons arriving there. This assumes a phase such that the burst contains 0.025 eV neutrons. There are additional losses because of the extended 1.3×4-in. collimation and because the aluminum in each chopper transmits only 80% of the neutrons. This decreases the flux at the sample to about 140 n/cm^{2}sec.

The total number of neutrons arriving at the sample is about 2300 n/sec. The sample thickness is adjusted so that only about 10% of these or 230 n/sec are scattered. If these are scattered isotropically, about 0.23% arrive at each detector or about 32 n/min. Since some of these are inelastically scattered, they are detected in many time channels. In a representative case for a gas the inelastically scattered neutrons are spread over 30 ten-μsec time channels. This indicates that counting rates of 64 c/h 10 μsec channel are expected if the counters are 100% efficient. The counting rates are of this order of magnitude (see Section 4, fig. 19).

The example selected does not give the highest counting rates but is within a factor of 2 of the counting rates where the reactor flux distribution peaks. Above 0.1 eV or below 0.02 eV the counting rates decrease rapidly. The ratio of true counts to background, the resolution and the time to accumulate enough statistics limit the range of initial energies that can be covered profitably. Fig. 6 shows how the intensities vary with neutron energy.

Measurements have been made to show how the

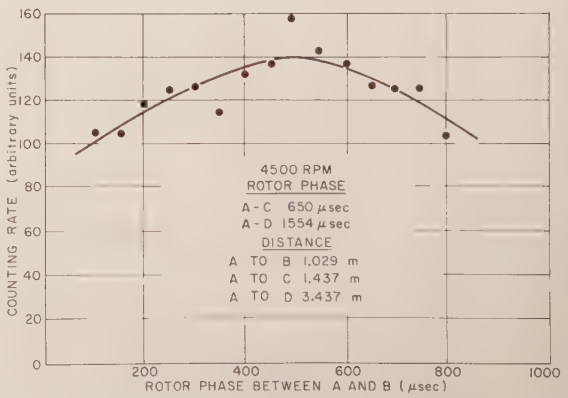

Fig. 16. The effect on the burst intensity of changing the rotor phase between chopper A and rotating collimator B.

rotor phases of the rotating collimators relative to the choppers, that is of B to A and C to A, affect the counting rates in the burst. With the rotors spinning at 4500 rpm and 1554 μsec rotor phase between A and D, first the phase between A and B, then that between A and C was changed and the

urst intensity measured. (Note that B and C otors were not as close to A as in later measure-ents.) Figs. 16 and 17 show the results. From ese it is concluded that the counting rate is not a itical function of the rotor phase setting or of the

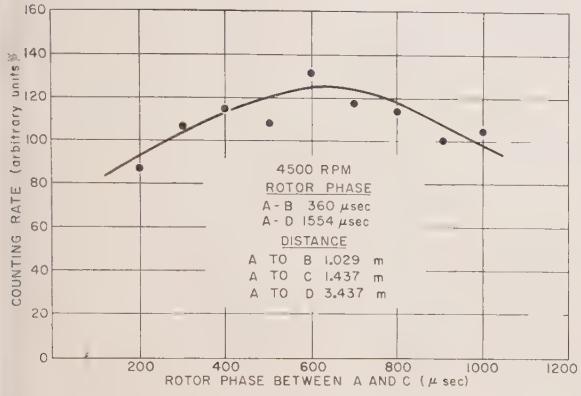

ig. 17. The effect on the burst intensity of changing the rotor phase between chopper A and rotating collimator C.

hase jitter of the rotating collimators. Some ad-ustment toward shorter rotor phase times can be ade that suppresses the fast background but ffects the burst intensity only slightly.

.7. BACKGROUNDS

As demonstrated in the previous section, the elocity selector counting rates per time channel re small. Thus the problem of background elimina-ion or its accurate compensation becomes a major roblem. This background can be from several ources and is of several types. The problem of amma-ray background has been eliminated by sing $B^{10}F_3$ proportional counters in which gamma ulses are small and are excluded by discrimination.

A detector consisting of 10 BF_3 counters set at ts usual bias has a counting rate of 0.6 c/h 10 μsec hannel when the reactor is down and the rotors are pinning at 4720 rpm. These counts are attributed o cosmic rays or to radioactivity of the material rom which the counters are constructed. This ource is small compared to other sources now resent and is time independent. Thus, no further onsideration to its elimination will be given.

The principle sources of background are neutrons. For the present discussion, a distinction will be made between fast or epi-cadmium neutrons and thermal or sub-cadmium neutrons because the backgrounds due to the latter can be easily suppressed with cadmium shielding. The fast neutrons are the difficult source of background in the MTR velocity selector. Backgrounds, called room backgrounds, from other experiments at the MTR produce about 4200 c/h in a detector with the reactor at 40 MW and the velocity selector beam stopped by the radiation door. Considering the time each time channel is open to accept data for a rotor speed of 4720 rpm, this background corresponds to 3.3 c/h for each 10 μsec channel, 0.6 c/h 10 μsec of which is due to non-reactor sources.

For a data run the background varies from 6–90 c/h 10 μsec channel and is time of flight dependent. (See § 4.1, fig. 19.) Most of this background originates from the HG-6 beam hole used by the velocity selector. Fast neutrons from the reactor stream down the beam hole and many of them are scattered by chopper A. However, some penetrate the first chopper, collimators B and C, and chopper D, the number depending upon the rotor phase of each rotor. Slow neutrons are almost completely scattered or absorbed by chopper A when it is closed. The fast neutrons scattered by chopper A and rotating collimator B are easily controlled by 2-foot-thick shielding around rotors A and B. Some effects due to fast neutrons scattered by C are noticed in the backward angle detectors, since it is close to these detectors. Chopper A and the rotating collimators are placed as close to the reactor and as far from the detectors as possible to limit these effects. The fast neutrons that penetrate the first three rotors and are scattered by rotor D constitute the main fast background. Since this source is in the middle of the detector area it is necessary to moderate and absorb the neutrons and not just scatter them. Also, it is more difficult to shield this area because of its proximity to the sample and its proximity to the flight paths from the sample to the detectors which must be left open. At the present time, rotor D is covered with about one foot of broated paraffin. To eliminate the fast neutrons that also penetrate D and are scattered by the sample, more effective rotating collimators are being built.

Fig. 18 shows how each rotor affects the background and the thermal neutrons. The time distribution triggered by chopper A (83-in. radius of curvature, 4720 rpm, rotor phases set for 0.025 eV) was measured with the beam monitor as successive rotors were put into operation. With only chopper

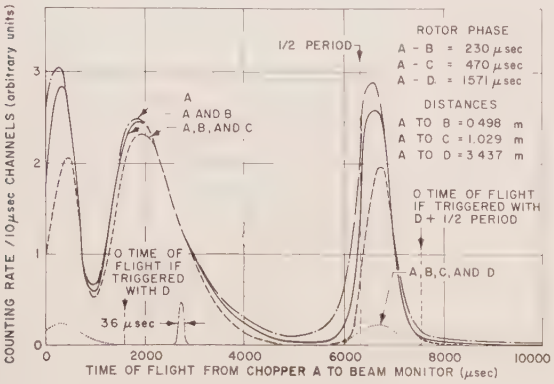
COUNTING RATE /10μsec CHANNELS (arbitrary units)
TIME OF FLIGHT FROM CHOPPER A TO BEAM MONITOR (μsec)
1/2 PERIOD
ROTOR PHASE
A - B = 230 μsec
A - C = 470 μsec
A - D = 1571 μsec
DISTANCES
A TO B = 0.498 m
A TO C = 1.029 m
A TO D = 3.437 m
A
A AND B
A, B, AND C
0 TIME OF FLIGHT IF TRIGGERED WITH D + 1/2 PERIOD
0 TIME OF FLIGHT IF TRIGGERED WITH D
A, B, C, AND D
36 μsec

Fig. 18. The effect of the successive rotors on the fast background and on the thermal neutron distribution.

A in operation, both fast neutrons that penetrate the aluminum plus nickel foil section of chopper A and neutrons from the $1/E$ region of the reactor flux distributions are detected at short times. The time distribution drops at 700 μsec because of the cadmium covered foils, then increases to display the thermal distribution. Another peak is observed at 6500 μsec due to fast background and to some $1/E$ neutrons traversing the choppers in the opposite direction. Slit assemblies with 83-in. radius of curvature are not completely closed to the $1/E$ neutrons in the reverse direction.

When both chopper A and rotating collimator B are in operation (rotor phase A–B = 230 μsec) the distribution at times other than near 2700 μsec are depressed because of the coarse velocity selecting action of B and because of the shielding effect of B for fast background. The addition of rotating collimator C causes an even more pronounced effect. Chopper D excludes all thermal neutrons except those in the burst and excludes many neutrons that contribute to the fast background. However, the actual situation is not quite as promising as indicated by this example, since this observation was made in the beam with the beam monitor. The part of the fast background that is in the beam does contribute to the time dependent background, shown in fig. 19, by being scattered by the sample, but this accounts for only about 10% of the time dependent background. The rest comes from those fast neutrons that are scattered by chopper D but are not absorbed by the shielding near chopper D. These are the neutrons that need to be absorbed.

The time distribution of fig. 18 is initiated by rotor A. When data as shown in fig. 19 are being taken, time distributions are initiated by rotor D. This time is indicated in fig. 18 and also a corresponding time one-half rotor period later. Since the second-half of the period excludes the thermal neutrons, an indication of the effects of the very fast neutrons is present. These have the same shape as the backgrounds of fig. 19. Each additional rotating collimator is seen to be more effective in this region than near the peak of the background at 0 and 6500 μsec.

Since the major background is due to fast neutrons penetrating rotors A, B, and C, the number and time distribution of the background neutrons as observed by the scattering detectors depends strongly on the phase setting of the choppers. Thus, the effect of backgrounds becomes greater at higher initial neutron energies and higher scattered neutron energies. The magnitude of the fast background detected depends strongly on the amount of shielding around D, increasing by a factor of 100 if the shielding is removed.

The problem of fast background is being attacked by two approaches. New rotating collimators made of nylon and of larger diameter are being designed to suppress this background. Meanwhile for each set of data, the backgrounds are measured using the sample changer and an empty sample container so that corrections can be made.

A measurement of the effect of the scattering of the fast neutrons from the sample can be made by placing 0.020 in. of cadmium in the beam before the sample to eliminate the effects of the thermal neutrons. Since the fast background is a smoothly varying function with time, it has proven just as effective to visually normalize the background to the data. The 256 10-μsec channels allow ample space beyond the thermal scattering effects at very short and very long time in which to make this normalization.

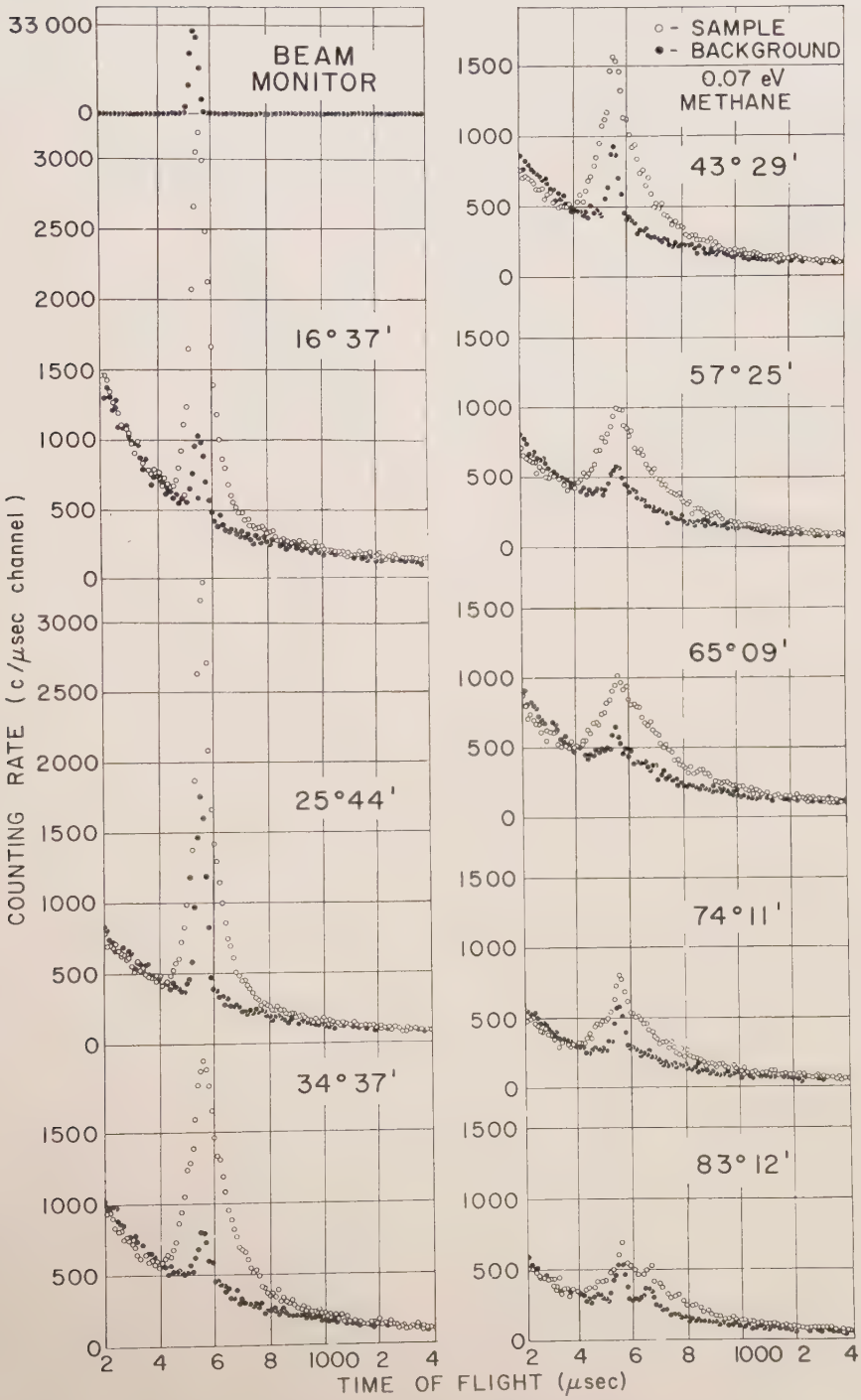

Fig. 19. Raw scattering data for eight angles obtained in a 22 h sample run and 22 h open run from a sample of methane. The aluminum container had 0.032-in. walls.

Thermal neutrons in the burst that are scattered by air near the sample constitute another source of background. The subtraction of the open data from the sample data allows for an almost complete subtraction of the effects due to this air scattering. But since the sample scatters about 10% of the thermal neutrons, only 90% of the beam goes beyond the sample while 100% passes through in an open run. Thus, the subtraction of the open data from the sample data over-compensates for the scattering of thermal neutrons by the air beyond the sample. Since the air scattering is small, no further correction to the final data is made at the present time for this effect. The unshielded path of the beam in air near the sample is made as short as possible to suppress this source of background.

The effect of the sample container is compensated for by taking the open data with an empty sample holder. The only problem arises when the empty sample holder is not similar to the sample container itself. The walls of the sample container are made as thin as possible to limit this effect. In the experiments with gases, it was found that the aluminum crystallites of the sample cans were not randomly oriented and that the effects due to aluminum during the sample and open runs were slightly different.

The problem of designing a chopper which effectively excludes fast neutrons is finding a material for which a small quantity has a high scattering coefficient. Nickel and hydrogenous plastic are as good as any; the 4.75-in. nickel rotors with phenolic side clamps have a transmission of 1% for fast neutrons. Because 10^{10} n/sec cm^2 of the thermal neutron flux are eliminated to produce the monoenergetic burst, the number of fast neutrons transmitted in the beam is still an appreciable fraction of the thermal neutrons, It is helpful that all observations are made in time space and the greatest part of the fast neutron background appears at a time when pertinent slow neutron data are not present. An increase in rotor speed narrows the burst width and eliminates more of the fast neutron background from the time of observation. However, an increase in speed increases the effect of the time independent background (room background) because each time channel is sensitive more often. The wide beam is a detriment to controlling the fast background, because the scattering material of the rotor is not swept into the beam as rapidly as with more confining choppers. The rotor must rotate about 5° before a major share of the nickel shell is effectively in the beam. However, this wide beam is necessary to give adequate counting rates with the source flux available.

4. Data

In the following subsections, examples of data are given. These are generally not the optimum sets or the most recent sets. Improvements are being made but data incorporating these improvements have not been taken for all samples.

4.1. METHANE AND THE SCATTERING LAW

Methane gas was selected as an initial sample for detailed experimental study to test the operating conditions of the velocity selector. The sample containers, 0.010 or 0.030-in.-wall aluminum cans 4.5 in. high and 2.125-in. inside diameter, are of a convenient size and shape to limit corrections due to multiple scattering and to sample thickness. The pressures are adjusted so that about 10–12% of the neutrons are scattered. The principal scatterer is hydrogen and thus the scattering is predominantly incoherent. Since the sample is a gas, the fraction of neutrons changing energy is larger and the resolution is not as critical as for a solid. Also several theories, with which the experimental data could be compared, have been proposed for scattering in methane.

Fig. 19 shows time distributions taken at eight angles and the beam monitor for a total running time of about 44 hours. The open circles are the sample data and the solid points the background data. It is seen that the background is time dependent, that it is not perfectly matched in sample and open runs, and that some effects of the sample container are indicated. At 83° an inelastic effect due to the aluminum can is evident.

Errors in determining the magnitude of the inelastic scattering effects are primariy due to counting statistics and to uncertainties in background corrections. The counting rates vary from run to run and from one point of the time distribution to another. To improve the statistics several

uns can be averaged together. The raw data of ig. 19 give an indication of counting statistics. Smooth curves drawn through the points improve he magnitude determination without loss of reso-

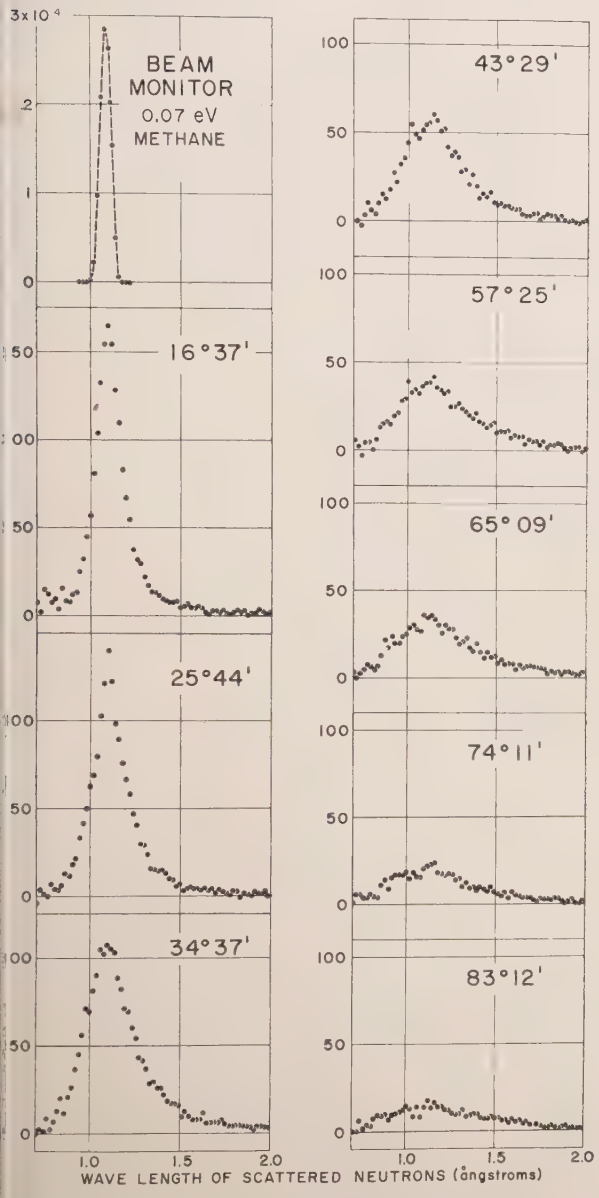

ig. 20. The differential cross sections for methane corresponding to fig. 19.

ition since the data are taken with 10-μsec hannels while the burst widths are 36 μsec, and me averaging is justified.

To correct for backgrounds, the open data are ibtracted from the sample data. If it is suspected that this subtraction does not completely compensate for the background, the open data are normalized to the sample data at very short and very long times where inelastic effects should be negligible. Then a subtraction is made. Other sources of error in the magnitudes are in the calibration of counter efficiencies, counter drift after normalization, sample thickness, air scattering, sample geometry and multiple scattering corrections.

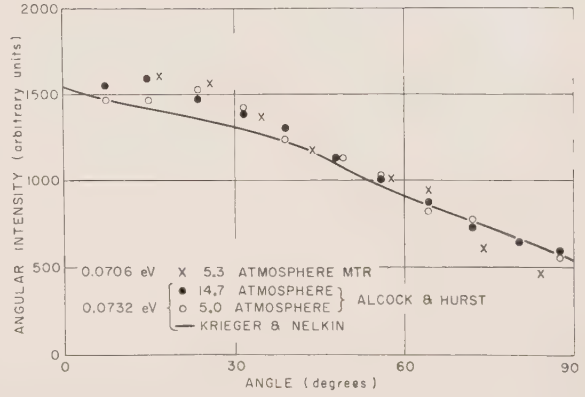

Fig. 21. The intensity distribution obtained by integrating the methane data of fig. 20 over energy. The solid line is the normalized theoretical intensity predicted by Krieger and Nelkin and the circles are the data of Alcock and Hurst.

Fig. 20 is the same data converted to $d^2\sigma/d\lambda d\Omega$ by means of the figures of merit determined for the detectors and the IBM-650 program. It is noted that the points are relatively smooth indicating that sufficient statistics were obtained. Also the peak of the distribution at 16° is about twice as wide as the beam monitor distribution, showing that the initial resolution is adequate. Integrating the data of fig. 20 over energy, the points of fig. 21 are obtained for the angular distribution of intensities. These agree in shape with those of Alcock and Hurst[24]) indicating that the normalization between counters is correct. A theoretical[25]) curve is also shown.

A more sensitive comparison is to convert all of the scattering data to the Scattering Law[26]) presentation. This intermixes data from several angles and for several initial energies giving a good

[24]) N. Z. Alcock and D. G. Hurst, Phys. Rev. **83** (1951) 1100.
[25]) T. J. Krieger and M. S. Nelkin, Phys. Rev. **106** (1957) 290.
[26]) P. A. Egelstaff, "The Theory of the Thermal Neutron Scattering Law", and P. Schofield, "Some Properties of the Space-Time Correlation Function", See ref.[1]). See also P. Schofield, Phys. Rev. Letter **4** (1960) 239.

check on all variables except the overall absolute magnitude and on the sources of error. Fig. 22 is the methane data presented as Scattering Law with the solid curve being the theoretical prediction for the

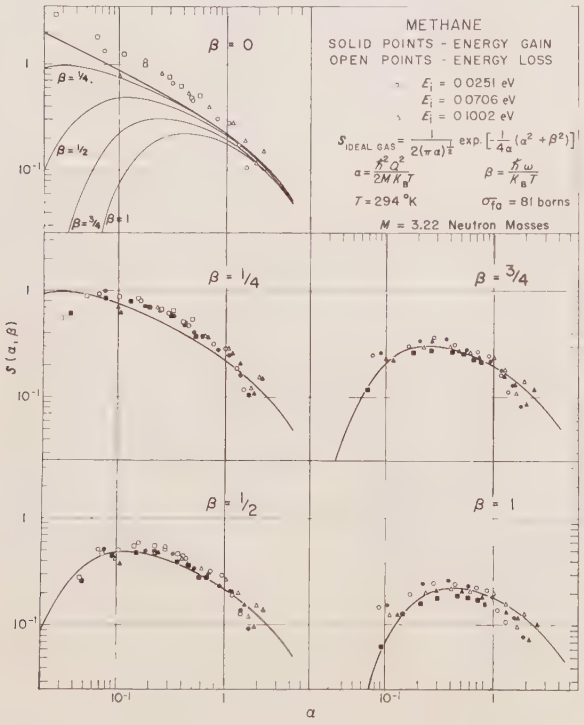

Fig. 22.
The methane data presented as Scattering Law per molecule.

ideal gas[26]). It is noted that the data do follow a relatively smooth curve and that the data intermix. An error in a figure of merit for a particular detector will be such that data from that angle will fall consistently off the Scattering Law curve. Such a discrepancy was observed in one case. An error in the assumption that calculated efficiencies as a function of energy can be used will be such that the Scattering Law data from several different initial energies will not intermix. No effect of this nature has been observed. An error in energy will produce a splitting of the $+\beta$ and $-\beta$ data. Such an effect was observed when incorrect distances were used. The fact that the points fall so close to the theoretical curve which yields the total cross section and that the angular intensities agree with the previously measured values indicates that the absolute normalization is also correct. As a further check, an integration over angle and energy gives the total cross section. The integration of the methane data[27]) indicate that the intensity calibrations are correct within the estimated errors.

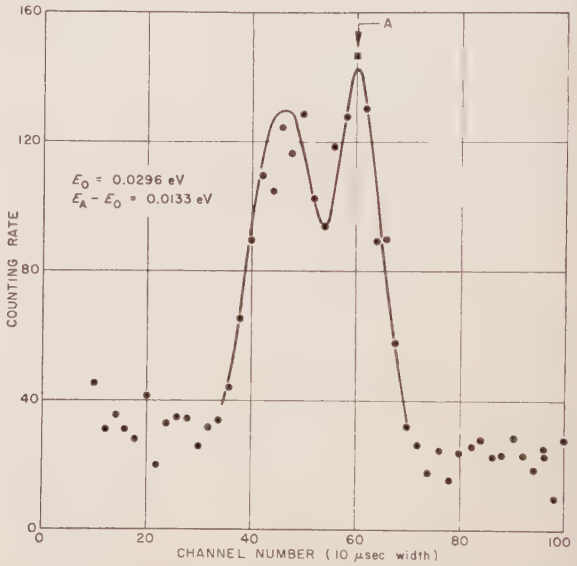

Fig. 23. An example of Be single crystal data for a 16 h run. The peak A corresponds to the point A of fig. 24.

4.2. BE SINGLE CRYSTALS AND THE DISPERSION RELATIONS

For measuring dispersion curves where the energy change and only the relative magnitude is important, most measurements have been made with triple axis spectrometers[3]) or beryllium filtered beams plus choppers[1,2]). The MTR velocity selector has been used to measure parts of the dispersion curves for a single crystal of Be. A single crystal of Be about 4 × 1 × 0.4-in. was placed at the sample position in a known orientation. Neutrons of a given energy were scattered from the sample (initial neutron energies between 0.01 and 0.1 eV were used) and the peaks due to discrete energy changes were observed. The counters were 4 in. wide, 2 in. deep and 4 in. high to limit the angle of acceptance of the scattered beam. Fig. 23 is an example of a 16-hour run. From the energy change, the initial energy, the scattering angle and the orientation of the crystal, the position of interaction in reciprocal space is determined and thus

[27]) Randolph, Strong and Brugger, Bull. Phys. Soc., Ser. II 6 (1961) 71.

points on the dispersion curves are obtained. Fig. 24 shows some of the dispersion relation points obtained, with the MTR velocity selector.

In these measurements a guess as to the desired settings of initial energy and scattering angle at

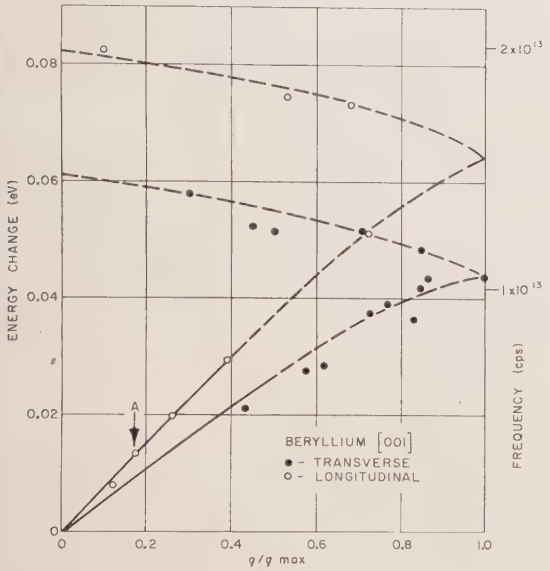

Fig. 24. Parts of the dispersion curves for Be obtained with the velocity selector.

which an inelastic peak due to a phonon in a pertinent direction of reciprocal space would be seen (method of successive approximations[3])) was made and the velocity selector was set to obtain these conditions. Along with this point many peaks were observed in the other angle detectors that yielded phonons at odd angles in reciprocal space. To use the phased chopper velocity selector for dispersion curve measurements most effectively, it is advantageous to have detectors that can be moved on the arc around the sample so the method of successive approximations can be applied at several pertinent points in reciprocal space simultaneously. This allows maximum utilization of the multiangle potential of this type of velocity selector. The fact that several phonons can be observed in several angles simultaneously with several hundred counts in the peaks shows that a phased chopper velocity selector can compete effectively with a triple axis spectrometer. It would be desirable to improve the resolution by a factor of two which can be done by doubling the rotor speed.

5. Conclusions

The preceding sections show how the MTR velocity selector is constructed and how it operates. This section summarizes the advantages of a phased chopper velocity selector and the particular advantages of the MTR velocity selector. Several limitations are also mentioned.

Since inelastic scattering experiments are low intensity measurements, an outstanding advantage of the phased chopper velocity selector is the large amount of data that is accumulated for any given operating period. By producing a burst of monochromatic neutrons and then measuring the energy of all scattered neutrons at many angles simultaneously, the several operations that are done successively by other instruments are measured concurretly with the phased chopper velocity selector. The amount of information obtained concurrently more than compensates for the loss in intensity due to chopping the beam into bursts. The amount of data depends upon the extent of the equipment, that is the number of detectors and number of time channels, and these can be increased to the limit of resolution, intensities, and funds to increase the potential of the machine.

Drifts or changes in the velocity selector phase or intensity are observed by the detectors and the beam monitor simultaneously. Thus the data taken at many angles and final energies concurrently, can be normalized and corrected for resolution and backgrounds.

With the phased chopper velocity selector it is possible to obtain information from angles very close to the incident beam to angles almost in the backward direction. By having sufficient time channels available for each angle, it is possible to measure the energies of all the scattered neutrons. A wide range of initial energy can be covered, the MTR velocity selector having taken data for special cases from 0.005 to 0.5 eV. The limits of the initial energy are determined by the signal-to-noise ratio, the resolution, and the time that is expedient to spend to gather the information.

Once the phased chopper is built and operating, and the calibrations are made, the operation is relatively simple. The initial energy or resolution may be changed as described in § 3.2 in a few

minutes. They are continuously variable and such changes do not necessitate moving any shielding or the detectors. Under the present operating conditions there are no overlap or second order effects. The MTR velocity selector has been operated for up to a week with no attention beyond punching out the data and changing the initial neutron energy each morning.

The resolution of the MTR phased chopper velocity selector as it is now operating is as good as most other instruments and within a factor of two of the best instruments making inelastic scattering measurements at this time. The advantage of the velocity selector is that its resolution may be improved without the great loss in data accumulation suffered by other instruments. By increasing the rotational speed, the resolution is improved but the number of neutrons/min in the burst is unchanged. Thus, by increasing the time channels and angles to correspond to this improved resolution no loss in intensity is suffered.

The MTR velocity selector was designed conservatively to meet the needs of inelastic scattering experiments. The rotational speeds and design of the rotors is such that conventional materials and equipment are used. The major problem that was solved is the phasing of two choppers, mounted in bearings, to a degree that guarantees good energy monochromatization. This has been solved as shown in § 3.2. Also, through this conservative approach, a machine has been constructed that is relatively easy and safe to operate. A minimum of mechanical failures has been experienced to date.

One of the disadvantages of the phased chopper velocity selector is the magnitude of the equipment involved. A multichannel time sorter and many detectors are needed to realize the potentials of this machine. Also, even though the MTR velocity selector is of conservative design, a good deal of shop time is needed to construct it. To adequately shield all the counters a large amount of shielding is needed.

The MTR velocity selector has several disadvantages that are in the process of being eliminated. Large 12-in. diameter rotating collimators made of nylon are being designed to remove the time dependent background. A new crystal controlled oscillator† is being built to improve the phase jitter. With the installation of these the rotational speed will be increased to improve the resolution.

Dèpending on the experimental philosophy involved, a phased chopper velocity selector or a triple axis spectrometer may be best suited for measuring the dispersion curves of single crystals. If the dispersion curves in all directions in one plane of reciprocal space are desired the velocity selector is better. If dispersion curves in a few discrete directions in reciprocal space are required, the triple axis spectrometer may be better. For most other inelastic scattering measurements the phased chopper velocity selector appears to be the best research device to give maximum data with high resolution.

Acknowledgement

The authors wish to acknowledge the contributions of many people; R. J. Flynn and R. M. Fors for their mechanical design and engineering, L. W. McClellan for initial electronic developments, F. L. Petree and L. G. Hale for the design and construction of the time analyzer, T. J. Boland and J. B. Thompson for initial phasing developments, R. B. Kennedy for electronic development and continuing maintenance and operation of the velocity selector, K. A. Strong for his assistance with the experiments, C. J. Slayden for many contributions to the programming and IBM computations, Dr. R. E. Schmunk for contributions to the physics development particularly the beryllium data, and Drs. P. D. Randolph and C. Coombes for physics developments, particularly the gas data. We wish to thank Dr. R. G. Fluharty for his continued interest and valuable counsel.

† *Note added in proof.* This oscillator has been installed. The phase jitter of $\pm$ 8 μsec mentioned in Section 3.2 is now $\pm$ 2 μsec. Use of a newly installed feed back system further surpresses the phase jitter to $\pm$ 1 μsec.

Additions to the reference or more accessable references have been called to our attention: Ref.[1]) P. A. Egelstaff, "The Measurement of the Scattering Law for a Moderator", AERE R/3593 (Available from H.M. Stationary Office). Ref.[26]) P. A. Egelstaff, "The Treatment of Thermal Neutron Scattering Law Data", AERE R/3622. (Available from H. M. Stationary Office).

NUCLEAR INSTRUMENTS AND METHODS 12 (1961) 103–110; NORTH-HOLLAND PUBLISHING CO.

THE DESIGN OF BUNCHING MAGNETS†

R. E. HOLLAND

Argonne National Laboratory, Argonne, Illinois

Received 17 February 1961

The design of a bunching magnet of the type suggested by Mobley and Van de Graaff has been investigated. A relationship between the magnetic flux and the difference in length of the extreme paths is presented. The properties of a uniform-field sector magnet with fringing-field focusing were investigated in detail. It was found that the divergence of the initial beam from an electrostatic accelerator could be expected to limit the maximum attainable bunching ratio (ratio of input acceptance time to output pulse width) when sinusoidal deflection is used. A slightly more complex deflection system increased the maximum attainable bunching ratio.

1. Introduction

The measurement of neutron velocity by time-of-flight has proved to be a good method of obtaining fast-neutron spectra. A related technique has been used to measure the lifetimes of short-lived nuclear states. In most cases, it is advantageous to use a pulsed beam; and where an electrostatic accelerator is used, a number of methods have been developed to accomplish this. A scheme proposed several years ago by R. C. Mobley[1]) and by R. J. Van de Graaff has some advantages, and is the subject of the present discussion.

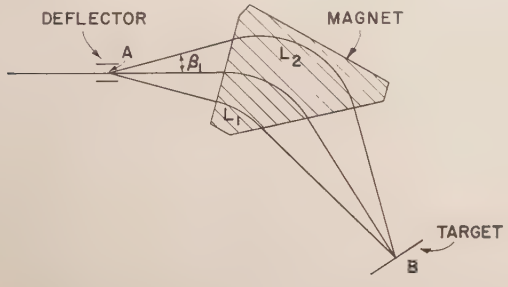

Fig. 1. Schematic representation of system for obtaining intensified pulses from a continuous beam of particles.

The principle involved is illustrated in fig. 1. Suppose the incident beam is swept across the face of the magnet in such a manner that the longest path through the magnet is taken by the first particle leaving the deflector. At later times, the particles are deflected to paths appropriate to their departure. Now if these things are arranged properly, all particles will arrive at the image point in a short pulse. Generally, it will not be convenient to match the sweep rate to the magnet exactly, and there will also be variations in velocity, direction, and position of the particles in the beam which will prevent an arbitrarily short pulse.

Except in some very special cases, it is desirable in neutron experiments that in addition (1) the beam should be focused to a small spot on the target, and (2) the angular divergence of the beam arriving at the target should be small. For the measurement of lifetimes these restrictions can be relaxed somewhat. Equations relating the energy spread and beam divergence, which are introduced by the buncher, to the output pulse width have been discussed by Fowler and Good[2]).

One of the important parameters of the scheme described above is the difference in lengths of the extreme paths in fig. 1. Let this difference be $(L_2 - L_1)$. Then the time interval over which particles can be accepted for bunching (acceptance time) is $(L_2 - L_1)/v$, where v is the velocity of the particles.

A relationship exists between $(L_2 - L_1)$ and the magnetic flux of the magnet. Consider the two paths L_1 and L_2, which are the members of a

† Work performed under the auspices of the U.S. Atomic Energy Commission.

[1]) R. C. Mobley, Phys. Rev. **88** (1952) 360.

[2]) T. K. Fowler and W. M. Good ,Nucl. Instr. and Meth. **7** (1960) 245.

continuous family of paths passing through the points A and B. From the principle of least action[3]), it follows that

$$\Phi = (L_2 - L_1)\frac{q}{c}mv = (L_2 - L_1)H\rho \qquad (1)$$

so that

$$L_2 - L_1 = \frac{\Phi}{H\rho},$$

where q is the charge on the particle, mv is the momentum of the particle, ρ is the radius of curvature of the path in the magnetic field H, Φ is the total magnetic flux enclosed between L_1 and L_2, and c is the velocity of light. The magnetic lens considered in this paper satisfies the condition that all intermediate paths pass through points A and B only in the paraxial approximation. Estimation of the deviation from eq. (1) for typical cases shows that it is less than a few per cent. For the case of uniform field, this relation becomes

$$L_2 - L_1 = \frac{A}{\rho}, \qquad (2)$$

where A is the area bounded by the two paths and the faces of the magnet.

These relationship are quite general and hold for any shape of magnetic field or any variation of magnetic field. Since for a given total magnetic flux, the difference in length of the extreme paths is determined, the input acceptance time given by

$$\Delta t = \frac{L_2 - L_1}{v}$$

is also determined by the total flux, independent of the shape of the magnet or variations in the magnetic field. These relationships are very useful in estimating the performance of a system.

2. Expansion of the Path Length in Terms of Deflection Angle

In this section we shall develop the behavior of a magnetic system such as that shown in fig. 2, without specifying in detail the magnetic field. In order to see how well the magnet "focuses in time", it is convenient to express the path length L in terms of the deflection angle β_1 (the angle between the ray and the median ray L_0) by the expansion

$$L = L_0 + \alpha_1\beta_1 + \alpha_2\beta_1^2 + \alpha_3\beta_1^3 + \ldots, \qquad (3)$$

where L_0 is the length of the path with no deflector voltage and α_1, α_2, α_3, ... are coefficients which can be obtained geometrically, as will be shown in Sec 3. Let us assume a sinusoidal sweep of the form

$$\beta_1 = -\beta_0 \sin \omega t\,. \qquad (4)$$

Notice that eq. (4) defines the zero of time as that time at which the particle taking the path L_0 leaves the object point.

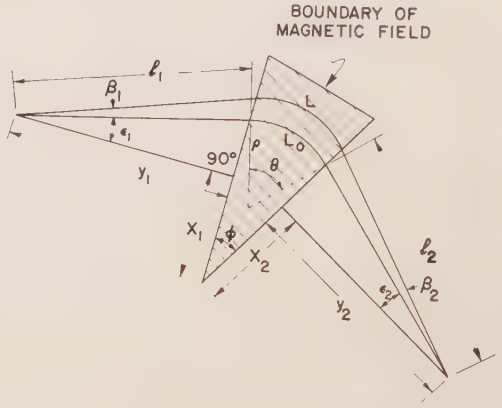

Fig. 2. Schematic representation of symmetric magnet. This diagram defines the notation used in the text.

A particle which left the object point at time t will arrive at the image plane at a time $t + L/v$. We wish to express the variation of arrival time with respect to the arrival of a particle traveling along the median ray of length L_0. For this reason we define an arrival time by

$$t_a = t + \frac{L - L_0}{v}. \qquad (5)$$

Now expand $\sin \omega t$ in (4) in a Taylor series and substitute (3) and (4) in (5) to get

$$t_a = \left(1 - \frac{\alpha_1}{v}\beta_0\omega\right)t + \alpha_2\beta_0^2\frac{\omega^2}{v}t^2 + \left(\frac{\alpha_1}{6} - \alpha_3\beta_0^2\right)\beta_0\frac{\omega^3}{v}t^3 + \ldots \qquad (6)$$

We can express our results in a way that eliminates the explicit dependence on velocity. This is desirable because the buncher can be made to operate over a range of velocities (energies) by varying

[3]) P. A. Sturrock, Static and Dynamic Electron Optics (Cambridge University Press, Cambridge, England, 1955) p. 29.

the magnetic field and one can see that the same formula describes the behavior of the system for all velocities. To do this we define a characteristic time, $\tau_0 = \alpha_1/v$, and then use the dimensionless parameters

$$\bar{t} = t/\tau_0 ,$$

$$\bar{t}_a = t_a/\tau_0$$

$$\bar{\omega} = \omega\tau_0 .$$

By use of these, eq. (5) can be rewritten as

$$\bar{t}_a = \bar{t} + \frac{L - L_0}{\alpha_1} \tag{7}$$

and eq. (6) as

$$\bar{t}_a = (1 - \beta_0\bar{\omega})\,\bar{t} + \frac{\alpha_2}{\alpha_1}\beta_0{}^2\bar{\omega}^2\bar{t}^2 + \left(\frac{1}{6} - \frac{\alpha_3}{\alpha_1}\beta_0{}^2\right)\beta_0\bar{\omega}^3\bar{t}^3 + \ldots \tag{8}$$

The ideal situation would be for $\bar{t}_a$ to be constant for all values of $\bar{t}$. This can be even approximately true only for $\bar{t}$ small. By demanding that the coefficient of the first term in (8) be zero, we find that the amplitude of deflection must satisfy the condition

$$\beta_0 = \frac{1}{\bar{\omega}} . \tag{9}$$

With eq. (9) satisfied, eq. (4) becomes

$$\beta_1 = -\frac{1}{\bar{\omega}} \sin \bar{\omega}\,\bar{t} \approx -\bar{t} ,$$

so $\bar{t}$ is approximately the deflection angle.

In this scheme nothing can be done about the second term of (8), but the coefficient of the third term can be made to vanish by choosing the frequency so that

$$\bar{\omega}^2 = 6\,\frac{\alpha_3}{\alpha_1} . \tag{10}$$

This possibility is not of much importance since the second term is largest over the usable range of values of $\bar{t}$.

The principal result of this section is eq. (7) which shows that the behavior of the system can be expressed without explicity mentioning the velocity and eq. (8) which gives a power series expansion in terms of parameters which depend on the magnetic field configuration.

3. Computations for a Magnet with a Uniform Field

In order to develop further the properties of the bunching system, we must specify the magnetic field in more detail. We have chosen the arrangement that appeared the easiest to attain in practice and whose performance seemed simplest to compute. The system, as shown in fig. 2, consists of a sector magnet with uniform field. Focusing in the z direction (normal to the plane of the figure) is obtained by the action of the fringing field. We shall consider only the case in which the object, image, and magnet are symmetric with respect to a plane bisecting the magnet. In fig. 2, the path marked L_0 is the path taken by the beam when the deflector voltage is zero. Other paths, specified by the angle β_1, have lengths L given by eq. (3). Once the deflection angle θ is given, all other parameters are given by the condition of symmetry and by the condition that the system be double focusing.

The difference between the length of a path specified by the angle β_1 and that of the central path L_0 is

$$L(\beta_1) - L(0) = \beta_1\rho + y_1 \sec(\varepsilon_1 + \beta_1) - y_1 \sec\varepsilon_1 + \beta_2\rho + y_2 \sec(\varepsilon_2 + \beta_2) - y_2 \sec\varepsilon_2 , \tag{11}$$

where ε_1, ε_2, β_2, y_1, and y_2 are defined in fig. 2. In the Appendix, we show that for this symmetric case

$$\varepsilon_1 = \arctan(\tfrac{1}{2}\tan\tfrac{1}{2}\theta) = \varepsilon_2 . \tag{12}$$

$$\beta_2 = \arcsin\{[\,x_1 + y_1\tan(\varepsilon_1 + \beta_1)\,](\sin\phi)/\rho - \sin(\phi + \varepsilon_1 + \beta_1)\} - \varepsilon_1 , \tag{13}$$

$$x_1 = \frac{\sin\varepsilon_2 + \sin(\phi + \varepsilon_1)}{\sin\phi}\rho - y_1\tan\varepsilon_1 , \tag{14}$$

and

$$y_1 = 2\rho\cot\tfrac{1}{2}\theta\cot\varepsilon = y_2 . \tag{15}$$

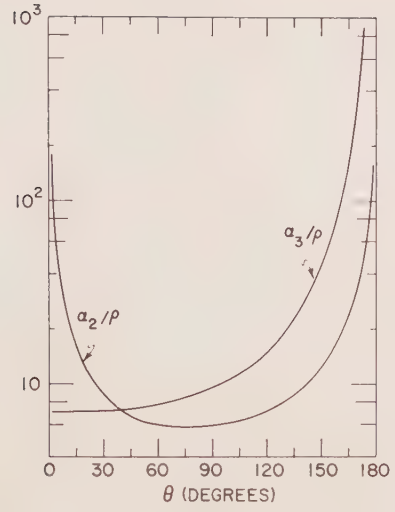

Fig. 3.

Fig. 3. A graph of the variation of the coefficients α_2/ρ and α_3/ρ used in the expansion of path length $L = L_0 + \alpha_1\beta_1 + \alpha_2\beta_1^2 + \alpha_3 B_1^3 + \ldots$ Best results are obtained when α_2 and α_3 are small.

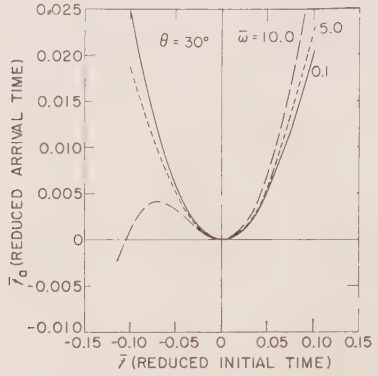

Fig. 4. Reduced arrival time $\bar{t}_a$ versus reduced initial time $\bar{t}$, for $\theta = 30°$ at a number of reduced frequencies $\bar{\omega}$.

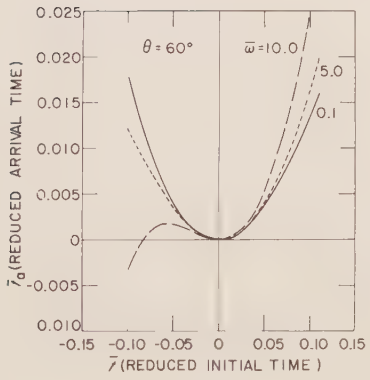

Fig. 5.
Reduced arrival time $\bar{t}_a$ versus reduced initial time $\bar{t}$, for $\theta = 60°$.

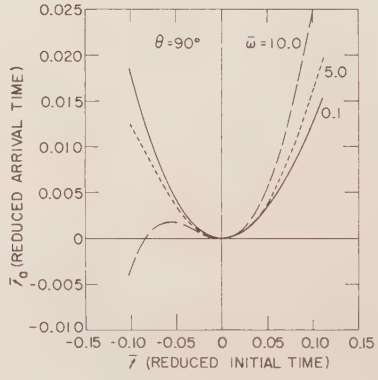

Fig. 6.
Reduced arrival time $\bar{t}_a$ versus reduced initial time $\bar{t}$, for $\theta = 90°$.

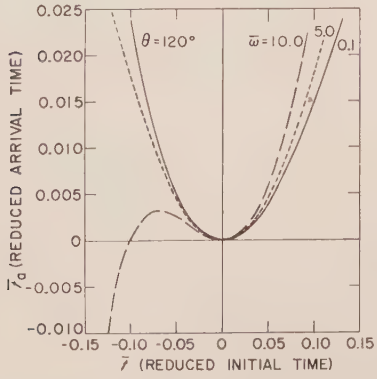

Fig. 7.
Reduced arrival time $\bar{t}_a$ versus reduced initial time $\bar{t}$, for $\theta = 120°$.

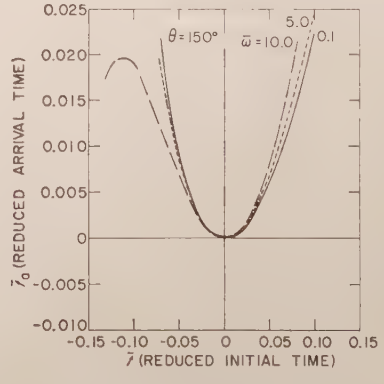

Fig. 8.
Reduced arrival time $\bar{t}_a$ versus reduced initial time $\bar{t}$, for $\theta = 150°$.

We can now explicity evaluate the coefficients α_1, α_2, and α_3 introduced in Sec. 2. We find

$$\alpha_1 = 4\rho\,, \tag{16}$$

$$\alpha_2 = \left[3\tan\varepsilon + 2\frac{\sin\phi}{\cos^2\varepsilon} + \frac{\sin(\phi+\varepsilon)}{\cos\varepsilon} + \cot\varepsilon \right]\rho\,, \tag{17}$$

$$\alpha_3 = \left[\frac{2\sin^2\varepsilon - 1}{3\cos^2\varepsilon} + \frac{\sin\varepsilon}{\cos^2\varepsilon}\left(2\frac{\sin\phi}{\cos\varepsilon} + \sin(\phi+\varepsilon)\right) + 2\frac{\sin\varepsilon\sin\phi}{\cos^2\varepsilon} + \frac{2}{3}\frac{\sin\phi}{\sin\varepsilon\cos\varepsilon} + \frac{1}{3}\frac{\cos(\phi+\varepsilon)}{\cos^3\varepsilon} \right.$$

$$\left. + (\tan\varepsilon + \tfrac{1}{2}\cot\varepsilon)\left(\tan\varepsilon + 2\frac{\sin\phi}{\cos^2\varepsilon} + \frac{\sin\phi+\varepsilon}{\cos\varepsilon}\right) + 2\tan^2\varepsilon + \tfrac{5}{3}\right]\rho\,. \tag{18}$$

The quantities α_2/ρ and α_3/ρ are plotted in fig. 3 as functions of θ.

Although eq. (7) can be evaluated approximately by use of α_1. α_2, and α_3, we evaluated it exactly by use of eq. (4) for β_1 with $\beta_0 = 1/\bar{\omega}$. The results of these computations are shown in figs. 4, 5, 6, 7, and 8 for $\theta = 30°$, 60°, 90°, 120°, and 150° for a range of values of $\bar{\omega}$. For $\bar{\omega}$ less than about 2.0, $\bar{t}_a$ is not influenced by the value of $\bar{\omega}$. At higher values of $\bar{\omega}$ (that is, at higher repetition rates) the spread in output time is increased. From these curves, as would be expected from the behavior of α_2, and α_3 shown in fig. 3, the best value of θ appears to lie between 60° and 90°.

4. Correction for Higher Orders

In principle one could make the variation in $\bar{t}_a$ arbitrarily small by including in the deflection voltage harmonic terms of the proper phase and amplitude. This, however, seems quite difficult to accomplish experimentally. We have considered a first approach to this in the following manner. If one applied to the deflection plates a dc bias in addition to the rf voltage, then the deflection angle will be

$$\beta = \beta_0\,[\,\sin\delta - \sin(\bar{\omega}\,\bar{t} + \delta)\,]\,, \tag{19}$$

where $(\beta_0 \sin\delta)$ is the deflection with no rf voltage applied. This introduces a quadratic term in $\bar{t}$, which can be made to cancel the term already present in $\bar{t}_a$. When eq. (19) is used instead of (4), eq. (7) is replaced by

$$\bar{t}_a = (1 - \beta_0\,\bar{\omega}\cos\delta)\,\bar{t} + \left(\tfrac{1}{2}\sin\delta + \frac{\alpha_2}{\alpha_1}\beta_0\cos^2\delta\right)\beta_0\,\bar{\omega}^2\,\bar{t}^2$$

$$+ \left(\tfrac{1}{6}\cos\delta - \frac{\alpha_3}{\alpha_1}\beta_0^2\cos^3\delta - \frac{\alpha_2}{\alpha_1}\beta_0\sin\delta\cos\delta\right)\beta_0\,\bar{\omega}^3\,\bar{t}^3 + \ldots \tag{20}$$

Now the vanishing of the first coefficient leads to

$$\beta_0 = \frac{1}{\bar{\omega}\cos\delta}\,. \tag{21}$$

Demanding that the coefficient of the second term vanish yields

$$\tan\delta = -2\frac{\alpha_2}{\alpha_1}\frac{1}{\bar{\omega}}\,. \tag{22}$$

The third term would vanish if

$$\bar{\omega}^2 = 6\left[\frac{\alpha_3}{\alpha_1} - 2\left(\frac{\alpha_2}{\alpha_1}\right)^2\right], \tag{23}$$

but, in the special cases we have investigated, no real value of $\bar{\omega}$ could be found to satisfy this condition.

Computations of

$$\bar{t}_a = \bar{t} + \frac{\Delta L(\beta_1)}{\alpha_1}$$

were made for 90° with eqs. (21) and (22) satisfied. The results are given in fig. 9.

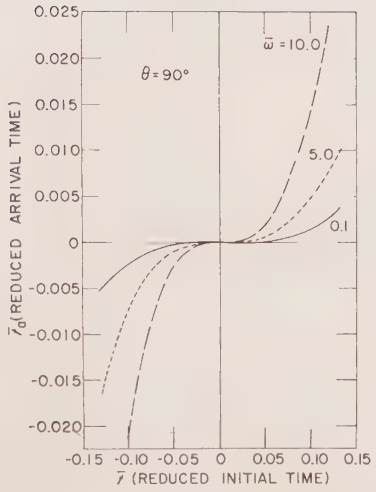

Fig. 9. Reduced arrival time $\bar{t}_a$ versus reduced initial time $\bar{t}$, for $\theta = 90°$ and for 3 different values of δ chosen to satisfy eq. (22).

5. Effects that Limit Bunching

Thus far the calculations have taken into account only the nonlinearity of the sinusoidal sweep voltage and the nonlinearity of the relationship between deflection angle β_1 and path length L. Inspection of figs. 3 to 8 would indicate that by making the range of $\bar{t}$ (and therefore the range of β_1) small enough, the range of arrival times can be made arbitrarily small. However, several factors which limit the smallness of the output pulse have not been taken into account. It is these we wish to discuss now.

One such effect is due to the finite size of the beam. We have not developed a detailed analysis of this, but one can easily estimate the difference between L_0 and the path length of a ray L' initially parallel to L_0 and separated from it by a distance d, as shown in fig. 10. We calculate the area enclosed by L' and L_0 as $\theta\rho d$, so from eq. (2), we find

$$\Delta L \approx \theta\, d\,,$$

where θ is as usual the angle of deflection. For θ near $\frac{1}{2}\pi$, $d = 0.3$ cm, and $v^{-1} = 36$ mμsec/m (4-MeV protons), the difference in arrival times of two extreme particles will be 0.1 mμsec. This is small enough to be of no concern for the systems we are contemplating.

A second source of broadening of the output pulse arises from energy variations within the beam of particles. For a beam from an electrostatic accelerator, one may expect variations in energy of the order of 0.1%. This corresponds to a variation in velocity of 0.05%. In a system in which the length L_0 is 3 m, and again with $v^{-1} = 36$ mμsec/m, the variation in arrival time because of variation in transit time will be of order of 0.05 mμsec. This again is negligible from our point of view.

A third and more serious limitation arises because the paths of particles comprising the beam are not parallel but at any instant diverge with a full angle typically of the order of 0.005 rad. This produces a spread in arrival times. For small deflection angles, this effect dominates, while at large deflection angles, the nonlinearities discussed in Sec. 4 dominate.

We define a quantity K called the bunching factor which is the ratio of initial acceptance time to spread of arrival times. We can estimate K in the following way. Assume that the beam diverges from the object point of the magnet with divergence only in the median plane of the magnet and with uniform current in all angles up to some maximum angle γ from the median ray L_0. By eq. (7), the resulting spread in arrival time will be

$$\frac{2\Delta L(\gamma)}{\alpha_1} \approx 2\gamma\,.$$

The total spread in arrival time will be $\Delta\bar{t}_a + 2\gamma$, so that

$$K = \frac{\Delta\bar{t}}{\Delta\bar{t}_a + 2\gamma}\,,$$

where $\Delta\bar{t}$ is the spread in the starting time $\bar{t}$ and $\Delta\bar{t}_a$ is the corresponding spread in arrival time. We

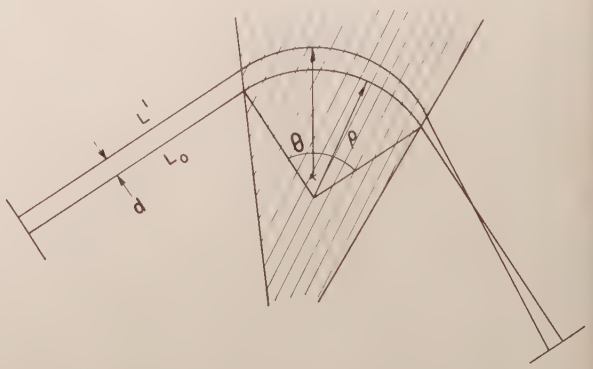

Fig. 10. Diagram which illustrates the estimation of the time spread introduced by the finite size of the beam.

now may estimate K from the curves in figs. 4 through 8. If we assume $\gamma = 0.0025$, then the behavior in a typical case is shown in fig. 11 for $\theta = 90°$, $\delta = 0$, and $\omega = 0.1$. Here the maximum value of K is about 15.

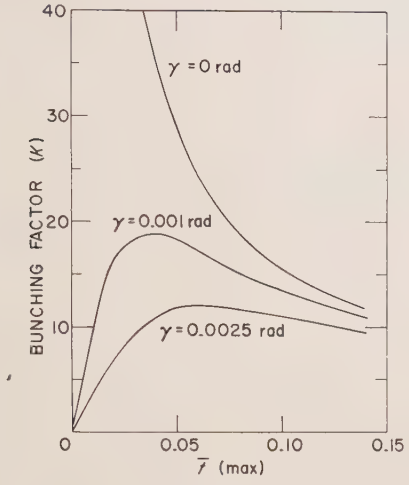

Fig. 11. Plot of bunching ratio K versus reduced acceptance time $\bar{t}_c$, for various values of beam divergence γ.

This estimate may overemphasize the effect of beam divergence. A more realistic approach would assume beam divergence in two directions with Gaussian distribution to calculate the root-mean-square spread in arrival times.

6. Summary

We have investigated the response of a simple bunching system in which the deflection voltage is sinusoidal, the magnet has a uniform field, and the focusing effect of the fringing field is used to produce a two-dimensional focus. The width of the output pulse cannot be made arbitrarily small because of nonlinearity of the relations between deflection voltage and time and between path length and deflection angle and because of spreads of the beam in space, in energy, and in angle.

To illustrate our discussion we have presented in table 1 a design based on the above discussion. This design accepts a 10-mμsec portion of the beam and bunches it to less than 1 mμsec. One should not

Table 1
Design parameters for bunching magnet that will accept a 4-MeV proton beam for 10 mμsec.

	Parameter	Symbol	Value
Beam	Energy		4 MeV
	Inverse velocity	$1/v$	36 mμsec/m
	Divergence (half angle)	γ	0.0025 rad
Magnet	Deflection of median ray	θ	90°
	Radius	ρ	50 cm
	Maximum input deflection accpeted	β_c	0.070 rad
	Magnetic field	B	5780 gauss
	Area of pole face	$A = 2t_c v \rho$	1390 cm^2
Deflector	Rf angular frequency	ω	60×10^6 rad/sec
	Maximum rf deflection	$\beta_0 = 1/\bar{\omega}$	0.231 rad
	Rf voltage†		31 000 V peak
Other parameters	Characteristic time	$\tau_0 = \alpha_1/v$	72 mμsec
	Reduced frequency	$\bar{\omega} = \omega\tau_0$	4.32
	Reduced acceptance time	$\bar{t}_c = t_c/\tau_0$	0.070
	Spread in reduced arrival time	$\Delta\bar{t}_a = \Delta t_a/\tau_0$	0.0077
	Bunching ratio	K	11
	Actual acceptance time	$2t_c$	10 mμsec
	Actual pulse width out	t_a	0.91 mμsec

† Computed on the assumption that the deflector plates have a length of 30 cm and a separation of 0.5 cm.

conclude from this that a magnet can be constructed to reduce the width of a pulse from 1 mμsec to 0.1 mμsec, since the factors involving beam energy spread and beam size have not been taken into account.

Recently a pulse-forming magnet of the type discussed in this paper has been built by High Voltage Engineering Company as part of a system for obtaining a high intensity pulsed beam[4]) at Case Institute of Technology. The magnet design was similar to that discussed in Sec. 3 and outlined in table 1. The bunching obtained was approximately that which we calculated. These workers have pointed one effect which we have not considered and which contributes appreciably to the width of the output pulse. This has been called the "linear-accelerator" effect, and comes about because the transit time of beam particles through the deflector plates is long enough so that voltage of the plates changes appreciably while the particles are between the plates. This induces an energy change in the beam which in turn varies the transit time between deflector and target and thus broadens the pulse.

Appendix

We wish to evaluate the parameters ε_1, ε_2, β_2, x_1, y_1, y_2 used in Sec. 3. Referring to fig. 2, we note that when the deflection angle θ has been given, all the parameters are fixed by the condition of symmetry ($l_1 = l_2$, $\varepsilon_1 = \varepsilon_2$) and by the condition that the system be double focusing. The conditions for double focusing have been put in convenient form by Cross[5]). He showed that to obtain focusing we must have

$$\tan \varepsilon_2 = \tfrac{1}{2}\left[\tan(\theta - \psi) + \frac{1}{\theta - \cot \eta} \right],$$

$$\frac{\rho}{l_2} = \tfrac{1}{2}\left[\tan(\theta - \psi) - \frac{1}{\theta - \cot \eta} \right],$$

where

$$\tan \psi = \frac{\rho}{l_1} + \tan \varepsilon_1 ,$$

$$\tan \eta = -\frac{\rho}{l_1} + \tan \varepsilon_1 .$$

For the symmetric case, in which $l_1 = l_2$ and $\varepsilon_1 = \varepsilon_2$, we obtain

$$\tan \varepsilon_1 = \tfrac{1}{2} \tan \tfrac{1}{2}\theta$$

$$\frac{l_1}{\rho} = \cot \varepsilon_1 .$$

We turn next to the evaluation of β_2. In the paraxial approximation $\beta_2 = \beta_1$. An accurate expression for β_2 can be obtained by rearranging an expression introduced by Geerk and Heinz[6]). They show that for a sector magnet with a uniform field

$$\sin(\varepsilon_2 + \beta_2) = [\, x_1 + y_1 \tan(\varepsilon_1 + \beta_1) \,] (\sin \phi)/\rho - \sin(\phi + \varepsilon_1 + \beta_1) ,$$

so that

$$\beta_2 = \arcsin \{ [\, x_1 + y_1 \tan(\varepsilon_1 + \beta_1) \,] (\sin \phi)/\rho - \sin(\phi + \varepsilon_1 + \beta_1) \} - \varepsilon_2 .$$

We further require that $\beta_2 = 0$ when $\beta_1 = 0$ (that is, that β_1 and β_2 are measured from L_0), so that we obtain

$$\sin \varepsilon_2 = (x_1 + y_1 \tan \varepsilon_1) (\sin \phi)/\rho - \sin(\phi + \varepsilon_1)$$

$$x_1 = \rho [\, \sin \varepsilon_2 + \sin(\phi + \varepsilon_1) \,]/\sin \phi - y_1 \tan \varepsilon_1 ,$$

which defines x_1 in terms of y_1, From fig. 2, y_1 is given by

$$y_1 = l_1 \cos \varepsilon_1 = 2\rho \cot \tfrac{1}{2}\theta \cos \varepsilon_1 .$$

We now have all parameters used in Sec. 3.

[4]) L. Cranberg, Bull. Am. Phys. Soc. **6** (1961) 9.
[5]) W. G. Cross, Rev. Sci. Instr. **22** (1951) 717.
[6]) J. Geerk and C. Heintz, Z. Phys. **133** (1952) 513, English translation AEC-tr-1890.

UCLEAR INSTRUMENTS AND METHODS 12 (1961) 111–114; NORTH-HOLLAND PUBLISHING CO.

ALPHA PARTICLE THICKNESS GAUGE USING A SOLID STATE DETECTOR

HERBERT L. ANDERSON

The Enrico Fermi Institute for Nuclear Studies, The University of Chicago, Chicago 37, Illinois

Received 7 March 1961

n alpha particle thickness gauge is described in which the nift in energy of α-particles in passing through the material is bserved directly by means of a solid state detector and pulse eight analyzer. Measurements of the thickness of 1 mg/cm² foils can be made easily to better than 1 %. The arrangement is useful for absolute energy loss measurements and some results are given for mylar.

. Introduction

Alpha particles have been used previously in the neasurement of the thickness of thin layers and lms. In general, the thickness is determined by omparing the absorption of alpha particles in the naterial in question with some standard substance, sually air. The method works best near the end of he range of the alpha particles, since it is here that hange in intensity with thickness is greatest. A ypical arrangement in the recent literature[1]) has he detector in a fixed position while the alpha mitter is mounted on a micrometer screw. With ir between the source and the detector and the istance near the range of the alpha particles, intro- uction of a thin foil reduces the counting rate. his can be compensated for by advancing the nicrometer screw. The thickness in terms of an "air quivalent" is obtained by direct reading of the nicrometer screw. A variant of this[2]) keeps the ource-to-detector distance fixed and reduces the ressure of the air to compensate for the effect f introducing the foil. By using a fixed geo- netry the effect of changing the solid angle of ne source subtended by the detector is avoided nd a sharper cutoff at the end of the range is btained.

Any method which observes the alpha particles ear the end of their range is inevitably limited in recision by the straggling which blurs the harpness of the cutoff. In this paper we describe an lternative method in which the thickness is etermined by observing directly the loss of energy ffered by the alpha particles in traversing the material in question. The measurements can be made rapidly and easily and the result registered electronically using a solid state detector and a pulse height analyzer as described below.

2. Solid State Detectors

Recent developments[3–12]) in solid state detectors have made the measurement of alpha particle energies relatively simple. These devices give a pulse whose height is linearly dependent on energy and whose resolving power can be made superior to other detectors in the same class (ionization chambers, proportional counters, scintillation coun-

[1]) K. Ramavataram and D. I. Porat, Nucl. Instr. and Meth. **4** (1959) 239.

[2]) M. de Croës, W. Parker and K. Sevier, Jr., Nucl. Instr. and Meth. **7** (1960) 160.

[3]) The following references [4–12]) are representative of early as well as recent work in solid state detectors. Additional references may be found by consulting these papers.

[4]) K. G. McKay, Phys. Rev. **76** (1949) 1537; **84** (1951) 829.

[5]) J. Mayer and B. Gossick, Rev. Sci. Instr. **27** (1956) 407.

[6]) J. M. McKenzie and D. A. Branley, Phys. Rev. Letters **2** (1959) 303.

[7]) F. J. Walter, J. W. T. Dabbs and L. D. Roberts, Bull. Am. Phys. Soc., Series II, **3** (1958) 181; **3** (1958) 304; **5** (1960) 38; **5** (1960) 22.

[8]) J. L. Blankensip and C. J. Borkowski, Proceedings of the Seventh Scintillation Counter Symposium, IRE Transactions on Nuclear Science (1960) 190.

[9]) S. S. Friedland, J. W. Mayer and J. A. Wiggins, Nucleonics **18** (1960) 54.

[10]) G. L. Miller, W. L. Brown, P. F. Donavan and J. M, Mackintosh, Proc. Seventh Scintillation Counter Symposium, IRE Transactions on Nuclear Science (1960) 185.

[11]) M. L. Halbert and J. L. Blankenship, Nucl. Instr. and Meth. **8** (1960) 106.

[12]) G. Amsel, P. Baruch and O. Smulkowski, Nucl. Instr. and Meth. **8** (1960) 92.

ters). The surface barrier counter is the solid state analogue of the conventional ionization chamber in which the incident particles produce electron-hole pairs instead of electron-ion pairs. The higher resolving power, obtainable in principle in the solid state detector, is due to the larger number of electrons which a given particle can produce. The average energy to produce an electron-hole pair is 3.0 eV in Ge and 3.6 eV in Si. By comparison a typical value for the energy to produce an ion pair in a gas is 30 eV. In practice, the resolving power is limited by the noise in the detector and in its associated amplifier. Several workers[6,8]) have recently reported spectra of alpha emitters with a full width at half maximum less than 0.3% in carefully made detectors. By comparison, a recent paper[13]) dealing with the alpha spectra observed with scintillation counters gives 4.5% as the resolution with which the 5.3-MeV alpha line in Po^{210} was recorded using CsI(Tl).

3. Arrangement

As a practical demonstration of the idea of using a solid state detector to measure thickness by the energy loss method we used a Au-Si surface barrier counter of the type described by Halbert and Blankenship[11]). Our counter was prepared at the Laboratory of Applied Sciences of the University of Chicago[14]) and we are indebted to Dr. A. Tuzzolino for supplying us with one.

The arrangement used is shown in fig. 1. A Pu^{239} (5.147 MeV) alpha source was supported about 1 cm away from the solid state detector. Thin foils were mounted over a hole in a lucite slide which could be inserted between the source and detector. The geometry was defined by a 8.0 mm diameter hole over the detector at a distance of 8.8 mm from the α-source. The opening over the source was 4.8 mm in diameter. The perpendicular distance from source to detector was 9.5 mm. The whole arrangement was mounted so that it could be enclosed in a brass container and evacuated. The distance between source and detector was kept small so that thickness measurements could be made directly in air. This gave a good counting rate with a relatively weak source but had the disadvantage of producing a considerable broadening in the peak due to the oblique traversals of the foil.

The counter itself had a sensitive area 1 cm × 1 cm and was operated with a bias of 20 volts, more than sufficient to collect all the electrons from the alpha particles. It was connected to a low noise cascode amplifier which in turn fed a 400-channel pulse height analyzer[15]).

4. Results

Figure 2 reproduces the data obtained in 1 minute of counting in each case when 0, 1, 2 and 3 layers of thin mylar foil (0.00025″ nominal thickness) were inserted between source and detector.

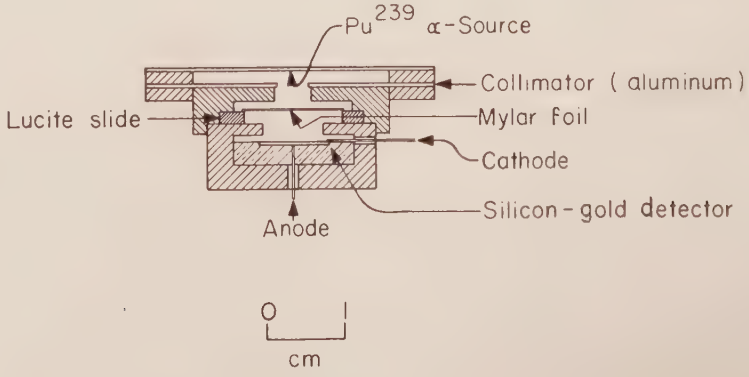

Fig. 1. Geometry for observing the energy loss by α-particles in thin foils using a solid state detector.

The mylar is quite uniform in thickness. The pieces used were all cut from a 100 cm^2 sheet which was

[13]) G. Bertolini, A. M. del Tusco and G. Restelli, Nucl. Instr. and Meth. 7 (1960) 350.

[14]) R. Takoko, M. Perkins, and A. Tuzzolino, Report of the Laboratory of Applied Sciences, University of Chicago (1960).

[15]) RIDL 34–12, Transistorized pulse height analyzer.

eighed and found to have a thickness of 0.905 g/cm². The bias setting on the analyzer suppressed the first 50 channels so that the 400 channels in the analyzer were used to record the pulse heights in channels 50 to 450, as shown in the figure. The linearity of the analyzer was checked with a calibrated pulse generator. The linearity of the response of silicon detectors of the type used here has demonstrated by Halbert and Blankenship[11]). of 1 channel produces a 10% change in the counting rate so that shifts of a fraction of a channel are readily detectable. In a practical test, the RMS error in the determination of the positions of this half intensity point in a series of 10-minute runs was 0.4 channels, equivalent to 0.6%.

From fig. 2 it can be seen that our detector had a resolution full width at half maximum of 1.7%. This was not a detriment in the present measure-

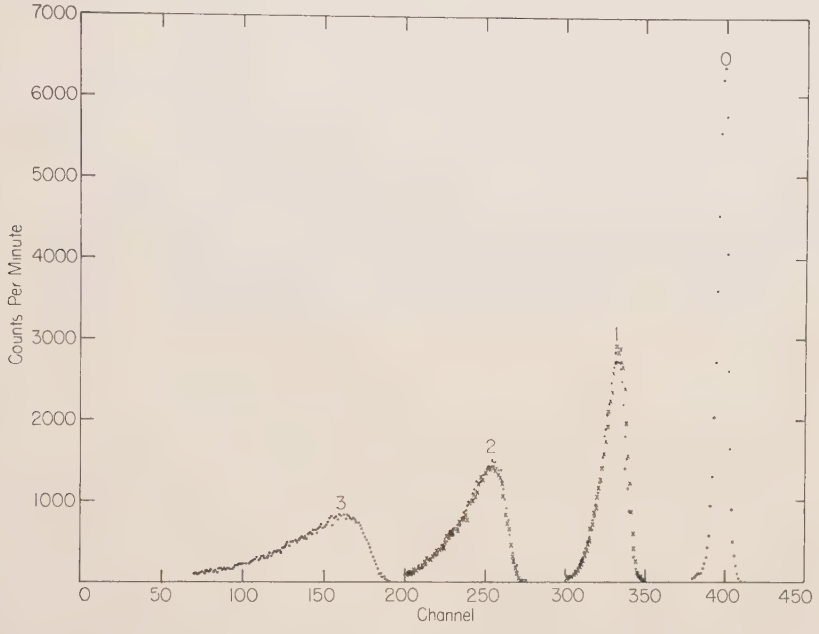

g. 2. Pulse height spectra obtained in vacuo with 0, 1, 2, and 3 layers of mylar 0.905 mg/cm² thick using a Pu^{230} α-source 147 MeV). Points labelled with × were obtained in air (1.054 mg/cm²) either without mylar (curve 1) or with 0.095 mg/cm² of mylar (curve 2).

The effect of adding foils is seen to shift the peak ownward. At the same time the pulse height stribution is noticeably broadened by the geo- etric effect mentioned above, to an extent that creases considerably with increasing foil thick- ss. The highest peak has its maximum at channel 9 and is due to the bare Pu^{239} α-source. The ad- tion of 1 mylar layer shifts the peak downward 68 channels. It is quite easy to determine the cation of the peak to within 1 channel in a 1- inute run with the source used. This reveals a ickness variation of 1.5%, or about 13 μg/cm² in e present case. A more sensitive indicator of the ickness is the half intensity point on the high ergy side of the peak. With a 1 mylar layer a shift ment of 1 mg/cm² foils because of the poor geometry used. For thinner foils the limit of sensitivity would appear to be about 1 μg/cm². A considerable improvement in sensitivity in the measurement of thinner foils, or with the present foils in better geometry, could be expected if the improved detectors (0.3% resolution) now available were employed.

Measurements were also carried out in air. By coincidence, the air at 746.4 mm Hg pressure and 40°C, reproduces almost exactly the distribution obtained with 1 layer of mylar. The measurements in air with zero or one layer of mylar are also shown in fig. 2. Thus, 0.905 mg/cm² of mylar is equivalent in stopping power to 1.054 mg/cm² of dry air.

The method lends itself to an absolute determination of the energy loss. The calibration depends on the knowledge of the energy of the α-source and the linearity of the system response. A small correction should be made for the gold coating (about 100 μg/cm^2) on the detector, which could give an energy loss of about 1.5 channels. Dividing 5.147

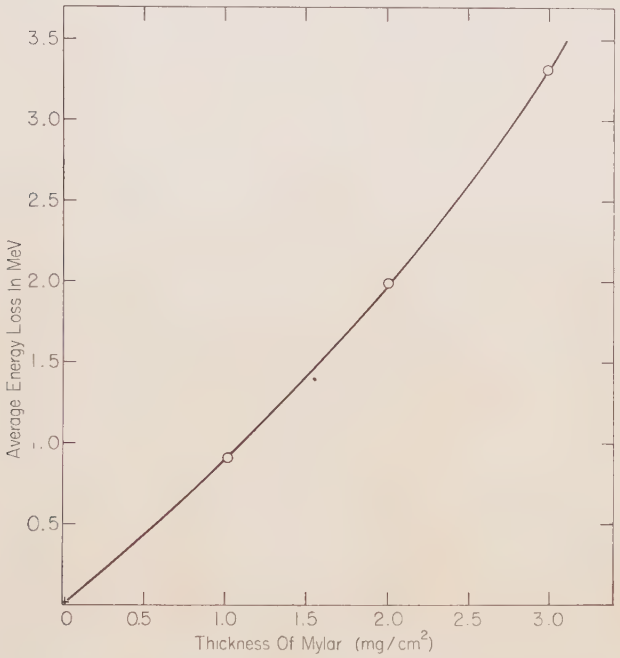

Fig. 3. Average energy loss of Pu^{239} α-particles (5.147 MeV) in mylar. Experimental points are compared with Brandt's[16] calculated values.

MeV by 400.5, we obtain 12.85 keV/channel as the calibration. The thickness of the Pu source, about 40 μg/cm^2, may be neglected for the present purposes. The stopping power of mylar may now be obtained by calculating the average energy loss from an integration over the pulse height distribution. The pertinent data from the 1-minute runs are collected in table 1. The results are shown plotted in fig. 3. Here the loss in energy in MeV is plotted as a function of thickness in mg/cm^2 of mylar. The effect of the gold coating on the detector is to shift the origin by 0.019 MeV and 0.018 mg/cm^2, as indicated in the plot by the cross. The obliquity increases the average thickness traversed by the α-particles by 9.7% over the values listed in column 2 of table 1.

The experimental points agree very well with the

TABLE 1

Summary of 1-minute measurements with various thicknesses of mylar in vacuo and in air

Layers of mylar	mg/cm^2	E_{max}	c/m at peak	$\frac{\Delta E}{E_{max}}$	$\bar{E}$
0	0	399	6396	0.017	397.6
1	0.905	331	2847	0.048	328.5
2	1.810	254	1460	0.118	244.3
3	2.715	159	839	0.340	141.1
0†	0	331	2939	0.047	329.4
1†	0.905	254	1509	0.118	244.1

† With 1.054 mg/cm^2 air.

Thickness of mylar is given in mg/cm^2. E_{max} is the channel at which the maximum count per minute occurs. The resolution full width at half maximum is $\Delta E/E_{max}$, while $\bar{E}$ is the average pulse height given in channels.

solid curve which was derived from the calculations of Brandt[16]), who has tabulated the stopping power of a number or organic materials for a variety of charged particles as a function of their energy. Moreover, the energy loss in air is within 1% of that given by Bethe[17]). The energy loss has already been tabulated for a wide variety of substances and it is a straightforward procedure to calculate this for any material whatever. Thus, our method, which provides an absolute measure of energy loss, can serve as an absolute measure of thickness, provided only that the chemical composition is known.

[16]) Werner Brandt, Research Report, Engineering Department, E. I. du Pont de Nemours and Company, Wilmington, Delaware (July 1960).

[17]) H. A. Bethe, Rev. Mod. Phys. **22** (1950) 213.

UCLEAR INSTRUMENTS AND METHODS 12 (1961) 115–123; NORTH-HOLLAND PUBLISHING CO.

INTRINSIC LINE BROADENING IN NaI(Tl) GAMMA-RAY SPECTROMETERS

C. D. ZERBY, A. MEYER and R. B. MURRAY

Oak Ridge National Laboratory†, Oak Ridge, Tennessee

Received 4 March 1961

evious experimental studies of the response of NaI(Tl) to mma rays have indicated that the pulse height is not strictly portional to the energy of the absorbed gamma. It is the rpose of this paper to point out that the nonproportional ponse to gammas implies a nonproportional response to ctrons, which results in an intrinsic broadening of the full-ergy peak in the pulse-height distribution from monoenergetic gamma rays. The magnitude of this effect is such that it sults in a significant contribution to the total line width for ntillation crystals of typical dimensions. The work reported re is based on Monte Carlo calculations using the nonproportional response of NaI(Tl) to electrons, an energy dependent function which was deduced from previous experimental work with gamma rays. Results of the calculations, applied to a 2.5-in. diameter by 2-in. high crystal, indicate a distinct broadening in the total absorption line in the case of Compton and pair-production events. The calculated fractional line width from this effect alone is negligible for energies below about 0.1 MeV and amounts to 2.6 % at 0.15 MeV, 5.0 % at 0.4 MeV, and 1.5 % at 2.5 MeV. The dependence of this effect on the crystal size and source geometry is discussed.

Introduction

In the use of NaI(Tl) scintillation crystals for mma-ray spectroscopy it is important to achieve minimum line width in the pulse-height spectrum sulting from monoenergetic gamma rays. Much tention has been devoted to the various factors ntributing to the line width of the full-energy ak; reviews of this subject are available elsehere[1–3]). To review briefly, the over-all line width n be considered as the sum of three contributions. he first is the statistical fluctuation in the production of photons in the scintillation crystal by the cident gamma ray. The second is the fluctuation the photon transfer. This includes escape of the otons from the scintillator, light collection in the ht guide, photoelectric conversion in the photothode and collection of the photoelectrons at the st dynode of the photomultiplier. The third contribution is the fluctuation in the multiplication of ctrons through the dynode string of the photoultiplier. Each of the above contributes to the oadening of the total absorption peak of the lse distribution resulting from an incident beam monoenergetic gamma rays.

It is the purpose of this paper to point out that the nonproportional response of NaI(Tl) to electrons gives rise to a further source of broadening of a gamma-ray line, and that the magnitude of this effect is such that it results in a significant contribution to the total line width for gamma-ray energies in the region of hundreds of kilovolts. This additional source of line broadening will be referred to here as *intrinsic broadening*.

It is appropriate to note at this point a distinction between the terms *linear* and *proportional* in connection with the relationship between pulse height L and gamma-ray energy E_γ. By *linear* response we mean $L = aE_\gamma + b$, with a and b constants, whereas a *proportional* response means $L = aE_\gamma$. The term *nonlinear response* has been somewhat loosely used in the past to denote a departure from a proportional response. The distinction is not a trivial one, however, as the intrinsic broadening effect discussed in this paper arises from any variation from a strictly proportional response; a response function which is linear (but nonproportional) would still result in an

Operated by Union Carbide Corporation for the U.S. omic Energy Commission.

[1]) W. E. Mott and R. B. Sutton, Handbuch der Physik **45**, edited by S. Flügge and E. Creutz (Springer-Verlag, Berlin, 1958) p. 86.

[2]) E. Breitenberger, Prog. Nucl. Phys. **4**, edited by O. R. Frisch (Pergamon Press, London, New York, 1955) p. 56.

[3]) G. T. Wright, J. Sci. Instr. **31** (1954) 377.

intrinsic broadening. The experimental response function is indeed found to be very nearly linear for gamma-rays energies above about 50 keV, but is nevertheless nonproportional.

Finally, we will refer in this paper to line width as $\Delta E/E$ where ΔE is the full width at half maximum of a peak occurring at pulse-height E.

ordinate is arbitrarily normalized to unity at 662 keV. The data points of fig. 1 are unpublished results of experiments at Argonne National Laboratory[6]). The three lowest-energy data points are to be considered as tentative pending further experiments. The solid and dashed curves of fig. 1 are calculated, as described below.

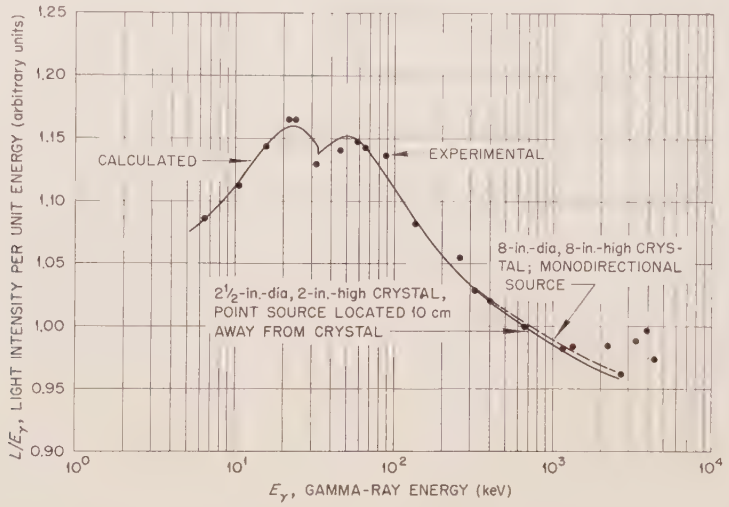

Fig. 1. Calculated and experimental values of the pulse-height response of NaI(Tl) crystals to totally absorbed gamma rays as a function of gamma-ray energy. Experimental data are taken from ref.[6]).

2. Scintillation Response of NaI(Tl) to Gamma Rays

The pulse-height versus energy relationship for the total absorption line of gamma rays on NaI(Tl) has been shown in numerous routine experiments, as indicated previously, to be a nearly linear function over a wide range of gamma-ray energies. A determination of the exact behavior of this relationship, however, requires very careful experimental methods, with special attention to the behavior of the electronic system used in recording pulse-height spectra. Detailed studies of this nature have been reported recently by Engelkemeir[4]) and by Managan[5]). Their results, based on different sets of experiments using basically different techniques, are in quite good agreement, and indicate a distinct nonproportionality in the pulse height versus energy relationship. This nonproportional behavior is most pronounced at energies below several hundred keV. An illustration of this nonproportionality is shown in fig. 1, in which the pulse height per unit energy, L/E_γ, is plotted versus E_γ. The

Attention may also be directed to the experiments of Peelle and Love[7]) who observed a nonproportional response of NaI(Tl) to gamma rays by yet another experimental method.

3. Scintillation Response of NaI(Tl) to Electrons

For the present discussion it is important to obtain the dependence of the response of NaI(Tl) on the initial energy of electrons which are stopped in the crystal. Although this dependence is not directly obtainable from experiments, it is possible to deduce the required data from the measured response to gamma rays.

For a given source of high-energy monoenergetic

[4]) D. Engelkemeir, Rev. Sci. Instr. **27** (1956) 589.

[5]) W. W. Managan, paper 5.10 of Proc. of the Sixth Tripartite Instr. Conf., AECL-805 (1959); See also: Applied Gamma-Ray Spectrometry, edited by C. E. Crouthamel (Pergamon Press, London, New York, 1960) Ch. 2.

[6]) Unpublished results of W. W. Managan, I. S. Sherman, S. I. Baker and A. J. MacKay, Argonne National Laboratory,

[7]) R. W. Peelle and T. A. Love, Rev. Sci. Instr. **31** (1960) 205.

gamma rays the multiplicity of interactions possible within the crystal can produce an energy spectrum of electrons which may vary considerably from one gamma ray to another. In the energy range below about 100 keV, however, gamma-ray interactions in sodium iodide are almost entirely due to the photoelectric effect and the scintillation response of the crystal can be attributed to primary photoelectrons and the subsequent electrons that ultimately appear as a result of filling the vacancy in the ionized atom. The uncomplicated nature of the response induced by low-energy gamma rays makes it relatively easy to use the experimentally observed low-energy gamma-ray data to calculate the response of the crystal to low-energy electrons, and will be discussed first.

In order to find the response induced by low-energy electrons, a model must be adopted to account for the transitions that take place as a result of a photoelectric event. For reasons of mathematical convenience the model adopted here represents a simplification of the actual physical processes following a photoelectric interaction. A more exact description of the electron spectrum following a photoelectric event is not required as the end result of the present calculation, i.e., the intrinsic line width, is rather insensitive to details of the electron spectrum in the low-energy region. The basic assumptions in the description of a photoelectric event are the following: (a) The iodine atom is assumed to possess three energy levels, with the K-shell binding energy = 33 keV, the L-shell binding energy = 5 keV, and the M-shell binding energy = 1 keV. (b) For gamma-ray energies above the K-shell binding energy photoelectric events are assumed to take place only through the K shell. This assumption is based on the fact that the photoelectric cross section for electrons in levels other than the K-shell amounts to less than 15% of the K-shell cross section at the K-edge energy, and decreases at higher photon energies[8]). Similarly, for gamma rays in the energy interval between the L-shell and K-shell binding energies photoelectric events are assumed to take place only through the L shell. (c) The contribution of sodium to the photoelectric process is neglected for gamma rays above 5 keV since its photoelectric cross section is very small compared with that of iodine[8]). Below 5 keV the cross sections are more nearly comparable, and photoelectric events may be considered in either the sodium K shell or the iodine M shell. The binding energies of both these shells are very nearly the same (about 1 keV) so that the electron spectrum from a photoelectric event in either atom is essentially the same, and no distinction need be made. (d) Photoelectron vacancies in the iodine K shell are assumed to be filled in all cases by an electron from the L shell with subsequent emission of a 28-keV K_α X-ray. The Auger effect is neglected since it accounts for only 14% of the transitions[9]). The K_β transitions are also neglected as they are weak compared to the K_α transitions (about 20%). Photoelectron vacancies in the iodine L shell are assumed to be filled in all cases by an Auger transition, as in this case the X-ray fluorescent yield accounts for only about 13% of the transitions[9]).

The electron spectrum resulting from photoelectric events may now be described in the following way. Incident gammas of energy $E_\gamma \leqslant 1$ keV are assumed to interact with a loosely bound electron to produce an electron of energy equal to that of the initial gamma ray. For gamma rays in the interval 1 keV $< E_\gamma \leqslant 5$ keV there results a photoelectron of energy ($E_\gamma - 1$ keV) plus a 1-keV Auger electron. For incident gamma rays in the interval 5 keV $< E_\gamma \leqslant 33$ keV a photoelectron of energy ($E_\gamma - 5$ keV) is produced leaving an L-shell vacancy which is filled by an Auger transition. The Auger electron is of energy 5 keV. For incident gammas of energy $E_\gamma > 33$ keV the resulting photoelectron is of energy ($E_\gamma - 33$ keV). The K-shell vacancy is filled by an L-shell electron resulting in a 28-keV X-ray and an L-shell vacancy. The 28-keV X-ray interacts as described above to produce an electron of energy 23 keV plus another L-shell vacancy. The two L-shell vacancies are filled by Auger transitions resulting in two 5-keV electrons.

[8]) C. M. Davisson, Beta- and Gamma-Ray Spectroscopy, edited by K. Siegbahn (North Holland Publishing Company, Amsterdam, 1955) Ch. II.

[9]) G. J. Nijgh, A. H. Wapstra and R. Van Lieshout, Nuclear Spectroscopy Tables (North Holland Publishing Company, Amsterdam, 1959).

Under these assumptions it is now possible to formulate a set of simultaneous equations of the form $L = \Sigma_i C_i E_i$ relating the pulse height L, observed upon gamma-ray excitation, to the energies E_i of the various electrons which result from a photoelectric event. The coefficients C_i which are sought in the solution represent the pulse height per unit energy for an electron of energy E_i. The experimental gamma-ray data are used to obtain L for various E_γ. This procedure is used to obtain the L/E_e curve up to 70 keV.

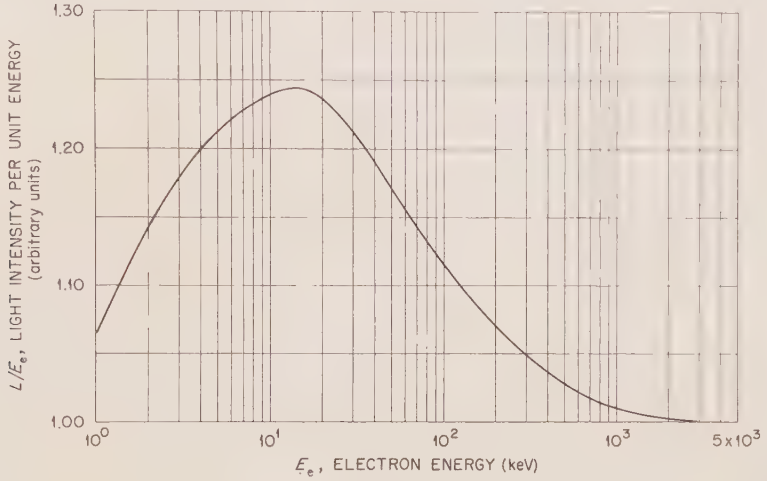

Fig. 2. Response of NaI(Tl) crystals to totally absorbed electrons as a function of electron energy. Curve is calculated on the basis of the experimental gamma-ray data as described in the text. The curve is arbitrarily normalized to unity at 3 MeV.

Since the experimental data do not fall on a perfectly smooth curve, and since the model of photoelectric interactions is particularly simple, the resulting values for L/E_e as a function of electron energy had a spread amounting to a maximum of 2.5% depending on whether they were derived from gamma-ray energies above or below the K edge. A smooth curve was constructed by averaging these data and is shown in fig. 2 for $1 \leqslant E_e \leqslant 70$ keV. For $E_e > 70$ keV, the curve was first drawn in an arbitrary fashion and then adjusted by calculations described below. The ordinate of the final L/E_e versus E_e curve was arbitrarily normalized to unity at 3 MeV.

4. Monte Carlo Calculations

For gamma-ray energies above approximately 100 keV, the analysis of the L/E_γ versus E_γ curve to deduce the response of NaI(Tl) to higher energy electrons is complicated by the variation in the spectrum of electrons ejected by different monoenergetic source photons. For this reason an existing Monte Carlo code[10]), which had been written to calculate the pulse-height response of NaI(Tl) to gamma rays, was altered to include the nonproportional response to electrons and was used in performing the analysis.

To determine the response to gamma rays in the Monte Carlo calculation, individual histories of the photons were generated and used first to determine the energies of the ejected electrons. In the case of a photoelectric event, the energies of the electrons were determined according to the model described above, whereas the energies of Compton electrons were determined directly from the kinematics of the scattering collisions made by the photons. In the case of pair production, however, the distribution of excess kinetic energy between the pair of electrons was not fixed and was made in a random way based on the energy spectrum given by the Born approximation.

Once the energies of all the electrons ejected in a given photon history were determined, the response

[10]) C. D. Zerby and H. S. Moran, "Calculations of the Pulse-Height Response of Gamma-Ray Scintillation Counters", to be published; This work is described briefly in ORNL-3016 (1960) 269.

of each electron was calculated with the aid of the assumed electron response curve, similar to fig. 2, and the accumulated light output from each photon history was calculated as the sum of the responses of all the electrons.

In the calculation the pulse-height response curve for gamma rays was first obtained in the form of a histogram and then recomputed to include the broadening resulting from the photomultiplier statistics. The full width at half maximum of the photomultiplier broadening was assumed to be given by $\Delta L = kL^{\frac{1}{2}}$ where L is the pulse height and k is a constant chosen according to typical experimental values. For the present purpose of calculating L/E_γ versus E_γ, the results are rather insensitive to the particular value of k. Accordingly, k was chosen such that $\Delta L/L$ amounts to 4% for the case of 662-keV gammas on NaI(Tl). After the photomultiplier statistics had been folded in, the pulse height corresponding to the maximum values of the total absorption peaks were plotted to give the L/E_γ versus E_γ curve.

The final electron response curve shown in fig. 2 was the result of an iterative procedure in which a trial function, L/E_e versus E_e, was first introduced into the Monte Carlo code. (The low-energy region of the trial function was, of course, that given by the preceding calculation.) The resulting L/E_γ versus E_γ curve was then compared with experiment; departures of the calculated curve from experiment dictated changes in the L/E_e curve to yield a second trial function, etc. The calculated gamma-ray response curve shown in fig. 1 for a 2.5-in. diameter by 2-in. high crystal is the result of the last iteration. The agreement of this curve with experiment, fig. 1, is considered to be satisfactory and permits the use of the L/E_e curve of fig. 2 in subsequent calculations of intrinsic line width.

5. Intrinsic Line Width

Since there is a variation in the accumulated light output for totally absorbed photons according to the preceding discussion, this should be reflected in a spread in the total absorption line in the pulse-height spectrum. This feature is clearly indicated by the Monte Carlo calculations and is shown in fig. 3 for the calculated total absorption peak for 662-keV gamma rays. The histogram indicates the extent of the intrinsic broadening, and the smooth curve shows the same peak after the photomultiplier broadening has been folded in. Although the histogram is ragged, to a certain extent, because of the statistical nature of the Monte Carlo calculations, the general features of the data can be easily explained. Of particular interest is the leading peak of the histogram at the lower pulse-height values which is contributed by first-collision photoelectric events and is prominent in all histograms for the lower energy gamma rays. Those counts above the photoelectric peak arise from Compton events followed by photoelectric absorption. These events produce counts at a larger pulse height than the first-collision photoelectric peak since the initial electron spectrum in the Compton events is a lower-energy spectrum. Figure 2 shows that a lower-energy spectrum corresponds to larger values of L/E_e and hence to a larger pulse height. The valley between the photoelectric peak and the Compton peak of fig. 3 is real and not a result of statistics in the Monte Carlo calculation.

Since the intrinsic broadening does not result in a line of gaussian shape, as can be seen in fig. 3, it is not correct to represent the broadening in terms of a line-width parameter. However, this parameter is a convenient way to indicate the extent of the intrinsic broadening and will be subsequently referred to as the effective intrinsic line width. The effective intrinsic line width, R_I, was calculated from the expression $R_I = (R^2 - R_p^2)^{\frac{1}{2}}$, where R is the line width at half maximum of the total-absorption line after including photomultiplier broadening and R_p is the line width of the photomultiplier broadening alone. A calculation of the relative squared deviation of the total-absorption line, based on the histogram, gives results which essentially agree with the results of this calculation. The solid curve in fig. 4 presents the effective intrinsic line width calculated for a 2.5-in. diameter by 2-in. high NaI(Tl) crystal using the electron response curve given in fig. 2. The curve in fig. 4 has a maximum at approximately 370 keV dropping rapidly toward zero on the low-energy side. At approximately 100 keV it should be almost zero since first-collision photoelectric events of incident

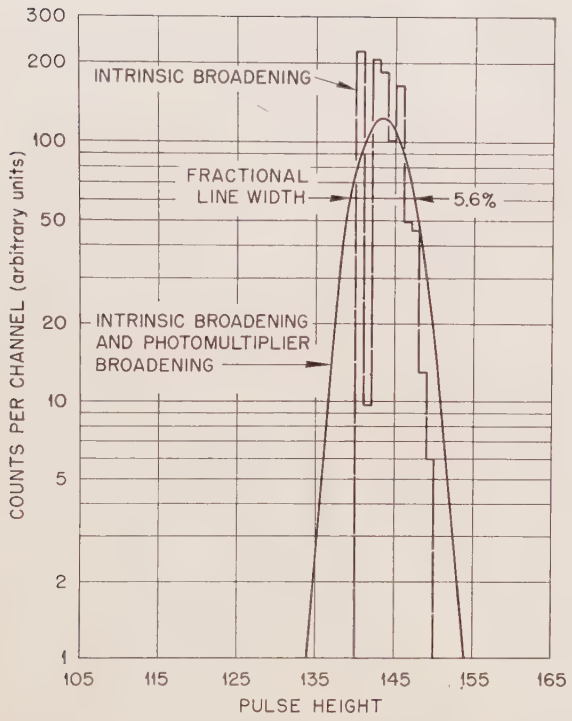

Fig. 3. Calculated pulse-height spectrum in the region of the total absorption peak of 662-keV gamma rays incident on a 2.5-in. diameter by 2-in. high NaI(Tl) crystal. The source was 10 cm from the face of the crystal. The assumed photomultiplier broadening amounts to 4.0% full width at half maximum.

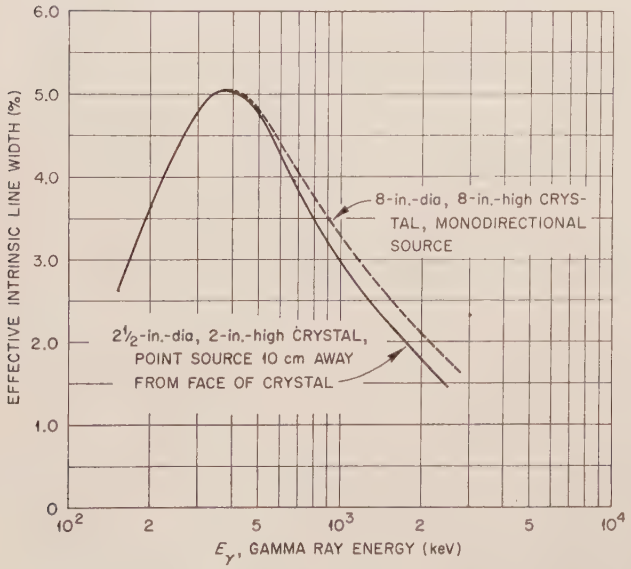

Fig. 4. Effective intrinsic line width of the total-absorption line as a function of the energy of gamma rays incident on two NaI(Tl) crystals of different sizes.

photons dominate the total absorption line and there will be little variation in the accumulated light output from one photon to another. On the high-energy side of the maximum the drop-off can be attributed to the fact that the L/E_e curve of fig. 2 becomes relatively flat above several hundred keV. The absolute line width ΔE increases less rapidly than the energy, and $(\Delta E/E)$ intrinsic is a decreasing function.

6. Geometrical Effects on the Intrinsic Line Width

It would be expected that the size of the crystal or the source-detector geometry would have some effect on the intrinsic line broadening. In the case of the source-detector geometry, however, there seems to be little effect. The present calculation was applied to a 2.5-in. diameter by 2-in. high crystal with a 662-keV point source at separation distances of 5, 10, 20, and 40 cm, and with a monodirectional beam illuminating the entire crystal face; no difference in the intrinsic broadening could be detected within the statistics of the calculations.

On the other hand, the size of the crystal does have an effect on the intrinsic broadening, although for moderately large crystals the broadening is rather insensitive to size. This can be seen in fig. 5 where the effective intrinsic line width is given for 662-keV, monodirectional gamma rays incident on various size crystals which have a diameter equal to the length. The rapid drop of intrinsic broadening as the size of the crystal decreases is due to the fact that for small crystals photoelectric events make the most important contribution to the total absorption line. The deposition of the full energy of a gamma ray by Compton events is unlikely by virtue of the high leakage rate of secondary gammas from a small crystal. Since there is no intrinsic broadening due to a photoelectric event, on the basis of the present model, the effective intrinsic line width decreases with crystal size and approaches zero for a very small crystal.

The weak dependence of the intrinsic broadening on the size of the crystal for moderately large crystals indicated in fig. 5 persists at energies other than 662 keV. This can be seen in fig. 4 where the effective intrinsic line width for an 8-in. by 8-in. crystal is compared with that of a 2.5-in. diameter

by 2-in. high crystal at different source energies. The difference is negligible at the lower energies and reaches a difference of only 0.25% at 2.5 MeV. The gamma-ray response curve for the 8-in. by 8-in. crystal is also shown in fig. 1.

7. Discussion

Having calculated the intrinsic line width as a function of gamma-ray energy and crystal size, it is now of interest to ask how this effect influences the over-all resolution of a gamma-ray spectrometer. Since the intrinsic line width is only one of several sources of line broadening, it is not possible to give a specific answer to this question that would fit every case. It is possible, however, to discuss the contribution of intrinsic broadening to the total line width within the framework of Breitenberger's[2]) theoretical studies of scintillation counter statistics. His analysis indicates that under certain assumptions applicable only to an idealized counter (including the assumption of strict proportionality in its response to gamma rays) the relationship between line width and energy should be of the form

$$(\Delta E/E)^2 = A + B/E \qquad (1)$$

where A and B are constants. Parameter A represents the variance in transfer efficiency of optical photons from their point of origin in the scintillator to the collection of photoelectrons at the first dynode of the photomultiplier. The function B/E describes the contribution of photomultiplier statistics, as previously indicated. It should be clearly understood that this expression is an idealization and is not expected to be fulfilled in the case of a real counter. In particular, the parameter A will be a function of energy in an actual scintillation spectrometer and not constant as in eq. (1). Equation (1) does provide, however, a starting point for the interpretation of scintillation counter statistics, so that it is instructive to plot $(\Delta E/E)^2$ versus $1/E$.

In fig. 6, curve (a) represents a plot of the square of the composite line width (R^2 in the present terminology), taking into account only the intrinsic broadening plus photomultiplier statistics. This is based on a photomultiplier line width of 4.0% at 662 keV and is derived directly from the results of the Monte Carlo calculation as shown in fig. 3. A photomultiplier line width of 4% or greater at a light intensity corresponding to a 662-keV gamma ray in NaI(Tl) was obtained in the experiments of Kelley *et al.*[11]), who illuminated the photocathode with an auxiliary light flasher. This value of 4% is thus considered as a lower limit to the performance

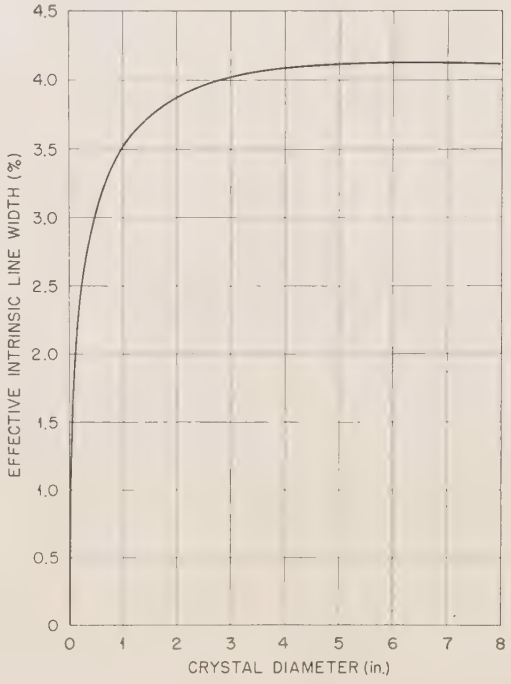

Fig. 5. Effective intrinsic line width of the total absorption line for 662-keV gammas incident on cylindrical NaI(Tl) crystals with diameter equal to the height. The gamma-ray beam was monodirectional, normal to the crystal face, and illuminated the entire face.

of the photomultiplier, and curve (a) represents a minimum line width to be expected from the combination of photomultiplier statistics plus intrinsic broadening.

In order to discuss the effect of intrinsic broadening on the total line width in an actual scintillation spectrometer, we must now introduce the transfer variance and a realistic value for the parameter B. In this approach it is assumed that the over-all line width can be expressed empirically as

$$(\Delta E/E)^2 = A + B/E + X(E)\,. \qquad (2)$$

In the above equation, $X(E) = R_I^2$, where R_I is

[11]) G. G. Kelley *et al.*, IRE Trans. Nucl. Sci. NS-3 (1956) 57.

the effective intrinsic line width. Thus the intrinsic broadening is added to a broadening of the form of eq. (1), where A and B are now determined by experiment. This determination of A and B is possible since intrinsic broadening does not make a major contribution to broadening below 100 keV. The studies of Bisi and Zappa[12]) indicate that for

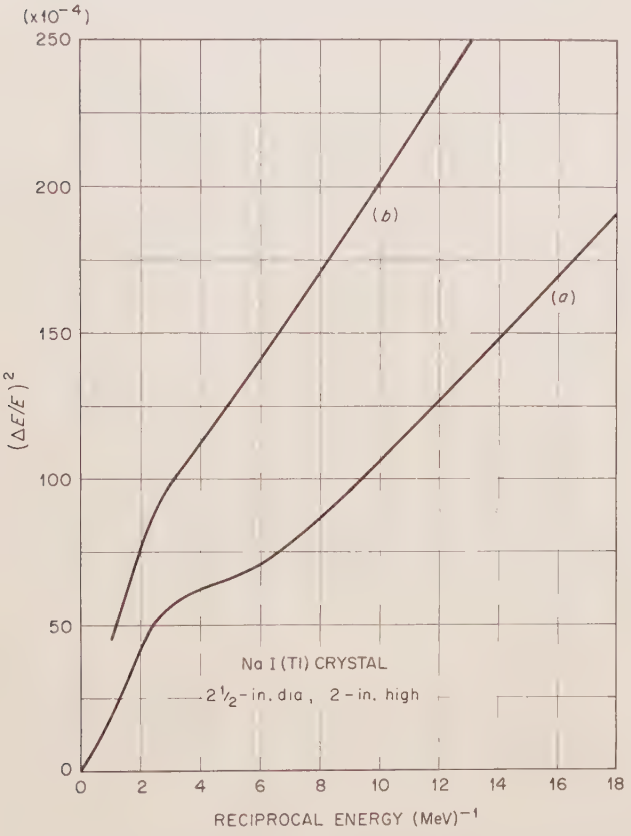

Fig. 6. Calculated values of $(\Delta E/E)^2$ for a 2.5-in. diameter by 2-in. high NaI(Tl) crystal. Curve (a) includes only intrinsic broadening plus photomultiplier statistics, and is derived directly from the Monte Carlo calculation assuming a 4.0% line width at 662 keV due to the photomultiplier. Curve (b) includes intrinsic broadening plus photomultiplierstatistics and a contribution from the transfer variance. Parameters describing the latter two effects were taken from experiment (ref.[12])).

such energies the quantity $(\Delta E/E)^2$ does, in fact, approximate a straight line. The procedure followed is to obtain A and B experimentally for low gamma-ray energies and then to add the intrinsic broadening as indicated in eq. (2) to obtain the over-all broadening for gamma-ray energies in the hundreds of keV.

The result of this procedure is given by curve (b) in fig. 6 for values of A and B given by Bisi and Zappa in connection with their fig. 3. These are assumed to be typical values of parameters A and B; however, inspection of their tables 2 and 3 indicates the strong dependence of these quantities on relatively minor changes in experimental conditions. It should also be added that Bisi and Zappa performed their experiments with different combinations of 1.5-in. diameter by 1-in. high NaI(Tl) crystals and Du Mont 6292 photomultipliers. Since their work is the most detailed resolution work on NaI(Tl) for low energy gamma rays, their values are used, although the present study applies strictly only to 2.5-in. diameter by 2-in. high crystals.

The value of A used to obtain curve (b) in fig. 6 corresponds to a transfer line width of 6.7% for gamma-ray energies below about 100 keV. B corresponds to a photomultiplier line width of 4.9% at 662 keV. Above about 100 keV A is energy dependent with part of the dependence accounted for by the work of Bisi and Zappa[12]). The term A in eq. (2) was altered by a factor to include only the Bisi and Zappa effect. This factor applies in cases where the incident gamma ray produces more than a single electron in the crystal. Specifically, the factor multiplying A is the sum of squares of the fractional energies, E_e/E_γ, of all electrons produced by a gamma ray of energy E_γ. In the present instance an approximate method was used to deduce this factor from histograms such as the one given in fig. 3.

Curve (b) in fig. 6 indicates that the hump in curve (a) of the same figure may be masked in a typical experiment. McGowan and Stelson's data[13]) on a 3-in. by 3-in. NaI(Tl) crystal can be matched quite well by curve (b) for reciprocal energies between 1 and 5 MeV^{-1}. This is undoubtedly fortuitous since the difference in crystal size and the extreme sensitivity of parameters A and B to minor experimental changes would not lead one to expect such agreement. The experimental line width is, furthermore, dependent on the nature of the gamma-ray source. For example, a gamma-ray

[12]) A. Bisi and L. Zappa, Nucl. Instr. **3** (1958) 17.

[13]) F. K. McGowan and P. H. Stelson, Oak Ridge National Laboratory. Data reported in ref.[11]); In particular, see plot on p. 136 of ref.[1]).

sum peak is expected to have a narrower line width than a single-gamma event of the same energy, by virtue of the fact that the transfer variance will be less in the former case[12]). This effect is completely analogous to the effect of multiple electron production considered above. In the low-energy region (below ≈ 70 keV) the gamma-ray sources are frequently composite sources of four K X-rays, and the several X-rays may span an energy range of several kilovolts; this clearly gives rise to a broader peak than expected from a strictly monoenergetic source.

The principal point to be made here is the fact that the intrinsic broadening contributes significantly to the over-all line width in the energy region of hundreds of kilovolts. For example, the calculated line width at 662 keV from curve (b) of fig. 6 amounts to 7.8% composed of a 4.9% contribution from the photomultiplier, a 4.6% contribution from the transfer process, and a 4.0% contribution from the intrinsic broadening.

It is of interest to inquire about the origin of the nonproportional response of NaI(Tl) to electrons, and to ask whether this effect exists in other alkali iodide scintillators. A theoretical model describing the scintillation process in thallium-activated alkali iodides has recently been described[14]). On the basis of this model the nonproportional response of an alkali iodide scintillator to electrons results from the fact that the probability of formation of an energy carrier depends on the specific energy loss of the incident particle in the scintillator. The L/E_e curve of fig. 2 is found to be in agreement with the predictions of this model and, in particular, is consistent with experimental scintillation efficiency versus dE/dx data for other charged particles on NaI(Tl). On the basis of this model the nonproportional response to electrons arises in a natural way as a consequence of the energy transport part of the scintillation process. This effect is also expected in other thallium-activated alkali iodides, e.g., CsI(Tl) or KI(Tl). Recent experiments[15]) on CsI(Tl) have confirmed its nonproportional response to gamma rays, with results very similar to those of NaI(Tl) as in fig. 1. Thus the intrinsic line broadening discussed in the present paper should apply to CsI(Tl) as well, although with possibly different quantitative values. Similarly, this effect is expected in other activated inorganic crystals such as KI(Tl) or LiI(Eu).

Acknowledgements

The authors are indebted to W. W. Managan of the Harshaw Chemical Company for stimulating their interest in this problem. We wish to thank S. I. Baker, I. S. Sherman, and their associates at Argonne National Laboratory for unpublished data on the response of NaI(Tl) to gamma rays. R. W. Peelle and F. K. McGowan have kindly reviewed the manuscript.

[14]) R. B. Murray and A. Meyer, Phys. Rev. **122** (1961) 815.
[15]) R. B. Murray and R. Gwin, Bull. Am. Phys. Soc., Ser. II, **5** (1960) 417; See also ORNL-3016 (1960) 293.

NUCLEAR INSTRUMENTS AND METHODS **12** (1961) 124–126; NORTH-HOLLAND PUBLISHING CO.

TRANSISTORIZED LINEAR GATE FOR PHOTOMULTIPLIER PULSES

F. F. LIU and F. J. LOEFFLER

Department of Physics, Purdue University, Lafayette, Indiana

Received 1 March 1961

A temperature compensated, linear pulse gating circuit employing transistors has been built which accepts pulses directly from the anode of photomultiplier tubes. Departures from linearity of less than 3 % result for input pulses in the range 50 mV to 200 mV.

Very often it is desirable when using a complex particle counter array to measure the pulse height distribution in a given counter corresponding to a particular kind of event. This can be done by using a pulse gating circuit that is opened by a trigger

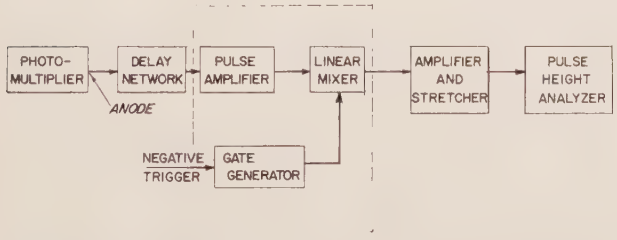

Fig. 1. Block diagram of system for obtaining pulse height distributions. Dashed lines indicate unit described in this note.

signifying a desired event, and that preserves the pulse height information of the pulse being gated. Devices of this sort are called linear gates and we describe below such a transistorized device which accepts negative pulses directly from the anode of a photomultiplier tube. These pulses are delayed, amplified and mixed in a linear mixer with a gate initiated by the trigger. For our application we then stretch the gated pulse and feed it into an Eldorado, Fairstein type amplifier which drives an Eldorado 20 channel pulse height analyzer.

Fig. 1 shows in block diagram form the arrangement of units including those necessary for our particular pulse height analyzer. The pulse out of the linear mixer is shown in fig. 2(c) and this can be considered the output of the device which we are describing. A brief description of the linear gate whose schematic diagram is shown in fig. 3, follows:

(1) The pulse amplifier accepts negative pulses of amplitude between 0.05 and 0.2 volts from the anode of a photomultiplier tube. A typical pulse is shown in fig. 2(a) and has approximately a 1 μsec tail. The amplifier is of conventional design with

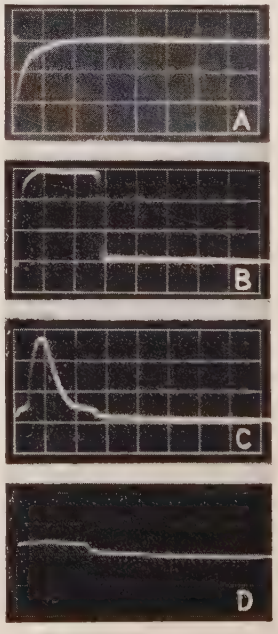

Fig. 2. Pulse wave forms in the linear gate. All time scales are 1 μsec/horizontal division. (a) A typical input pulse to the linear gate. Vertical sensitivity is 0.05 volt/division. (b) Gate wave form at input of linear mixer. Vertical sensitivity is 2.5 volts/division. (c) Gated output pulse from linear mixer. Vertical sensitivity; 1 volt/division. (d) Mixer output with signal pulse delayed by about 5 μsec. Vertical sensitivity; 0.5 volts/divison.

emitter degeneration and is adjusted to a gain of 20 thus producing pulses of the type illustrated in fig. 2(c).

(2) The gate generator is a univibrator producing a gate 7 volts high and 2 μsec wide as shown in fig. 2(b). The negative trigger to initiate the gate can be as small as 0.05 volts and it is shaped in order to reliably trigger the univibrator by a diode network. The gate is delivered to the linear mixing circuit via an emitter follower in order to give appropriate impedance matching.

(3) The linear mixer is the transistor counterpart of the Rossi circuit. The gate is delivered to one base and the pulse from the amplifier to the other base. At the common emitter appears the smaller of the two signals applied to the bases. In this application the gate is always the largest so that the output is the pulse to be analyzed. This pulse is then fed to an emitter follower which drives the

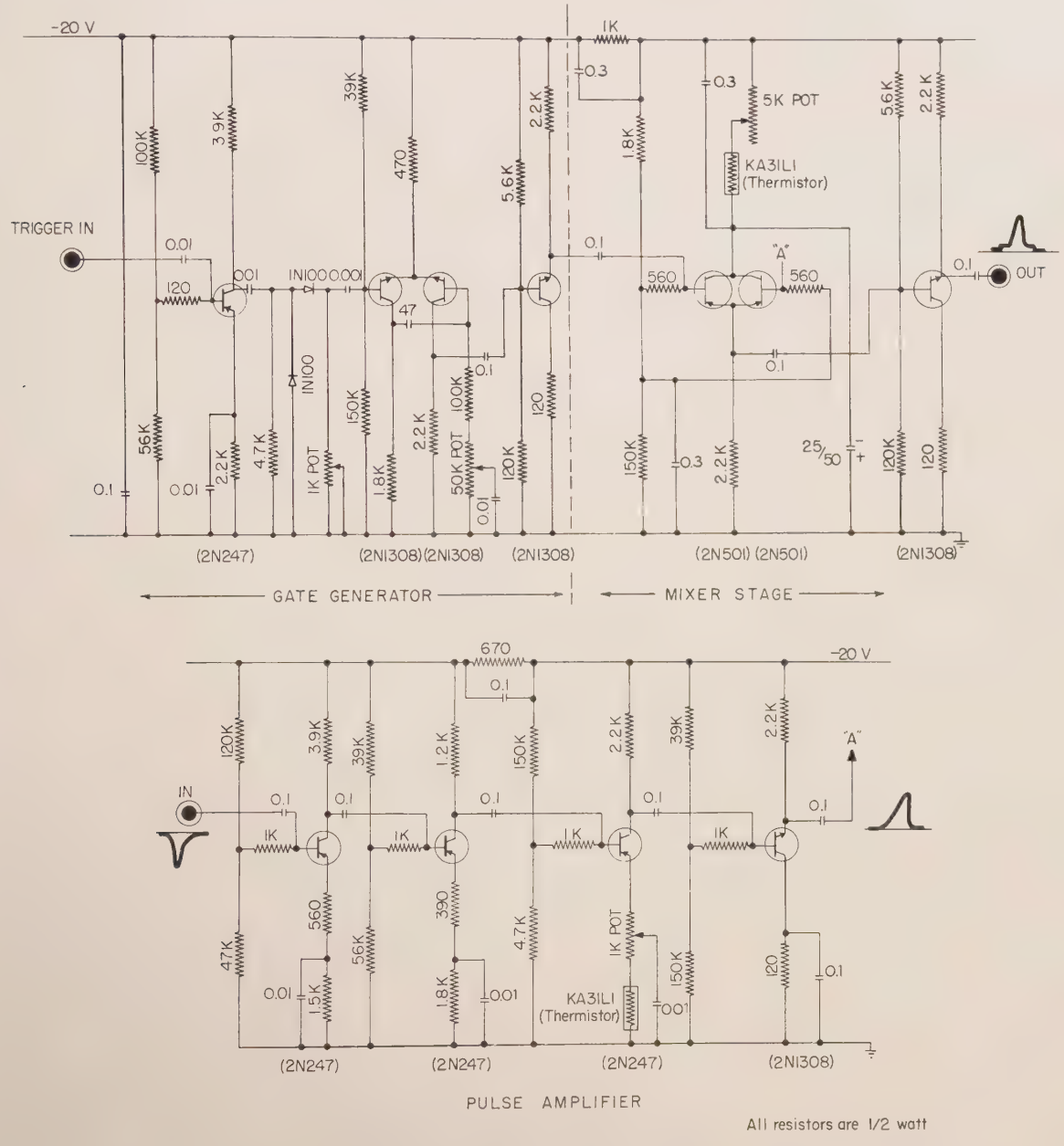

Fig. 3. Schematic diagram of linear gate.

appropriate pulse height analyzing equipment. As can be seen in fig. 2(c), there is a pedestal of about 0.2 volts which we have not bothered to remove since it represents a constant D.C. component in the pulse height spectrum. The output of the linear mixer is shown in fig. 2(d) with the pulse into the pulse amplifier delayed by 50 ft of RG 65 cable.

The overall linearity of the circuit as shown in fig. 1 was tested using a precision mercury-relay pulse generator and over the input range of 0.05 to 0.2 volts the deviation of any measured point from a common straight line was less than 3% of its value. As the above amptitude range is exceeded the performance gradually worsens.

The transistorized part of the circuit was tested for temperature dependence over a 10°C range around room temperature. This was then compensated for by the use of thermistors so that now the change in gain per degree C is less than 0.01% over the above range.

We would like to thank Prof. T. R. Palfrey for his suggestions concerning the linear mixing circuit.

† Supported in part through funds provided by the U.S. Atomic Energy Commission.

NUCLEAR INSTRUMENTS AND METHODS 12 (1961) 127–130; NORTH-HOLLAND PUBLISHING CO.

UTILIZATION OF TUNNEL DIODES IN FAST TRIGGER CIRCUITS

THOMAS A. RABSON

Rice University, Houston, Texas

Received 27 March 1961

A basic trigger circuit is described which utilizes tunnel diodes in their switching mode. An important feature of this circuit is its fast switching and reset times (10^{-8} sec). Applications of this basic circuit to pulse height discrimination, pulse shaping, coincidence measurements, and square wave generation are discussed. The specific application of these circuits to problems in nuclear instrumentation are also considered.

1. Introduction

The tunnel diode is a device which is capable of performing switching operations in the period of a few nanoseconds. The limiting factor involved in reducing the switching time is the junction capacitance of the diode, which is of the order of a few picofarads. In using tunnel diodes in fast pulse shaping circuits and trigger circuits one of the most difficult problems is that of resetting the diode to its original condition after it has "fired". A very successful way of doing this is to reflect the voltage step, which is produced when the diode switches, from the load end of a transmission line terminated so that it has a negative reflection coefficient. The reflected pulse returns with the opposite voltage and resets the diode.

The width of the pulse is equal to twice the transit time of the pulse along the transmission line. This basic principle has been applied to several types of circuits: a low level pulse height discriminator, a pulse shaping circuit or one shot, a coincidence circuit, a d-c level detector and a relaxation oscillator. These applications are discussed in this article.

2. Basic Circuit

The functions that may be performed by a tunnel diode are dependent on the circuit in which they are employed[1]). Operation as an amplifier requires some sort of external biasing such that the diode is in the region of its negative resistance. Stability requirements restrict the resistance in the biasing circuit to less than the magnitude of the negative resistance, R_N, exhibited by the tunnel diode. A diagram representing the tunnel diode characteristics and the load line it has when biased in the above manner is shown in fig. 1a. If the biasing resistance is greater than R_N, the load line appears flatter, and there are two stable states for the

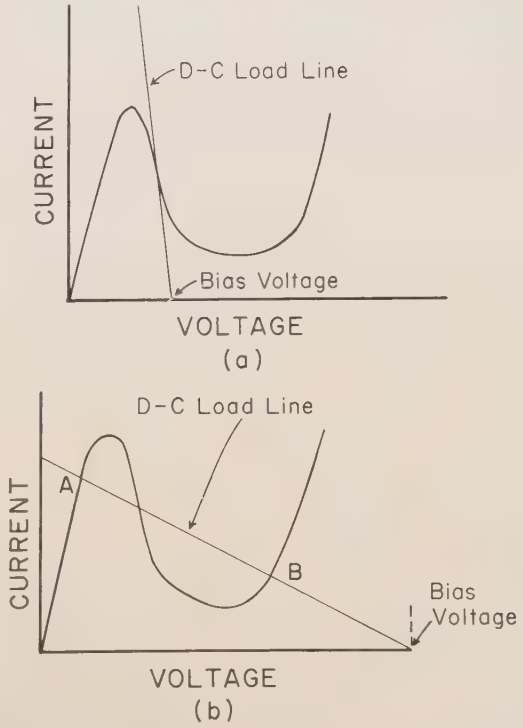

Fig. 1. (a) Tunnel diode characteristics with a load line showing the tunnel diode biased in its negative resistance region. (b) Tunnel characteristics with the load line adjusted to exhibit the switching characteristics of the diode.

[1]) Lesk, Holonyak and Davidsohn, Electronics 32, No. 48 (1959) 60.

circuit, indicated by points A and B in fig. 1b. Neither of these stable states is in the negative resistance region of the diode. In this configuration the diode acts as a switch.

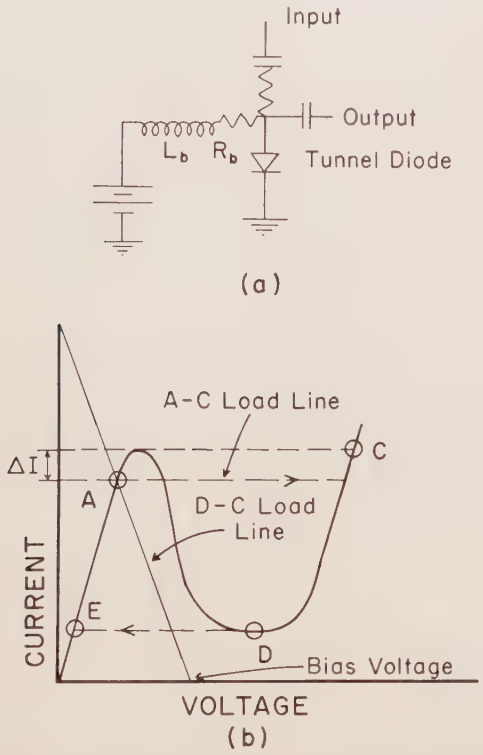

Fig. 2. (a) Basic tunnel diode biasing circuit; (b) Tunnel diode characteristics with both the d-c and a-c load line.

If an inductive element is used in the biasing circuit, as shown in fig. 2a, then the d-c load line and the a-c load line differ. The d-c load line is shown in fig. 2b. The diode is stable at point A. For any fast input pulses one must use the so-called a-c load line, which for a large inductor L is essentially horizontal.

If the input pulse is large enough to raise the a-c load line above the peak current of the diode indicated by ΔI, it switches over to point C, as indicated in fig. 2b. After the input pulse decays the diode travels along the diode characteristic curve from C to D with a speed dependent on the value of L and the diode characteristics. After reaching D it jumps to E then the current builds slowly back up to the initial operating point A.

If the bias voltage is adjusted so that the d-c load line intersects the tunnel diode characteristic in the negative resistance region the circuit will behave as a relaxation oscillator and continually go through the above cycle without external triggering being necessary.

3. Use as a Pulse Height Discriminator

It is obvious that the height of the input pulse necessary to "fire" the circuit of fig. 2 depends on the bias voltage. This circuit can therefore be used as a pulse height discriminator, but its long "dead" time makes it unattractive for this purpose. Not until the circuit returns completely to point A is it again operative, although it can be fired by large pulses from the time it reaches point E. In order to overcome the reset problem the circuit shown in fig. 3a was developed. A 400 Ω delay line with a

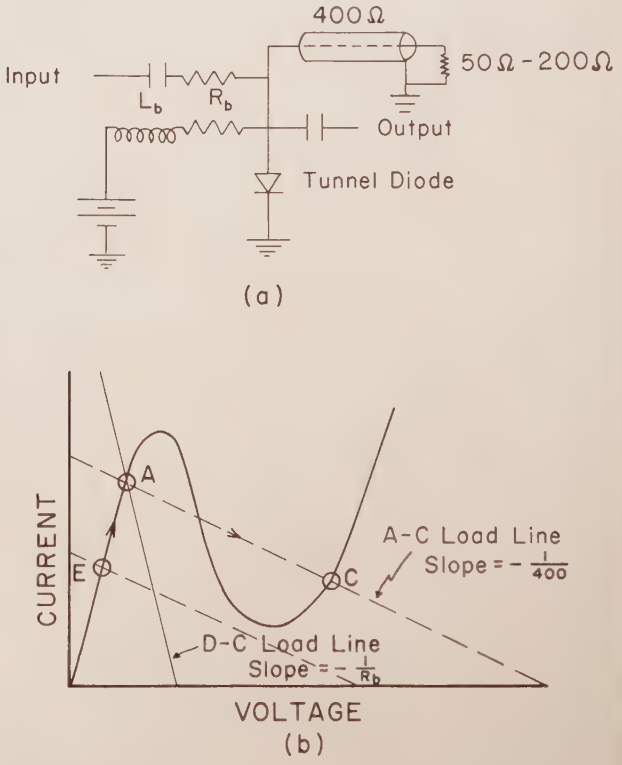

Fig. 3. (a) Tunnel diode circuit with delay line "reset". (b) Tunnel diode characteristics illustrating operation of the circuit shown in (a) as a pulse height discriminator.

200 Ω termination is shunted across the tunnel diode. Otherwise the circuit is the same as shown in fig. 2. A 200 Ω termination is used rather than a short circuit in order to reduce the number of

reflections in the line after the tunnel diode returns to its stable state, thereby reducing the dead time.

The complete operation of the circuit upon application of an input pulse can be understood in terms of fig. 3b. The a-c input impedance of the delay line is great enough so that the switching action of the tunnel diode is preserved. The reflected pulse from the delay line is of sufficient magnitude to cause the a-c load line to drop below the current minimum level and thereby cause the diode to switch back to point E. One or two more reflections on the line brings the circuit back up to point A. It should be emphasized that the delay line is not used simply for pulse clipping and shaping but for resetting the tunnel diode to its original operating point. The output can be obtained directly across the tunnel diode itself, or a cathode follower or grounded collector transistor output circuit can be used to supply isolation.

Pulses obtained with a 0.7 μ sec delay line and a d-c bias below the diode peak current are shown in fig. 4. Pulses of only a few millivolts in amplitude were sufficient to trigger the circuit.

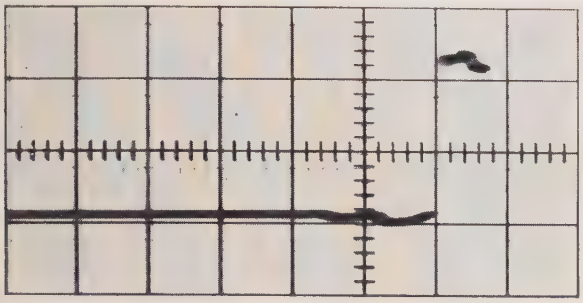

Fig. 4. Oscilloscope picture of the output pulse from the circuit of fig. 3a when it is used as a pulse height discriminator with a 0.7 μ second delay line.

Horizontal scale = 1 μ sec/division
Vertical scale = 0.1 V/division.

4. Use as a Relaxation Oscillator

The use of the tunnel diode in relaxation oscillator circuits has been described in the literature[2]). If the basic circuit, described previously using the delay line reset, is d-c biased in the negative resistance region it switches back and forth between the two states where the a-c load line intersects the tunnel diode characteristic in the positive resistance range. This is because the point at which the d-c load line crosses the negative resistance portion of the curve is not a stable operating point.

The period of oscillation is equal to four times the time it takes a pulse to travel the length of the delay line. Because of this fact, the circuit has quite stable frequency characteristics.

Rise and fall times of less than 10 nanoseconds can be obtained from such circuits. Oscilloscope pictures of the output of this circuit with delay

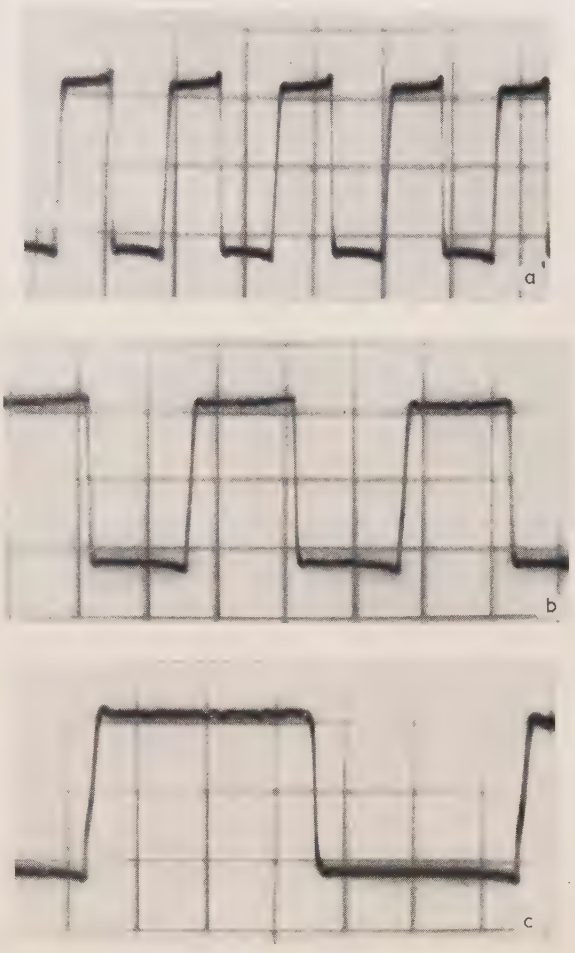

Fig. 5. Oscilloscope picture of the output from the circuit of figure 3a when it is biased to operate as a free running multivibrator: (a) Using a 0.25 μsec delay line; (b) using a 0.5 μsec delay line; (c) using a 1 μsec delay line.

Horizontal scale = 0.5 μsec/division
Vertical scale = 0.2 V/division.

[2]) C. M. Barrack and M. C. Watkins, Electronic Design 8, No. 13 (1960) 54.

lines of 0.25, 0.5, and 1 μsec are shown in fig. 5.

Another interesting property of this circuit is that the onset of oscillations is dependent on the diode being d-c biased in the negative resistance range. This suggests the use of this circuit as a d-c voltage or current level discriminator. Whenever the d-c voltage and current level is within the range necessary to bias the diode in the negative resistance region a signal output will be obtained consisting of a square wave.

5. Use as Coincidence Circuit

It is obvious that if two or more parallel inputs are used and the bias level is set so that one pulse is not sufficient to trigger the circuit, then this circuit will also serve as a coincidence or "and" circuit. The advantage this circuit has over the conventional diode coincidence circuit is that the output pulse can be made much larger than either input pulse. Input pulses of uniform height are necessary for the operation of this circuit. This fact makes it convenient to use the tunnel diode coincidence circuit in conjunction with two or more tunnel diode pulse height discriminator circuits, whose output is uniform.

6. Conclusions

The use of circuits utilizing tunnel diodes offer several advantages over circuits utilizing conventional tubes and transistors. Most of these advantages are a result of their fast switching speed, their operation at low levels, and their temperature stability. Pulse height discriminator circuits having a recovery time of less than 1 μsec, have been built which will trigger on pulses as low as 20 mV in amplitude. They can be used with the output pulses directly from conventional 10 stage photomultiplier tubes used in conjunction with NaI crystals for gamma-ray spectroscopy. Also the output pulses from solid state ionization chambers, after passing through amplifiers with gains in the range of 20 dB, can be discriminated with these circuits.

Coincidences between the outputs of two tunnel diode discriminators have been measured using the tunnel diode "and" circuit described above. The resolving time of the coincidence circuit is limited by the pulse widths of the input signals.

The most serious difficulties in using several of these circuits in the same network are caused by the fact that tunnel diodes are bilateral devices, consequently there is no isolation between the input and the output. Some of these problems can be overcome with appropriate circuit design, utilizing, for instance, transistors for isolation.

The circuits described above were developed for electronic instrumentation systems used in nuclear spectroscopy. The main advantages of the above circuits are centered around the fact that they are simple and provide stable operation at low levels. This means that pulse height discrimination and coincidence measurements may be carried out at pulse height levels some two to three orders of magnitude below the levels required with standard vacuum tube circuits. This reduction in operating level results in a considerable reduction in the amount of amplification necessary, with its inherent distortion and delay, for the performance of the required electronic operations. This fact coupled with the simplicity of tunnel diode circuits results in a considerable decrease in the complexity of many of the electronic systems.

NUCLEAR INSTRUMENTS AND METHODS **12** (1961) 131–137; NORTH-HOLLAND PUBLISHING CO.

TRANSMISSION AND LINE BROADENING OF RESONANCE RADIATION INCIDENT ON A RESONANCE ABSORBER†

S. MARGULIES and J. R. EHRMAN

University of Illinois, Urbana, Illinois

Received 13 February 1961

The transmission of resonance radiation emitted from a source of finite thickness and passing through an external resonance absorber is discussed. The transmission integral is examined for both a linear and a Gaussian distribution of radioactive atoms in the source. Several special cases are presented, and the general case is evaluated by numerical integration. Over the range of values considered, the transmitted line shape closely approximates a Breit-Wigner curve whose width is greater than the natural width of the transition. This line broadening, caused by resonance absorption in the source and in the external absorber, is presented graphically as a function of source and absorber thickness.

1. Introduction

R. L. Mössbauer's discovery that recoilless emission and absorption of nuclear gamma radiation can occur[1]) has stimulated a host of recent investigations[2]). Interest in this process has grown rapidly because the Mössbauer effect allows the direct observation of many phenomena formerly thought unmeasurable. A terrestial measurement of the gravitational red-shift[3]), a test of the equivalence principle for rotating systems[4]), and the observation of the Zeeman splitting of excited nuclear levels[5]), are but a few of the experiments made possible by the Mössbauer effect. In addition, the effect is finding many applications in the measurement of the internal fields in solids.

When recoilless emission and absorption of gamma radiation occurs, the conditions for nuclear resonance fluorescence are inherently satisfied. The numerous applications of the Mössbauer effect follow from the fact that, in such cases, the very narrow lines resulting from transitions from metastable nuclear levels can actually be observed: resonance lines with widths in the range 10^{-10} to 10^{-5} eV, which correspond respectively to gamma transitions from levels whose half-lives vary between 10^{-5} and 10^{-10} sec, have been measured.

Although experiments involving the Mössbauer effect can be performed with either a transmission or a scattering geometry, most of the work done so far has employed the former approach[6]). A typical transmission experiment consists of measuring the resonance radiation passing through a resonance absorber, as a function of the relative velocity between source and absorber. In this manner, a resonance line shape is traced out. Since the great utility of the Mössbauer effect depends upon the measurement of such lines, a consideration of the line shape is of interest. In what follows, we will be concerned with the transmission

† This work has been supported in part by the joint program of the U.S. Office of Naval Research and the U.S. Atomic Energy Commission.

[1]) R. L. Mössbauer, Z. Physik **151** (1958) 124.

[2]) For a listing of recent experiments, see the bibliography contained in Proceedings of the Allerton Park Conference on Mössbauer Effect, University of Illinois, Urbana, Illinois, June 5–7, 1960 (unpublished).

[3]) R. V. Pound and G. A. Rebka, Jr., Phys. Rev. Letters **4** (1960) 337.

[4]) H. J. Hay, J. P. Schiffer, T. E. Cranshaw and P. A. Egelstaff, Phys. Rev. Letters **4** (1960) 165.

[5]) R. V. Pound and G. A. Rebka, Jr., Phys. Rev. Letters **3** (1959) 554;
G. DePasquali, H. Frauenfelder, S. Margulies and R. N. Peacock, Phys. Rev. Letters **4** (1960) 71;
S. S. Hanna, J. Heberle, C. Littlejohn, G. J. Perlow, R. S. Preston and D. H. Vincent, Phys. Rev. Letters **4** (1960) 177.

[6]) H. Frauenfelder, D. R. F. Cochran, D. E. Nagle and R. D. Taylor, Nuovo Cim. **19** (1961) 183.

of resonant gamma radiation emitted from a source of finite thickness†, and passing through a finite resonance absorber. In particular, we will consider two types of sources; one in which the radioactive atoms are distributed uniformly and one which has a Gaussian distribution of emitting nuclei.

2. General Formulation

In our calculation of the transmitted intensity, we will assume that a fraction f of all decays occur without recoil energy loss[7]). The resonance radiation resulting from these decays will be taken to have an emission and absorption spectrum of Breit-Wigner shape. The remaining fraction of the radiation is non-resonant, and is subject only to ordinary electronic absorption. We will consider a source having arbitrary area, and extending in depth from $x = 0$ to $x = \infty$. The distribution of emitting atoms along the x-axis will be denoted by $\rho(x)$. We will deal only with the radiation emitted normal to the area of the source, as shown in fig. 1. The distribution of the absorbing atoms in both the source and absorber will be taken to be uniform.

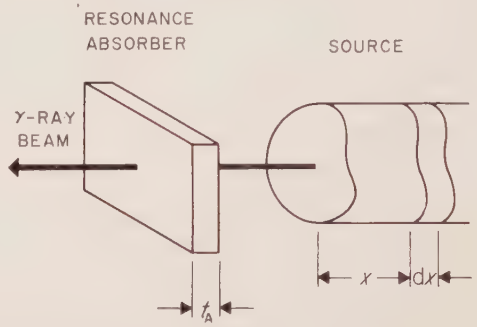

Fig. 1. Geometry used to calculate the transmission of γ-radiation through a resonance absorber moving with a velocity v relative to the source.

Under these circumstances, the transmission through a resonance absorber of thickness t_A, moving with a velocity v relative to the source, is given by

$$p(\mathscr{S}) = e^{-\mu_A t_A}\left\{(1-f)\int_0^\infty dx\,\rho(x)e^{-\mu_S x} + f\,\frac{\Gamma}{2\pi}\int_{-\infty}^{\infty} dE\,\exp\left[-f'_A n_A a_A \sigma_0 t_A \frac{\Gamma^2/4}{(E-E_0)^2+\Gamma^2/4}\right]\right.$$
$$\left.\times\int_0^\infty \frac{dx\,\rho(x)}{(E-E_0+\mathscr{S})^2+\Gamma^2/4}\exp\left[-\left(f'_S n_S a_S \sigma_0 \frac{\Gamma^2/4}{(E-E_0+\mathscr{S})^2+\Gamma^2/4}+\mu_S\right)x\right]\right\}. \quad (1)$$

In this equation, Γ is the full width at half-height of both the emission and absorption lines which are centered about E_0, and σ_0 is the absorption cross-section at resonance††. The subscripts S and A identify the following source and absorber quantities:

f' = probability of resonance absorption without recoil,
n = number of atoms per cubic centimeter of volume,
a = fractional abundance of the atoms which can absorb resonantly,
μ = ordinary mass attenuation coefficient, evaluated at E_0.

The quantity $\mathscr{S} = (v/c)E_0$ characterizes the Doppler shift between the source and absorber.

The first term in (1) represents the transmission of the non-resonant fraction of the radiation, and is independent of the Doppler shift $\mathscr{S}$. In the second term, which is the resonant contribution, the x-integral represents the emission and self-absorption in the source. We will neglect the μ_S appearing in the exponential of this integral, since the mass absorption is usually much smaller than the resonance absorption. The remaining factors in the second term represent the absorption in the external resonance absorber. The lower limit on the energy integral has been taken as $-\infty$ instead of zero for convenience.

[7]) W. Marshall and J. P. Schiffer, The Debye-Waller Factor in the Mössbauer Effect, A.E.R.E., Harwell (1960), (unpublished).

† The case of a beam of γ-radiation, having a Breit-Wigner energy spectrum, passing through a resonance absorber, has been considered by W. M. Visscher in The Evaluation of the Transmission Integral, Los Alamos Scientific Laboratory (1959) (unpublished). This corresponds, in effect, to the non-resonant absorbing source described in Section 5.

†† The absorption cross-section at resonance is given by

$$\sigma_0 = 2\pi\lambda\!\!\!^{-2}\,\frac{2I^*+1}{2I+1}\,\frac{1}{1+\alpha}$$

where $\lambda\!\!\!^{-}$ is the wavelength of the γ-ray, I^* and I are the nuclear spins of the initial and final states, respectively, and α is the conversion coefficient for the transition.

Equation (1) can be seen to be independent of the sign of the Doppler shift $\mathscr{S}$. Since only relative motion between source and absorber is pertinent, $\mathscr{S}$ can be included in the absorber part of the transmission integral instead of the source part, if desired.

Equation (1) can easily be generalized for the case when the emission and absorption lines consist of more than one component (as when electric or magnetic splitting exists) by forming appropriate sums. In this paper we will limit ourselves to the overlap of a single emission line with a single absorption line, each centered about E_0. For convenience, we will translate the energy axis so that both lines are centered about $E = 0$ in the absence of any Doppler shift; that is, $(E - E_0)$ will be replaced by E.

Sources for Mössbauer experiments are generally prepared in either of two ways†:

1. The activity is electroplated or otherwise deposited on a source backing. The activity is then diffused into the host lattice by heating[8]).

2. The activity and the host atoms are co-plated on a backing, thereby building up a lattice containing the radioactive atoms as integral parts[9]).

The second method produces a source in which the emitting atoms are uniformly distributed in depth. The same type of distribution results from the first method if the backing is very thin and the diffusion time is very long. On the other hand, if either the backing is thick or the diffusion time is short, then the first method produces an activity distribution which is approximately Gaussian. Both types of distribution will be discussed below.

3. Uniform Source Distribution

We first consider a source of thickness t_S, having N radioactive atoms per unit length:

$$\rho(x) = \begin{cases} N \text{ atoms/cm}, & t_S \geq x \geq 0 \\ 0 \quad , & x > t_S \, . \end{cases} \tag{2}$$

Since Nt_S is the total number of radioactive atoms and $e^{-\mu_A t_A}$ represents the non-resonant electronic absorption in the external absorber, we will deal with a normalized transmission $P(\mathscr{S})$ defined by

$$P(\mathscr{S}) = p(\mathscr{S})/(e^{-\mu_A t_A} N t_S) \, . \tag{3}$$

For the distribution given in (2) the x part of the transmission integral can easily be evaluated, and we find

$$P(\mathscr{S}) = (1 - f)\left[\frac{1 - e^{-\mu_S t_S}}{\mu_S t_S}\right] + f\frac{2}{\pi\Gamma}\frac{1}{T_S}\int_{-\infty}^{\infty} dE \exp\left(\frac{-T_A\Gamma^2/4}{E^2 + \Gamma^2/4}\right) \times \left[1 - \exp\left(\frac{-T_S\Gamma^2/4}{(E + \mathscr{S})^2 + \Gamma^2/4}\right)\right] . \tag{4}$$

Here, $T_S = f'_S n_S a_S \sigma_0 t_S$ and $T_A = f'_A n_A a_A \sigma_0 t_A$ are effective source and absorber thicknesses, respectively. The first term in this equation is the non-resonant transmission, and will henceforth be denoted by $(1 - f)P(\text{uniform})$. As $\mu_S t_S$ approaches zero, this quantity approaches $(1 - f)$. The second term in (4), containing an integral over energy, represents the resonant contribution. Before discussing the general evaluation of the integral, we will first consider two special cases.

3.1. THIN SOURCE AND ABSORBER

When both source and absorber are thin in the sense that $T_S \ll 1$, $T_A \ll 1$, we can expand both exponentials in the second term of (4) and keep only lowest-order terms in effective thickness. Integrating over energy, we obtain

† Occasionally the target foil, which has been irradiated in a pile or in an accelerator beam to produce the desired radioisotope, may serve directly as a source. In such a case, the distribution of emitting atoms can be quite complex, and will not be treated here.

[8]) R. V. Pound and G. A. Rebka, Jr., Phys. Rev. Letters **3** (1959) 554.

[9]) S. S. Hanna, J. Heberle, C. Littlejohn, G. J. Perlow, R. S. Preston and D. H. Vincent, Phys. Rev. Letters **4** (1960) 28.

$$P(\mathscr{S}) = \left[(1 - f)P(\underset{\text{non res.}}{\text{uniform}}) + f\left(1 - \frac{T_S}{4}\right) \right] - f\frac{T_A}{2}\frac{1}{1 + (\mathscr{S}/\Gamma)^2}. \tag{5}$$

The bracketed term in this equation represents the transmission when $\mathscr{S}$, the relative Doppler shift between source and absorber, is large. This asymptotic value is less than unity because of the self-absorption in the source. The second term represents the dip in the transmission due to resonance absorption in the external absorber. It is seen that the transmitted line, in the case of thin source and absorber, has a Breit-Wigner shape, but has an apparent width Γ_a which is twice that of either the emission or absorption spectrum. This broadening results from the overlap of the emission and absorption lines.

3.2. THIN SOURCE – TRANSMISSION AT ZERO DOPPLER SHIFT

When the effective source thickness T_S approaches zero (as, for example, in a source which has little resonance absorption because $a_S \to 0$), the transmission at zero Doppler shift can be found in terms of T_A, the effective absorber thickness. Expanding the term containing T_S in (4) and keeping only the lowest-order term leads to

$$P(0) \approx (1 - f)P(\underset{\text{non-res.}}{\text{uniform}}) + f\, e^{-\frac{1}{2}T_A}\, J_0(\tfrac{1}{2}iT_A), \qquad T_S \to 0, \tag{6}$$

where J_0 is the Bessel function of zero order. Because of the nature of resonance absorption, the resonant contribution to the transmission does not decrease exponentially with absorber thickness, but instead, shows a saturation behavior.

3.3. UNIFORM SOURCE – GENERAL CASE

Attempts to evaluate (4) analytically for arbitrary source and absorber thicknesses have been unsuccessful. Consequently, we have performed a numerical integration on the University of Illinois digital computer ILLIAC for values of T_S and T_A between zero and ten. It has been found empirically that over this range the transmitted line is, to a very good degree of approximation, a Breit-Wigner curve whose full width at half-height Γ_a, depends upon the value of T_S and T_A. The general variation of transmission with Doppler shift $\mathscr{S}$ is shown in fig. 2. The results of our numerical integration, in the form of the variation of Γ_a/Γ as a function of T_A with T_S as parameter, are shown in fig. 3. Note that as T_S and T_A both approach zero, Γ_a/Γ approaches the value two, since the conditions described in section 3.1 are applicable.

4. Gaussian Source Distribution

For the case of a Gaussian distribution of radioactive atoms, we will use

$$\rho(x) = (2N/\sqrt{\pi})\, e^{-x^2/t_S^2} \text{ atoms/cm}, \qquad x \geqslant 0. \tag{7}$$

Here t_S represents a characteristic diffusion depth whose value depends upon the details of the source preparation. The above distribution is normalized so that Nt_S once again represents the total number of radioactive atoms.

Substitution of this Gaussian distribution into (1) leads to the following expression, which is normalized in the sense defined by (3):

$$P(\mathscr{S}) = (1 - f)\, e^{(\frac{1}{2}\mu_S t_S)^2} [\, 1 - \Phi(\mu_S t_S/2)\,] + f\frac{\Gamma}{2\pi}\int_{-\infty}^{\infty} \frac{dE}{(E + \mathscr{S})^2 + \Gamma^2/4} \exp\left(\frac{-T_A\Gamma^2/4}{E^2 + \Gamma^2/4}\right)$$
$$\times \left[1 - \Phi\left(\frac{T_S\Gamma^2/4}{2\,[\,(E + \mathscr{S})^2 + \Gamma^2/4\,]}\right)\right] \exp\left(\frac{T_S\Gamma^2/4}{2\,[\,(E + \mathscr{S})^2 + \Gamma^2/4\,]}\right)^2, \tag{8}$$

where Φ represents the error function,

$$\Phi(y) = (2/\sqrt{\pi})\int_0^y e^{-u^2}\, du.$$

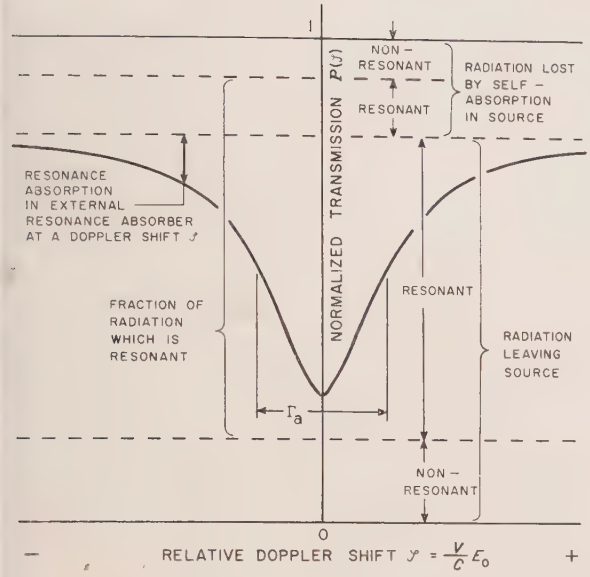

Fig. 2. Normalized transmission of γ-radiation through a resonance absorber as a function of the relative Doppler shift between source and absorber. The apparent full width at half-height of the transmitted line is denoted by Γ_a.

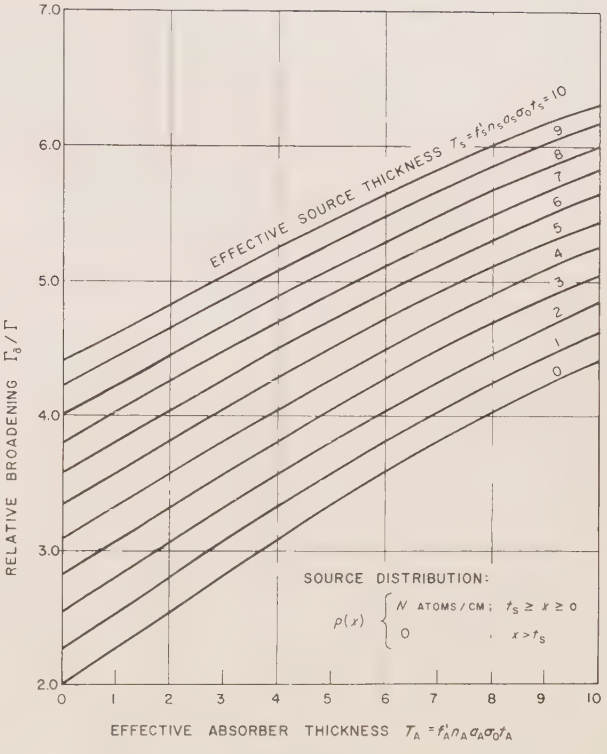

Fig. 3.

The first term in (8) corresponds to the transmission of the non-resonant fraction of the radiation, and will be denoted by $(1-f)P_{\text{non-res.}}(\text{Gaussian})$. Again, as $\mu_S t_S$ approaches zero, the non-resonant contribution approaches $(1-f)$. The resonant contribution to the transmission is contained in the second term of (8). Before discussing the general evaluation of this equation, we will consider two special cases.

4.1. THIN SOURCE AND ABSORBER

If both source and absorber effective thicknesses satisfy the conditions $T_S \ll 1$, $T_A \ll 1$, we can expand the exponentials and the error function in the second term of (8), and keep only first-order terms in thickness. After integrating over energy, one obtains

$$P(\mathscr{S}) = \left[(1-f)P_{\text{non-res.}}(\text{Gaussian}) + f\left(1 - \frac{T_S}{2\sqrt{\pi}}\right)\right] - f\,\frac{T_A}{2}\,\frac{1}{1+(\mathscr{S}/\Gamma)^2}. \tag{9}$$

In this equation the bracketed term represents the asymptotic transmission as $\mathscr{S} \to \infty$, and differs from unity because of self-absorption in the source. The second term results from resonance absorption in the external absorber. The transmitted line shape has the Breit-Wigner form, but is twice as wide as either the emission or the absorption line. Note that (9) differs from (5) only in that the Gaussian source results in more self-absorption than the uniform source. This conclusion follows from the choice of normalization for the Gaussian distribution and is subject to the thin source approximation used to derive both equations.

4.2. THIN SOURCE – TRANSMISSION AT ZERO DOPPLER SHIFT

Expansion of the appropriate terms to lowest order when $T_S \to 0$ allows (8) to be evaluated at the point $\mathscr{S} = 0$. Since both the Gaussian distribution of (7) and the uniform distribution described by (2) are normalized in the same way, it is not surprising that (6) once again follows for this special case, but with $P_{\text{non-res.}}(\text{uniform})$ replaced by $P_{\text{non-res.}}(\text{Gaussian})$.

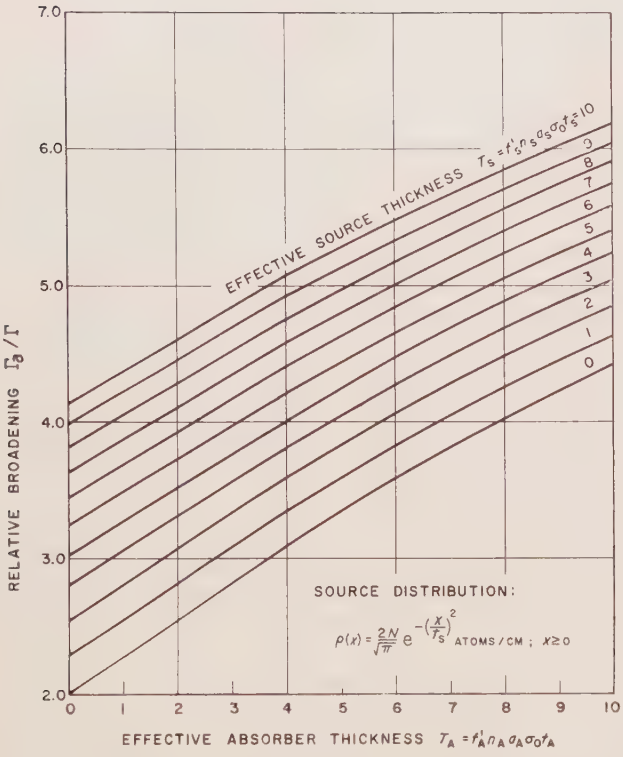
RELATIVE BROADENING Γ_a/Γ
EFFECTIVE ABSORBER THICKNESS $T_A = f'_A n_A \sigma_A \sigma_0 t'_A$
EFFECTIVE SOURCE THICKNESS $T_S = f'_S n_S \sigma_S \sigma_0 t'_S$
SOURCE DISTRIBUTION:
$\rho(x) = \frac{2N}{\sqrt{\pi}} e^{-\left(\frac{x}{T_S}\right)^2}$ ATOMS/CM ; $x \geq 0$

Fig. 4. Broadening of the transmitted line for a source having a Gaussian distribution of emitting atoms.

4.3. GAUSSIAN SOURCE – GENERAL CASE

Equation (8), representing the transmission from a source which has a Gaussian distribution of radioactive atoms, could not be evaluated analytically for arbitrary values of T_S and T_A. Again, we have performed a numerical integration on ILLIAC for the range $10 \geq (T_S, T_A) \geq 0$. As in the uniform case, it has been found empirically that the resulting transmitted lines differ but little from Breit-Wigner curves whose full widths at half-height vary with source and absorber thicknesses (see fig. 2). The calculated broadening of the transmitted line as a function of T_S and T_A is shown in fig. 4. As T_S and T_A approach zero, the conditions of section 4.1 apply, and Γ_a/Γ approaches the value two.

5. Non-Resonant Absorbing Sources

As has been shown, the width of the transmission curve obtained from a resonantly absorbing source of finite thickness is always greater than twice the natural width of the transition. The way to obtain the narrowest lines with any given radioisotope is to use a source backing which has zero abundance of atoms that can absorb resonantly. In this way, only the external resonance absorber contributes to the line broadening. When this is the case, the ordinary electronic absorption, neglected so far for the resonant fraction of the radiation, must be considered. The transmission under these circumstances is given by

$$p(\mathscr{S}) = e^{-\mu_A t_A}\left\{(1-f)\int_0^\infty dx\,\rho(x)\,e^{-\mu_S x} + f\frac{\Gamma}{2\pi}\int_{-\infty}^{\infty} dE \exp\left(\frac{-T_A\Gamma^2/4}{(E-E_0)^2+\Gamma^2/4}\right)\times\int_0^\infty \frac{dx\,\rho(x)\,e^{\mu_S x}}{(E-E_0)+\mathscr{S})^2+\Gamma^2/4}\right\}. \quad (10)$$

The x-integral is the same in both the non-resonant and the resonant terms of this equation, and can be evaluated for the uniform distribution of (2) and the Gaussian distribution of (7). The transmission, normalized according to (3), is found to be

$$\left.\begin{aligned} P(\mathscr{S}) &= [\,(1-f) + fI(\mathscr{S})\,]\left[\frac{1-e^{-\mu_S t_S}}{\mu_S t_S}\right] \\ &= [\,(1-f) + fI(\mathscr{S})\,]P(\underset{\text{non-res.}}{\text{uniform}}) \end{aligned}\right\} \text{ uniform source} \quad (11)$$

and

$$\left.\begin{aligned} P(\mathscr{S}) &= [\,(1-f) + fI(\mathscr{S})\,]\,[\,e^{(\frac{1}{2}\mu_S t_S)^2}\,(1-\Phi(\mu_S t_S/2))\,] \\ &= [\,(1-f) + fI(\mathscr{S})\,]\,P(\underset{\text{non-res.}}{\text{Gaussian}}) \end{aligned}\right\} \text{ Gaussian source} \quad (12)$$

where

$$I(\mathscr{S}) = \frac{\Gamma}{2\pi}\int_{-\infty}^{\infty}\frac{dE}{(E+\mathscr{S})^2+\Gamma^2/4}\exp\left(\frac{-T_A\Gamma^2/4}{E^2+\Gamma^2/4}\right). \quad (13)$$

In either case, the shape of the transmitted line is the same, only the amplitude being affected by the electronic absorption. This behavior follows from the fact that the ordinary mass attenuation coefficients

are energy independent over the width of the emission and absorption lines. The shape of the transmitted line is determined by the energy integral of (13). Since this integral corresponds to the $T_S = 0$ case for either a uniform or a Gaussian source it has, in effect, already been considered. In the results presented below, it should be remembered that $I(\mathscr{S})$ must be substituted into either (11) or (12) to obtain the transmission, $P(\mathscr{S})$.

When the resonance absorber satisfies the condition $T_A \ll 1$, the integral of (13) reduces to

$$I(\mathscr{S}) = 1 - \frac{T_A}{2} \frac{1}{1 + (\mathscr{S}/\Gamma)^2}, \tag{14}$$

again representing a Breit-Wigner curve whose width at half-height is 2Γ.

For arbitrary values of T_A, the transmission also approximates a Breit-Wigner curve, but the apparent width Γ_a varies with the absorber thickness in the manner described by the $T_S = 0$ curve in either fig. 3 or fig. 4.

When there exists no Doppler shift between source and absorber, the energy integral of (13) can be evaluated:

$$I(0) = e^{-\frac{1}{2}T_A} J_0(iT_A/2) . \tag{15}$$

In section 3.2 and 4.2, where very thin sources were considered, the evaluation of the energy integral led to the approximation given in (6). In the case of a non-resonantly absorbing source, no approximations are needed, and the result of (15) is exact. Since $I(\infty) = 1$, we can combine (15) with either (11) or (12) to get the useful result

$$\frac{P(\infty) - P(0)}{P(\infty)} = f [\, 1 - e^{-\frac{1}{2}T_A} J_0(iT_A/2) \,] . \tag{16}$$

Note added in proof: Equation (16), firxt applied to the analysis of Mössbauer experiments by the Los Alamos group, is often being used when it is not applicable. It must be remembered that (16) is

1) exact only for non-resonantly absorbing sources; it is a good approximation for sources where $T_S \ll 1$;

2) derived on the assumption that the emission and absorption lines overlap exactly at zero relative velocity between source and absorber. If, as is often the case, there exists an energy shift between emission and absorption spectra, $P(0)$ must be replaced by $P(\mathscr{S}_0)$, where $\mathscr{S}_0$ is the Doppler shift required to produce coincidence;

3) valid for source and absorber half-widths equal to Γ, the natural width of the transition. It is still correct if these widths are not the natural width, provided that they are equal: $\Gamma_S = \Gamma_A$. In this case, however, the maximum absorption cross-section σ_0 must be multiplied by the factor Γ/Γ_S to keep the total absorption constant.

We wish to emphasize that (16) can be used to extract f and f' from absorption measurements only if the conditions assumed in the derivation are at least approximately satisfied.

Acknowledgement

We wish to thank Professor H. Frauenfelder as well as Dr. E. Lüscher, Dr. P. Debrunner, and Mr. J. H. Hetherington for many interesting discussions.

NUCLEAR INSTRUMENTS AND METHODS **12** (1961) 138–150; NORTH-HOLLAND PUBLISHING CO.

ON THE NATURAL PULSING OF CYCLOTRON EXTERNAL BEAMS IN THE NANOSECOND RANGE

F. ŢINTĂ, N. MARTALOGU, R. DUMITRESCU and T. MAGDA

Institutul de Fizică Atomică, Bucureşti, România

Received 23 January 1961

The shape and the duration of the natural pulse in the Y-120 cyclotron external beam were investigated in the case of acceleration of hydrogen molecular ions and alpha particles. The experimental technique and the results obtained are presented. The factors on which the pulse shape and the duration depend are discussed and the importance of the dynamics of the accelerating process is shown, especially of radial oscillations. It was concluded that in the case in which ions from a single orbit enter the deflection channel, the natural pulse shape is determined by the extraction law from the cyclotron ion source, having the form $i_s = A(V_0 \cos\theta_0^{\frac{3}{2}})$. The equations which can represent the pulse shape in the cyclotron external beam are stated. Some problems connected with the use of the natural pulsing of the cyclotron external beam in the nanosecond range are examined.

1. Introduction

The natural pulsing of a cyclotron beam is a consequence of ion phase-grouping during the accelerating process, especially of the initial region dynamics, when a great part of the trajectory lies in the high-frequency electrical field.

The cyclotron beam takes the form of a succession of bursts which occupy rather short time-intervals as compared with the period of accelerating alternate voltage. The range of the ratio is $\frac{1}{10} - \frac{1}{50}$. The duration of these pulses is thus of the order of nanoseconds. It should be noted that this effect came as a result of a theoretical analysis of the accelerating dynamics in the region of the first orbits[1]), its experimental confirmation and utilization being realized only at a later date[2–5]).

The discovery of accelerated ion phase-grouping phenomenon changed the notions concerning the working of the fixed frequency cyclotron. B. L. Cohen revised the cyclotron theory in order to account for this new development.

This work now represents the most complete theoretical study of dynamic processes transpiring within the cyclotron (see Handbuch der Physik **44** (Springer, 1959)[6]).

According to Cohen phase-grouping may be described by means of the relation

$$\theta = -\frac{eV_0}{2m\omega^2 d^2}\sin^2\theta_0\,, \tag{1}$$

which shows the relationship between the relative phase angle of an accelerated ion within the cyclotron and the electrical phase at the moment this ion leaves the source (at the origin, the electrical field reaches maximum value); e and m are respectively the charge and mass of the considered ion

V_0 = the RF half maximum dee-to-dee voltage;
d = the dees gap width;
ω = the resonant angular frequency ($\omega = eB/mc$).

Under given practical conditions the relation (1) may be written in the form:

$$\theta = -G\sin^2\theta_0\,, \tag{2}$$

where

$$G = \frac{eV_0}{2m\omega^2 d^2}\,. \tag{3}$$

In view of the fact that departure phases can have all possible values, ions will group themselves between angles corresponding to extreme values of the expression $-G\sin^2\theta_0$ and hence all ions will find themselves in the phase range:

$$-G \leqslant \theta \leqslant 0\,. \tag{4}$$

[1]) D. Bohm and L. Foldy, Phys. Rev. **72** (1947) 649.
[2]) M. Jakobsen and J. H. Manley, Phys. Rev. **95** (1954) 600.
[3]) J. H. Manley and M. Jakobson, Rev. Sci. Instr. **25** (1954) 368.
[4]) S. D. Bloom, Phys. Rev. **98** (1955) 233.
[5]) S. D. Bloom, C. O. Muelhause and H. E. Wagner, Phys. Rev. **99** (1955) 654.
[6]) B. L. Cohen, Rev. Sci. Instr. **24** (1953) 589.

onsidering that in the case of the cyclotron

$$\omega = \frac{e}{mc} B \tag{5}$$

$$E = \frac{e^2}{2mc^2} B^2 R^2 , \tag{6}$$

here B is the magnetical induction field,
R = cyclotron final orbit radius, and
E = the ions final energy,
he G expression may be written

$$G = \frac{R^2}{4d^2} \frac{eV_0}{E} . \tag{7}$$

rom this it can be inferred that for any given yclotron (d and R) the grouping angle ought to be irectly proportional to the dee voltage and to the atio between ion charge and energy.

For a given charge the grouping angle would herefore be inversely proportional to the final nergy†.

Important experimental possibilities are raised y the characteristic feature of the cyclotron beam: amely, that of being naturally pulsed in the nano-econd range. Its uses for time-of-flight spectro-netry of fast particles are very interestings espe-ially of neutrons with $E > 1$ MeV[7,8,9]). Measure-nents can also be made on lifetimes of the order of 0^{-9}, of nuclear states excited through various uclear reactions[4]). There are still other technical ses of the cyclotron's natural pulsing (modula-tion)[10]). The pulsing of particle beams in the nano-second range is being more widely applied as an experimental method. In the case of other accelerators, such as direct accelerators, the pulsing is carried out by the use of special devices[11,12,13]).

The pulse duration of the cyclotron beam, as observed in its utilisation in nuclear spectroscopy experiments generally varies within sufficiently large limits and its consistency with the theoretical value of grouping interval is not verified.

It should be noted that for the same energy (E), geometrical parameters (d, h, R), and dee voltage (V_0), other factors may also determine the pulse duration (such as tuning and extraction conditions). No method or adjusting criterion is available for establishing the cyclotron optimum working conditions from the viewpoint of natural pulsing. The ion time-distribution, i.e. the natural pulse form, though interfering in the duration ascertainment, has hardly been explored. The results obtained so far are inconclusive, if not, indeed, contradictory[15]).

The fact that pulse duration is dependent more on the particular adjustment conditions than on cyclotron general parameters has not been extensively explained.

In the present work we have tried to determine the main factors on which the shape and duration of natural pulsing of the external cyclotron beam depend and to explain this dependence. In this manner, the means for obtaining a more acceptable natural pulsing regime was laid down.

2. The Experimental Arrangement

The measurements on natural modulation pulses have been carried out by time analysis, under high resolution conditions, of the pulse of prompt gamma-ray emission generated by the interaction of

† In the same work, ref.[6]), an alternative equation is resented for the case of cyclotrons with ion source feelers. The uthor obtains this equation by changing the initial speed onditions (at $t = 0$):

$$\tfrac{1}{2} m\dot{x}^2 = eV_0 \cos\theta_0 . \tag{8}$$

This leads to a solution such as

$$\theta = -2 \left(\frac{D}{d} \cos\theta_0\right)^{\frac{1}{2}} \sin\theta_0 . \tag{9}$$

rouping under such conditions would be considerably larger nd even Cohen admits that the results are exaggerated. We onsider that also in the "feeler" dee case, a relation like (1) is ore accurate. Actually, in order that $\dot{x}$ at $t = 0$ be given by), the distance between source slit and feeler must be equal o zero, in other words, there must be an infinite electrical field. his field is practically limited by the break-down conditions a region where gas pressure is not very low.

In most cases, the distance between the feelers is of about he same order as the distance between the dees. For the Y-120 yclotron of the Institute for Atomic Physics of Bucharest, $D = 50$ mm and $d_f = 30$ mm.

[7]) J. E. Draper, Phys. Rev. **90** (1953) 362 A.
[8]) J. E. Draper, Bull. Am. Phys. Soc. Ser. II, **1** (1956) 290.
[9]) J. E. Draper, Rev. Sci. Instr. **29** (1958) 137.
[10]) V. S. Panasiuk, Atomnaya Energia **3** (1957) 47.
[11]) C. M. Turner and S. D. Bloom, Rev. Sci. Instr. **29** (1958) 480.
[12]) W. M. Good, Nucl. Instr. and Meth. **6** (1960) 323.
[13]) T. K. Fowler and W. M. Good, Nucl. Instr. and Meth. **7** (1960) 245.
[14]) G. F. Bogdanov, A. A. Kurashov, B. V. Rybacov and V. A. Sidorov, Atomnaya Energia **1** (1956) 66.
[15]) M. Konrad, Rev. Sci. Instr. **29** (1958) 840.

the beam particles with an aluminium target. The gamma rays were detected by means of a rapid scintillation counter with a stilben crystal. The marking signal was obtained with a plastic scintillator, inserted within the aluminium target, which was directly excited by the accelerated charged particle flux (p,α). In this scintillator the light pulse was produced by a great number of particles (on the order of 10^4), so that the rise time of this pulse could mark, with sufficient accuracy, the total reflection angle is 45°. This special structure made possible an approximately threefold increase of the light flux on photocathode surface. Special care of isolation and screening have been taken which allowed the elimination of perturbatory influences in the radio-frequency range and the measurement of the current of ions falling on the target. A shield was also provided against gamma-ray and neutron. background that may result for other objects exposed to the beam.

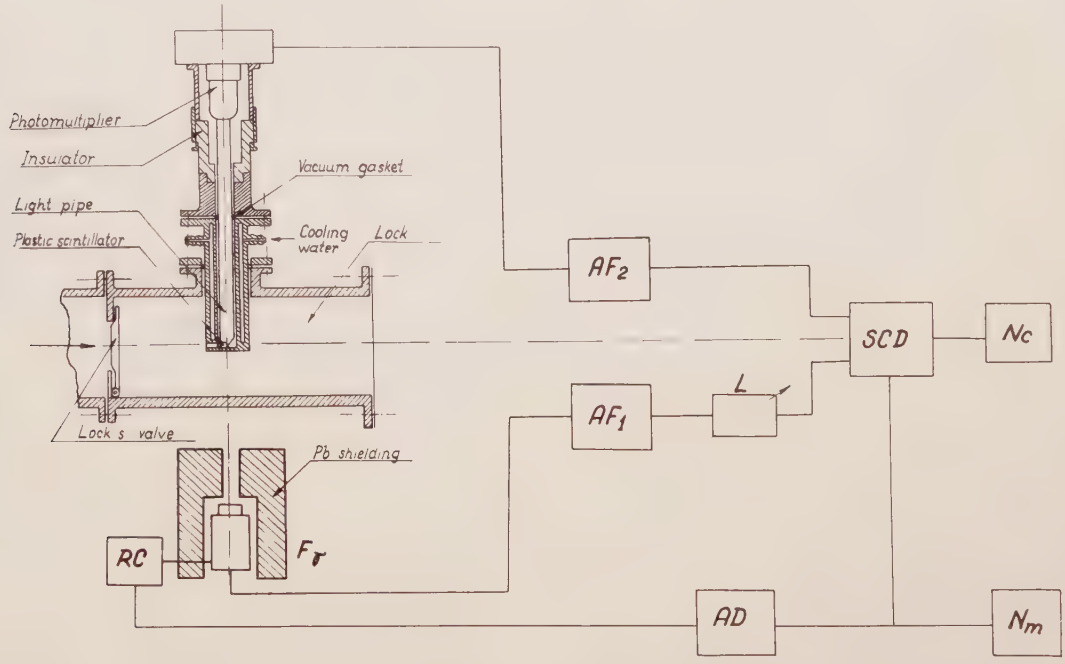

Fig. 1. The experimental setup, the nanosecond timing and the block diagram of the analyzing system. RC-slow cathode follower; AF_1, AF_2-distributed amplifiers and limiters; L-delay line; SCD-fast differential coincidence circuit; AD-slow amplifier and pulse-height discriminator; F_γ-gamma detector; N_c-scaler; N_m-Monitor scaler.

arrival of the accelerated particle pulse. This light pulse was conveyed to a photomultiplier photocathode by means of a plexiglass light pipe; its amplitude depended on the intensity of the intercepted beam. The photomultipliers used for producing electrical pulses were of the RCA 5819 type. In order to obtain a better time resolution, only a central zone of photocathode was used. The experimental arrangement used is shown in fig. 1. The tubular aluminium target is introduced into a vacuum-system lock. This target contains the plastic scintillator and plexiglass light pipe, of a special structure with a plane surface of which the

The electrical pulses from the two photomultipliers, sent from the targets room by means of coaxial cables of the type RK-50, amplified, limited in the upper part, and shaped through distributed amplifiers and limiters, were applied at the input of a fast differential coincidence circuit, having high time resolution and provided with a calibrated delay line, as described in a previous work[17]).

In order to control measurements and to obtain the best possible resolution, a discriminator was introduced on the slow side. This discriminator recorded only the pulses which exceed the limit determined by the threshold. Their total number

was recorded on a monitor-scale. Fig. 2 shows a control curve in self-coincidence, obtained with a Co^{60} source. It is to be noted that it exhibits fairly good symmetry, which is of great importance for measurement interpretation.

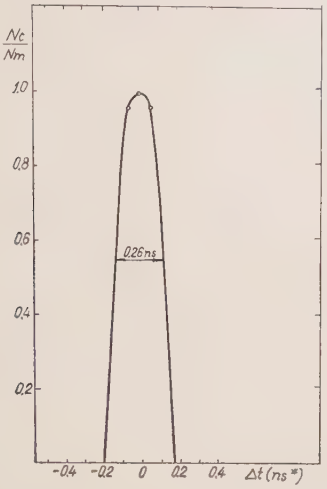

Fig. 2. The control curve of fast coincidence circuit.

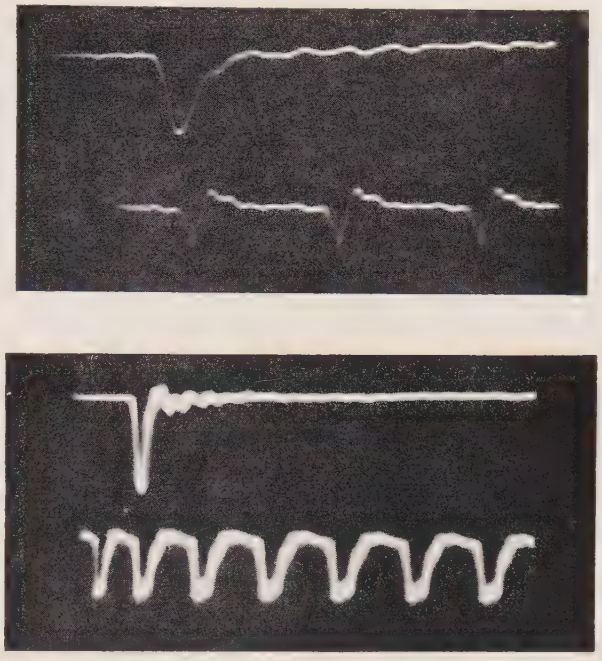

Fig. 3. Photographs of synchroscope display of gamma counter and timing pulses in different conditions.

For general adjustment of the device, the two pulse successions could be made visible with a fast twin synchroscope DESO-1. In fig. 3, (a) and (b), are shown images thus obtained, the upper curve corresponds to the outer counter-pulses (γ) which release the time basis, and the lower one to the timing pulses which operate with a frequency of roughly 10 MHz. As the pulse duration is of the nanosecond order, there is no question of a true reproduction of their shape, the frequency range of the synchroscope being only 60 MHz.

For a given recording duration and at a given delay time to the timing pulse, the number of recorded pulses is in proportion to the beam intensity within the analyser resolution. By representing this number as a function of the relative delay (the representation of the delay line), a curve is obtained reproducing—within the resolution limit—the shape of pulse of accelerated particles. In the present case the resolution could not be accurately measured by a separate experiment but from the results obtained it should be inferred to be of the nanosecond order (10^{-9}s).

It is to be remarked that using a sampling method, as in the case above, one can obtain *not* the exact shape of a single pulse but a mean in the considered measure interval.

At any rate, this mediated shape is the one that appears in practically all measurements made by the pulsed beam method and actually determines the spectrometer resolution.

Compared with other utilized methods of analysis where the timing signal is obtained from cyclotron radio-frequency voltage[14,15,16,18]), the above method offers the advantage of being insensitive to the phase and frequency variations which inherently appear during the functioning process and may at times exceed in value the very duration of current pulse.

3. Measurements and Results

The measurements have revealed that the form and duration of cyclotron natural pulses vary greatly, depending on the special working conditions for a given energy value and the same dee

[16]) G. F. Bogdanov, N. A. Vlasov, S. N. Kalinin, B. V. Rybacov and V. A. Sidorov, Atomnaya Energia **3** (1957) 204.

[17]) N. Martalogu, F. Ţintă, R. Dumitrescu, I. Korgueva and M. Molea, Revue de Physique **4** (1959) 457.

[18]) A. Kurashov, A. F. Linev and B. V. Sidorov, Atomnaya Energia **5** (1958) 135.

voltage, not being univocally determined by the d, V_0, e/m, ω parameters.

In figs. 4, 5 and 6 the $N = f(t)$ curves are reproduced (reduced to monitor), which were obtained for molecular hydrogen ions H_2^+ accelerated to an energy of 11 MeV (therefore below the thereshold of $Al^{27}(p,n)$ reaction).

In fig. 7 are shown the $N = f(t)$ curves obtained for alpha particles accelerated at 22 MeV, with dee voltages nearing those used for H_2^+. Neutrons

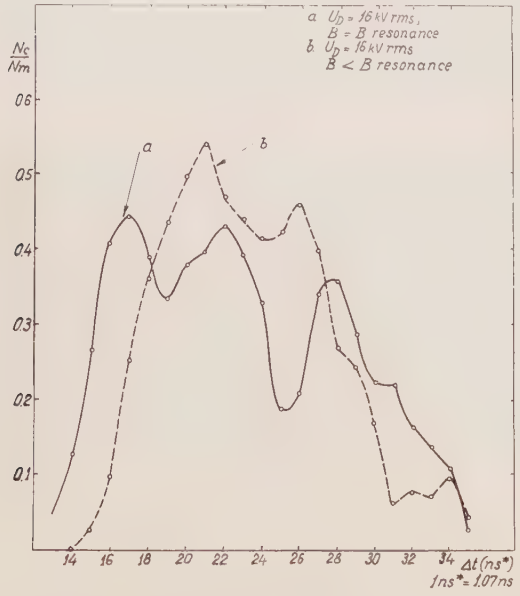

Fig. 4. H_2^+ natural bunching pulses of large duration and loose shape. Obs: The coincidence counting rate N_c corresponds to the beam current (in arbitrary units) at a given time by taking into account the monitor data: The same remark is valid for the figures 5, 6, 7, 8,, 9 and 10.

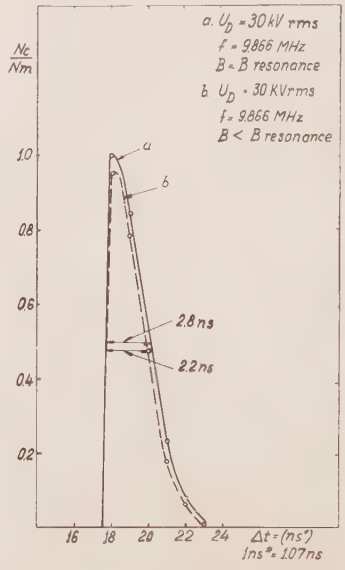

Fig. 6. H_2^+ natural bunching pulse of the smallest duration and obvious asymmetry.

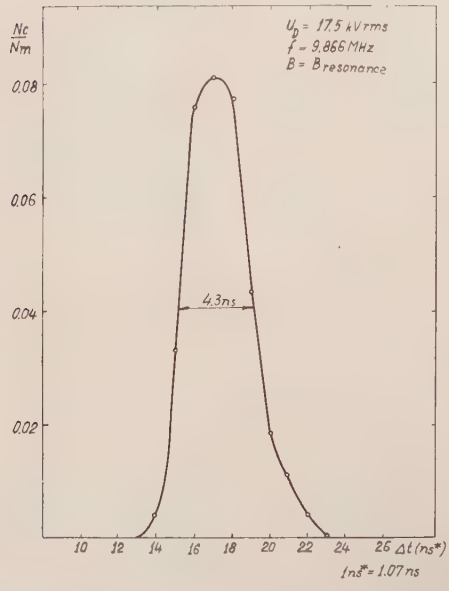

Fig. 5. H_2^+ natural bunching pulse of small duration.

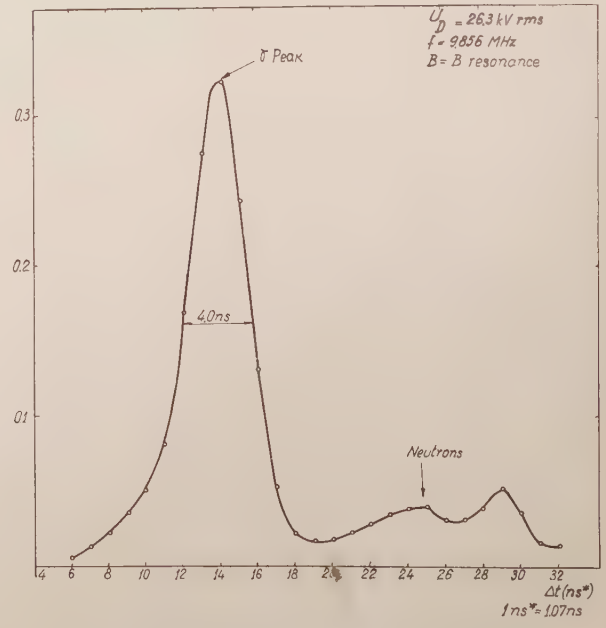

Fig. 7. Alpha-particles natural bunching pulse.

resulting from (α, n) or (α, 2n) reactions are separated owing to the distinct time-of-flight of the target counter-distance and are recorded distinctly at larger delays.

On the present theoretical basis, phase-grouping and, consequently, the pulse shape and duration

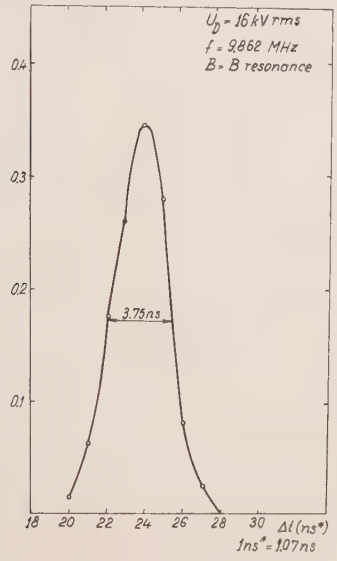

Fig. 8. H_2^+ natural bunching pulse for a low dee voltage.

ought to have been for all these cases practically the same.

The dee-to-ground voltage showed values of about 28 kV_{rms} and the accelerating frequency near 10 MHz (T = 100 ns).

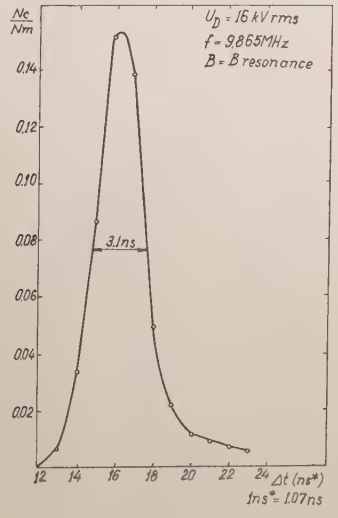

Fig. 9. H_2^+ natural bunching pulse for $B = B$ resonance.

The pulse duration for various dee voltages was measured at the same final energy in order to check if this varies linearly with the applied voltage value as according to the theory. Fig. 8 shows, for instance, the results obtained for 15 kV_{rms} (H_2^+).

It has been generally found that under given

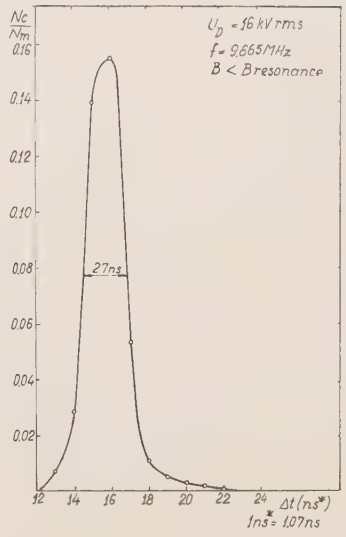

Fig. 10. H_2^+ natural bunching pulse for $B = B$ resonance.

functioning conditions a decrease of the voltage on the dees does not result in a corresponding tightening up of natural modulation pulse, the results being, in some cases, in the opposite direction. Contrarily very small changes of the cyclotron tuning parameters, such as alteration of magnetic field with a small fraction rate around resonance value, led to detectable variations in the pulse shape and duration (figs. 9, 10).

Because of their effects, the operations of accelerating dynamics adjustment devices, as are in the Y-120 cyclotron case the compensatory coils of median plane and especially azimuthal "shims" (fig. 11) which were operated by distant control during the accelerator functioning, prove to be much more important.

Pulse-time measurements were combined with optical observations of the beam cross section by means of a plate coated with a luminescent substance upon which the beam was focused (fig. 11, W). The obtained image was not always, contrary to expectation, a single bright spot, but, in many

cases, it appeared as a discontinuous aggregate of 2–4 spots which were generally quite separable and not co-linear. Fig. 12 shows the sketch of such an image. It has been found that when more than one spot was obtained, the natural measured pulse showed a decidedly longer duration and assumed a loose shape, as shown in fig. 4. In certain cases, 2 or more quite well separated maxima could be obtained. By current adjustment in the median plane compensatory coils, the c and d spots could be made to disappear, while by operating the 4 pairs of azimuthal shims, only one of the a and b spots would remain in place. Transition occurred gradually; intensity growth in one spot being accompanied by decrease in the other.

of the effect of introducing some diaphragms to geometrically limit certain beam cross-sections before the deflection and focusing systems as well as after them, or between the focusing system with quadrupole lenses and deflector magnet. Positive results (at times, sufficiently important) have been obtained generally, despite a reduction in the beam intensity.

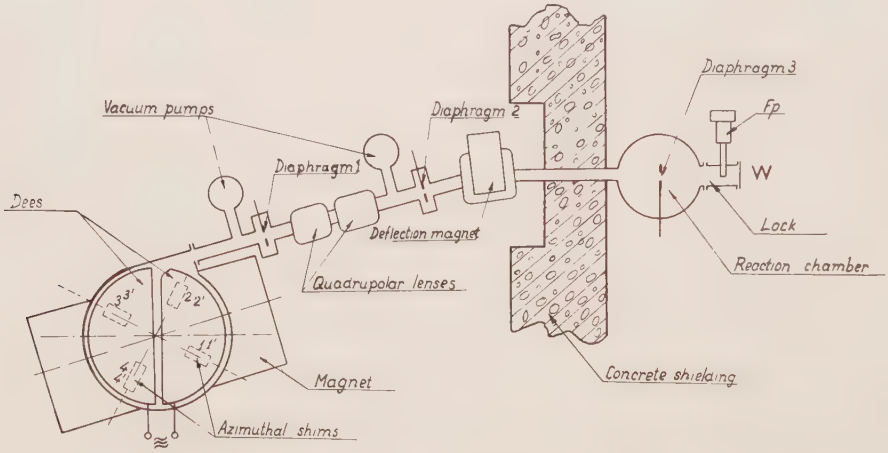

Fig. 11. The general arrangement of the Y-120 cyclotron.

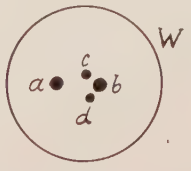

Fig. 12. Beam image on the luminescent plate. (Obs.: the drawing represents only the position of the spots.)

The obtainment of a single spot (a single beam) coincided with observation of a small duration natural pulse of generally regular shape such as in fig. 5 and 6.

Aiming, for practical uses, at diminishing the pulse duration, as its spatial distribution observation was not possible in all cases, a study was made

These remarks have made it clear that spatial dispersion of the beam is accompanied by energy and temporal dispersion. Energy spread could be estimated—introducing diaphragms after the focusing system and before deflector magnet—by the magnetic field intensity, the chosen geometry, and the distance between a and b spots. In certain cases, for a nominal energy of 11 MeV for H_2^+, the difference between a and b beams amounted to 300 keV.

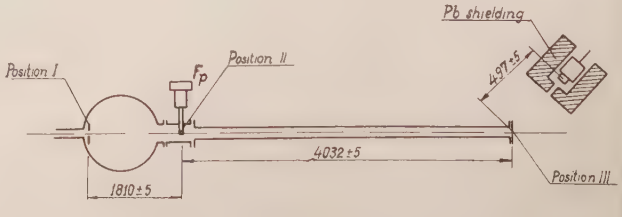

Fig. 13. The positions of the target during the experiments.

Pulse duration measurements have been made at various distances from the cyclotron beam exit (fig. 13) by recording the gamma rays emitted by an aluminium target intercepting a portion of the

beam at the different points. The same device was utilized for obtaining timing pulses and, of course, adequate measures were taken to record only gamma rays coming from a single place. Results obtained by these measurements permitted the ascertainment of the accelerated ions', mean energy by the time-of-flight method, but they did not show that pulse width changes linearly with the

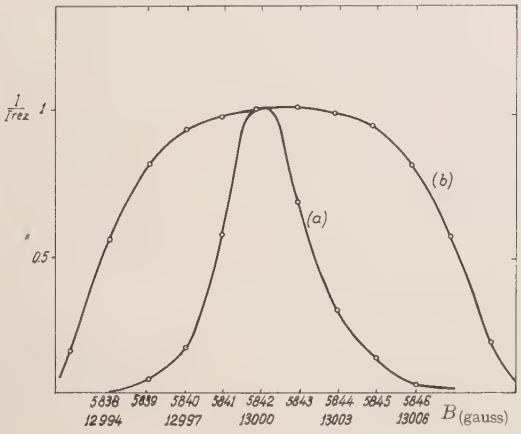

Fig. 14.
Beam extraction curve. a. Sharp resonance. b. Broad resonance.

flight path. These results agree with those gathered by others[19]), who even noticed a pulse duration decrease with the gradual flight path increase. This situation can only be explained by assuming that lower energy ions are leaving the cyclotron prior to those of higher energy; this shows also that pulse duration is not directly determined by the energy dispersion.

It was assumed from the beginning of this study that large time and energy dispersions of the ions are connected to the relationship between the radial oscillation amplitude and the separation between successive orbits during the accelerating process. These assumptions have also been confirmed by finding an abrupt growth of pulse duration occurring simultaneously with a magnetic field symmetry deterioration caused by the chamber displacement within the main magnet or the dees' vertical displacement. Measurements and adjustments of magnetic field azimuthal symmetry (which allowed the reduction of the first harmonic of the field from a value of about 15 gauss to one of below 2 gauss) and a good adjustment of the dees displacement geometry and the extraction channel have led to a noticeable reduction of pulse duration. A still greater operating stability was thus obtained.

During the adjustment period it was noted that selection of magnetic field geometry (and thus of accelerating dynamics) which is sensitive in altering the cyclotron beam extraction curve, as in fig. 14 (a), generally leads to short natural pulses under conditions of good stability.

In the cases of the shortest natural pulse durations it was found that their form exhibited a characteristic asymmetry as in fig. 6. But this was not the situation which was most stable or most frequently obtained. Generally, stability of working conditions during which natural pulsing occurred was not very good and the reproduction of certain conditions determining the dynamics of the acceleration process at times proved difficult.

The maintenance of the same values of frequency, magnetic field, voltage on dees, deflecting voltage, positions for source and azimuthal shims (that is, all remote-controlled parameters under normal cyclotron working conditions) could not ensure a perfect reproduction of pulsing, although the selected beam intensity and general accelerator conduct remained practically unchanged. Supplementary adjustments were always necessary, even in the case where a thermal stability was realised.

Pulses which were more frequently obtained were of the shape seen in fig. 5, and these must be taken as representing the normal state. In all, 238 plots concerning natural modulation pulse shape have been made during the experimental operations.

4. Discussion of Results and Conclusions

Though, as was shown above, shape and duration of natural pulses obtained are affected by finite resolution of the time analyser, the acquired data show that this influence is sufficiently small as not to conceal the main features or the more fundamental changes occurring to these impulses. A comparison between the obtained results and the estimation based on present theoretical data[6]) could be made only with reference to pulse base width, as it corresponds to the grouping interval,

[19]) B. V. Rybacov and V. A. Sidorov, Spektrometria bystryh neitronov (Moskva, 1958).

G. Taking, as an example, the case of acceleration molecular hydrogen ions, H_2^+, to an energy of 11 MeV with an accelerating voltage of 27 kV $_{rms}$ ($V_0 = 27\sqrt{2} = 38.2$ kV) and using the Y-120 cyclotron ($R = 525$ mm and $d = 50$ mm), one obtains, on the basis of formula (7)

$$G = \left(\frac{R}{2d}\right)^2 \frac{eV_0}{E} = 0.095 .$$

Thus, at a period of RF of 100 ns ($f = 10$ MHz, the grouping interval will be $t = GT = 9.5$ ns. As one can easily see, the formula inferred by us has the advantage of being easily applied, energies being constantly measured in eV. As mentioned above, the same result is obtained for 22 MeV alpha particles. This value agrees fairly well with experimental data obtained in the case of shorter duration pulses. The shape of these pulses allows better time resolutions up to an order of magnitude (half-width at half-maximum) to be obtained. For somewhat larger duration pulses (fig. 4) experimental results led us to conclude that it is a question of deflection channel entrance of ion groupings belonging to different orbits. This is brought about by the existence of certain radial oscillations. As the radial grouping holds a finite interval, being roughly $\frac{1}{3}$ of the distance between successive orbits, this process can take place when the final radial oscillation amplitudes are smaller than the distance between two successive orbits. In this case, the ions of the various orbits enter the deflection channel with various phases and therefore at different times. This occurs on account of phase variation from one orbit to another during the acceleration process.

Phase variation from one orbit to another in the final beam region is to be attributed, to the largest extent, to the rapid field decrease at the magnet edge. In this zone the magnetic field, B, is smaller than the resonance one, B^*, so that ions come late with respect to the phase of RF voltage. The delay of ion groupings on successive orbits is

$$T = T_i - T - \frac{2\pi}{\omega}\left(\frac{B^*}{B} - 1\right). \tag{10}$$

For our cyclotron the difference between B^* and B is 1.5–2% (ref.[21])), so that for $f = 10$ MHz:

$$T = \frac{2\pi}{\omega}\frac{B^* - B}{B} = 2 \times 10^{-9}\,\mathrm{s} . \tag{11}$$

For larger oscillation amplitudes and depending on the position of the instantaneous rotation centre, ions of different orbits whose difference of order is n, may enter the deflection channel. In such a case, the time difference becomes:

$$\Delta T = n\frac{2\pi}{\omega}\frac{B^* - B}{B} . \tag{12}$$

The above considerations reveal that in the case of radial oscillations the ions belonging to orbits of lower order (hence of smaller energy) will enter first, followed after ΔT by ions of the final orbit (of greater energy). In this way the above assumption appears justified, and the results concerning pulseduration changes with flight path can be explained.

The energy dispersion of the beam, evaluated by measuring bright spot distances on the W fluorescent plate, (fig. 11) suggests that orbits with difference of order up to 7 can enter the deflection channel. This is in agreement with pulses with large duration and irregular shapes observed under such conditions (fig. 4).

The improvement made with the aid of various diaphragms introduced on the beam path can be explained in a similar way. These diaphragms may select ion groupings resulting from a single orbit; also the condition of shortest pulses coincides with the acquisition of a cyclotron sharp tuning curve. In this case, a good separation of various orbits takes place in the deflection channel.

The above considerations call for certain reservation concerning the time-of-flight method of measuring the cyclotron beam energy spread; this method is used assuming that energy distribution on pulse duration is uniform[20]).

It is also possible that the particle groupings which form the pulses may not be identically reproduced for consecutive rotation periods, as radial oscillation frequency differs from the accelerating frequency. The probability that ions from various orbits enter the deflection channel during the same radio-frequency cycle diminishes with increasing separation between successive orbits resulting from

[20]) K. G. Malmfors, J. Kjellman and A. Nilson, Nucl. Instr. **1** (1957) 186.

[21]) A. Valeriu, Studii si cercetări de Fizică **10** (1959) 329.

increasing the acceleration voltage. Moreover, this increase of acceleration voltage also decreases total phase shift during the acceleration process.

It thus becomes possible to obtain shorter pulses of the cyclotron beam for higher radio-frequency voltages in apparent contradiction to (1) grouping relation.

A certain decrease in pulses duration can, in specific cases, be obtained by turning to critical extraction conditions: voltage adjustment of the deflecting plate or the magnetic field. In this case, some of more tightly energetic and temporal grouped ions will be selected out of the ion bunch. This will undoubtedly result in a certain reduction of beam intensity. Best results have been obtained by a slight lowering of the magnetic field to below the value corresponding to highest extracted beam intensity.

In cases when the pulse base width agrees with grouping duration (G) it can be considered that ions originating from a single orbit could be selected. Pulse shape takes, as shown above, a peculiar aspect (fig. 6). We considered that in such a case, pulse shape of the external cyclotron beam ought to be determined by source extraction conditions at the outset of the accelerating process. We tried to infer this shape in the various ion extraction assumptions from the ion source, considering the relative phase evolution during the accelerating process. Using ΔN for the number of source-emitted ions in a phase interval $\Delta\theta_0, \theta_0 = \omega_e t_0$ being the phase of the voltage applied on the extracting dee, the following relation may be written for the ion current

$$i_s = \frac{e\Delta N}{\Delta t_0} = \frac{e\omega_e \cdot \Delta N}{\Delta\theta_0} = f(\theta_0) \,. \tag{13}$$

The relation (13) expresses, therefore, the dependence of the current of the ions drifting out of the ion source upon the instantaneous value of the accelerating voltage for $V = V_0 \cos \omega_e t_0$.

The pulse shape at the cyclotron exit may be described by

$$i_p = \frac{e\Delta N}{\Delta t} = \frac{e\omega_e \Delta N}{\Delta\theta} = g(\theta) \,, \tag{14}$$

θ representing the phase at the end of the accelerating process. For an outside observer $\Delta\theta = \omega_e \Delta t$. From relation (2)

$$\Delta\theta = -2G \sin\theta_0 \cos\theta_0 \, \Delta\theta_0 \,. \tag{15}$$

In relations (13), (14), (15), $\Delta\theta_0$ and $\Delta\theta$ ought to be very small. If ΔN represents the same ion number in (13) and (14), it follows that

$$g(\theta)\,\Delta\theta = f(\theta_0)\,\Delta\theta_0 \,. \tag{16}$$

Relations (15) and (16) are to be compatible so that

$$g(\theta) = \frac{f(\theta_0)}{-2G \sin\theta_0 \cos\theta_0} \,. \tag{17}$$

Taking into account that $\theta_0 = \arcsin\sqrt{-\theta/G}$ it is clear that $g(\theta)$ is determined by $f(\theta_0)$. The graphic representation of the function $g(\theta)$ gives the pulse shape, if a correct expression for $f(\theta_0)$ is found.

Several possibilities were examined for $f(\theta_0)$:

1. That $f(\theta_0) = A$ is the situation in which the current of ions would not depend either on phase or dees voltage, being invariable in time. (Of course, only those ions are accelerated which leave the source in the phase-range $= -\frac{1}{2}\pi < \theta_0 < \frac{1}{2}\pi$.) In this case

$$g(\theta) = \frac{A}{-2G \sin\theta_0 \cos\theta_0} = \frac{A}{-2G\sqrt{-\theta/G}\,\sqrt{1 - |\theta|/G}} \,. \tag{18}$$

If we take grouping interval G as the reference unit either for the for phase angle or for time, and consider that negative sign for phase means that ion phase is late against the phase of RF voltage we get a function of the form:

$$y = \frac{K}{\sqrt{x}\,\sqrt{1-x}} \tag{19}$$

in which $0 \leqslant x \leqslant 1$. The function is all the time positive and at field existence boundaries becomes $+\infty$. Its integral is convergent along the whole existence domain: according to previous considerations it is necessary that

$$\int_{-G}^{0} g(\theta)\,\mathrm{d}\theta = \int_{-\frac{1}{2}\pi}^{+\frac{1}{2}\pi} f(\theta_0)\,\mathrm{d}\theta_0 \,. \tag{20}$$

Relation (20) was used for checking up the calculation. This function, as well as the integral, was computed for a uniform succession of x values, comprised between 0 and 1. The function is represented in fig. 15a. As it may be seen, the

curve is symmetrical to the centre of the existence domain. In the case of a finite resolution of the time analyser, better than G, pulses with two symmetrical peaks should be observed. In the present case, the resolution of the time analyser would have allowed the separation of these two peaks, if they had actually existed.

2. We proceeded to examine the situation in which the emitted source current depends on the electric voltage applied on the extractor dee, respectively $f(\theta_0) = A\ (V_0 \cos\theta_0)^n$.

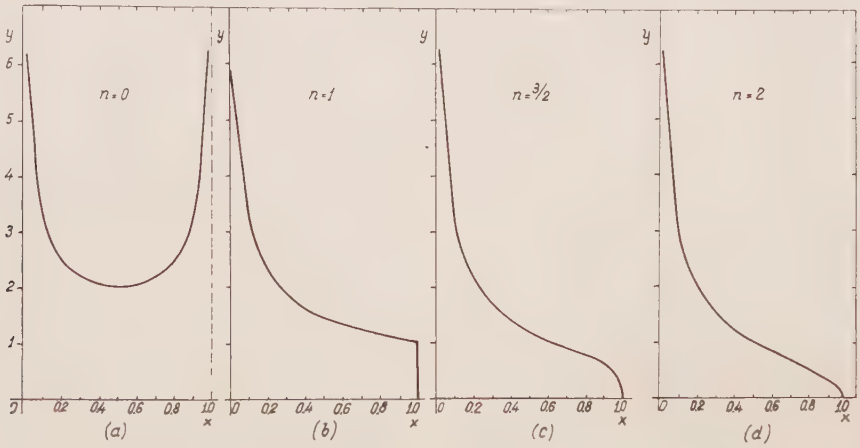

Fig. 15. Graphs of $g(\theta)$ functions corresponding to various extraction laws.

Similarly, as in the case $n = 0$ the following functions were obtained:

$$n = 1\,, \quad y = \frac{K}{\sqrt{x}} \qquad (21) \qquad \text{(fig. 15b)}$$

$$n = \tfrac{3}{2}\,, \quad y = K\frac{\sqrt[4]{1-x}}{\sqrt{x}} \qquad (22) \qquad \text{(fig. 15c)}$$

$$n = 2\,, \quad y = K\frac{\sqrt{1-x}}{\sqrt{x}}\,. \qquad (23) \qquad \text{(fig. 15d)}$$

These functions have been calculated for identical x value series comprised between 0 and 1, as well as their definite integrals. Computations were made with CIFA-2 electronic computer. More difficult was the integral computation for $n = \frac{3}{2}$ which cannot be integrated through a finite combination of elementary functions. As it may be seen, curves show a marked asymmetry and corresponding pulses would present a single peak. We consider that the most justified expression for $f(\theta_0)$ corresponds to function (22), and that the current of ions is drifted out of the ion source according to spatial charge low. There, of course, can be no discussion of physical existence of an instantaneous current of ions infinitely great just at the beginning of grouping interval, electrostatic repulsion—among other things—prevents it, so this value will, in any case, be a finite one, though very considerable compared to the rest of grouping interval. This fact appears to be in accord with the examination of other experimental data. Indeed, the plot of the total current of ions increases continuously with applied dee voltage and no saturation phenomenon is observed up to voltages of about 80 kV_{rms} (ref.[22])). Its aspect suggests a parabola of $\frac{3}{2}$ degree; approximating the results obtained by straight line, this one would not pass through the origin. The fact that no external beam is to be obtained practically within a certain minimum value of accelerating voltage, is explained (besides relativistic effects) through the smallness of the separation between successive orbits which is impeding the beam's extraction.

In order to obtain analytically a curve closer to those which could be experimentally observed, the functions were also calculated which corresponded to a resolution curve of Gauss shape for equivalent semi-widths (resolutions): $\delta = 0.15$ G and $\delta = 0.3$ G, for $-0.7 < x_1 < 1.4$ $(n = \frac{3}{2})$

[22]) N. D. Fedorov and I. A. Holmovskii, Pribory i tekhnika eksperimenta, Nr. 6 (1959) 27.

$\delta = 0.15\text{G}$; $y = \int_{-\infty}^{+\infty} \frac{\sqrt{1-x}}{x} e^{-\frac{(x-x_i)^2}{0.033}} dx$ (24) (fig. 16a)

$\delta = 0.3\text{G}$; $y = \int_{-\infty}^{+\infty} \frac{\sqrt{1-x}}{\sqrt{x}} e^{-\frac{(x-x_i)^2}{0.13}} dx$ (25) (fig. 16)

These curves (especially (24)) resemble fairly the ones we obtained in the case of the narrow pulses.

reaches the maximum value, respectively:

$$\frac{d}{dx_i} \int_{-\infty}^{+\infty} y(x) r(x - x_i)\, dx = 0 \qquad (27a)$$

$$\frac{d^2}{dx_i^2} \int_{-\infty}^{+\infty} y(x) r(x - x_i)\, dx < 0\,. \qquad (27b)$$

For the function (22) the following results were obtained:

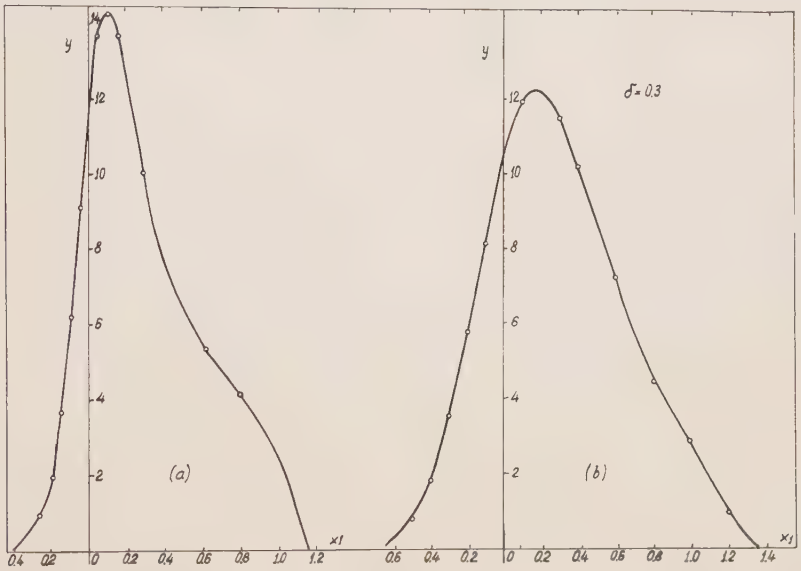

Fig. 16. Theoretical shapes of the cyclotron natural pulses corresponding to a gaussian resolving curve.

The marked asymmetry becomes, obviously, less distinct when analyser resolution is not so good. For a given case, it is normal to consider the time analyser resolution curve itself itself (the prompt coincidence curve instead of Gauss curve). Careful examination of spectrum raised by time-of-flight method in other cyclotrons, at good time-resolution conditions reveals in some cases that the gamma line shape presents an asymmetry of the same kind.

The highest resolution (half-width at half-maximum) to be obtained by using cyclotron natural bunch, may be computed, according to what has been stated above, as follows:

$$\int_{-\infty}^{+\infty} y(x) r(x - \rho)\, dx = \tfrac{1}{2} \int_{-\infty}^{+\infty} y(x) r(x - x_m)\, dx \qquad (26)$$

in which $r(x)$ is the resolution curve equation of the experimental device and x_m the value of x_i for which the integral

$$\int_{-\infty}^{+\infty} y(x) r(x - x_i)\, dx$$

1. Rectangular resolution curve, with half-width of $\delta = 1.15$, $\rho = 0.18$.

2. Gaussian resolution curve, with half-width $\delta = 0.15$. $\rho = 0.255$.

3. Gaussian resolution curve with half-width $\delta = 0.3$, $\rho = 0.485$.

The above example illustrates the fact that final half-width greatly depends on analyser resolution characteristics and that the resultant resolution cannot be computed by combining two terms quadratically, one corresponding to the pulse, the other to the analyser's resolution.

This suggests that it may be useful if stable acceleration dynamic conditions could be realised to permit ion extraction from the final orbit only and employ time analysers with higher resolutions than the ones used currently so far. In this situation, cyclotron work with heavy ions could especially offer very attractive possibilities, the G grouping

interval being narrower than when working with protons, deuterons or alpha particles. The examination of relation (7) shows, further, that in the case of protons it is more convenient as far as natural pulse is concerned, that they be accelerated as hydrogen molecular ions.

At a given final radius—for instance in the case of a given cyclotron—acceleration frequency is the same for accelerating protons or hydrogen molecular ions, for an identical energy per nucleon. However, the grouping interval G or the pulse duration will be twice as great in the first case at an identical voltage on dees:

$$G_{\mathrm{p}} = \left(\frac{R}{2d}\right)^2 \frac{eV}{E}; \tag{28}$$

$$G_{\mathrm{H_2^+}} = \left(\frac{R}{2d}\right)^2 \frac{eV}{2E}; \tag{29}$$

$$G_{\mathrm{p}} = 2G_{\mathrm{H_2^+}}. \tag{30}$$

In order to make maximum use of the cyclotron natural bunching possibilities it appears necessary that a better geometry and higher stability of magnetic field and dees should be worked out. What was shown above may be used as an indication for a corresponding cyclotron adjustment.

We are grateful to the I.A.P. cyclotron operating crew, especially to engineer M. V. Macovei, for their assistance during the experiment. We are also thankful to Dr. K. G. Malmfors for the data he so kindly sent to us.

NUCLEAR INSTRUMENTS AND METHODS 12 (1961) 151–154; NORTH-HOLLAND PUBLISHING CO.

SIMPLE SCHEME FOR USING THE SELECTIVE STORAGE OF A MULTICHANNEL PULSE HEIGHT ANALYSER IN COINCIDENCE COUNTING

ROLF NORDHAGEN

Fysisk Institut, Universitetet i Oslo, Blindern, Norway

Received 18 March 1961

A description is given of a simple scheme for using one single channel analyser in the simultaneous selective storing of two coincidence spectra in the memory of a R.C.L. 256 channel pulseheight analyser. An extension of this scheme to observing simultaneously four spectra coincident with four adjacent channels is mentioned.

1. Selective Storage

A selective storage system is incorporated in most comercially available multichannel pulseheight analysers with parallel memory (ferrite cores). In these analysers the pulseheight information is transformed to a digital number and counted by an address scaler. This selects the pulseheight channel into which the pulse is stored. By adding a fixed number of counts to the address scaler simultaneously with the incoming information, a pulse can be selectively stored in a part of the memory different from where it should otherwise appear. This is achieved by resetting the address scaler to the fixed number instead of zero at the beginning of a count cycle. To prevent overlap of the different memory parts during selective storage the address overflow is taken from the channel preceding the channel to which reset is made. In this way further advance of the address scaler is stopped.

The selective storage system to be described in this communication is used in connection with a 256 channel analyser made by R.C.L.[1]). In this analyser the selective storage mode splits the memory into four parts by taking the address overflow from the carry of the 2^5 digit in the address scaler. Separate inputs are provided for signals resetting the address scaler to channel 64, 128 or 192. In the absence of any of these signals a pulse will be stored in the first quarter at the memory, the simultaneous appearance of a signal at the "reset to 64" input will store it in the second quarter etc. For moderate counting rates the system can be used to simultaneously analyse the pulses from four separate counters. The pulses are all added together into the main input of the analyser, and separate pulse circuits attached to each of the four counters provide the reset signals storing each pulse in the appropriate part of the memory.

In coincidence counting a separate coincidence gate in the analyser is activated to permit the analysis of a pulse. When no fast resolving times are required a simple scheme is to take the coincidence pulses from the output of a single channel analyser. In a two counter experiment the output of one counter is fed into the analyser and of the other via the single channel analyser to the coincidence gate. The pulses analysed will be those in coincidence with the part of the spectrum falling between the boundaries of the single channel analyser. When coincidence spectra are required for more than one setting of the single channel analyser, it is tempting to shorten this time-consuming process by the use of the selective storage mode. The storing signals then has to be provided by single channel analysers, all attached to the same counter and feeding their outputs to the appropriate reset inputs (fig. 1). It is important here to note that in addition the outputs from the single channel analysers have to be added together and fed to the coincidence gate input. Consequently the full use of the selective storage will need four

[1]) Model 20611 256 Channel Pulseheight Analyser, Radiation Counter Laboratories Inc. Skokie, Ill., U.S.A.

single channel analysers and the adding circuit with proper polarity.

2. Simplified Scheme

It is the purpose of this communication to report the considerably simpler scheme presently in use with the R.C.L. analyser installed at the Oslo University Van de Graaff laboratory. As the region

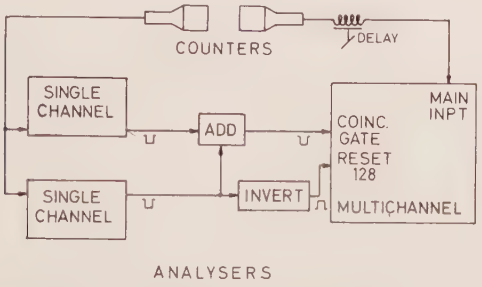

Fig. 1. 2 channel coincidence selective storage scheme. Separate, differential channels.

of pulse-height studied here (from a NaI scintillation counter irradiated with γ-rays from 0.5 to 12 MeV) is too large to have all details revealed by 64 channels only, the memory is split into two parts of 128 channels each†.

Therefore only one routing signal, reset to 128, is necessary. The important simplification occurs, however, when we relax the requirement that each of the two coincidence channels should be independently variable. By letting their adjacent boundaries be a common one and the upper channel

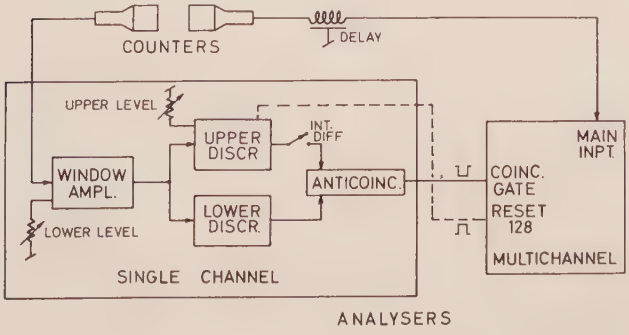

Fig. 2. Simple selective storage modification of standard single channel analyser. – – – – – – Additional output.

be an integral discriminator, only one single channel analyser may be used as shown in fig. 2.

The single channel analysers employed are a modified version of the Johnstone analyser[2]), with the lower level set by the bias of the input window amplifier and the upper level set by an independently variable bias on the upper level discriminator When a pulse passes the upper level the output from the lower level discriminator is blocked. The absence of this anticoincidence will let the analyser work as a integral discriminator above the lower level. For simple selective storage the negative output from the single channel analyser in the integral mode is fed to the multichannel analyser coincidence gate. A separate positive output from the upper level†† is fed to the "reset to 128" input. When a pulse then crosses both levels a coincident pulse appearing at the main multichannel input will be let through the coincidence gate and also routed to the second half of the memory. To appear in the first half the upper level must not be crossed and the routing system will act as an anticoincidence for this part of the memory.

If a separate unit is built for coincidence selective storage the possibility of also making the upper channel differential should be considered. This is easily achieved by inserting a single discriminator

† The R.C.L. analyser (delivered in April 1959) had to be slightly modified to work properly on selective storage.

The timing of the reset pulses had to be altered. These have to be present after the normal "address reset to 0" occurs when a pulse enters the analyser. However, to prevent memory shift during pulse storage, a busy signal will block the reset signals during this period. The busy signal is provided at least in the diagrams, but appears immediately a pulse enters the analyser. To give the reset signals a chance to work, the busy signal is later delayed, but insufficiently, and the reset signals are blocked simultaneously with the disappearance of the "reset to 0" pulse and will not change this reset. When the reset block signal is taken from the cathode of the left half instead of the right half of V-740 in the Analog to Digital Converter the first fast pulse initiating analysis is not added on to it. With the built in delay this will give a sufficient gap after the disappearance of "reset to 0" pulse to allow changing the setting of the address scaler.

Some confusion was introduced by the drawings of the accumulate switch at the memory control panel. The selective storage section IX was seen to provide reset to 0 pulses, but it should, and does, provide 2^5 carry pulses from the address scaler to the address overflow to cut the memory short at 64 channels. This can be changed to 128 at the back section of the "Recording in Channels" (S 117) switch from where the input to S-108 sect. IX actually is taken.

†† Taken from the cathode of the upper level trigger tube 6BQ7A through an added cathode follower.

[2]) C. W. Johnstone, Nucleonics **11**, No. 1 (1953) 36.

with its separate bias between the two normal discriminators in the standard single channel analyser. The positive output of this discriminator is then fed to the "reset to 128" input, but otherwise nothing is

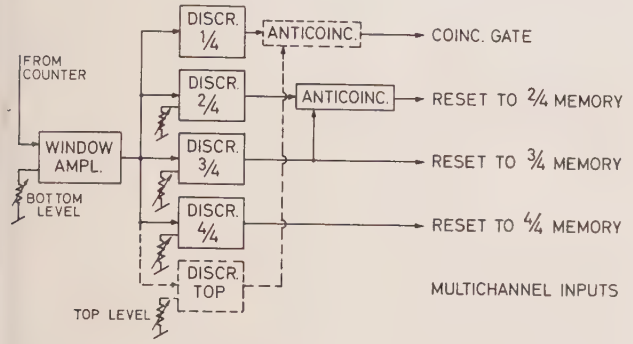

Fig. 3. 4 channel coincidence selective storage unit. All channels adjacent. – – – – Additional circuitry for differential top level.

altered in the single channel analyser itself. The scheme is easily extended to several channels with adjacent boundaries. A four channel device as shown in fig. 3, will consist of four single discriminators fed by one amplifier. The bottom level discriminator is feeding a negative pulse to the coincidence gate, and from the succeeding levels are fed positive storing signals to the successive reset inputs. If also the top channel is wanted as a differential one, a fifth discriminator has to be added which will block the bottom level output when fired. An extra anticoincidence has to be added in the output from the second discriminator to block this output when also the third discriminator fires. This is to prevent simultaneous resetting the memory to the first channel in both the second and the third quarter of the memory, instead of in the third alone. No anticoincidence is needed in the third discriminator output, as resetting to the first channel in the fourth quarter is equivalent to the simultaneous resetting in both the second and third quarter.

3. Adjustment and Timing

Adjusting channel settings to the appropriate pulseheights is done in the self-coincidence scheme, where the same counter feeds not only any single channel analysers but also the main multichannel input.

In the simple scheme with one single channel analyser the multichannel analyser can be working in the normal accumulate mode and the coincidence gate can be activated by the other analyser in the differential mode. The single channel analyser should again be turned to integral operation before selective storage is used. Frequently coincidence gates are set in the part of the spectrum lying above channel 128. Only the lower part of the spectrum may often then be needed and is displayed in the first 128 channels. It should be kept in mind that if self-coincident selective storage is attempted with this setting no pulses are stored properly.

The main problem in making these schemes work is to achieve appropriate timing. The standard single channel analysers work on the falling edge of the analysed pulses to ensure that crossing of the upper level has taken place. With RC-differentiated pulses this gives rise to considerable "walk" in time with pulse size. At moderate counting speeds this can be overcome in the customary manner by sufficiently delaying the main input pulses and letting the coincidence and storing pulses be wide enough to encompass the time variation. When a single channel analyser is used for selective storage, however, no such timing problems exist. The delay caused by the multichannel analyser "reset to 0" in the reset system takes care of any tendency of the bottom level discriminator to give an output before any higher levels have been crossed by an incoming pulse. Thus the discriminators can work on the front edge of the input pulses, and the anticoincidences and outputs can be taken directly without any pulse shaping†. This scheme must only be used with specially made units, as they will not work on their own as standard differential analysers. The way self-coincidences are used to set the discriminators levels is also affected. Now selective storage has to be used for setting.

4. Conclusion

The simple scheme with one single channel analyser has been used and found to be very helpful for

† The anticoincidences can easily be obtained in the Johnstone analysers by feeding the negative outputs from the discriminator triggers to the free third grid in the discriminator tubes to be blocked.

general survey work. For complicated experiments one of the more refined systems seems necessary. An additional feature found to be very valuable is the possibility of comparing different coincidence counting rates without laborious normalisation of over-all counting rates.

Acknowledgements

The present work was sponsored by the Royal Norwegian Council for Scientific and Technical Research and this is gratefully acknowledged. The author is indebted to Mr. J. Sandstad for helpful discussions.

NUCLEAR INSTRUMENTS AND METHODS **12** (1961) 155–168; NORTH-HOLLAND PUBLISHING CO.

BETRIEBSZUSTÄNDE DES MIKROTRONS MIT GETEILTEM MAGNET (RACETRACK MICROTRON)

A. PAULIN

J. Stefan Institut, Ljubljana, Jugoslavia

Eingegangen am 17. Januar 1961

The possibility of building a racetrack microtron for electrons is discussed. With proper adjustment of distances, voltages and phases between various elements the electrons can be obtained by field emission in the accelerating gap. Strong focusing magnetic fields are not necessary for currents smaller than 1 μA. For currents above 1 μA it would be convenient to use quadrupole lenses for the focusing of the accelerated beam. There is a possibility of building a high energy electron accelerator with extremely low energy spread using the microtron in combination with a linear accelerator.

1. Einführung

Die Beschränkung des gewöhnlichen Mikrotrons auf kleine Energien führte Schwinger[1]) auf den Vorschlag den Magnet in zwei Hälften zu teilen und anstatt einen Resonator im Magnetfeld eine Serie

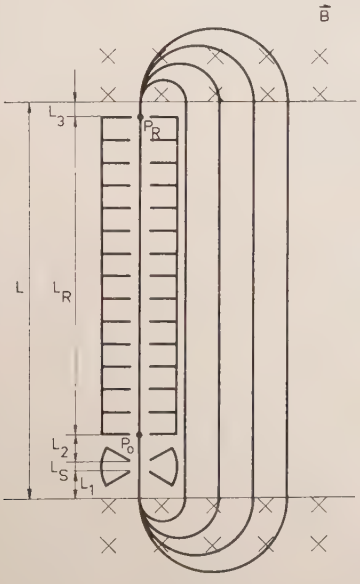

Abb. 1.

von Resonatoren außerhalb des homogenen Magnetfeldes anzubringen (Abb. 1). Damit würde es ermöglicht den Luftspalt des Magneten beinahe an den Durchmesser des Teilchenstrahles zu verkleinern und den Energiegewinn ΔW_r pro Umlauf sehr zu vergrößern. Für die Resonanzbedingungen würden wir somit ein Magnetfeld haben, daß technisch viel günstiger wäre als das, welches bei gewöhnlichen Mikrotronen verlangt wird (1070 Gauß bei $\lambda = 10$ cm). Das modiffizirte Prinzip beruht auf der Tatsache, daß das Elektron im ER-Gebiet für jeden Durchlauf die gleiche Zeit braucht und es gilt die eine Bedingung des gewöhnlichen Mikrotrons[2]):

$$T_{n+1} - T_n = \Delta T = \frac{2\pi}{ec^2} \frac{\Delta W_r}{B} = b\tau\,, \quad b = 1, 2, \ldots \quad (1)$$

wobei T_n die Umlaufszeit beim n-ten und τ die Hochfrequenzperiode ist.

Es wird im Folgenden versucht zu zeigen, daß es für den Bau eines solchen Mikrotrons schon mit heute zur Verfügung stehenden Bauelementen keine übergroßen Schwierigkeiten gäbe. Ein ökonomisch gerechtfertigter Elektronenbeschleuniger bis zur Strahlungsdämpfungsgrenze größter Energiehomogenität (etwa $0.5^0/_{00}$) und wie bei allen Mikrotronen mit vollständiger Herausziehung des Elektronenstrahles wäre möglich.

Die zweite Bedingungsgleichung des gewöhnlichen Mikrotrons, die mit der Einspritzung der Elektronen zusammenhängt, kann nicht direkt auf das "Racetrack Microtron" übertragen werden. Es muß ein leicht ausführlicher Weg zur Gewinnung der Elektronen und der Übergang in das ER-Gebiet

[1]) L. I. Schiff, Rev. Sci. Instr. **17** (1946) 6.

[2]) P. A. Redhead, H. LeCaine und W. J. Henderson, Can. J. Research A **28** (1950) 73.

gefunden werden. Weiter wird versucht zu zeigen, daß es mit der Stabilität und Fokussierung des Elektronenstrahles keine Schwierigkeiten gibt.

2. Beschleunigung

Bei der folgenden Behandlung setzen wir eine Vorrichtung gemäß der Abb. 1 voraus. Dabei soll der Linearbeschleuniger der Beschleunigung, der Hohlraumresonator der Gewinnung der Elektronen dienen. Die gegenseitigen Entfernungen und Phasen sollen so festgesetzt werden, daß die phasenstabile Fläche nicht zu klein wird und daß die Beschleunigungselemente die Elektronen nicht nur beschleunigen sondern auch fokussieren.

Fliegt das Elektron synchron mit der elektromagnetischen Welle des Linearbeschleunigers, kann sein Energiezuwachs leicht bestimmt werden. Dasselbe gilt für den Hohlraumresonator, wenn wir voraussetzen, daß sein elektrisches Feld dem Felde eines planparallelen Kondensators gleicht. Da die Elektronen schon nach einigen Umläufen fast die Lichtgeschwindigkeit erreichen (ER-Gebiet), dürfte es angebracht sein, die Phasengeschwindigkeit v_p der elektromagnetischen Welle gleich der Lichtgeschwindigkeit zu nehmen. So würden die Teilchen besonders bei dem ersten Durchgang hinter dem Wanderfeld zurückbleiben; deswegen werden sie weniger beschleunigt. Die Tatsache, daß bei den ersten Durchgängen die Elektronengeschwindigkeit noch merklich von der Lichtgeschwindigkeit abweicht, bringt der ersten Bedingungsgleichung (1) neue hinzu.

Beschränken wir uns auf die Nähe der Simetrieachse des Linearbeschleunigers und setzen $v_p = c$ voraus. So befinden sich die Teilchen im elektromagnetischen Felde[3]:

$$E_z = E_m \, e^{-\alpha z} \cos\left[\omega\left(t_z - \frac{z}{c}\right) + \varphi\right] \tag{2}$$

$$E_r = -\frac{\pi}{\lambda} E_m \, e^{-\alpha z} \, r \sin\left[\omega\left(t_z - \frac{z}{c}\right) + \varphi\right] \tag{3}$$

$$B_\psi = \frac{E_r}{c}, \tag{4}$$

wo r, φ und $z = c \int_0^{t_z} \beta \, dt$ zylindrische Koordinaten bezeichnen, und beim Eintritt in die Röhre der Länge $L_R = \lambda l_R$ $z = t_z = 0$ gesetzt wird. Im ER-Gebiet gewinnt das Sollelektron beim Durchlaufen der Röhre die Energie $\Delta W_r = eU_R \cos\varphi_r$ wo die Anfangsphase φ in die Resonanzphase φ_r übergeht und

$$U_R = \int_0^{L_R} E_m \, e^{-\alpha z} \, dz = \frac{1 - e^{-\alpha L_R}}{\alpha} E_m .$$

2.1 GEWINUNG UND VORBESCHLEUNIGUNG DER ELEKTRONEN

Mann könnte die Elektronen in das Beschleunigersystem einspritzen oder am unteren Rande des Beschleunigungsspaltes des Resonators (Abb. 1) eine thermische Kathode anbringen. Vielleicht wäre es günstiger die Elektronen anstatt von einer thermischen Kathode, durch Feldemission zu gewinnen. Impulsbetriebene Feldemissionskathoden lieferten bereits Ströme von 30 A[4]). Da der Strom exponential mit der angelegten Spannung zunimmt, hat die Feldemission auch den Vorzug, daß die meisten Elektronen im Augenblick starten, wo am Resonator die größte Spannung herrscht und wir gerade diese Elektronen in das phasenstabile Bereich einfangen. Um eine möglichst hohe Güte des Resonators und niedrige Durchschlagsgefahr zu erreichen, soll der Beschleunigungsspalt möglichst lang sein. So ist es günstig den Resonator so zu konstruieren, daß die Elektronen, die zur Zeit maximaler Feldstärke an der Kathode starten, den Resonator in dem Augenblick verlassen, wo die Feldstärke auf Null fällt. Wenn am Beschleunigungsspalt der Länge $L_s = \lambda l_s$ die Spannungsamplitude U_s liegt, so gilt zwischen beiden die Relation[5])

$$\frac{e}{2\pi W_0} \frac{U_s}{l_s} = \tan 2\pi \, l_s , \qquad W_0 = m_0 c^2 . \tag{5}$$

[3]) J. C. Slater, Microwave Electronics (Van Nostrand, Princeton, N. J.) 1950.
[4]) W. P. Dyke und W. W. Dolan, Advances in Electronics 8 (1956) 89.
[5]) A. Paulin, Nucl. Instr. and Meth. 5 (1959) 107.

Die Endgeschwindigkeit beträgt in diesem Falle

$$\beta_s = \frac{A_s}{(1 + A_s^2)^{\frac{1}{2}}}, \qquad A_s = \frac{e}{2\pi W_0} \frac{U_s}{l_s}. \tag{6}$$

In praktischen Fällen wird β_s etwa 0.8 bis 0.9 betragen. Die Elektronen bleiben im Linearbeschleuniger besonders beim Eintritt hinter der Welle zurück. Wenn wir, was sich auch in bezug auf die Fokussierung als günstig erweisen wird, voraussetzen, daß das Elektron beim Eintritt ein Feld $E_z = E_m$ und beim Verlassen $E_z = 0$ vorfindet, so können wir in erster Aproximation annehmen, daß sich das Sollelektron im Felde

$$E_z = \frac{U_R}{L_R}\left(1 - \frac{1}{t_R} t_z\right) \tag{7}$$

befindet, wo t_z die Zeit bei z und t_R am Ende der Röhre ist und durch den Ausdruck $\omega t_R = 2\pi l_R + \frac{1}{2}\pi$ gegeben ist. In Abb. 2a und 2b ist neben dem elektrischen Felde, welches das Elektron gemäß Gl. (7)

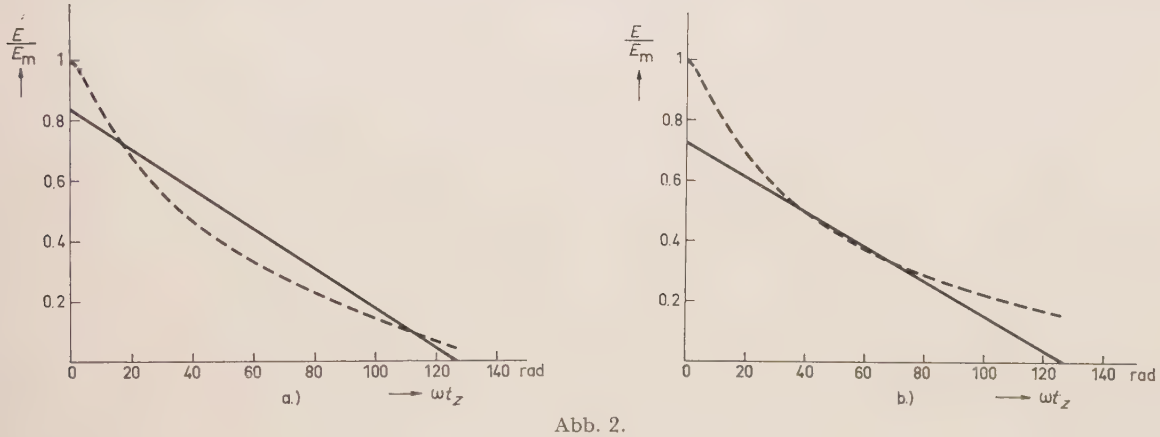

Abb. 2.

wahrnehmen würde, das Feld eingetragen, das das Elektron tatsächlich vorfindet. Die Kurven sind numerisch für $l_R = 20$, $\gamma_m = 20$, $\gamma_s = 2.36$, a) $\exp(\alpha L_R) = \sqrt{2}$ und b) $\exp(\alpha L_R) = 2$ berechnet worden. Da wir mit $\gamma = (1 - \beta^2)^{-\frac{1}{2}}$

$$W_0 \frac{d\gamma_z}{dt} = ec\,\beta_z E_z \tag{8}$$

schreiben können, so folgt mit Hilfe von

$$d\gamma_z = \frac{\beta_z}{(1 - \beta_z^2)^{\frac{3}{2}}} d\beta_z \tag{9}$$

die Verbindung

$$\beta_z\gamma_z = \beta_s\gamma_s + A_R\left[\omega t_z - \frac{1}{2\omega t_R}(\omega t_z)^2\right], \qquad A_R = \frac{1}{2\pi}\frac{\gamma_m}{l_R}, \tag{10}$$

wo γ_m der maximal mögliche Energiezuwachs $(e/W_0)U_R$ ist.

Für das Elektron, daß die Beschleunigerröhre verläßt, gilt

$$\beta_R\gamma_R = \beta_s\gamma_s + \tfrac{1}{2}A_R\,\omega t_R. \tag{11}$$

Wie aus der Gleichung (6) leicht zu ersehen ist, kann $\beta_s\,\gamma_s = A_s$ gesetzt werden.

Bis jetzt haben wir vorausgesetzt, daß die Beschleunigungsröhre so lang ist, daß das Elektron, welches in der Phase 0 in die Röhre eintritt, dieselbe in der Phase $\frac{1}{2}\pi$ verläßt. Doch wie hängt die reduzierte Länge l_R von β_s und γ_m ab? Im Folgenden wird eine Näherungsrechnung für l_R hergeleitet.

Die Bedingung, daß die Phase in Gl. (2) von 0 auf $\frac{1}{2}\pi$ anwächst, kann durch

$$\int_0^{\frac{1}{2}\pi} \mathrm{d}\left[\omega\left(t_z - \frac{z}{c}\right) + \varphi\right] = \tfrac{1}{2}\pi$$

geschrieben werden. Dieser Ausdruck geht durch das Differenzieren der linken Seite in

$$\int_0^{\omega t_R} (1 - \beta_z)\, \mathrm{d}\omega t_z = \tfrac{1}{2}\pi \tag{12}$$

über. Da in der Gleichung (10) β_z schon nahe 1 ist, können wir

$$1 - \beta_z \approx \frac{1}{2(\beta_z \gamma_z)^2} \tag{13}$$

setzen. Aus den Gleichungen (10), (12) und (13) folgt

$$\pi = \int_0^{\omega t_R} \left[\frac{A_R}{2\omega t_R}(\omega t_z)^2 - A_R\, \omega t_z - \beta_s \gamma_s\right]^{-2} \mathrm{d}\omega t_z \tag{14}$$

und nach der Lösung des Integrals

$$\pi = \frac{A_R}{C^2}\left(\frac{1}{\beta_s \gamma_s} + \frac{\overline{\beta}_z}{2\pi l_R C} \ln \frac{C + A_R}{C - A_R}\right),$$

$$C = A_R\left(1 + \frac{1}{\pi A_R l_R}\gamma_s \beta_s \overline{\beta}_z\right)^{\frac{1}{2}}, \qquad \overline{\beta}_z = \frac{4 l_R}{4 l_R + 1}. \tag{15}$$

Wenn $4 l_R \gg 1$ kann die Gl. (15) vereinfacht werden:

$$\pi = \frac{A_R}{C^2}\left(\frac{1}{\beta_s \gamma_s} + \frac{1}{2\pi l_R C} \ln \frac{C + A_R}{C - A_R}\right),$$

$$C = A_R\left(1 + \frac{1}{\pi A_R l_R}\gamma_s \beta_s\right)^{\frac{1}{2}}. \tag{15a}$$

Durch die Einführung des Linearbeschleunigers wird das Magnetfeld weniger durch die Resonanzbedingungen (1) als durch die Abmessungen des Linearbeschleunigers begrenzt. Der Durchmesser des ersten Elektronenkreises muß größer als der Halbmesser der Beschleunigerröhre sein. Die Elektronen dürfen bei der zweiten und weiteren Beschleunigungen vom Hohlraumresonator gebremst sein. Damit könnte man die Fokussierungseigenschaften des Hohl-raumresonators, wie noch gezeigt wird, ausnützen und seinen Verbrauch an Mikrowellenenergie, der im Vergleich zum Energieverlußt im Linearbeschleuniger groß sein würde, herabsetzen. Nehmen wir die Hochfrequenzphase des Resonators und seine Entfernung $L_2 = \lambda l_2$ vom Linearbeschleuniger so, daß die schon die Lichtgeschwindigkeit besitzenden Elektronen die Mitte des Resonantorspaltes zur Zeit $\omega t = \frac{1}{2}\pi$ (entspricht $(U_s/L_s \cos \omega t = 0)$ passieren und zur Resonanzphase φ_r in die Beschleunigerröhre einfliegen! Eine einfache Rechnung würde ergeben, daß der Hohlraumresonator um die Phase

$$\Delta\varphi = \frac{\pi}{2} + \frac{\pi l_s - \varphi_r}{1 - \beta_s} \tag{16}$$

der Hochfrequenz im Linearbeschleuniger voreilen und von demselben die reduzierte Länge

$$l_2 = \frac{\beta_s}{2\pi} \cdot \frac{\pi l_s - \varphi_r}{1 - \beta_s} \tag{17}$$

enfernt sein soll. Setzen wir aber voraus, daß die Elektronen in dem Augenblick in den Hohlraumresonator einflögen, als das Feld sie gerade zu bremsen anfinge und somit die Elektronen dem Resonator die Energie auf Kosten des Linearbeschleunigers liefern würden, so übergehen die Gleichungen (16) und (17) in

$$\Delta\varphi = \frac{\pi}{2} + \frac{2\pi l_s - \varphi_r}{1 - \beta_s} \tag{16a}$$

und

$$l_2 = \frac{\beta_s}{2\pi} \cdot \frac{2\pi l_s - \varphi_r}{1 - \beta_s} . \tag{17a}$$

Mit Hilfe von Gleichungen (15a), (6), (5), (17), (16) und (11) kann mit $\lambda = 10$ cm und $\varphi_r = 18°$ folgende Tabelle zusammengestellt werden:

Tabelle 1

L_R (m)	l_R	γ_m	A_s	β_s	γ_s	U (MV)	l_s	l_2	$\Delta\varphi$ (rad)	$\beta_R\gamma_R$	β_R	γ_R
1	10	20	1.07	0.731	1.465	0.449	0.1306	0.0415	1.93	11.32	0.996	11.4
2	20	20	2.13	0.905	2.36	1.230	0.180	0.380	4.21	12.25	0.996	12.3
1	10	10	2.10	0.903	2.33	1.210	0.179	0.367	4.13	7.22	0.990	7.3

Die Werte für γ_m sind ähnlich wie sie aus den Daten für Mark II[6]) folgen würden, wenn wir ihn entsprechend verkürzen. Die Werte für γ_R können nur als informative Werte gelten und das wegen der Aproximation, die wir mit Gleichung (7) eingeführt haben. Genauere Daten sollten numerisch mit Hilfe des Feldes, in dem sich das Elektron tatsächlich befindet, berechnet werden. Der Verlauf ist für $l_R = 20$, $\gamma_m = 20$ in Abb. 2. eingetragen. Für $\exp(\alpha L_R) = 2$ folgt $\gamma_R = 13.7$, $\omega t_R = 127.0$ rad und für $\exp(\alpha L_R) = \sqrt{2}$ folgt $\gamma_R = 10.5$ und $\omega t_R = 127.2$ rad.

2.2. Der Übergang in echte Mikrotronbeschleunigung

Das Elektron, welches bei der ersten Beschleunigung den Linearbeschleuniger im Augenblick verläßt, als das Beschleunigungsfeld auf 0 gefallen ist, soll für den Weg von P_R bis P_0 die Zeit $T_{R,0}$ verbrauchen und in der Phase $\varphi_{r,1}$ in die Beschleunigungsröhre wieder eintreffen. So gestellt sich zur Bedingungsgleichung (1) noch die zweite Bedingungsgleichung

$$T_{R,0} = \frac{2\pi W_0}{ec^2} \cdot \frac{\gamma_R}{B} + \frac{L_{R\,0}}{c\beta_R} = \left(a_0 - \frac{\omega t_R - 2\pi l_R - \varphi_{r,1}}{2\pi}\right)\tau , \quad L_{R,0} = L + L_1 + L_s + L_2 + L_3 , \tag{18}$$

wo a_0 eine ganze Zahl ist, hinzu. Mit Hilfe von (1) folgt aus (18)

$$b\frac{\gamma_R}{\Delta\gamma_r} + \frac{l_{R,0}}{\beta_R} = a_0 - \frac{\omega t_R - 2\pi l_R - \varphi_{r,1}}{2\pi} . \tag{19}$$

Obgleich beim zweiten Einfliegen in den Linearbeschleuniger das Elektron schon beinahe die Lichtgeschwindigkeit besitzt, kann die Verschiebung wegen dem linearen Teil doch nicht gänzlich unberück-

[6]) R. F. Post und N. S. Shiren, Rev. Sci. Instr. **26** (1955) 205.

sichtigt bleiben. Wir sind noch nicht in echter Mikrotonbeschleunigung, bei welcher das Sollelektron immer dieselbe Resonanzphase besitzt.

Um von P_0 zu P_0 zu gelangen braucht das Elektron bei n-ter Beschleunigung die Zeit

$$T_n = \frac{1}{c}\int_0^{L_R} \frac{dz}{\beta_{z,n}} + \frac{1}{c}\frac{L_{R,0}}{\beta_n} + \frac{2\pi W_0}{ec^2 B}\gamma_n . \tag{20}$$

Da wir beim zweiten und weiteren Durchgängen durch den Linearbeschleuniger

$$\gamma_{z,n} = \gamma_{n-1} + D_n(1 - e^{-\alpha z}), \qquad D_n = \frac{\gamma_m}{1 - e^{-\alpha L_R}}\cos\varphi_n \tag{21}$$

setzen können, so folgt mit der Gleichung (20):

$$T_n = \frac{2\pi W_0}{ec^2 B}\gamma_n + \frac{L_{R,0}}{c\beta_n} + \frac{1}{c\alpha}\left[\ln\frac{\sqrt{\gamma_n^2 - 1} - \gamma_n}{\sqrt{\gamma_{n-1}^2 - 1} - \gamma_{n-1}} - \frac{A_n}{(A_n^2 - 1)^{\frac{1}{2}}}\ln\frac{A_n\gamma_n - 1 - \sqrt{A_n^2 - 1}\sqrt{\gamma_n^2 - 1}}{A_n\gamma_{n-1} - 1 - \sqrt{A_n^2 - 1}\sqrt{\gamma_{n-1}^2 - 1}}\, e^{\alpha L_R}\right]$$

$$= \left(a_n - \frac{\varphi_{r,n} - \varphi_{r,n+1}}{2\pi}\right)\tau , \qquad \gamma_n = \gamma_R + \sum_{k=1}^{n}\Delta\gamma_k , \qquad A_n = \gamma_{n-1} + D_n , \tag{22}$$

wobei a_n eine ganze Zahl ist. Die Resonanzphasen $\varphi_{r,n}$ sollen positiv sein, um nicht im defokussierenden Gebiet zu liegen und um nicht das stabile Phasengebiet zusehr zu verkleinern[7]). Man kann auch ohne äußere Einspritzung durch Varieren von Spannungen am Beschleunigungsspalt und an der Beschleungungsröhre, durch Varieren der gegenseitigen Entfernungen solche Bedingungen aufstellen, daß wir in echte Mikrotronbeschleunigung gelangen. Es könnte auch wünschenswert sein anstatt einen zwei Vorbeschleunigungsresonatoren zu nehmen. Bei den Daten gemäß der Tabelle 1 scheint es erlaubt zu sein anzunehmen, daß die Energie γ_2 schon groß genug ist um die Elektronengeschwindigkeit gleich der Lichtgeschwindigkeit zu nehmen. So können in diesem Falle die Bedingungsgleichungen des "Racetrack Microtrons" wie folgt zusammengefaßt werden:

$$b = \frac{2\pi W_0}{ec\lambda}\cdot\frac{\Delta\gamma}{B}, \tag{1a}$$

$$b\frac{\gamma_R}{\Delta\gamma_r} + \frac{l_{R,0}}{\beta_R} = a_0 - \frac{\omega t_R - 2\pi l_R - \varphi_{r,1}}{2\pi}, \tag{19}$$

$$b\frac{\gamma_1}{\Delta\gamma_r} + \frac{l_R}{\alpha L_R}\left[\ln\frac{\sqrt{\gamma_1^2 - 1} - \gamma_1}{\sqrt{\gamma_0^2 - 1} - \gamma_0} - \frac{A_1}{\sqrt{A_1^2 - 1}}\ln\frac{A_1\gamma_1 - 1 - \sqrt{A_1^2 - 1}\sqrt{\gamma_1^2 - 1}}{A_1\gamma_0 - 1 - \sqrt{A_1^2 - 1}\sqrt{\gamma_0^2 - 1}}\, e^{\alpha L_R}\right] + \frac{l_{R,0}}{\beta_1}$$

$$= a_1 - \frac{\varphi_{r,1} - \varphi_{r,2}}{2\pi}, \tag{22a}$$

$$b\frac{\gamma_2}{\Delta\gamma_r} + \frac{l_R}{\alpha L_R}\left[\ln\frac{\sqrt{\gamma_2^2 - 1} - \gamma_2}{\sqrt{\gamma_1^2 - 1} - \gamma_R} - \frac{A_2}{\sqrt{A_2^2 - 1}}\ln\frac{A_2\gamma_2 - 1 - \sqrt{A_2^2 - 1}\sqrt{\gamma_2^2 - 1}}{A_2\gamma_1 - 1 - \sqrt{A_2^2 - 1}\sqrt{\gamma_1^2 - 1}}\, e^{\alpha L_R}\right] + \frac{l_{R,0}}{\beta_2}$$

$$= a_2 - \frac{\varphi_{r,2} - \varphi_r}{2\pi}, \tag{22b}$$

$$b\frac{\gamma_3}{\Delta\gamma_r} + 2l = a_2 + b . \tag{22c}$$

Wegen des zu großen Durchmessers des Linearbeschleunigers wird b größer als 1 genommen werden müssen. Auf den ersten Blick könnte es scheinen, daß es in den Gl. (22a) und (22b) nicht notwendig ist β verschieden

[7]) E. M. Moroz, Dokl. Akad. Nauk SSSR **106** (1956) 986.

von 1 zu nehmen und für den Ausdruck in Klammern einen von αL_R verschiedenen Wert zu nehmen. Doch die Werte $\gamma_0 = 12.5$, $\gamma_1 = 25.3$, $\exp(\alpha L_R) = 2$, $l_R = 20$ würden eine Verschiebung von etwa 15° ergeben. Deswegen wird, wenn wir $b = 2$ setzen, $a_2 - a_1 = 1$ gesetzt werden müssen um immer eine positive Phase zu haben. Die Verschiebung zufolge der Gl. (22b) ist schon viel kleiner.

3. Stabilität

Die Bedingungsgleichung (1) des "Racetrack Microtrons" ist im ER-Gebiet gleich der Bedingungsgleichung des gewöhnlichen Mikrotrons. Hat man die Bestimmung der phasenstabilen Flächen in der Phasen-Energieebene nach Schmelzer[8]) im Auge, so ist leicht einzusehen, daß beim "Racetrack Microtron" im ER-Gebiet die phasenstabile Fläche dieselbe Form als beim gewöhnlichen Mikrotron hat. Im Übergangsgebiet wird jedoch die phasenstabile Fläche etwas verschoben sein. Man müßte sie für jeden Fall einzeln verfolgen, wenn man deren genaue Form können möchte.

Nach Roberts[9]) kann man durch Teilung beider Magnete in mehrere Segmente stabile AG-Fokussierung erzielen. Setzen wir aber ein homogenes Magnetfeld mit scharfem Rande (das homogene Magnetfeld fällt mit dem geometrischen Ende der Pole auf Null) voraus, dann bildet die eine Magnethälfte in horizontaler Richtung den Elektronenstrahl identisch ab und tangiert den Strahl in vertikaler Richtung nicht. Die Lage ist ähnlich wie bei einem Linearbeschleuniger, bei dem einem Beschleuniger ein leerer Raum vom $L_{R,0}$, bzw. $L_{R,0} + 2\pi\rho$ (ρ = Halbmesser des Strahles im Magnetfeld) folgen und der Elektronenstrahl wieder in denselben Beschleuniger zurückkehren würde. Wie beim Linearbeschleuniger liegt auch hier eine langsame Änderung des Elektronenstrahles in radialer Richtung vor.

Es bestehen doch einige Unterschiede. Bei den ersten Durchgängen ist die Elektronengeschwindigkeit nicht gleich der Phasengeschwindigkeit. Wegen der vielen Durchläufe des Elektronenstrahles durch dieselbe Beschleunigungsröhre wird man die Abstoßungskräfte der Raumladung auch im ER-Gebiet etwas später als beim Linearbeschleuniger vernachlässigen können. Da die Phasenstabilität nicht durch die Beschleunigungsröhre, sondern durch das Mikrotron als Ganzes bestimmt wird, so liegt im Gegensatz zum Linearbeschleuniger, das stabile Sollelektron im Gebiet wo die Beschleunigungsröhre fokussiert. Nach einigen Umläufen wächst die Teilchenenergie sehr an. Die Elektronen fliegen dahin, weder von den Raumladungseffekten, noch von den fokussirenden Kräften der elektromagnetischen Welle beeinflußt zu werden. Die Kräfte beider sind schon viel zu klein.

Ein homogenes Magnetfeld mit scharfem Rande ist unrealisierbar. Damit wirklich ein jeder Elektronenstrahl die eine Magnethälfte senkrecht verlassen, senkrecht in die andere eintreten und senkrecht wieder die Beschleunigungsröhre durchfliegen würde, könnte man beim Aus-bzw. Wiedereintritt an der Grenze der einen Magnethälfte und der linearen Strecke das Magnetfeld schwächen oder verstärken. Das können für jeden Strahl separat in senkrechter Richtung verschiebbare Eisenstücke oder mit veränderlichem Strom durchflossene Spulen bewirken. So würde jeder Strahl separat korrigiert sein. Da die Strahlen genügend auseinander liegen, dürfte das dem Konstrukteur keine größeren Schwierigkeiten bereiten. Wegen der Möglichkeit der Korrektion wären die Anforderungen auf die Homogenität des Magneten kleiner als beim gewöhnlichen Mikrotron mit gleicher Zahl von Umlaufsbahnen.

3.1 EINFLUSS DES MAGNETRANDES

Der korrigierte Strahl sollte senkrecht die eine Magnethälfte verlassen und wieder senkrecht in die andere eintreten. Die Außenteile des Strahles hätten, wenn auch eine ganz kleine, Geschwindigkeit in radialer oder vertikaler Richtung. Auf diese Teilstrahlen wirkt nach Herzog[10]) das Streufeld des Magneten als eine dünne Linse mit der Brennweite $f_x = \rho \operatorname{cotan} \varepsilon$ in radialer bzw. $f_y = -\rho \operatorname{cotan} \varepsilon$ in vertikaler Richtung. Dabei bildet der betreffende Teilstrahl den Winkel ε mit der senkrecht austretenden Geraden. Ein Teilstrahl wird beim Verlassen der einen Magnethälfte in einer Richtung fokussiert und

[8]) C. Schmelzer, Z. Naturforschg. **7a** (1952) 808.
[9]) A. Roberts, Ann. Phys. **4** (1958) 115.
[10]) R. F. K. Herzog, Acta phys. Austriaca **4** (1951) 431.

in anderer Richtung defokussiert. Beim Wiedereintritt in das Magnetfeld geschieht gerade das Umgekehrte. Der Teil, der früher fokussiert wurde, wird jetzt defokussiert und umgekehrt. Da eine Kombination einer fokussierenden und defokussierenden Linse gleicher Brennweite in einer Fokussierenden resultiert, wirkt also das zerstreute Feld beim Verlassen und Wiedereintritt des Magnetfeldes schwach fokussierend, zumindest nicht defokussierend. Wir können die weitere Behandlung auf die defokussierenden Kräfte der Raumladung und die fokussierenden Kräfte des Linearbeschleunigers beschränken.

3.2. FOKUSSIERUNGSKRÄFTE DER BESCHLEUNIGUNGSELEMENTE

Wie schon anfangs angenommen wurde, starten die Elektronen im Beschleunigungsspalt des Holraumresonators (Abb. 1), der sie auch vorbeschleunigt. Dieselben werden beim ersten Durchgang durch die Beschleunigungsröhre des Linearbeschleunigers zusätzlich vorbeschleunigt, die eine Magnethälfte dreht sie um 180° und läßt sie in die leere lineare Strecke eintreten. Die zweite Magnethälfte bringt sie wieder in die mit Beschleunigungselementen besetzte Strecke. Die Beschleunigungswirkung einzelner Beschleunigungselemente auf die Beschleunigung der Teilchen wurde schon am Anfang ermittelt. Jetzt soll noch deren Fokussierungswirkung – die Wirkung senkrecht auf die Strahlenachse – bestimmt werden. Es werden getrennt behandelt die Beschleunigungsröhre des Linearbeschleunigers im ER-Gebiet, somit beim zweiten und weiteren Durchgängen, die Beschleunigungsröhre bei erster Beschleunigung, der Beschleunigungsspalt des Hohlraumresonators beim zweiten und weiteren Durchgängen und seine Fokussierungseigenschaft bei der Vorbeschleunigung. Um zu übersehbaren Resultaten zu kommen, werden mehrere Vereinfachungen angenommen. Bei der Berechnung der Bewegungsgröße p wird $r - r_1$ und bei der Berechnung von $r\,p = p_1$ als konstant angenommen. In der Beschleunigungsröhre wird nur die gewünschte Grundkomponente der Wanderwelle berücksichtigt.

Wir gehen von der Kraft $\boldsymbol{F}$, die auf ein Elektron im elektromagnetischen Felde ausgeübt wird, aus. Da die radiale Geschwindigkeit gegenüber der axialen vernachlässigt werden kann, können wir:

$$F_r = e(E_r - c\beta B_\psi) = -e(1-\beta)\frac{\pi}{\lambda}E_m \sin\left[\omega\left(t_z - \frac{z}{c}\right) + \varphi\right] e^{-\alpha z} r \tag{23}$$

schreiben, wobei wir für E_r und B_ψ die Ausdrücke (3) und (4) eingesetzt haben. Für den zweiten und weitere Durchgänge ändert sich der Ausdruck

$$\sin\left[\omega\left(t_z - \frac{z}{c}\right) + \varphi\right]$$

beim Durchlaufen der Röhre nur wenig. Da auch schon β sehr nahe an 1 liegt, und es somit als konstant angenommen werden kann, schreiben wir für

$$z = c\int_0^{t_z} \beta\,\mathrm{d}t \approx c\beta t_z$$

und

$$\sin\left[\omega\left(t_z - \frac{z}{c}\right) + \varphi\right] \approx \omega t_z(1-\beta)\cos\varphi + \sin\varphi\,.$$

So folgt für die Änderung der Bewegungsgröße:

$$p_2 - p_1 = -\frac{\pi}{2}\frac{eE_m}{\lambda\omega} r_1 \int_0^{\omega t_R} \frac{e^{-H\omega t_z}}{(\gamma_{n-1} + D - D\,e^{-H\omega t_z})^2} \cdot \left[\frac{\omega t_z}{2} \cdot \frac{1}{(\gamma_{n-1} + D - D\,e^{-H\omega t_z})^2}\cos\varphi + \sin\varphi\right] \mathrm{d}\omega t_z\,,$$

$$H = \frac{\alpha L_R}{\omega t_R} = \frac{\alpha L_R}{2\pi l_R} \tag{24}$$

und nach der Lösung

$$p_2 - p_1 = -\frac{\pi W_0}{2c^2} f \frac{1 - e^{-\alpha L_R}}{\alpha L_R \cos\varphi_n} r_1 \left(\frac{1}{6H} \left\{ -\frac{\alpha L_R}{\gamma_n^3} + \frac{1}{(D + \gamma_{n-1})^3} \left[\ln \frac{\gamma_n}{\gamma_{n-1} \cdot e^{-\alpha L_R}} \right. \right. \right.$$

$$\left. \left. \left. + (D + \gamma_{n-1}) \left(\frac{1}{\gamma_{n-1}} - \frac{1}{\gamma_n} \right) + \frac{(D + \gamma_{n-1})^2}{2} \left(\frac{1}{\gamma_{n-1}^2} - \frac{1}{\gamma_n^2} \right) \right] \right\} \cos\varphi_n + \left(\frac{1}{\gamma_{n-1}} - \frac{1}{\gamma_n} \right) \sin\varphi \right). \quad (25)$$

Aus der Definitionsgleichung $p = m(\mathrm{d}r/\mathrm{d}t)$ folgt mit der Annahme, daß $p(z) = p_1 = \text{konst.}$ der Ausdruck

$$r_2 - r_1 = \frac{p_1}{m_0} \int_0^{t_z} \frac{\mathrm{d}t}{\gamma_{z,n}}. \quad (26)$$

Die Gleichung (26) ergibt mit (21)

$$r_2 - r_1 = \frac{c}{W_0} \frac{1}{A} \left(L_R + \frac{1}{\alpha} \ln \frac{\gamma_n}{\gamma_{n-1}} \right) p_1 . \quad (27)$$

Beim ersten Durchgang durch die Beschleunigungsröhre kann der Ausdruck

$$\sin \left[\omega \left(t_z - \frac{z}{c} \right) + \varphi \right]$$

der Gleichung (23) nicht als konstant angesehen werden. Vielmehr können wir näherungsweise annehmen, daß er sich gemäß der Gleichung (7) ändert. Durch die Gleichsetzung der Audrücke (2) und (7) gewinnen wir den Ausdruck für cos, bzw. sin der Phase, die das Elektron beim Durchlaufen der Röhre sieht. Mit der Beachtung der Ausdrücke (13) und (10) kommen wir zur Relation

$$p_2 - p_1 = -\frac{\pi}{2} \frac{eE_m}{\lambda\omega} r_1 \int_0^{\omega t_R} \frac{\left[e^{-2\alpha z} - \left(\frac{1 - e^{-\alpha L_R}}{\alpha L_R} \right)^2 \left(1 - \frac{1}{\omega t_R} \omega t_z \right)^2 \right]^{\frac{1}{2}}}{\left[A_s + A_R(\omega t_z) - \frac{1}{2\omega t_R} (\omega t_z)^2 \right]^2} \mathrm{d}\omega t_z . \quad (28)$$

Da in allen praktischen Fällen αL_R zwischen 0.1 und 0.4 liegen dürfte und somit $2\alpha z$ immer kleiner als 0.8 wäre, setzen wir

$$e^{-2\alpha z} = 1 - 2\alpha z + \tfrac{1}{2}(2\alpha z)^2 .$$

Somit übergeht (28) in

$$p_2 - p_1 = -\frac{\pi}{2} \frac{eE_m}{\lambda\omega} r_1 \frac{1}{A_R^2 + 2A_R A_s/R} \left[-\sqrt{\kappa} \left(\frac{1}{R - v} + \frac{1}{R - u} \right) - \sqrt{\theta} \left(\frac{1}{v} + \frac{1}{u} \right) \right.$$

$$\left. + (-\xi u^2 - 3\eta u - 2\theta - \xi uv - \eta v) \frac{I_u}{u - v} + (\xi v^2 + 3\eta v + 2\theta + \xi uv + \eta u) \frac{I_v}{u - v} \right],$$

$$R = \omega t_R , \qquad S = \frac{1 - e^{-\alpha L_R}}{\alpha L_R} ,$$

$$\xi = (2\alpha L_R - S^2)/R^2 , \qquad \eta = (S^2 - \alpha L_R)/R , \qquad \theta = 1 - S^2 , \qquad \kappa = \xi R^2 + 2\eta R + \theta ,$$

$$u = \left[1 + \left(1 + 2 \frac{A_s}{A_R R} \right)^{\frac{1}{2}} \right] R , \qquad v = \left[1 - \left(1 + 2 \frac{A_s}{A_R R} \right)^{\frac{1}{2}} \right] R .$$

$$I_u = \frac{1}{\sigma}\left[\arcsin\frac{(\xi u+\eta)(R-u)-\sigma^2}{(\eta^2-\xi\theta)^{\frac{1}{2}}(R-u)} - \arcsin\frac{(\xi u+\eta)(-u)-\sigma^2}{(\eta^2-\xi\theta)^{\frac{1}{2}}(-u)}\right],$$

$$I_v = \frac{1}{\mu}\left[\ln\frac{vR+\xi-\sqrt{\kappa}}{(R-v)} - \ln\frac{\xi-\sqrt{\theta}}{-v}\right],$$

$$\sigma^2 = -(\xi u^2+2\eta u+\theta), \qquad \mu^2 = \xi v^2+2\eta v+\theta,$$

$$v = (\xi v+\eta)/\mu, \qquad \xi = (\eta v+\theta)/\mu. \tag{29}$$

Die Produkte mit I_v und besonders mit I_u tragen nur wenig zum Ganzen bei. Da schon im physikalischen Bilde und auch bei der Berechnung Vereinfachungen angenommen worden sind und somit das Ganze nur eine Schätzungsrechnung ist, brauchen wir die Ausdrücke mit I_u und I_v nicht zu beachten.

Durch Einsetzen der Gleichung (10) in (26), wobei wir

$$\beta_z = 1, \qquad \omega t_R = 2\pi l_R$$

setzen und

$$A_s/2\pi l_R A_R \ll 1$$

annehmen resultiert:

$$r_2 - r_1 = \frac{p_1}{m_0}\frac{1}{\omega A_R}\ln 4\pi l_R\frac{A_R}{A_s}. \tag{30}$$

Die Fokussierungseigenschaften des Beschleunigungsspaltes sind von J. S. Bell[11]) bearbeitet worden. Bei der Berechnung von p nimmt er neben r auch β konstant und bekommt:

$$p_2 - p_1 = -\frac{e}{2c}\frac{1-\beta^2}{\beta}r_1(E_{z,1}-E_{z,2}) \approx -\frac{e}{2c}\frac{r_1}{\gamma^2}(E_{z,1}-E_{z,2}). \tag{31}$$

Für den Resonatorspalt beim Starten hat der obige Ausdruck keine Bedeutung. Die Zusammenziehung des Elektronenstrahles ist viel stärker als es dem obigen Ausdruck entsprechen würde. Es kommen viel mehr die fokussierenden elektrostatischen Kräfte zur Wirkung als die defokussierenden magnetischen. Bei weiteren Durchgängen geht aber für den Fall, daß das Sollelektron zur Zeit $\omega t = \frac{1}{2}\pi$ die Mitte des Resonatorspaltes passiert in den für die Fokussierung günstigen Ausdruck

$$p_2 - p_1 = -\frac{e}{c}\frac{E_m}{\gamma^2}r_1\cos\pi\left(\tfrac{1}{2}-l_s\right) \tag{32}$$

über. Die Änderung von r kann

$$r_2 - r_1 = \frac{p_1}{m}\frac{1}{f}l_s \tag{33}$$

geschrieben werden.

Für größere Energien nimmt J. S. Bell $\beta = 1$ und beachtet die Änderung von r beim Durchfliegen des Resonators. Zufolge dem Endausdruck, den er angibt, sollte der Resonatorspalt unabhängig von der Phase, bei der das Elektron die Resonatormitte durchfliegt, fokussieren, was im Wiederspruch zur Gleichung (31) steht.

Die experimentellen Ergebnisse der soweit gebauten Mikrotrone scheinen keinen wesentlichen Stromverlust nach dem zweiten Durchgang wegen ungenügender Fokussierung zu zeigen[2]). So dürfte man annehmen, daß viele Elektronen den Vorbeschleunigungsresonator mit kleiner Radialgeschwindigkeit verlassen. Mit Gl. (30) kann berechnet werden, daß der Divergenzwinkel für $L_R = 2$ m, $\gamma_m = 20$ und

[11]) J. S. Bell, Proc. Phys. Soc. B66 (1953) 802.

$A_s = 2.13$ einen Wert von 1.6 $(r_2 - r_1)$ annehmen darf um nicht in dem Linearbeschleuniger schon beim ersten Durchgang verloren zu gehen. Für $L_R = 1$ m, $\gamma_m = 20$ und $A_s = 1.07$ kann der Winkel 5.2 $(r_2 - r_1)$ betragen. Daraus sieht man deutlich, daß beim gleichen Energiegewinn für die Fokussierung ein kurzer Linearbeschleuniger einem langen vorzuziehen ist.

3.3. EINFLUSS DER RAUMLADUNG

Wie sich mit wachsender Energie der fokussierende Einfluß der Beschleunigungselemente schnell dem Werte Null nähert, schwinden auch die coulombischen Abstoßungskräfte des Elektronenstrahles. Eine genaue Rechnung ist hier schwieriger als bei den Beschleunigungselementen. Die Verteilung der Elektronen ist nicht bekannt. Der Strom im Elektronenpaket beträgt bei einer Arbeitsperiode 1 : 1000 etwa 10^4 des effektiven Stromes. In den folgenden Schätzungsrechnungen nehmen wir an, daß die Elektronen gleichmäßig im Strahl mit dem Durchmesser $2r_b$ verteilt sind. So kann nach dem Einsetzen der Werte für E_r und B_ψ in die Gleichung (23) für die nach außen wirkende Kraft

$$F = M \frac{1}{\beta_b} (1 - \beta_b \beta_e) r \approx M(1 - \beta_b \beta_e) r , \qquad M = \frac{e}{\varepsilon c} \frac{I_b}{2\pi r_b^2} \tag{34}$$

geschrieben werden. Dabei ist I_b der Augenblicksstrom, der mit β_b fliegenden Elektronen.

Es muß unterschieden werden zwischen dem Weg durch den Linearbeschleuniger, den alle Bahnen ziemlich gleichzeitig durchfliegen und zwischen den Bahnen im Magnetfelde und in der leeren linearen Strecke, wo die Elektronenbahnen getrennt sind. Nehmen wir einfachkeitshalber an, daß der Elektronenstrom I_b immer der gleiche ist. Dort wo nur Elektronen einer Energie vorhanden sind, übergeht die Gleichung (34) in

$$F = M \frac{1}{\gamma^2} r \tag{35}$$

woraus für die Änderung der Bewegungsgröße

$$p_2 - p_1 = M r_1 \frac{1}{\gamma^2} \frac{2\pi\rho + L}{\beta c} \tag{36}$$

folgt.

Die radiale Kraft schwindet mit γ^2. Dasselbe geschieht beim Durchfliegen des Linearbeschleunigers. Doch da hier die Kräfte von allen Strömen zusammengezählt werden müssen, spielt hier eine Rolle die Zahl der Durchgänge. Eine vereinfachte, leichter zu überblickende Form für die Ausdrücke der Kraft F_k beim k-ten $(1 \leq k \leq n)$ Durchgang des Elektrons bekommen wir, wenn wir in der Gleichung (34) im Produkt nur das kleinere β verschieden von 1 nehmen. Weiter nehmen wir an, daß beim ersten Durchgang $(1 - \beta_z)_1$ vom Anfang zum Ende der Beschleunigungsröhre gemäß der Gleichung (10) variert, während beim zweiten Durchgang die Energie durch die ganze lineare Strecke (der Länge L, nicht L_R) linear zunimmt. Bei weiteren Durchgängen wird angenommen, daß $(1 - \beta)_k$ konstant bleibt. So folgen die Ausdrücke:

$$F_1 = M(n + 1)(1 - \beta_z)_1 r ,$$

$$F_2 = M[(1 - \beta_z)_1 + n(1 - \beta_z)_2] r ,$$

$$\ldots\ldots\ldots$$

$$F_k = M[(1 - \beta_z)_1 + (1 - \beta_z)_2 + (1 - \beta)_3 + \ldots + (1 - \beta)_{k-1} + (n - k + 2)(1 - \beta)_k] r \tag{37}$$

und für die Bewegungsgröße

$$(p_2 - p_1)_1 = M(n+1)\,\tfrac{1}{4}\tau\, r_1\,,$$

$$(p_2 - p_1)_2 = M\,(\tfrac{1}{4}\tau + nN)\, r_1\,,$$

. . . . . .

$$(p_2 - p_1)_k = M\left[\tfrac{1}{4}\tau + N + \frac{L}{2c}\left(\frac{1}{\gamma_2^2} + \frac{1}{\gamma_3^2} + \ldots + \frac{1}{\gamma_{k-1}^2} + (n-k+2)\,\frac{1}{\gamma_k^2}\right)\right] r_1\,,$$

$$N = \int_0^{t_2} (1 - \beta_z)_2\, \mathrm{d}t = \frac{L}{2c\beta\Delta\gamma}\left(\frac{}{\gamma_{n-1}} - \frac{1}{\gamma_n}\right). \tag{38}$$

Das Zuwachsen von r wird an Hand des Ausdruckes

$$(r_2 - r_1)_k = \frac{p_{1,k}}{m_0}\int_0^{t_2}\frac{\mathrm{d}t}{\gamma_z}$$ berechnet:

$$(r_2 - r_1)_1 = \frac{1}{m_0}\,\frac{1}{\omega A_R}\left(\ln 4\pi l_R\,\frac{A_R}{A_s}\right) p_{1,1}\,,$$

$$(r_2 - r_1)_2 = \frac{1}{m_0}\,\frac{L_R}{c\beta\Delta\gamma}\left(\ln\frac{\gamma_2}{\gamma_1}\right) p_{1,2}\,,$$

. . . . . .

$$(r_2 - r_1)_k = \frac{1}{m_0}\,\frac{L}{c\beta\Delta\gamma}\left(\ln\frac{\gamma_k}{\gamma_{k-1}}\right) p_{1,k}\,. \tag{39}$$

Wegen der elektrostatischen Fokussierung des Vorbeschleunigungsresonators dürfte die Anfangsgeschwindigkeit der Elektronen zur Achse und nicht weg von ihr gerichtet sein. Die schnelle Vergrößerung der Masse verursacht, daß sich die Radialgeschwindigkeit rasch verkleinert. Solange die Summe des radialen Impulses des elektromagnetischen Feldes der Beschleunigungsröhre (Gl. (29)) und des radialen Impulses wegen der Raumladungskräfte (Gl. (36) und Gl. (38)) gleich Null sind, werden die genügend gebündelten Elektronen bis zum nächsten Durchgang durch den Beschleuniger nicht verlorengehen. Für die Parameter $\lambda = 10$ cm, $\exp(\alpha L_R) = \sqrt{2}$, $l_R = 20$, $\gamma_m = 20$, $\gamma_1 = 10.5$, $2\rho_1 = 5$ cm, $L = 2.1$ m, $n = 50$ und $r_b = 3$ mm, findet dieses Gleichgewicht bei einem Strom von 0.26 A statt. Stellen wir für den zweiten Durchgang wieder die Forderung auf, daß die Summe der radialen Impulse des Hohlraumresonators (Gl. (32)), der Beschleunigungsröhre (Gl. (25)) und der Raumladungseffekt (Gl. (36), (38)) gleich Null sind, so resultiert für die gleichen Parameter wie oben und $\varphi_r = 18°$ als Grenzstrom ein Strom von 0.15 A. Bei weiteren Durchgängen schwinden die Fokussierungskräfte des Linearbeschleunigers schneller als die Abstoßungskräfte der Raumladung. Der Ausdruck $\frac{1}{4}M\tau$ in Gl. (38) bleibt auch bei größeren Elektronenenergien. Doch trotzdem dürfte man annehmen, daß wegen der wachsenden Masse der Elektronen, deren radiale Verschiebung bei späteren Umläufen keiner Beachtung mehr bedürfe. Wenn wir annehmen, daß der Beschleuniger eine Arbeitsperiode von 1 : 1000 hat und daß der phasenstabile Bereich sich über ein Zehntel der Hochfrequenzperiode erstreckt, könnte der Beschleuniger einen effektiven Strom von 10 μA fassen.

3.4. MAGNETISCHE LINSEN

Bei größeren Augenblicksströmen müßte eine Art starke Fokussierung eingeführt werden. Nach Roberts[9]) sollte jede Magnethälfte in mehrere Segmente geteilt werden um eine AG-Wirkung zu erzielen. Das wäre kompliziert. Vielleicht wäre es einfacher, wenn man in der leeren linearen Strecke Quadrupollinsen anbringen würde. Die Entfernung

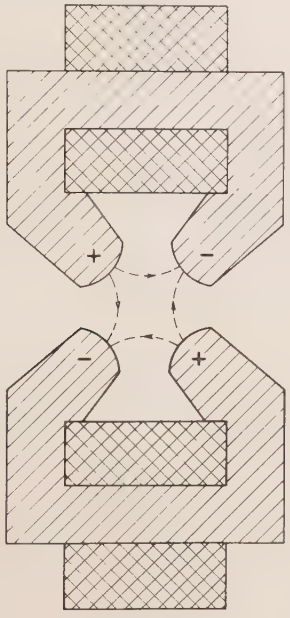

Abb. 3.

zwischen den Strahlen würde etwa 6 cm betragen ($\lambda = 10$ cm, $b = 2$). Bei geeigneter Konstruktion (vgl. Abb. 3) müßte diese Entfernung genügen. Bei Aus- und Eintritt aus bzw. in die Magnetpolhälfte könnten die Pole sägezahnartig enden, womit auch Linsen entstehen, die in einer Richtung fokussieren, in anderer defokussieren. Die Linsen sollte man für jeden Strahl separat dimensionieren, um den radialen und horizontalen Brennpunkt in dem Linearbeschleuniger zu haben. Doch bis zu einem Impulsstrom von etwa 0.1 A heben sich die fokussierenden und defokussierenden Kräfte des Mikrotrons auf und es scheint nicht nötig zur AG-Fokussierung zu greifen.

4. Schlussfolgerungen

Sind die vorherigen Ausführungen richtig, so steht dem Bau eines "Racetrack Microtrons" bis ins GeV Gebiet, wo wegen der Strahlungsdämpfung auch den Beschleunigern mit Energiegewinn einiger MeV pro Umlauf eine Grenze gesetzt ist, nichts im Wege. Der Elektronenstrahl würde vom Start bis zum Beschleunigungsende 1 bis 2 μsek brauchen. Heute stehen kommerzielle Klystrone bis 30 MW Impulsleistung und 10 μsek Impulsdauer zur Verfügung. Die Impulsdauer ist lang genug, um die Elektronen den ganzen Beschleunigungsprozeß durchmachen zu lassen und die Energie eines Klystrons genügt, um sowohl den Hohlraumresonator als auch den Wanderwellenbeschleuniger zu speisen. Die Elektronen könnten im Beschleuniger selbst gewonnen und vorbeschleunigt werden. Somit entfiele die Komplikation mit dem Einspritzen. Bei einem günstigen Beschleuniger sollten etwa 5 bis 10 MeV pro Umlauf gewonnen werden. Für den Mikrotronbetrieb ist es günstig eine möglichst kurze lineare Strecke zu haben. Bis zu einem Augenblickstrom von 0.1 A, das würde bei den heutigen Mikrowellenröhren einem effektiven Strom von 10 μA entsprechen, dürften keine zusätzlichen Fokussierungs systeme notwendig sein, voraußgesetzt daß der Elektronenstrahl zu Beginn der Beschleunigung genügend gebündelt ist. Bei größeren Strömen sollte man zu magnetischen Linsen greifen.

Das "Racetrack Microtron" hätte die gute Eigenschaft der Energiehomogenität (bei 100 Umläufen $0.5^0/_{00}$). Es könnte als Einspritzer in einen Linearbeschleuniger gebraucht werden. Da die Teilchen praktisch schon mit Lichtgeschwindigkeit dahineilen, besteht keine Gefahrt, daß sie defokussiert werden und auch das phasenstabile Bereich hat keine Bedeutung mehr. Man könnte die Pakete zuerst durch einen Teilbeschleuniger fliegen lassen, wobei das Sollelektron bei einer negativen Phase liegt, die ihm voreilenden Elektronen weniger die ihm nacheilenden mehr Energie gewinnen würden. Beim nächsten Teilbeschleuniger sollte sich das Sollelektron bei gleicher positiven Phase befinden. Die Elektronen, die früher weniger Energie gewonnen haben, gewinnen jetzt mehr und umgekehrt. Soweit wir die Flanke der Sinuskurve mit einer Geraden ersetzen dürfen, gewinnen somit alle Elektronen denselben Energiezuwachs und der Absolutbetrag der Energieabweichung bliebe derselbe. Bei einem Mikrotron mit Energiezuwachs von 10 MeV

pro Umlauf, der als Einspritzer in einen Linearbeschleuniger von 10 GeV Endenergie dienen würde, betrüge somit die Abweichung weniger als $\pm$ 1 MeV. Die Baukosten eines "Racetrack Microtrons" dürften bedeutend niedriger als die Kosten eines Linearbeschleunigers von derselben Energie sein. Insbesondere dürfte aber seine Energiehomogenität für seinen Wert sprechen.

Den Herrn Dipl. Ing. N. Bezić, Dr. P. Gosar and Dr. S. Poberaj danke herzlichst für die kritische Durchlesung des Manuskriptes.

NUCLEAR INSTRUMENTS AND METHODS 12 (1961) 169–179; NORTH-HOLLAND PUBLISHING CO.

EXPERIMENTAL VERIFICATION OF THE SPACE CHARGE LAW ($I = k(e/m)^{\frac{1}{2}}V^{\frac{3}{2}}$) FOR ION BEAMS FROM A PLASMA ION SOURCE

W. L. RAUTENBACH

Nuclear Physics Division, National Physical Research Laboratory, Pretoria, South Africa

Received 13 February 1961

Application of the space charge law to ion beam formation using plasma ion sources as well as the results of previous experiments to verify this law are briefly discussed.

By strictly observing the conditions under which this law may be applied, and by establishing them empirically, it is possible, to verify the space charge law experimentally for a magnetic ion source with end extraction using the acceleration system of a laboratory isotope separator. The problems encountered in proving the space charge law show that caution must be exercised in applying the law, especially to ion beams from different types of ion sources, as the discharge conditions under which the law holds must first be establish for each type.

1. Introduction

The similarity principle for the flow of charged particles taking the effects of space charge into account, better known as the space charge law[1,2,3]), finds wide application in electron beam forming systems[4]). It is generally acknowledged that this law should also be applicable to ion beam forming systems using plasma ion sources[5,6]). However in this case it cannot be applied with the same confidence as in the case of electron beams because this law has not yet, to the best knowledge of the author, been satisfactorily verified.

The object of this paper is to determine if the space charge law may be applied to a typical ion beam forming system using a plasma ion source.

2. The Space Charge Law

A beam of charged particles is characterised by the following parameters: the beam current I, the beam energy eV (where V is the acceleration potential), the charge to mass ratio (e/m) of the particles, and the beam form. The space charge law implies that the beam form will remain invariant on changing e, m, V and I and that these beam parameters will be connected by the equation

$$I = k(e/m)^{\frac{1}{2}}V^{\frac{3}{2}}\,, \qquad (1)$$

where k is a constant depending on the geometry of the system, if the following conditions are satisfied:

(a) The emitter is an equipotential surface emitting particles with zero initial velocity.

(b) The current from the emitter is space-charge-limited, i.e. the accelerating field is zero at the surface of the emitter.

(c) The electrostatic field distribution remains invariant, i.e. the electrode configuration and the form of the emitter must remain the same as well as the ratios of the potentials on the electrodes, the emitter potential being taken as zero.

2.1. APPLICATION OF THE SPACE CHARGE LAW TO ION BEAM FORMATION FROM PLASMA ION SOURCES

Fig. 1 shows the usual beam forming system for a plasma ion source. A plasma is generated by a gas discharge to the left of the front plate of the ion source. By applying a positive voltage V to the ion source with respect to the extraction electrode, ions are withdrawn from the plasma through the outlet

[1]) I. Langmuir and K. T. Compton, Rev. Mod. Phys. **3** (1931) 273.

[2]) H. C. Hamaker, Physica **9** (1942) 135.

[3]) B. Meltzer, Proc. Phys. Soc. (London) B **62** (1949) 431, 813.

[4]) See for instance: H. F. Ivey, Advances in Electronics and Electron Physics **6** (1954) 137.

[5]) W. Walcher in "Electromagnetic Isotope Separators and Application of Electromagnetically Enriched Isotopes", edited by J. Koch, (North-Holland Publishing Company, Amsterdam, 1958) Chapter 13.

[6]) T. Consoli, P. Hubert, R. le Quinio and D. Véron, Nucl. Instr. and Meth. **4** (1959) 376.

and form a beam which passes through a hole in the extraction electrode. The positive space charge in the ion beam shields the plasma almost completely from the extraction field[7]). The transition between plasma and beam is also sharp[7]). Therefore one may consider the plasma to be separated from the beam by a boundary at plasma potential V_p relative to the front plate, emitting a space-charge-limited ion current[8]). This satisfies the first part of condition (a) of sec. 2 as well as condition (b).

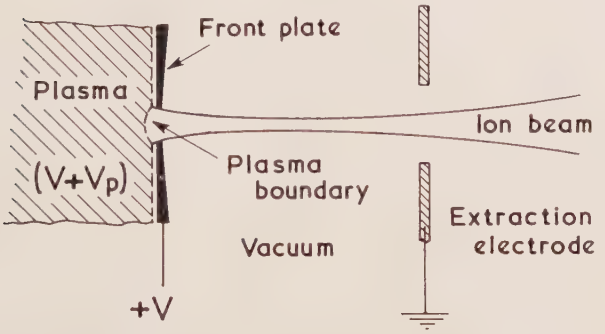

Fig. 1. A typical beam forming system for a plasma ion source.

Ions are transported from the plasma to the boundary by a weak penetrating field[7]) arriving with an average kinetic energy

$$\tfrac{1}{2}mv^2 = kT_e\,, \qquad (2)$$

where v is the average velocity of an ion, k Boltzmann's constant and T_e the electron temperature of the plasma. For a low pressure discharge in a magnetic field this energy usually amounts to a few electron volts[7]). The energy of emission is therefore small compared to the final energy if the ions are accelerated through several kilovolts and one may consider the second part of condition (a) of sec. 2 to be approximately satisfied.

For plasma ion sources it is difficult to satisfy condition (c) because the form of the plasma boundary is determined by the density distribution of the ion current flowing across the plasma boundary, given by

$$j_+ = n_+(kT_e/17.3m)^{\frac{1}{2}}\ ^{9}) \qquad (3)$$

where n_+ is the ion density in the plasma, and the extraction field configuration. Changing the form of the boundary changes the beam form because the ions are initially accelerated perpendicular to the boundary. This effect is known as plasma focussing.

In practice only the form of the ion beam and not that of the boundary can be determined and we make the reasonable assumption that identical beam forms correspond to identical plasma boundaries. Therefore condition (c) will only be satisfied at identical beam form, constant electrode configuration and voltage ratios on the electrodes.

Identical beam forms can only be obtained if the distribution in ion currents across the plasma boundary remain constant. This will be the case if the ion density distribution in the plasma stays constant (see eq. (3)).

Only experimental results obtained under these conditions may be used to verify the space charge law (1).

2.2. DISCUSSION OF PREVIOUS ATTEMPTS TO VERIFY EQ. (1)

Most of the experimental results quoted in favour of, or against (1) have the common weakness that the results were not obtained at constant beam form and are therefore not valid[10]). The only exception occurs in the work of Almén and Nielsen[11]) for beam formation in an electromagnetic isotope separator. Their results are in accord with (1) but doubt exist if these results can be considered as a satisfactory verification of the space charge law because the criterion for constant beam form is minimum line width for the separated isotopes at the collector of the isotope separator. This will only be the case if the degree of space charge compensation due to slow electrons in the ion beam[12]), which is appreciable in the region of the magnetic field[13]), remains the same irrespective of the ion species and the beam energy and this is open to doubt.

[7]) D. Bohm in "Characteristics of Electrical Discharges in Magnetic Fields", edited by A. Guthrie and R. K. Wakerling, (McGraw-Hill, New York, 1949) Chapter 3.

[8]) P. C. Thonemann, Progress in Nuclear Physics **3** (1953) 219.

[9]) D. Kamke and H. J. Rose, Z. für Physik **145** (1956) 83.

[10]) W. Fischer and W. Walcher, Zeitschrift für Naturforschung **10a** (1955) 857.

[11]) O. Almén and K. O. Nielsen, Nucl. Instr. **1** (1957) 302.

[12]) See for instance ref.[5]), Chapter 14.

[13]) W. L. Rautenbach, Thesis, Potchefstroom (1959).

3. Description of the Experiment

3.1. GENERAL CONSIDERATIONS

In order to verify (1) it is necessary to determine the following beam parameters for beams of the same form: the total ion currents I, the extraction voltage V, and the partial ion currents I_i for all charge to mass ratios $(e/m)_i$ present in the beam. The partial ion currents are used to determine an effective value of (e/m) which must be used in (1). The effective value of (e/m) is defined by:

$$(e/m)^{-\frac{1}{2}} = \sum_i I_i \, (e/m)_i^{-\frac{1}{2}} / \sum_i I_i \,, \tag{4}$$

taking the sum over all the ion species present in the beam.

If the beam form can be represented by a parameter $W_{\frac{1}{2}}$, at present undefined, then a curve of $W_{\frac{1}{2}}$ versus I can be obtained at constant V and constant effective (e/m). Consider two curves respectively characterised by V_k, $(e/m)_k$ and V_l, $(e/m)_l$. If (1) is applicable and I_k and I_l respectively denote ion currents at identical beam form then

$$I_l = I_k \left[\frac{(e/m)_l}{(e/m)_k} \right]^{\frac{1}{2}} \left(\frac{V_l}{V_k} \right)^{\frac{3}{2}} . \tag{5}$$

This implies that for each value of I_l one can define a current I'_l by

$$I'_l = I_l \left[\frac{(e/m)_k}{(e/m)_l} \right]^{\frac{1}{2}} \left(\frac{V_k}{V_l} \right)^{\frac{3}{2}} , \tag{6}$$

which, if used as a co-ordinate instead of I_l will yield a curve coinciding with the one characterised by V_k and $(e/m)_k$. Conversely, coincidence of the curves after transforming by (6) verifies (1).

This method is ideally suited for verifying the space charge law because (1) is not only checked for all beam forms but the troublesome comparison of beam forms to determine if they are identical is unnecessary.

3.2. DESCRIPTION OF APPARATUS AND EXPERIMENTAL PROCEDURE

The electrostatic beam forming system of the laboratory isotope separator at Pretoria[14]) represents a typical beam forming system and is well suited for undertaking these measurements. Not

[14]) W. E. Frahn, W. L. Rautenbach and L. E. Wåhlin, Nucl. Instr. and Meth. **7** (1960) 253.

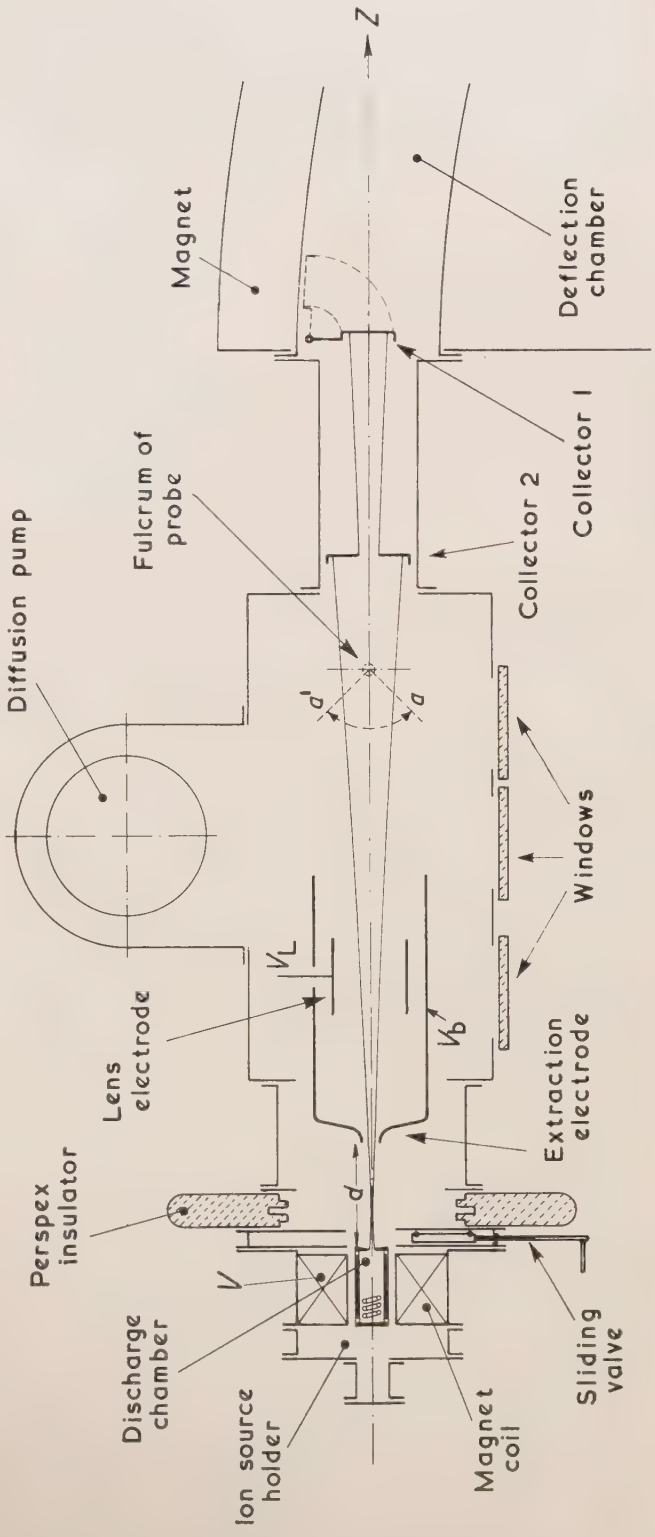

Fig. 2a. The beam forming system of the isotope separator.

only is the plasma ion source capable of supplying ions covering a wide range in (e/m) but it is also easy to determine the distribution in (e/m) for each beam. Slight modification to the instrument enables one to determine the beam form accurately.

by a synchromotor through a reducing gear box and is biased at — 100 V in order to repell all secondary electrons. The extraction electrode in turn is biased at $V_b = -500$ V to prevent these electrons from reaching the ion source.

When registering the beam form the lens voltage

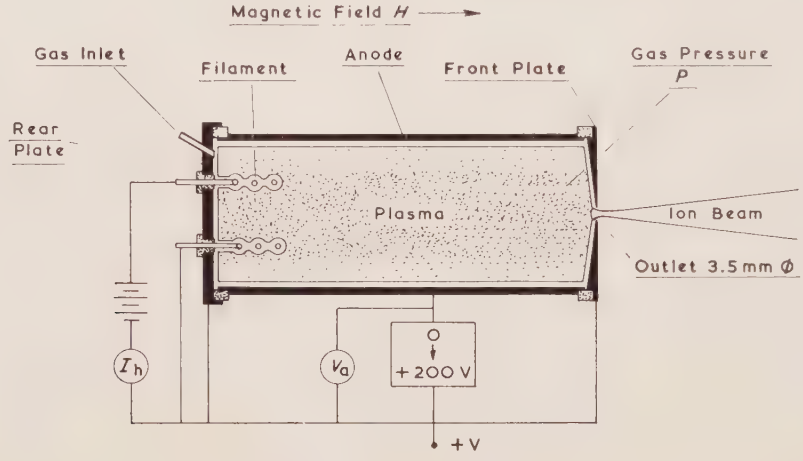

Fig. 2b. Diagram of ion source discharge chamber.

Fig. 2a shows the beam forming system of the isotope separator. The ion source unit is operated at a high positive voltage V with the extraction electrode a distance d from it. The resulting ion beam is symmetrical with respect to the z-axis because the beam forming system is of rotational symmetry. This symmetry simplifies determination of the beam form considerably because it is only necessary to determine the radial beam current density at two positions after the beam has left the electrostatic system. In practice the beam form is not influenced by electrostatic fields after acceleration with the result that plasma focussing determines the beam form, yielding a beam which diverges from the vicinity of the ion source outlet[13]). Therefore all ion beams are diverging and it is only necessary to determine the radial current distribution at one point in order to determine the beam form. This is done by driving a cylindrical probe (diameter 2.5 mm, length 2.5 mm) at constant angular velocity along arc a–a′ through the middle of the beam while registering the probe current on a chart recorder. The probe axis is perpendicular to z-axis and direction of motion giving a constant collector area in all positions. The probe is driven is maintained at ground potential. Under the usual running conditions of the isotope separator the beam current may be measured by applying a positive voltage to the lens so as to focus the beam on collector 1 which can be moved into the beam. In this experiment ion beams of higher intensities and divergences are handled and it is therefore necessary to incorporate a second larger collector nearer to the lens, connected in parallel to the first, with a part of the beam passing through a hole in its centre. The main and stray magnetic fields of the deflecting magnet prevent the escape of secondary electrons from these collectors.

Collector 1 can be moved out of the beam and the different ion currents I_i corresponding to charge to mass ratios $(e/m)_i$ can be determined at the collector of the isotope separator in order to obtain an effective value of (e/m) for each beam.

The pressure in the acceleration chamber varies between 7 and 12 $\times$ 10^{-6} mm Hg and has a negligible effect on the beam form between ion source and probe especially as there are weak electrostatic fields present in this region preventing space charge compensation due to slow electrons[15]).

[15]) See ref.[5]), Chapter 14.

Only ion beams which do not strike the extraction electrode are considered. Incidence of the ion beam on this electrode is determined by measuring the current to it.

The gas ion source (fig. 2b) is a low voltage magnetic type with end extraction and is of similar construction to those employed by Nielsen[16]). The shape of the front plate and the diameter of the outlet remain as shown unless otherwise specified. The following ion source parameters can be altered: the anode voltage V_a, the magnetic field H, the gas pressure P inside the discharge chamber and the filament heating current I_h. [P is determined from the gas flow as measured by the velocity of a mercury bubble, the conductance of the outlet and the temperature of the discharge chamber. The gas flow is regulated using a needle valve.]

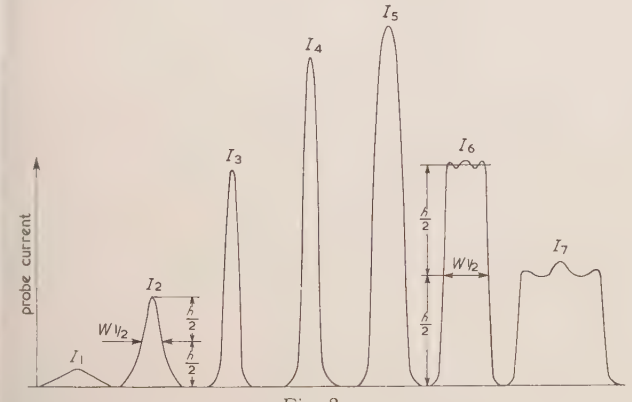

Fig. 3a.

Traces obtained by chart recorder. I denotes total ion current with $I_1 < I_2 < \ldots I_6 < I_7$. ($P$, V_a, H, V, d and e/m are constant).

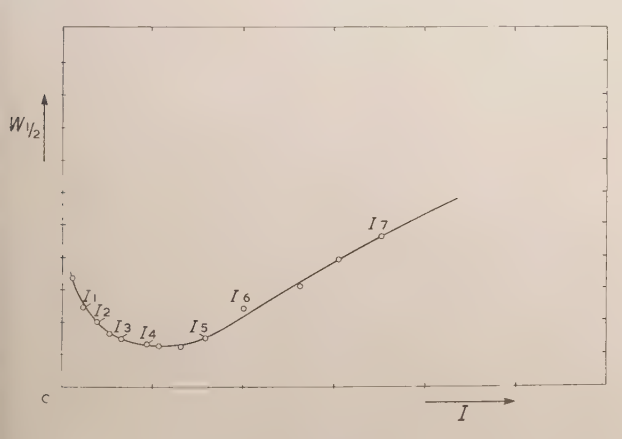

Fig. 3b.

Beam width, $W_{\frac{1}{2}}$, versus ion current, I according to fig. 3a.

[16]) K. O. Nielsen, Nucl. Instr. **1** (1957) 289.

The following is an example of a typical measurement undertaken with this system: While maintaining the parameters P, V_a, H, V and the extraction distance d constant the filament heating current I_h is adjusted in order to obtain different values of the ion current I. The beam form is registered for suitable ion currents, fig. 3a showing the traces obtained by the chart recorder ($I = I_1$, I_2 and I_3 correspond to ion beams from concave plasma boundaries, $I = I_4$ to the transition region and $I = I_5$, I_6 and I_7 to convex boundaries[13]).

The beam width at half maximum height of the curves is a useful parameter to characterize the beam form. Fig. 3b shows the curve obtained if the beam width, $W_{\frac{1}{2}}$, as defined in fig. 3a for the different beam forms, is plotted versus the ion current I for a given gas. The effective value of (e/m) is a constant for such a curve.

In this way curves can be obtained for argon, krypton and xenon at different values of ion source and beam parameters.

Two main difficulties arise during the measurements: the first is to maintain constant pressure in the discharge chamber and the seond is to avoid fluctuations in the beam current while measuring the beam form and beam current. The only way to ensure constant pressure is to do the measurements in the shortest possible time after setting the variable leak while checking the gas flow all the time. If the flow does change the measurements are repeated as it is difficult to reproduce a given pressure by adjusting the flow rate. Changes in the pressure during the determination of a curve of $W_{\frac{1}{2}}$ versus I manifest themselves by a change in beam width for beams from convex plasma boundaries (see sec. 4.1). Variation in ion current is mainly due to changes in the filament heating current I_h which is supplied by a motor generator. Short-time stability is considerably improved by using an accumulator in parallel with the generator output, I_h being adjusted by a resistance in series with the filament. Although the variation in beam current is reduced to less than 5% in this way it is still mainly responsible for the scatter in experimental points and close watch must be kept on the ion current from the ion source to ensure that it remains within acceptable limits while each beam form is registered.

4. Interpretation of the Measurements

4.1. INFLUENCE OF THE ION SOURCE PARAMETERS ON THE BEAM FORM

According to sec. 2.1, eq. (1) can only be checked if the ion source parameters are adjusted in such a way as to maintain constant voltage ratios and discharge conditions. With the emitter potential taken as zero, constant voltage ratios in the beam forming system implies:

(Voltage of front plate) $/V = V_p/V = c_1$

(Voltage of extraction electrode) $/V = (V + V_p + |V_b|)/V = c_2$

(Voltage of lens electrode) $/V = (V + V_p)/V = c_3$,

where c_1, c_2 and c_3 are constants. The plasma voltage V_p is a few tens of volts below the anode voltage for this type of discharge[17]),

$$V_p = V_a - \Delta . \tag{7}$$

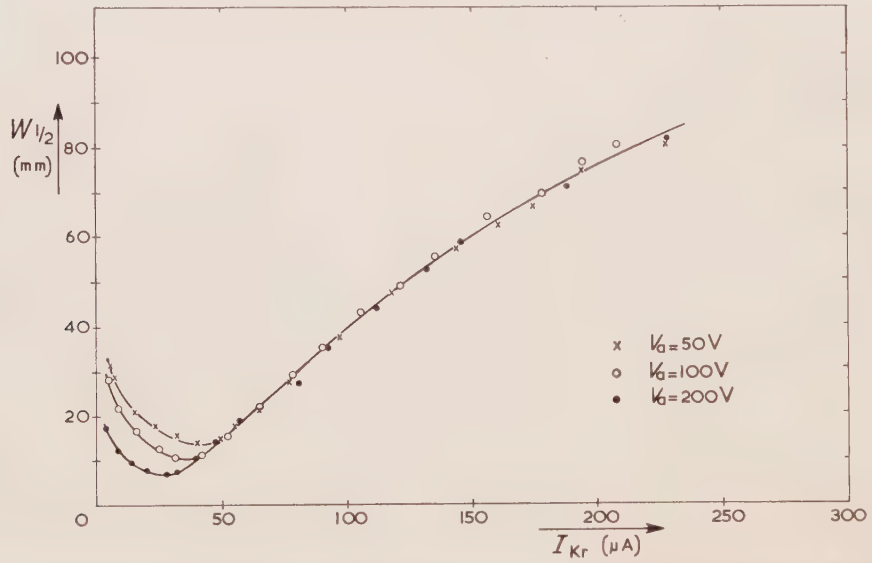

Fig. 4. The effect of anode voltage, V_a, on beam width. (Krypton gas, V = 40 kV, d = 80 mm, H = 300 gauss, P = constant.)

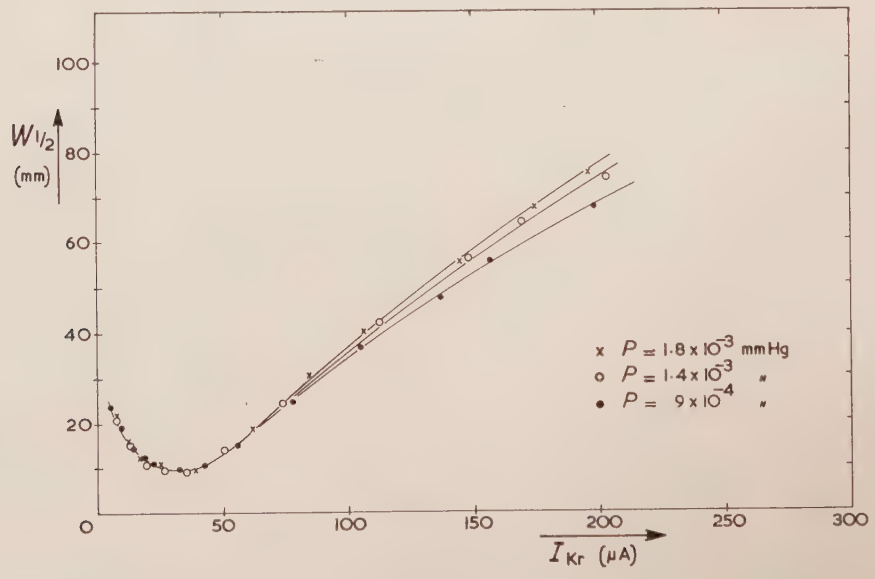

Fig. 5. The effect of gas pressure on the beam width. (Krypton gas, V = 40 kV, d = 110 mm, H = 300 gauss, V_a = 140 V.)

[17]) J. Kistemaker and J. Snieder, Physica **19** (1953) 950.

The maximum value of V_a is 200 V and with a bias voltage $V_b = -500$ V on the extraction electrode, $c_2 \approx 1$ and $c_3 \approx 1$ if $V \geqslant 20$ kV. The only remaining condition is that the plasma potential sould be proportional to the extraction voltage. Therefore

$$(V_a - \Delta)/V = c_1 . \qquad (8)$$

the gas pressure influences the beam form for beams from convex plasma boundaries only. The reason why the beams from concave boundaries are not influenced is not as yet known.

Changing the ion source magnetic field from 150 gauss to 300 gauss while keeping V, P and V_a constant yields curves for beam width versus ion

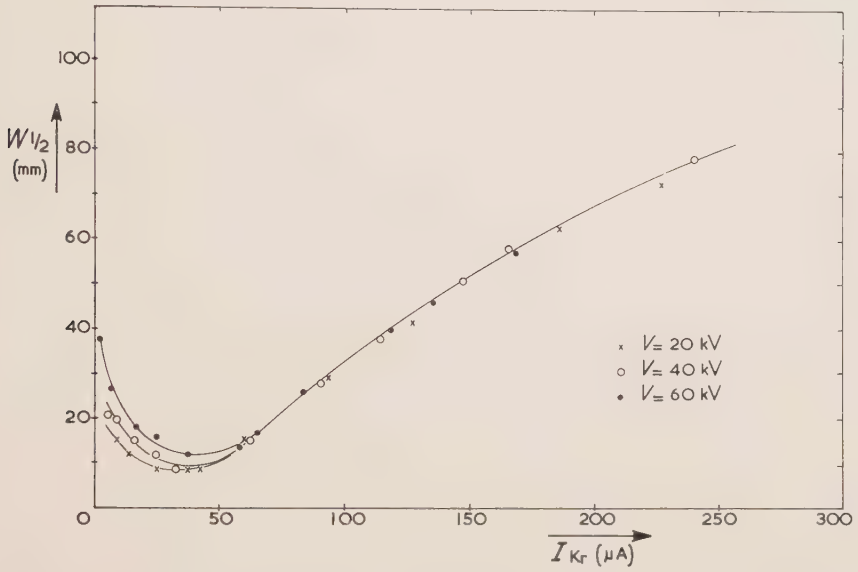

Fig. 6. Beam width, $W_{\frac{1}{2}}$, versus krypton beam current, I_{Kr}, at $V = 20$, 40 and 60 kV. The experimental points at 20 and 60 kV are transformed to 40 kV using eq. (6). ($d = 110$ mm, $H = 300$ gauss, $V_a = 100$ V, P = constant.)

Fig. 4 shows the influence of different anode voltages on the beam form, the curves being obtained at constant V, d and ion source parameters P and H. [Changing V_a from 50 V to 200 V changes the effective value of $(e/m)^{\frac{1}{2}}$ by a few per cent which has a negligible effect on the beam form.] It is important to notice that the voltage ratio given by c_1 influences the beam form for beams from concave plasma boundaries only. This can be understood qualitatively because the field between plasma and outlet will have a stronger effect on the beam form for concave plasma boundaries lying far behind the outlet than for convex boundaries near to the outlet where the extraction field is stronger.

The radial ion current density distribution from the discharge depends on the gas pressure[13]). At constant ion current the beam form should therefore depend on the gas pressure inside the discharge chamber. The dependence of beam form on pressure is given in fig. 5. Contrary to expectation current which coincide. This result shows that the magnetic field does not affect the plasma potential or the ion current density distribution from the plasma. The influence of the stray magnetic field on the beam form is also negligible.

The experimental results presented in this section show conclusively that the space charge law cannot hold if the ion source is operated at arbitrary values of ion source parameters.

4.2. PARTIAL VERIFICATION OF THE SPACE CHARGE LAW

The result presented in the previous section show that the space charge law should be applicable to beams from convex plasma boundaries if the ion source is operated at constant gas pressure because these beam forms are independent of the voltage ratios. Fig. 6 shows the results when the curves obtained at $V = 20$ kV and $V = 60$ kV are transformed to $V = 40$ kV using eq. (6). This

verifies the space charge law in the simplified form

$$I = k_1 V^{\frac{3}{2}}, \tag{9}$$

where k_1 is a constant, for beams from convex plasma boundaries.

For beams from concave plasma boundaries the beam form is independent of gas pressure. Therefore (1) should be applicable provided the voltage ratio remains constant. This is achieved by maintaining V_a and V constant while obtaining curves for A, Kr and Xe. Fig. 7 shows the results when the curves for Xe and A are transformed to that of Kr, using (6). This verifies (1) in the form

$$I = k_2(e/m)^{\frac{1}{2}}, \tag{10}$$

where k_2 is a constant, for ion beams from concave plasma boundaries.

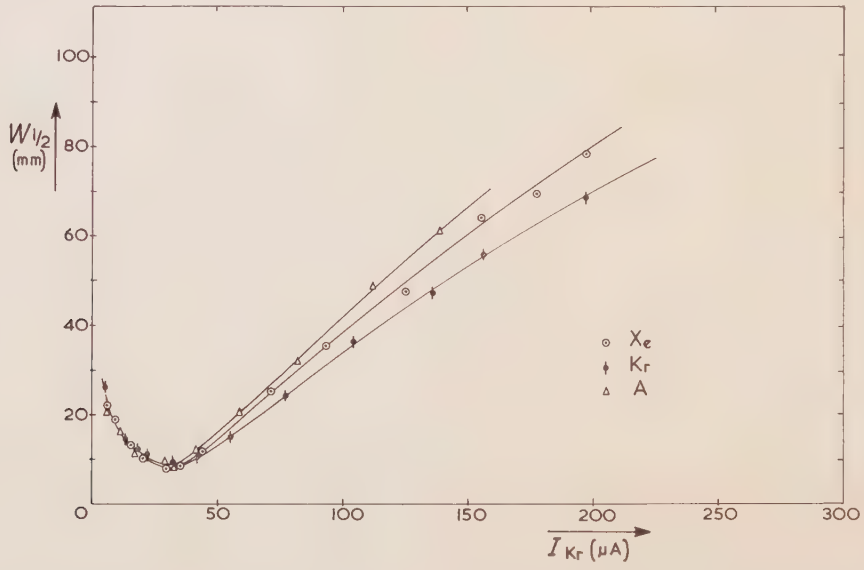

Fig. 7. Beam width, $W_{\frac{1}{2}}$, versus beam current for argon, krypton and xenon. The experimental points for A and Xe have been transformed to that of Kr, using eq. (6). (V = 40 kV, d = 110 mm, H = 300 gauss, V_a = 140 V, P_{Xe} = constant, P_{Kr} = constant, P_A = constant.)

4.3. VERIFICATION OF THE SPACE CHARGE LAW FOR ALL BEAM FORMS

The previous results show that (1) can only be expected to hold for all beam forms for different gases at different extraction voltages V if:

(i) The voltage ratio is kept constant, i.e. the value of Δ in (8) must be known.

(ii) Equivalent pressures must be established for the different gases which will yield identical distributions in ion current across the plasma boundary.

On assuming Δ to be independent of V_a and taking Δ = 20 V, then at V = 20 kV, 40 kV and 60 kV the values of V_a should respectively be 80 V, 140 V and 200 V according to (8). The experimental results for Kr are given in fig. 8 when the curves at 20 kV and 60 kV are transformed by (6) to the curve at 40 kV. [The 20 kV results were obtained at V_a = 86 V instead of V_a = 80 V because a slightly better fit with the other curves is then obtained.] Similar results are obtained for A, Kr and Xe for values of d between 30 and 150 mm and outlet diameters of 1.5, 3.5 and 5 mm. These results show conclusively that the simplified space charge law given by (9) is generally true for all beam forms.

To establish equivalent pressures for the different gases is more difficult but can be done as follows: curves similar to those of fig. 5 are obtained at constant values of V_a, V and d for A, Kr and Xe. From these curves calibration curves, like fig. 9 for Kr, can be constructed for beam width versus pressure at different beam currents. The A and Xe currents which should yield the same beam form are calculated from (6) and are also shown on fig. 9.

If a single curve of beam width versus ion current for one gas, say Xe, is taken, then the equivalent pressure in one of the other gases can be obtained from the calibration curve by requiring that the beam widths should be the same at corresponding currents. Once the equivalent pressure has been obtained, say for Kr, then a curve of beam width versus Xe current can be constructed from the calibration curve. Fig. 10 shows curves for Kr and A fitted to Xe in this way. These curves, as well as curves for other equivalent pressures coincide very well, showing that the space charge law as given by (10) is true.

The results presented so far verify eq. (1) in the

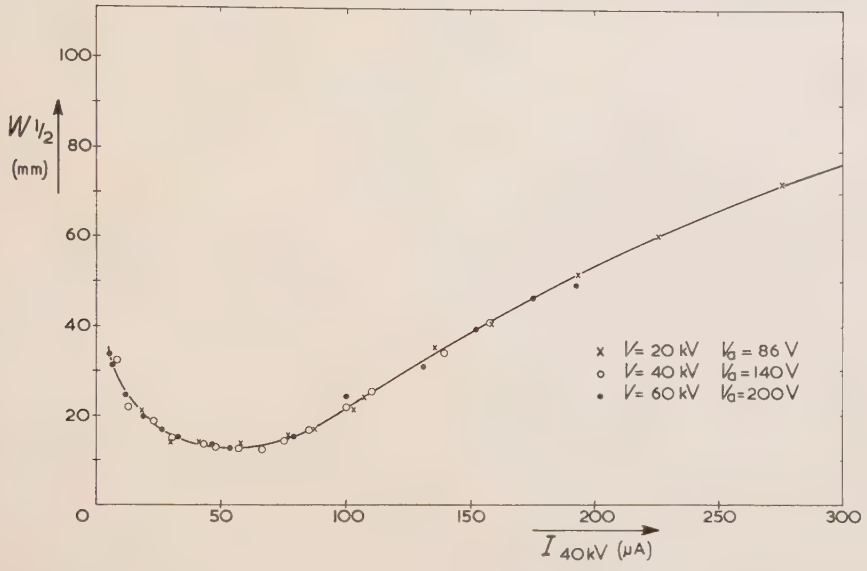

Fig. 8. Beam width, $W_{\frac{1}{2}}$, versus ion current obtained at constant voltage ratio. The experimental points at $V = 20$ kV and 60 kV being tranformed to $V = 40$ kV using eq. (6). (Krypton gas, $d = 60$ mm, $H = 300$ gauss, $P =$ constant.)

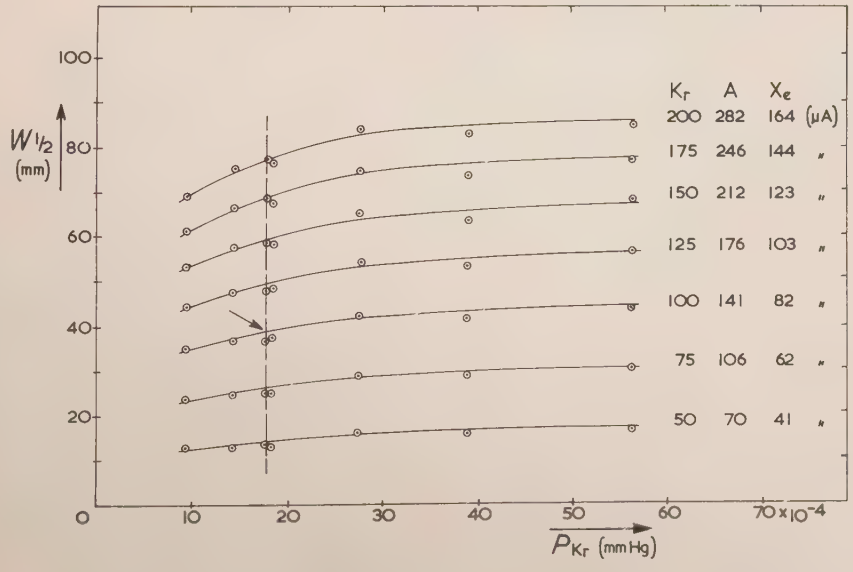

Fig. 9. Krypton calibration curve of beam width, $W_{\frac{1}{2}}$, versus pressure at different values of beam current. Corresponding A and Xe currents as calculated from eq. (6) are shown. The arrow indicates fitting point for Xe curve. ($V = 40$ kV, $d = 110$ mm, $H = 300$ gauss, $V_a = 140$ V.)

form of two separate equations namely (9) and (10) and show that (1) should be generally true if the beam forming system is operated at constant voltage ratio and equivalent pressures in the discharge chamber of the ion source. Fig. 11 shows the experimental results when the system is operated under these conditions. The curves for A, (20 kV) and Kr, (60 kV) are transformed to the Xe, (40 kV) curve using (6). The curves do not coincide very well for beams from the convex plasma boundaries because it is difficult to reproduce a given pressure accurately.

These results show conclusively that the space charge law is generally true for all beam forms provided the beam forming system is operated in accord with condition (c) of sec. 2.

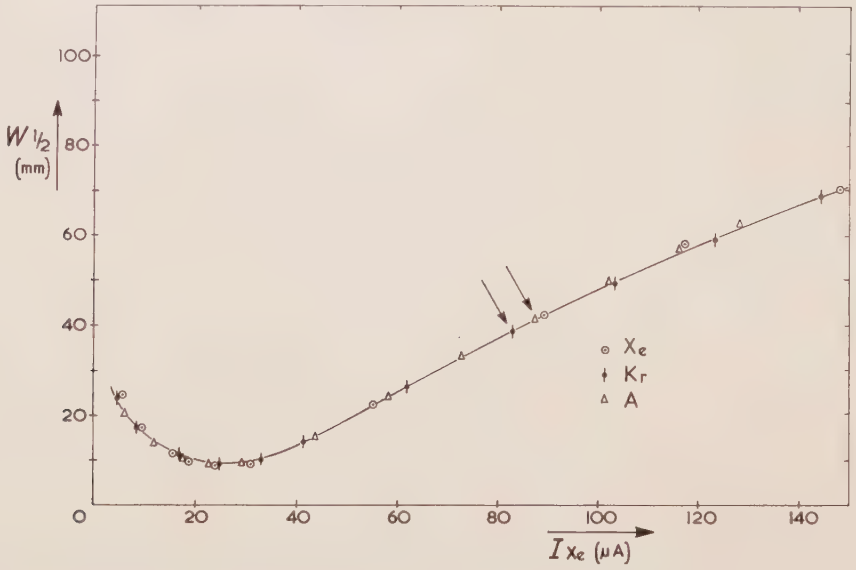

Fig. 10. Curve of beam width, $W_{\frac{1}{2}}$, versus Xe current as well as the points for A and Kr obtained from the calibration curves The arrows show fitting points. (V = 40 kV, d = 110 mm, H = 300 gauss, V_a = 140 V.)

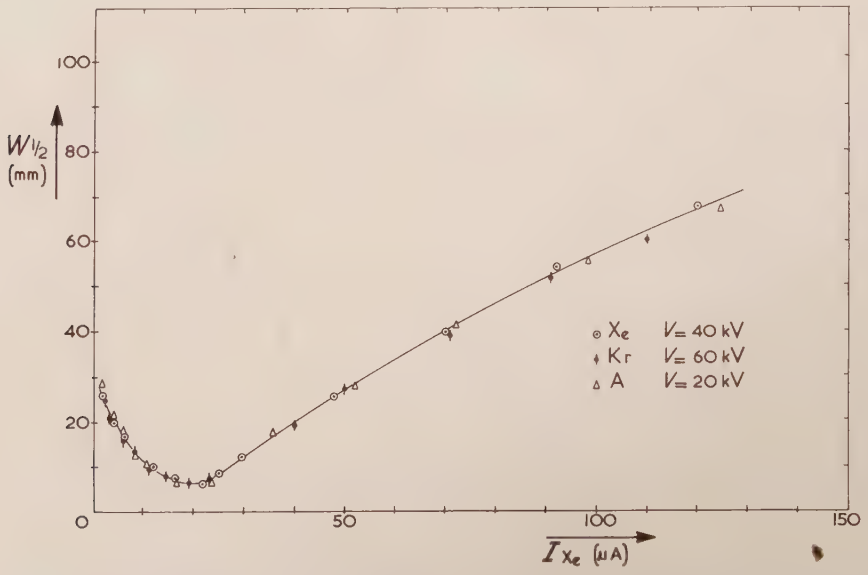

Fig. 11. Beam width, $W_{\frac{1}{2}}$, versus ion current for Xe, Kr and A at constant voltage ratio and equivalent pressures. The experimental points for A and Kr being transformed to that of Xe using eq. (6). (d = 110 mm, H = 300 gauss.)

5. Remarks

Due to the difficulties involved in determining equivalent pressures for different gases and in reproducing a given pressure in the discharge chamber, the use of the space charge law is practically restricted to ion beams from concave plasma boundaries for magnetic ion sources with end extraction. This is no serious limitation as most beam forming systems operate under these conditions. For some instruments, like the isotope separator at Pretoria, it is advantageous to employ ion beams from convex plasma boundaries[13,14]) because these beams have better ion optical properties due to the pronounced difference in beam form[18]). The simplified space charge law, as given by (9), will be useful for these systems provided constant pressure can be maintained in the discharge chamber.

In practical applications of beam forming systems similar to the one described it is important to notice that the beam form for beams from concave and convex plasma boundaries are respectively affected by the anode voltage and the gas pressure in the discharge chamber. These parameters may therefore be used to obtain slight modification in beam form at constant beam current.

Care should, however, be taken not to extend results obtained for beam formation using noble gases in the discharge chamber to gases which readily form negative ions, thereby changing the voltage difference between plasma and anode[17]).

Proof of the space charge law for the beam forming system described in this paper shows that the assumptions about beam formation from a plasma ion source (see sec. 2.1) are basically correct. This implies that the space charge law should be true for beam formation from all plasma ion sources. In practice, however, results similar to those given in this paper will have to be obtained for each type of ion source in order to determine under which discharge conditions the space charge law will hold.

Acknowledgements

The author is indebted to Mr. J. J. Selier and K. Lubbinge for assistance with the measurements.

[18]) W. L. Rautenbach, to be published.

NUCLEAR INSTRUMENTS AND METHODS 12 (1961) 180–186; NORTH-HOLLAND PUBLISHING CO.

HODOSCOPE SYSTEM FOR EXPERIMENTS ON THE SCATTERING OF COSMIC RAY MU-MESONS

PART III - THEORY OF THE HODOSCOPE

M. A. MEYER, J. A. M. DE VILLIERS and A. J. VAN DER WALT

Physics Department, Potchefstroom University for C.H.E., South Africa

Received 2 March 1961

The hodoscope which was designed for experiments on the scattering of cosmic ray mu-mesons has proved to be a very effective and fast method for determining the scattering function of mu-mesons. The electronic circuits and recording characteristics were described in previous publications. The present publication is concerned with the theory of the instrument. In its present form the useful energy region of this hodoscope is below about 600 MeV but this can easily be increased to energies below a few GeV's.

1. Introduction

In previous publications[1,2]) the electronic circuits and performance were discussed of a hodoscope which was designed for the study of the scattering of cosmic ray mu-mesons. Since the publication of these papers, the arrangement of the counter systems has been changed for various reasons of which the most important is to obtain a narrower energy range of mesons.

The principle of the method is essentially the following. The direction of the trajectory of the meson before and after scattering is determined by employing three systems of geiger counters A, B and C (fig. 1) each consisting of two layers of crossed counters. The scatterer was placed between the two layers of counters of the system B.

In the new arrangement, the system D consists of two crossed layers each consisting of 12 counters rather than a single layer. A single layer, as used in the previous arrangement, has the disadvantage of giving rise to a relatively high rate of casual coincidences. In the present arrangement, events were recorded in which only one counter in each of the six layers of the three systems A, B and C were discharged coincidently with the discharge of at least one counter in each of the layers of the system D without any of the counters of the system E being discharged. The counters of the systems A, B and C through which the particle has passed were identified by means of neon lamps, one for each counter. The panel on which the neon lamps were mounted was photographed whenever such an event occurred.

The efficiency of the system E is of great importance. In order to increase the probability that a particle which penetrates the absorber below the system D will discharge a counter in layer E, these counters were arranged in two layers. If the efficiency of the system E is not high then a number of particles of higher energy than would follow from the range in the absorbers will be recorded. These particles will contribute heavily to the small angle region and hence give rise to a scattering distribution which decreases faster with increasing angle of scattering than would have been the case in an ideal experiment.

A typical photograph of a trajectory is shown in fig. 2. The lines represent the projections of the trajectory on two mutually perpendicular planes. It is evident that a trajectory is uniquely specified by the four numbers p, p', q, q' (fig. 2) which indicates the differences of the numbers of the

[1]) M. A. Meyer, P. H. Stoker and J. A. M. de Villiers, Nucl. Instr. 3 (1958) 278.

[2]) M. A. Mever and J. A. M. de Villiers, Nucl. Instr. 3 (1958) 285.

discharged counters. These numbers are of primary importance and represent the only information obtainable from the photographs. Trajectories having the same values for $pp'qq'$ may be recorded in a number of ways. This number is given by

$$n_0 = n_1 n_2 \tag{1.1}$$

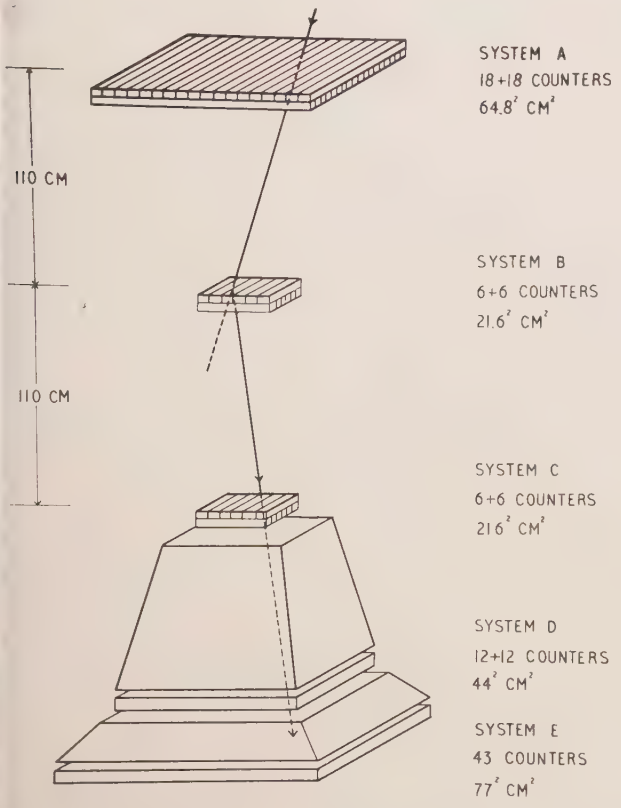

Fig. 1. The experimental arrangement.

where

$$n_1 = \begin{cases} 6 - |p'| \text{ if } |p| \leqslant 6 \\ 12 - |p + p'| \text{ if } |p| \geqslant 6 \\ 0 \text{ if } |p + p'| \geqslant 12 \end{cases} \Big\} \text{ if } p \text{ and } p' \text{ have the same sign.}$$

$$\begin{cases} 6 - |p'| \text{ if } \| p| - |p' \| \leqslant 6 \\ 12 - |p| \text{ if } \| p| - |p' \| \geqslant 6 \\ 0 \text{ if } |p| + |p'| \geqslant 17 \text{ or } |p| \geqslant 12 \end{cases} \Big\} \text{ if } p \text{ and } p' \text{ have opposite signs.} \tag{1.2}$$

The number n_2 is obtained from similar expressions but with the p's replaced by the q's.

Equations (1.1) and (1.2) and other formulae remain unchanged for the following eight combinations of the four numbers $pp'qq'$,

$$\begin{array}{llll} pp'qq' & pp'-q-q' & -p-p'qq' & -p-p'-q-q' \\ qq'pp' & qq'-p-p' & -q-q'pp' & -q-q'-p-p' \end{array} \tag{1.3}$$

Any of these trajectories will in future be called a $pp'qq'$-trajectory. Hence a $pp'qq'$-trajectory may be recorded in

$$\nu = \nu_0 n_0 = \nu_0 n_1 n_2 \tag{1.4}$$

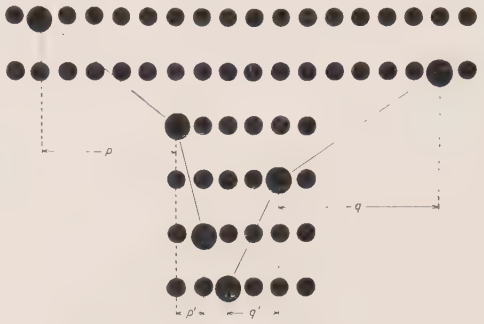

Fig. 2. Arrangement of the Hodoscope Neons showing a pp^1qq^1 trajectory of $-5-1\ 62$, classified in the group $|p-p'|$, $|q-q'| = 4, 4$.

TABLE 1

Constants for some of the trajectories of the group $|p-p'|$, $|q-q'| = 4, 4$

pp' qq'	ν_0	ν	φ_0	G	νG
04 04	4	16	10°43′	0.983	16
15	8	16	10°42′	0.976	16
1–3	8	48	10°43′	0.984	47
2–2	8	64	10°43′	0.980	63
3–1	8	80	10°43′	0.971	78
40	8	96	10°43′	0.957	92
51	8	80	10°42′	0.938	75
62	8	64	10°37′	0.915	59
73	8	32	10°35′	0.889	28
15 15	4	4	10°38′	0.968	4
1–3	8	24	10°42′	0.976	23
2–2	8	32	10°42′	0.973	31
.	.	+	.	.	+
.	.	.	.	.	.
.	.	.	.	.	.
.	.	+	.	.	+
51 51	4	100	10°38′	0.894	90
62	8	160	10°36′	0.873	140
73	8	80	10°33′	0.848	68
62 62	4	64	10°33′	0.853	55
73	8	64	10°33′	0.828	53
73 73	4	16	10°25′	0.804	13

$\sum \nu_k = 4096$ $\quad \bar{\varphi}_0 = 10°40'$ $\quad \sum \nu_k G_k = 3802$

ways, where, as follows from (1.3),

$$\nu_0 = \begin{cases} 8 \text{ in general} \\ 4 \text{ if } |p| = |q| \text{ and } |p'| = |q'| \\ 4 \text{ if } p = 0 = p' \text{ or } q = 0 = q' \\ 1 \text{ if } p = p' = q = q' = 0\,. \end{cases} \tag{1.5}$$

Typical values for ν_0 and ν are shown in table 1 (columns two and three) which illustrates the way in which the constants of the apparatus were tabulated.

2. Angle of Scattering

The incident and scattered directions (fig. 3) of the particle will be denoted by the projected angles (γ, β) and (γ', β') respectively. The angle of scattering, ϕ, is related to these angles and may be obtained as follows. Let the direction of the trajectory before and after scattering be represented by the unit vectors $\boldsymbol{n}$ and $\boldsymbol{n}'$ respectively. Then

$$\boldsymbol{n} = \boldsymbol{i} \sin\gamma - \boldsymbol{j} \cos\gamma \sin\beta - \boldsymbol{k} \cos\gamma \cos\beta$$

$$\boldsymbol{n}' = \boldsymbol{i} \sin\gamma' - \boldsymbol{j} \cos\gamma' \sin\beta' - \boldsymbol{k} \cos\gamma' \cos\beta'$$

where $\boldsymbol{i}$, $\boldsymbol{j}$ and $\boldsymbol{k}$ are unit vectors in the directions of the x-, y- and z-axes. The angle of scattering is then given by

$$\cos\varphi = \boldsymbol{n}\cdot\boldsymbol{n}' = \sin\gamma \sin\gamma' + \cos\gamma \cos\gamma' \sin\beta \sin\beta' + \cos\gamma \cos\gamma' \cos\beta \cos\beta' \tag{2.1}$$

The angle γ is not determined directly with this instrument but rather the angle α (fig. 4). It is therefore important to write this equation in terms of α and β. It is easily follows from fig. 4 that

$$\cos\gamma \cos\beta = \cos\lambda \cos\alpha, \qquad \sin\lambda = \cos\gamma \sin\beta$$

and consequently that

$$\cos\gamma = \frac{\cos\alpha}{\sqrt{1 - \sin^2\alpha \sin^2\beta}}, \qquad \sin\gamma = \frac{\sin\alpha \cos\beta}{\sqrt{1 - \sin^2\alpha \sin^2\beta}}.$$

An expression for $\mathrm{d}\gamma$ in terms of $\mathrm{d}\alpha$ will later be required. It follows from these equations that

$$\mathrm{d}\gamma = \frac{\cos\beta}{1 - \sin^2\alpha \sin^2\beta}\,\mathrm{d}\alpha\,.$$

Since the angles appearing in these expressions are less than about 20°, it follows that $\sin^2\alpha \sin^2\beta \ll 1$ and hence with an error of less than one per cent,

$$\cos\gamma = \cos\alpha, \ \sin\gamma = \sin\alpha \cos\beta, \ \mathrm{d}\gamma = \cos\beta\,\mathrm{d}\alpha\,. \tag{2.2}$$

The angle of scattering, as follows from (2.1) and (2.2), is therefore given by

$$\cos\phi = \cos(\alpha - \alpha') \cos(\beta - \beta')\,. \tag{2.3}$$

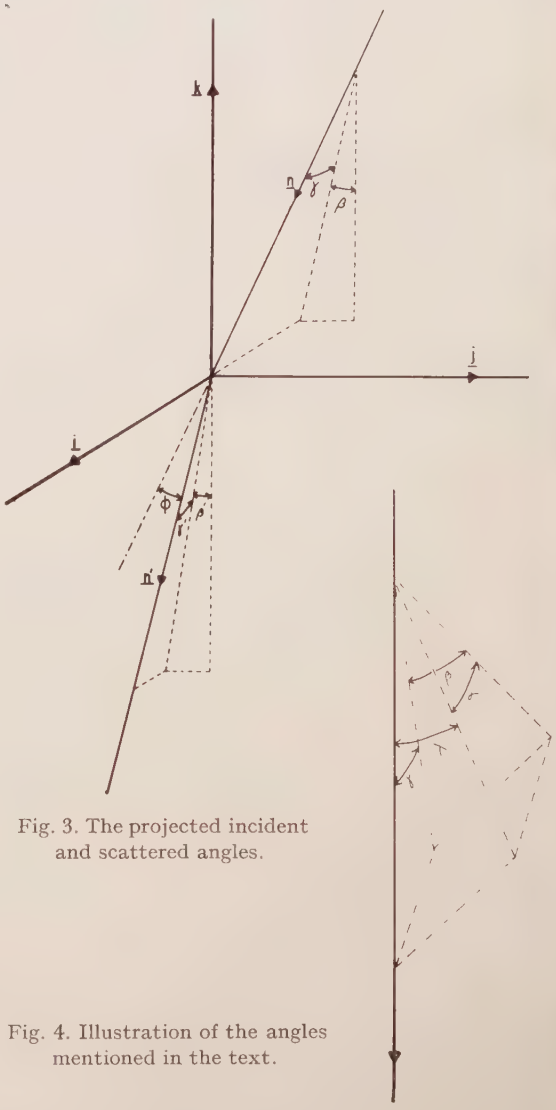

Fig. 3. The projected incident and scattered angles.

Fig. 4. Illustration of the angles mentioned in the text.

Since the differences $(\alpha - \alpha')$ and $(\beta - \beta')$ are also less than about 20° one may use the following approximate expression for the angle of scattering,

$$\phi^2 = (\alpha - \alpha')^2 + (\beta - \beta')^2 \tag{2.4}$$

which easily follows from (2.3).

It will be convenient to have an expression for the angle of scattering of a particle which passes through the centre of three squares, each square being defined by two crossed counters in each of the

three systems. Let the four numbers characterising the trajectory be $pp'qq'$. The angle of scattering is then given by

$$\cos\phi_0 = \cos(\alpha_0 - \alpha_0')\cos(\beta_0 - \beta_0') \qquad (2.5)$$

where

$$\cos\alpha_0 = \frac{l}{(l^2 + p^2a^2)^{\frac{1}{2}}}, \qquad \cos\alpha_0' = \frac{l}{(l^2 + p'^2a^2)^{\frac{1}{2}}}$$

$$\cos\beta_0 = \frac{l}{(l^2 + q^2a^2)^{\frac{1}{2}}}, \qquad \cos\beta_0' = \frac{l}{(l^2 + q'^2a^2)^{\frac{1}{2}}} \qquad (2.6)$$

and l is the distance between the systems and a the diameter of the counters. It follows from (2.5) and (2.6) that φ_0 has the same value for the eight combinations mentioned in (1.8). Typical values for ϕ_0 are shown in table 1 (column four). The angle ϕ_0 will be called the average angle of scattering of the trajectory designated by $pp'qq'$. Since $pa/l \ll$ etc, one may also calculate the four angles from the following approximate formulae.

$$\alpha_0 = pa/l, \quad \alpha_0' = p'a/l, \quad \beta_0 = qa/l \text{ and } \beta_0' = q'a/l. \qquad (2.7)$$

These formulae, together with (2.4) yield the following approximate formula for ϕ_0

$$\phi_0 = (a/l)\{(p - p')^2 + (q - q')^2\}^{\frac{1}{2}}. \qquad (2.8)$$

It follows from this expression that the trajectories having the same differences $|p - p'|$, $|q - q'|$ such as 0404, 0415, etc. (table 1) represents events which have approximately the same ϕ_0. These trajectories were therefore grouped together and will be called a group. The trajectories of the group $|p - p'|$, $|q - q'| = (4.4)$ are shown in table 1. The weighted mean of ϕ_0 and the standard deviation, σ, for a number of groups are shown in table 2.

TABLE 2

Typical constants for a few groups

$(p-p', q-q')$	(0,0)	(2,3)	(4,4)	(3,8)	(2,11)
0_0	0	6′50′	10°40′	16°0′	20°48′
α	0	1.5′	6′	7.4′	11.8′
$\Sigma\nu_k$	1296	9680	4096	5696	3360
$\Sigma\nu_k\alpha_k$	1244	9205	3802	5041	2803

3. Determination of the Scattering Function

The number of particles recorded which pass through three squares, each square being defined by two crossed counters in each system, may be obtained as follows. It is well-known that the intensity of mu-mesons from the direction θ with the vertical may be represented by

$$I = I_0\cos^n\theta.$$

The exponent, n, depends on the energy of the mesons and in this experiment is very nearly equal to 2. The exact value of n is not important in this experiment. The rate at which mu-mesons pass through an elementary area $dx\,dy$ of a square of the system B which is received in the elementary solid angle dw at an angle θ with the vertical is

$$I_0\cos^2\theta\,dx dy\cos\theta\,dw. \qquad (3.1)$$

The angle of incidence and the elementary solid angle is related to the projected angles γ and β (fig. 5) by the relations

$$\cos\theta = \cos\gamma\cos\beta \qquad \text{and} \qquad dw = \cos\gamma\,d\gamma\,d\beta$$

which, by means of (2.2), may be written as

$$\cos\theta = \cos\alpha\cos\beta \qquad \text{and} \qquad dw = \cos\alpha\cos\beta\,d\alpha\,d\beta. \qquad (3.2)$$

Hence (3.1) becomes

$$I_0\cos^4\alpha\cos^4\beta\,dx\,dy\,d\alpha\,d\beta. \qquad (3.3)$$

If $f(\phi)\,dw'$ represents the probability that a meson in the energy range under consideration will be scattered into the solid angle dw' at an angle ϕ with respect to its original direction, then the number of

particles received in the solid angle dw from the direction (α, β) by the elementary area $dx\ dy$ of a square of the system B and scattered into the elementary solid angle $dw' = \cos\alpha' \cos\beta'\ d\alpha'\ d\beta'$ at an angle ϕ with respect to the original direction (fig. 5) is

$$dn = I_0 \cos^4\alpha \cos^4\beta \cos\alpha' \cos\beta' f(\phi)\ d\alpha\ d\beta\ d\alpha'\ d\beta'\ dx\ dy\ . \tag{3.4}$$

In order to obtain the total number of particles recorded by the three arbitrary squares in each of the systems A, B and C one has to integrate (3.4) over those values of the variables characterising the three squares. Before integrating the above expression, the following may be noted. Firstly, the limits of α and α' are determined only by x and the limits of β and β' are determined only by y. Indicating the upper and lower limits of α and α' by 2 and 1 respectively, one obtains from fig. 5 that, to a high degree of approximation,

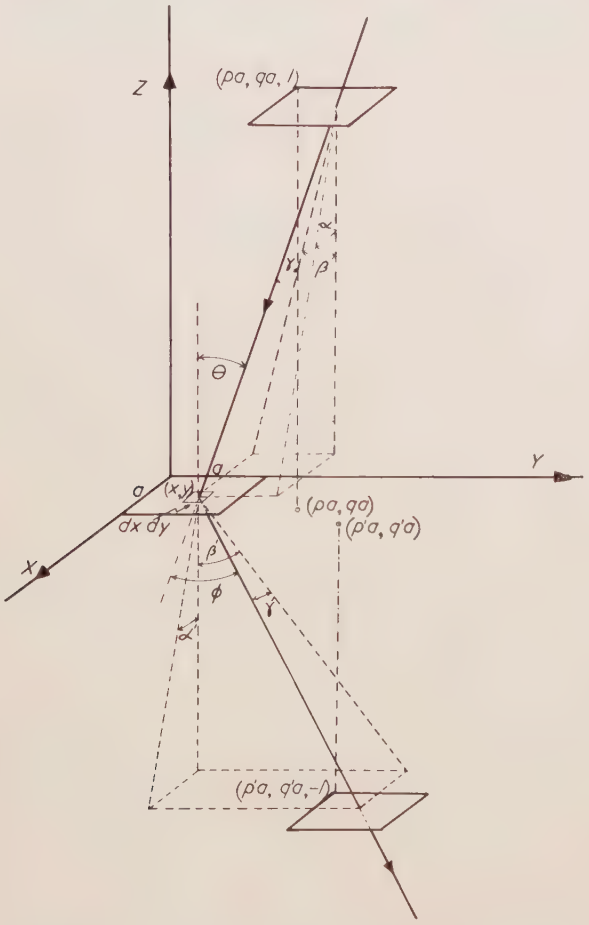

Fig. 5. Illustration of the limits of integration.

$$\alpha_2 = \alpha_0 + \frac{a - x}{l}\ , \qquad \alpha_2' = \alpha_0' + \frac{x}{l}$$

$$\alpha_1 = \alpha_0 - \frac{x}{l}\ , \qquad \alpha_1' = \alpha_0' - \frac{a - x}{l} \tag{3.5}$$

where α_0 and α_0' are given by (2.7). The limits for α' follows from the sign convention in fig. 2. Similar expressions hold for the upper and lower limits of β and β'. The upper and lower limits of x are a and 0 respectively. Secondly, one notes that the factor $\cos^4\alpha \cos^4\beta \cos\alpha' \cos\beta'$ is practically constant over the range of integration. It is sufficiently accurate to replace this factor in (3.4) by the quantity

$$G = \cos^4\alpha_0 \cos^4\beta_0 \cos\alpha_0' \cos\beta_0' \tag{3.6}$$

where the angles α_0, β_0, α_0' and β_0' represent the appropriate angles for a particle passing through the centres of the three squares under consideration. These angels are given by (2.6). Typical values for G are shown in table 1. It is easily seen that G has the same value for the eight possibilities mentioned in (1.3). Lastly, one notes that the angle of scattering, ϕ, is a function only of $\alpha - \alpha'$ and $\beta - \beta'$. Hence the scattering function may be written as

$$f(\phi) = F(\alpha - \alpha'\ ,\ \beta - \beta')\ . \tag{3.7}$$

The total number of particles passing through the three squares under considerations is therefore given by

$$n = I_0 G \iiint d\beta\ d\beta'\ dy \int_0^a \int_{\alpha_1'}^{\alpha_2'} \int_{\alpha_1}^{\alpha_2} F(\alpha - \alpha', \beta - \beta')\ d\alpha\ d\alpha'\ dx$$

$$= I_0 G \iiint d\beta\ d\beta'\ dy \int_0^a \int_{\alpha_1'}^{\alpha_2'} \{\psi(\alpha_2 - \alpha', \beta - \beta') - \psi(\alpha_1 - \alpha', \beta - \beta')\}\ d\alpha'\ dx$$

where $\partial\psi/\partial\chi = F$ and $\chi = \alpha - \alpha'$. Hence

$$n = -I_0 G \iiint \mathrm{d}\beta\, \mathrm{d}\beta'\, \mathrm{d}y \int_0^a \mathrm{d}x \left[\int_{\chi_0 + \frac{2a-2x}{l}}^{\chi_0 + \frac{a-2x}{l}} \psi(\chi, \beta - \beta')\, \mathrm{d}x - \int_{\chi_0 + \frac{a-2x}{l}}^{\chi_0 - \frac{2x}{l}} \psi(\chi, \beta - \beta')\, \mathrm{d}x \right]$$

where $\chi_0 = \alpha_0 - \alpha_0'$.

Hence

$$n = -I_0 G \iiint \mathrm{d}\beta\, \mathrm{d}\beta'\, \mathrm{d}y \int_0^a \mathrm{d}x \left[2\Psi\left(\chi_0 + \frac{a-2x}{l}, \beta - \beta'\right) - \Psi\left(\chi_0 + \frac{2a-2x}{l}, \beta - \beta'\right) - \Psi\left(\chi_0 - \frac{2x}{l}, \beta - \beta'\right) \right]$$

where $\partial\Psi/\partial\chi = \psi$ and hence $\partial^2\Psi/\partial\chi^2 = F$. Expansion of the expression in the square brackets and integration over x yields.

$$n = -I_0 G a \left(\frac{a}{l}\right)^2 \iiint \mathrm{d}\beta\, \mathrm{d}\beta'\, \mathrm{d}x \left\{ F(\chi_0, \beta - \beta') + \frac{1}{4}\left(\frac{a}{l}\right)^2 F_\chi''(\chi_0, \beta - \beta') + \frac{1}{40}\left(\frac{a}{l}\right)^4 F_\chi''''(\chi_0, \beta - \beta') + \dots \right\}$$

where $F^n{}_\chi$ denotes the nth derivative of F with respect to the variable χ. Finally, integration over β, β' and y gives

$$n = I_0 G\, a^2 \left(\frac{a}{l}\right)^4 \left[F(\chi_0, \eta_0) + \frac{1}{4}\left(\frac{a}{l}\right)^2 \left\{ F_\chi''(\chi_0, \eta_0) + F_\eta''(\chi_0, \eta_0) \right\} + \dots \right.$$

where $\eta_0 = \beta_0 - \beta_0'$ and $F^n{}_\eta$ denotes the nth derivative of F with respect to η. It will be assumed that these terms are the only important ones in the series expansion. The conditions for the validity of this assumption will presently be invesitigated. Since $F(x, y) = f(\phi)$ where

$$\varphi = (\chi^2 + \eta^2)^{\frac{1}{2}},$$

it is easily seen that

$$n = I_0 G a^2 \left(\frac{a}{l}\right)^4 \left[f(\varphi_0) + \frac{1}{4}\left(\frac{a}{l}\right)^2 \left\{ f''(\varphi_0) + \frac{1}{\varphi_0} f'(\varphi_0) \right\} + \dots \right] \tag{3.8}$$

where

$$\phi_0 = (\chi_0^2 + \eta_0^2)^{\frac{1}{2}} = [(\alpha_0 - \alpha_0')^2 + (\beta_0 - \beta_0')^2]^{\frac{1}{2}}$$

which is therefore given by (2.8). Evidently the factor G and the angle ϕ_0 in (3.8) remain unaltered for the ν trajectories mentioned in (1.4).

Hence the total number of $pp'qq'$-trajectories recorded is

$$N(\varphi_0) = \nu I_0 G a^2 \left(\frac{a}{l}\right)^4 \left[f(\varphi_0) + \frac{1}{4}\left(\frac{a}{l}\right)^2 \left\{ f''(\varphi_0) + \frac{1}{\varphi_0} f'(\varphi_0) \right\} \right].$$

Similar expressions hold for each of the trajectories in table 1. Summation over all trajectories having the same values for $|p - p'|$, $|q - q'|$ as in table 1, yields

$$\sum N_k(\varphi_0) = I_0\, a^2 \left(\frac{a}{l}\right)^4 \left[f(\bar{\varphi}_0) + \frac{1}{4}\left(\frac{a}{l}\right)^2 \left\{ f''(\bar{\varphi}_0) + \frac{1}{\bar{\varphi}_0} f'(\bar{\varphi}_0) \right\} \right] \sum \nu_k G_k$$

where $\bar{\phi}_0$ represents the weighted mean of the angles having the same values for $|p - p'|$, $|q - q'|$.

Typical values for $\sum \nu_k G_k$ are given in table 2. If the thickness of the counter walls, is taken into account then a/l must be replaced by $(a - 2\delta)/l$. Therefore

$$f(\bar{\varphi}_0) + \frac{1}{4}\left(\frac{a - 2\delta}{l}\right)^2 \left\{ f''(\bar{\varphi}_0) + \frac{1}{\bar{\varphi}_0} f'(\bar{\varphi}_0) \right\} + \dots = \text{constant} \frac{\sum N_k(\varphi_0)}{\sum \nu_k G_k}. \tag{3.9}$$

This equation was used to determine the scattering function $f(\bar{\phi}_0)$ at the angle $\bar{\phi}_0$ for mesons in the

energy determined by the thicknesses of the absorbers. This function must be compared with the theoretical scattering functions after these have been integrated over the energy range under consideration.

It still remains to consider the region of validity of the assumption regarding the convergence of the series expansion leading to (3.8). Let us first consider the region of pure multiple scattering, when

$$f(\phi) = C \exp(-\phi^2/\lambda^2) .$$

The quantity λ is a function of the energy of the mesons and the thickness of the scatterer. Then

$$f(\varphi) + \frac{1}{4}\left(\frac{a-2\delta}{l}\right)^2 \left\{ f''(\varphi) + \frac{1}{\varphi} f'(\varphi) \right\} = f(\varphi) \left\{ 1 + \left(\frac{a-2\delta}{\lambda l}\right)^2 \left(\frac{\varphi^2}{\lambda^2} - 1\right) \right\} .$$

It follows from this equation that the correction terms may be neglected when

$$1 \gg \left(\frac{a-2\delta}{\lambda l}\right)^2 \left(\frac{\varphi^2}{\lambda^2} - 1\right) .$$

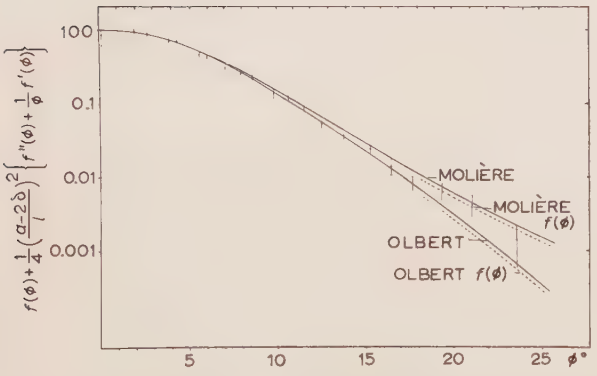

Fig. 6. A typical experimental scattering function in the $p\beta$ range 186–429 MeV/c compared with the theories of Olbert and Molière.

It is therefore seen that the convergence of the series in the case of multiple scattering depends upon the energy of the mesons and the thickness of the scatterer. For a fixed diameter of the counters, this condition will be satisfied by increasing λl. The quantity λ may be increased by lowering the energy of the mesons or increasing the thickness of the scatterer. For example, if $a - 2\delta = 3.33$ cm and $l = 110$ cm, then $(a - 2\delta)/l = 1.74°$ and for 400 MeV mesons and a 2 cm scatterer $\lambda = 5°$. In this case, the correction is -12% at $\phi = 0°$, 0% at $\phi = 5°$ and 12% at $\phi = 7°$. These corrections may be determined by graphical methods. The scattering of higher energy particles may be studied by increasing l and the thickness of the scatterer.

In the region of single scattering where

$$f(\phi) = C/\phi^4$$

C being independent of ϕ, it follows that

$$f(\varphi) + \frac{1}{4}\left(\frac{a-2\delta}{l}\right)^2 \left\{ f''(\varphi) + \frac{1}{\varphi} f'(\varphi) \right\} = f(\varphi) \left\{ 1 + \left(\frac{a-2\delta}{l}\right)^2 \frac{4}{\varphi^2} \right\} .$$

It is seen that the convergence in this case in independent of the energy of the mesons and the thickness of the scatterer. If $(a - 2\delta)/l = 1.74°$, as previously, the correction is 12% at 10° and about 5% at 15°.

A typical example of a scattering function determined by this method is shown in fig. 6 which also illustrates the magnitude of the second term in (3.9). This result and others, will be discussed elsewhere.

Acknowledgements

This work was made possible by a grant from the South African Council for Scientific and Industrial Research.

NUCLEAR INSTRUMENTS AND METHODS 12 (1961) 187–191; NORTH-HOLLAND PUBLISHING CO.

ADAPTATION OF A $\pi\sqrt{2}$ BETA-RAY SPECTROMETER FOR COINCIDENCE EXPERIMENTS

ZIEMOWID SUJKOWSKI†

Nobel Institute of Physics, Stockholm 50, Sweden

Received 9 March 1961

A large iron-core double-focusing β-ray spectrometer with a mean radius of 50 cm has been adapted for coincidence experiments involving electrons. Scintillation detectors were used. It is shown that satisfactory protection of the photomultipliers from the magnetic field can be obtained by means of a local field compensation with suitable Helmholtz coils. Some examples of applications are given. The doppler shift of the Th (B + C + C″) A-line due to the α-decay of Bi^{212} is demonstrated. Some α–e^- and γ–e^- directional correlations have been measured.

1. Introduction

Application of the coincidence technique to β- or internal conversion electrons is now generally acknowledged as a very useful method in nuclear spectroscopy, especially in studying complex decay schemes. In most of the experiments a selection of the electron momentum or energy is necessary. Great progress in this respect has been made by the application of the magnetic β-ray spectrometers. Up to the present time lens spectrometers have been most often employed, mainly because of their high transmission and the relatively easy access to the source, making possible convenient handling of the detector for the coincident radiation. Several such instruments have been described in connection with various experiments. Gerholm and Pettersson[1]) discussed recently the application of a lens spectrometer to γ–e^- angular correlation measurements. In some cases, however, even higher precision in the electron momentum selection is required than can be obtained with standard lens spectrometers.

The application of the magnetic β-ray spectrometers of a double-focusing $\pi\sqrt{2}$ type could be very fruitful to this end. An additional advantage of using such an instrument for angular correlation work is, that the correction for the finite size of the spectrometer aperture is simple and generally small. This is not the case for lens spectrometers. The main drawback, apart from the lower transmission, is the difficulty in handling the source and the detectors. Since the use of fast scintillation counters is indispensable in this kind of work, and commercial photomultipliers are very sensitive to the magnetic field, a suitable protection of the detectors from the field of the spectrometer must be provided. As will be shown below, this last difficulty can be overcome by the method of local field compensation rather than by magnetic shielding. A large, high precision double-focusing iron-core beta-ray spectrometer has been adapted in this way for coincidence measurements with scintillation detectors. A number of directional correlations and other coincidence experiments have been performed and some examples will be given.

† On leave of absence from the Institute of Nuclear Research of the Polish Academy of Sciences, Warsaw, Poland.

2. Description of the Arrangement

2.1. LOCAL FIELD COMPENSATION

The main difficulty in applying the scintillation detection technique to double-focusing β-ray spectrometers is, as was mentioned above, the sensitivity of commercial photomultipliers to the magnetic field. In the case of magnetic lens- or sector-type spectrometers, where practically only the stray field acts on the detector, shielding with a material of high permeability may be sufficient to protect the counter from this effect. In the case of $\pi\sqrt{2}$ double-focusing spectrometers any ferromagnetic material near the detector would introduce serious distortions of the magnetic field and affect the focusing properties. Moreover, the

[1]) T. R. Gerholm and B. G. Pettersson, Nucl. Instr. and Meth. 4 (1959) 107.

shielding could be effective only in a limited range of the field†. Since scintillation detectors are often desirable even for measurements of singles spectra of electrons, especially if high counting rates are expected, other solutions had to be looked for. Long light-guides have sometimes been used, with a photomultiplier placed outside the magnetic field (see e.g. Stockendal and Hultberg[4])). The drawback of this method is that, due to the poor light collection from the scintillating material, the resolving power of the detector is impaired and the pulses due to the low- and moderate-energy electrons (below about 100–150 keV, as in the experiments of Ryde and Sujkowski[5])) are hardly distinguishable from the noise. The method would be still less suitable for coincidence measurements, where the resolving power of the detector for the coincident radiation is most often essential for the experiment. For the same reason, as well as from the constructional point of view, a measurement of the angular correlation in such an instrument with long guiding of the light pulses seems hardly possible.

Another solution to this difficulty was offered by Johansson and Ryde[6]). They placed a scintillation detector (crystal mounted directly on a photomultiplier) inside the vacuum tank of the $\pi\sqrt{2}$ β-ray spectrometer, but instead of magnetic shielding, a local compensation of the magnetic field was attained by means of a Helmholtz coil. It was shown that neither the relative intensities nor the shape of the conversion lines were affected by the presence of the coil over the range of the measurement.

The advantage of this method was made use of in the present investigation. Two similar Helmholtz coils were used, one of them placed around the electron detector and the other around the source. Both coils were fed with the main spectrometer current suitably shunted. Similarly as in the work of Johansson and Ryde, a single shunt setting could be used over the entire measuring region with the compensation remaining constant. The circuit diagram of the coils is shown in fig. 1.

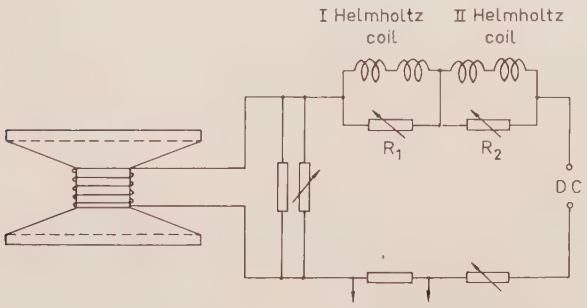

Fig. 1. Circuit diagram for the compensating coils.

The possible effects that the distortions of the magnetic field introduced by the compensating coils may have on the focusing properties of the spectrometer were checked in several manners. The singles spectrum of the conversion electrons from the active deposit of thoron (ThB + C + C″) was first measured with a conventional GM counter, then with a scintillation detector placed inside the first compensating coil and finally with both this and the second compensating coil (at the source side) connected. Five electron lines were recorded each time: A(24.509 keV), B(36.150 keV), F(148.08 keV), I(222.22 keV) and L(422.84 keV) (Ellis' notation, energies of the first 4 lines quoted according to Siegbahn and Edvarson[7])). The same experiment was then repeated with a Bi^{207} sample and the 570 keV-K and 1064 keV-K conversion lines. No disturbing effects were observed. The relative intensities and line shapes remained constant with an accuracy of better than 2% and the relative positions of the lines ($B\rho$) with an accuracy of better than about 0.2%.

† It should be noted, however, that a particular design of a spectrometer may make it possible to overcome this difficulty. A beautiful example of such a design is the large, air-core $\pi\sqrt{2}$ spectrometer at Chalk River, recently described by Graham *et al.*[2]). Both the source and the detector are there placed outside the main vacuum tank and are easily accessible. Magnetic shielding of scintillation detectors proved to be possible and coincidence measurements with this instrument have recently been reported by Ewan *et al.*[3]).

[2]) R. L. Graham, G. T. Ewan and J. S. Geiger, Nucl. Instr. and Meth. **9** (1960) 245.

[3]) G. T. Ewan, R. L. Graham and J. S. Geiger, Nucl. Phys. **22** (1961) 610.

[4]) R. Stockendal and S. Hultberg, Arkiv f. Fysik **15** (1958) 33.

[5]) H. Ryde and Z. Sujkowski, to be published in Arkiv f. Fysik.

[6]) B. Johansson and H. Ryde, Arkiv f. Fysik **16** (1960) 501.

[7]) K. Siegbahn and K. Edvarson, see K. Siegbahn, ed., Beta- and Gamma-Ray Spectroscopy (North-Holland Publishing Company, Amsterdam, 1955).

3. Experimental Set-Up for Angular Correlation

In all coincidence experiments the electrons were detected with a thin plastic scintillation foil and an RCA 6342 photomultiplier. Various detectors were used to record the coincident radiation according to the requirements of the experiment and are described below.

rotating disc, coinciding with the axis of the Helmholtz coil. In order to check the centering as well as the field compensation, a NaI(Tl) crystal, coupled directly to the RCA 6342 photomultiplier, was mounted on the rotating disc and the γ-ray scintillation spectrum of Bi^{207} was recorded at various angular positions with a 100-channel pulse-

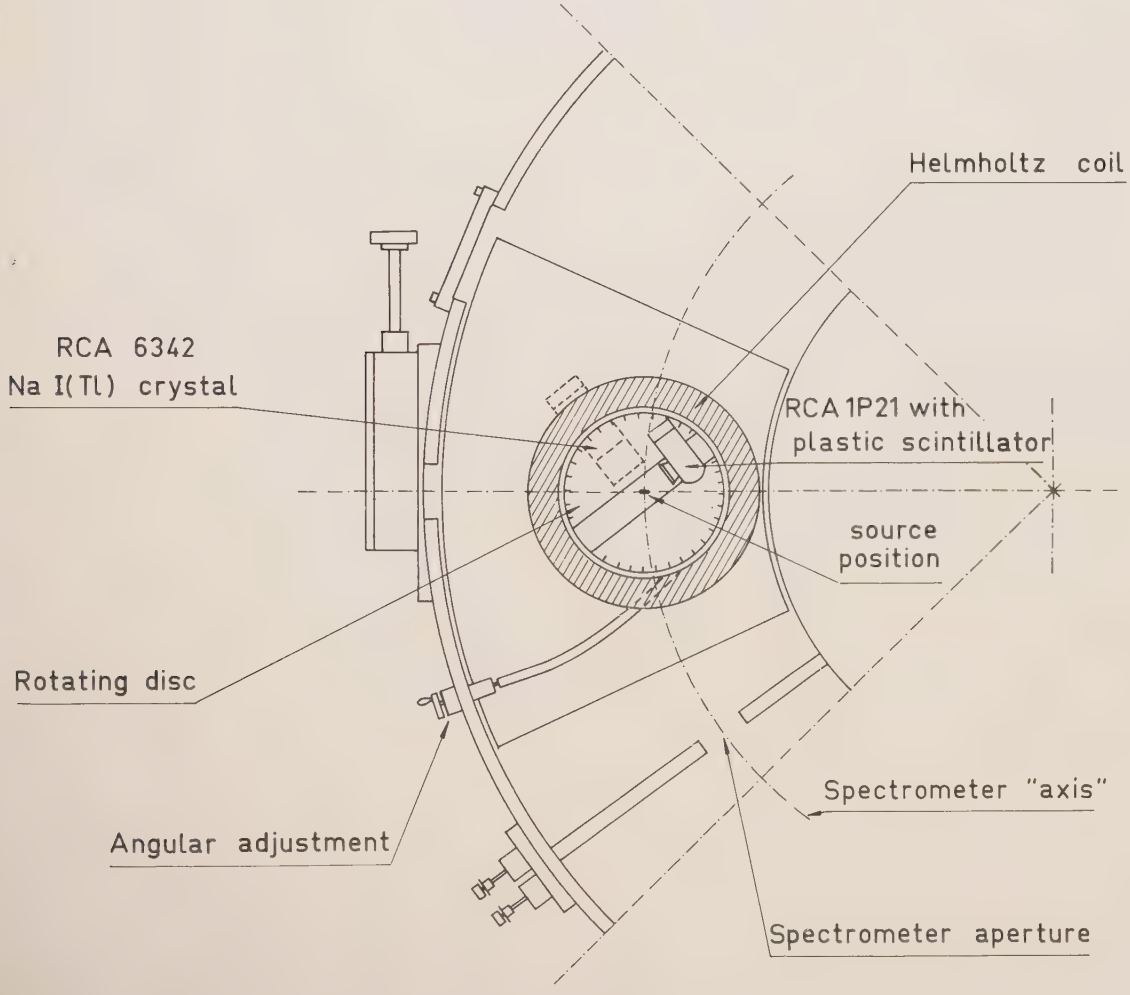

Fig. 2. Compensating coil and mechanical construction used for the angular correlation experiments.

The arrangement for measuring the angular correlations is shown schematically in fig. 2. The γ- or α-detector was placed on a rotating disc, which could be operated from outside. The arrangement constructed by Hultberg for a study of the angular distributions of photoelectrons[8]) was adapted for this purpose.

The source was centered on the axis of the

height analyzer. It was found that at higher fields (4658 gauss·cm, corresponding to the focusing of the 976 keV conversion electrons from Bi^{207}) the effect of the radial inhomogeneity of the spectrometer field was large enough to alter the compensation at different angular positions. The effect could be compensated almost completely by placing the

[8]) S. Hultberg, Arkiv f. Fysik 15 (1959) 307.

two coils of the Helmholtz coil slightly obliquely to each other, with the larger opening towards the outer wall of the spectrometer. This, once adjusted experimentally, remained valid for all the field strengths used. It may be noted, however, that for still higher fields a special design of the compensating coil might be needed for angular correlation work.

4. Examples of Measured Coincidence Spectra and Directional Correlations

The instrument has been used for several investigations and some examples can be quoted here.

1. The conversion electron spectrum of Tl^{208} in coincidence with α-particles from the decay of Bi^{212} was measured. An RCA 1P21 photomultiplier and a thin plastic scintillator were used to detect the α-particles. A fast coincidence circuit of about 30 mμ sec resolving time was used.

Fig. 3 shows the well-known A-line from the decay of Th(B + C + C″) as measured in a singles spectrum and in coincidence with the α-particles. By measuring coincidences at $\theta = 180^0$ and 97° the Doppler shift due to the recoil after the α-decay could be demonstrated. The recoil energy

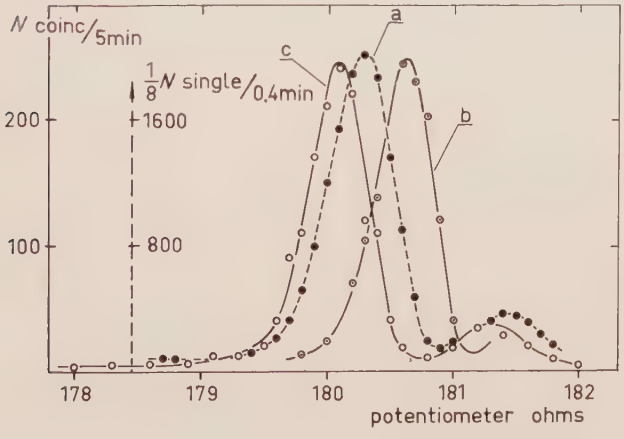

Fig. 3. Doppler shift of the A-line of the Th(B + C″+ C) spectrum. Curve (a)-singles spectrum, (b)-coincidence spectrum, $\theta = 180°$, (c)-coincidence spectrum, $\theta = 97°$.

of the Tl^{208} nucleus is ≈ 116 keV, which corresponds to about a 178 eV shift of the energy of the 24.509 keV conversion electrons. The experimental value for the angles given above is (140 ± 25) eV. This, when corrected for the finite size of the detector, gives the value (155 ± 25) eV, in very good agreement with the expected value. It may be noted that special care in preparing the source must be taken in order to avoid the effects of the source thickness and of the penetration of the active deposit into the backing. The latter was discussed first by Siekman and de Waard[9]), whose procedure of the source preparation was used in the present investigation.

2. The α–e^- directional correlation was measured for the same source and for the A-line (the L_I conversion line of the 40 keV γ-transition in Tl^{208}). The distribution was found to be isotropic to within the error of about 1%. This is in accordance with what one could expect for this transition (the spin and parity sequence of the cascade is $1 - (\alpha; L = 3{,}5) \to 4 + (\gamma; \mathrm{M1}) \to 5 +$, see Horton[10])) if we assume that the particle parameters for M1 γ-transitions converted in L_1 shells are small, especially at low energies. Though there are no theoretical calculations of the particle parameters for the conversion electrons from the higher shells, one can, however, expect a similarity between the K and L_1 shells ($s_{\frac{1}{2}}$ electrons). The K-shell particle parameters b_2 for M1 transitions are smaller than 1 and decrease sharply at low energies[11,12]) and the estimate that b_2 (M1, L_1 shell) $\leqslant 0.12$, which would fit the present result, seems by analogy quite reasonable. The possibility that the attenuation of the α–e^- directional correlation is stronger and more environmentdependent than is the α–γ correlation cannot, however, be excluded. [The latter correlation was measured by Horton[10]) and Weale[13]) and the anisotropy was found to be $W(90°)/W(180°) \approx 1.29$.]

3. The well-studied 1064 keV K-conversion electron – 570 keV γ-ray directional correlation in the decay of Bi^{207} was measured. A $1\frac{3}{4}'' \times 1''$ NaI(Tl) crystal mounted on the RCA 6342 photomultiplier was used as the γ-ray detector. A fast-slow coincidence circuit having a 30 mμsec resolving-time was

[9]) J. G. Siekman and H. de Waard, Phys. Rev. **107** (1957) 1731; see also J. G. Siekman (Groningen, 1959) thesis.

[10]) J. W. Horton, Phys. Rev. **101** (1956) 717.

[11]) M. E. Rose, L. C. Biedenharn, G. B. Afrken, Phys. Rev. **85** A68 (1952) 5.

[12]) A. K. Ustinova, ZETP **37** (1959) 307.

[13]) J. W. Weale, Proc. Phys. Soc. A68 (1959) 35.

used. The angle was varied from $\theta = 60^0$ to $\theta = 220^0$ in small steps in order to check for any possible distortions. The same experiment was repeated with the RCA 1P21 photomultiplier and with the angle varied from $\theta = 60^0$ to $\theta = 270^0$. In both cases the distribution was found symmetric about $\theta = 180^0$. The least square fit of the data gave the values of the coefficients for the Legendre polynomials in the correlation function: $A_2 = 0.238 \pm 0.006$ and $A_4 = -0.019 \pm 0.012$. The theoretical values of these coefficients are: $A_2 = 0.232$, $A_4 = -0.023$, if we assume the particle parameter $b_2 = 1.048$ (ref.[11])). Mc Gowan[14]) reports $A_2 = 0.241 \pm 0.004$ and $A_4 = -0.0216 \pm 0.0075$ and Gerholm and Pettersson[1]) give $A_2 = 0.240 \pm 0.007$.

4. Another example of γ–e^- directional correlations which have been measured is the 401 keV γ–279 keV-K conversion electron cascade in the decay of Pb^{203}. This correlation has recently been studied by Deutch and Goldberg[15]) and found to fit the distribution $W(\theta) = 1 + b_2A_2P_2(\cos\theta)$, where $b_2A_2 = -0.052 \pm 0.015$. Our measurements give a much smaller value $b_2A_2 = -0.034 \pm 0.007$. In view of the very good agreement for the measurement on the Bi^{207} source and the absence of any observed instrumental distortion, it is difficult to think of some systematic error affecting our result†. According to Deutch and Goldberg there should be no observable attenuation of the correlation depending on the source form and the source backing. The sources used in the present work were vacuum evaporated from a hydrochloric acid solution onto an Al foil. The details of this work will be published elsewhere[16]).

† When this work was completed it came to our knowledge that the same correlation was measured recently also by the Uppsala group in an extended study of the nuclear structure effects on the conversion coefficients (T. R. Gerholm *et al.*, to be published in Nucl. Phys.; private communication from T. R. Gerholm and B. S. Pettersson). The agreement of the present value with their result seems to be very good.

Acknowledgements

The author would like to take this opportunity to express his sincere gratitude to Professor Manne Siegbahn, Head of the Nobel Institute, for the hospitality shown to the author during his stay in Stockholm and for the excellent working facilities put at his disposal. His thanks go also to Dr. Bertil Johansson for many valuable suggestions, for his help concerning the coincidence measurements and his knowledge of pulse technique which he so unhesitatingly put at the author's disposal. The maintenance grant from the Syskonen-Wesséns Stiftelse and the leave of absence from the Institute of Nuclear Research in Warsaw are thankfully acknowledged. Finally my thanks go to Miss G. K. Oelsner, B. Sc., for correcting the English.

[14]) F. K. McGowan, Phys. Rev. **92** (1953) 524.
[15]) B. I. Deutch and N. Goldberg, Phys. Rev. **117** (1960) 818.
[16]) Z. Sujkowski, to be published in Arkiv f. Fysik.

NUCLEAR INSTRUMENTS AND METHODS 12 (1961) 192-194; NORTH-HOLLAND PUBLISHING CO.

THE PREPARATION OF THIN ^{18}O TARGETS

A. H. F. MUGGLETON and F. A. HOWE

Atomic Weapons Research Establishment, Aldermaston, Berks.

Received 22 March 1961

This article describes a technique for producing thin films containing ^{18}O, suitable for nuclear spectroscopy. Tungsten oxide is first prepared from heavy water enriched in ^{18}O; it is then evaporated in vacuum on to thin carbon backings.

1. Introduction

Thin ^{18}O targets were required for studying the energy levels of ^{19}O and ^{20}O from the $^{18}O(d, \alpha)$, $^{18}O(d, p)$ and $^{18}O(t, p)$ reactions, respectively[1]). Thicker targets were also necessary to study the delayed neutrons emitted following the β-decay of ^{17}N which was produced in the $^{18}O(t, \alpha)$ reaction[2]).

Initially targets were made by a modified version of the technique described by Holmgren *et al.*[3]). This method depends on the production of a thin iron or nickel foil which is subsequently oxidised by heating in an ^{18}O atmosphere. Iron foils were used in preference to nickel due to their greater rate of oxidation. Although satisfactory targets were produced by Holmgren's technique the following disadvantages were encountered:

1. Self supporting iron foils, of the required thickness (50–100 $\mu g/cm^2$) were difficult to make due to the stresses set up in the foil during deposition by vacuum evaporation. These stresses caused the foils to either shred or curl during mounting necessitating an extensive annealing operation.

2. Once mounted across the target holder aperture ($\frac{1}{2}''$ long $\times$ $\frac{1}{4}''$ wide slot) the foils were very prone to splitting.

3. Oxidation of the iron foils was a delicate and tedious operation with a low yield of useful specimens.

To overcome these difficulties it was decided to investigate a new approach to the problem. The technique finally decided upon divides naturally into two parts, (i) the production of a suitable compound of enriched ^{18}O, and (ii) the vacuum evaporation of this compound to prepare thin targets.

2. Preparation of ^{18}O enriched Tungsten Oxide

Tungsten oxide was chosen as a suitable compound since tungsten is easily oxidised in a water saturated atmosphere and the oxide formed can be vacuum evaporated without any great difficulty. Furthermore it is important in nuclear spectroscopy that a wide separation of mass numbers exists between the element being investigated and any other elements present. The separation between oxygen and tungsten adequately fulfills this requirement. Finally, tungsten oxide is a stable compound which can be stored without deterioration.

^{18}O enriched to 95%, is available as either a gas or in the form of $D_2{}^{18}O$†. Handling of this expensive isotope in the D_2O form overcomes problems of conservation and was therefore chosen for the technique described.

An exploded view of the apparatus used for the preparation of the enriched oxide is shown in fig. 1. The main vessel (b) is of borosilicate glass which is easily cleaned and allows visual observation of the process; (c) and (d) are removable shields made of nickel and glass respectively. The top plate (e) is of brass sealed to chamber (b) by means of an "O-ring" and contains several glass to metal seals to which 0.020″ tungsten filaments can be affixed.

Approximately 0.2 ml of enriched water was introduced into the small bulb (a) by means of a micro-hypodermic syringe with an extended needle. This drop of water was frozen by immersing the small reservoir in a solid CO_2-trichlorethylene slush

[1]) S. Hinds and R. Middleton, (to be published).

[2]) S. Hinds, R. Middleton, A. E. Litherland and D. J. Pullen, Phys. Rev. Letters (February 1961).

[3]) H. D. Holmgren *et al.*, Rev. Sci. Inst. 25 (1954) 1026.

† Available from the Weizmann Institute, Rehovoth, Israel.

and the apparatus evacuated through the side arm by means of an oil diffusion pumping unit until a pressure of $\approx 5 \times 10^{-4}$ torr was maintained. With the chamber isolated from the vacuum system, the reservoir was gently heated to vaporise the enriched water. Cleaned tungsten filaments were heated one at a time to approximately 2500°C by passing a current through them. The tungsten oxide formed immediately re-evaporated and deposited on to the removable shields. Coolant applied to the reservoir

Fig. 1. An exploded view of the apparatus used in the preparation of enriched tungsten oxide

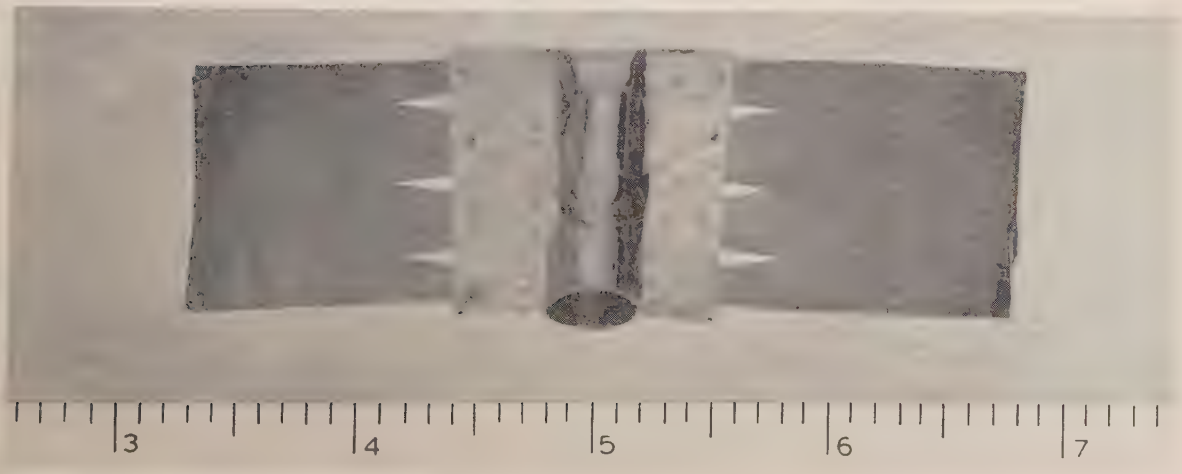

Fig. 2. Source used to evaporate tungsten oxide. (Scale in cm.)

caused remaining water vapour to be condensed. After isolating the reservoir from the chamber by means of the vacuum stopcock shown, air was admitted to the system. A mixture of WO_3 (yellowish-green), W_4O_{11} (violet) and WO_2 (deep brown)[4]) was formed, and removal of these oxides from the shields and top plate was accomplished by brushing with a soft clean brush.

3. Evaporation of Enriched Tungsten Oxide

Tungsten oxide has been successfully evaporated from a platinum boat (fig. 2). The boat consists of a centre section made from 0.003″ platinum sheet formed around a $\frac{1}{8}$″ diameter twist drill and welded along the seams. Current is conducted to the boat by two tantalum strips spot welded to the platinum. Platinum was chosen to prevent the oxide being reduced, a factor which makes the usual source materials such as tungsten, tantalum and molybdenum unsuitable. This design of boat furthermore affords a saving in evaporant, since it is quite directional. Evaporation of tungsten oxide proceeded satisfactorily in a vacuum of $\approx 10^{-5}$ torr at a temperature of $\approx 1200°C$. Typical values are, vacuum $\approx 10^{-5}$ torr, temperature 1200°C, distance of boat from target 9.8 cm, amount of material in boat 10 mg, density deposit 40 $\mu g/cm^2$.

Thin films up to 100 $\mu g/cm^2$ were produced by this method, the tungsten oxide being deposited on to self supporting carbon backings (5–10 $\mu g/cm^2$). The carbon backings were made by a technique developed by Bradley[5]).

Heavier ^{18}O targets (≈ 1 mg/cm^2) were made during the preparation of the enriched oxide by locating a suitably mounted carbon foil, or other convenient substrate, within the glass shield (b) fig. 1, thus permitting direct deposition of the $W\,^{18}O$ as it formed. Surplus tungsten oxide was collected from the shields as described previously. The reverse side of the substrate must be effectively shielded to avoid random deposition due to the relatively poor vacuum involved in this operation.

Carbon becomes deposited upon accelerator targets by the beam cracking residual hydrocarbon vapours, evolved from "O-rings", etc. Thus the use of carbon as a substrate material introduces no new undesirable element. Moreover, carbon foils are immensely strong, in view of the weight/area involved (5–10 μg-cm^2), are thermally insensitive and very pure chemically.

Acknowledgements

The authors would like to thank Mr. C. Parsons who prepared many of the targets.

[4]) C. J. Smithells, Tungsten, A Treatise on its Metallurgy, Properties and Applications, 3rd Edition (Chapman & Hall Ltd, London, 1952).

[5]) D. E. Bradley, Brit. Journal, Appl. Phys. **5** (1954) 55.

NUCLEAR INSTRUMENTS AND METHODS 12 (1961) 195–197; NORTH-HOLLAND PUBLISHING CO.

A STABLE 0.1% BEAM CURRENT INTEGRATOR FOR THE RANGE 0.1 TO 20 μA

G. J. F. LEGGE

Physics Department University of Melbourne

Received 10 March 1961

A beam current integrator is described which is stable against short term calibration drifts. It has an accuracy of 0.1% and is linear to the same degree from 0.1 μA to 20 μA, above which the calibration changes by 0.1% per 20 μA.

1. Introduction

The trend of present day low energy nuclear physics towards precision experiments involving good counting statistics has necessitated, at the same time, the use of accurate techniques of beam current integration. Several circuits have been designed for integrating beam currents to an accuracy of 0.1% or better[1]). However three faults have been prevalent amongst most such designs: some have been subject to drift and hence in need of frequent calibration, others are limited in their available current ranges, and a great number employ expensive equipment such as a vibrating reed electrometer. The following design then is an attempt at producing a beam current integrator which is stable against calibration drift, is accurate to 0.1% for beam currents of 0.1–20 μA, and at the same time is restricted to relatively inexpensive components.

The circuit employs the usual condenser, which is charged up by the beam current to a given reference voltage level, and then discharged completely in a time short compared to the charging time; whereupon the process repeats itself, providing an output pulse every time the condenser is discharged.

The stability is achieved by the use of diode valves, which have an inherently better triggering stability than the usual triode or multielectrode valves[2]). Thus stability is limited mainly by drift in the voltage reference source and in two trigger diodes, both of which are compensated for heater-cathode drifts.

Since, for 0.1% accuracy over the whole current range, it is necessary that the time for discharge never exceed $\frac{1}{1000}$ of the charging time, the discharge current must be at least 1000 times the maximum beam current used. In this instrument the 20 mA plate current of a 6AU6 valve is used to discharge the condenser at a uniform rate until a second trigger circuit cuts off the discharge as the voltage across the condenser passes through zero. The 6AU6 valve had the least leakage current, from plate to all other electrodes, of many that were tested under severe cut-off conditions. However even this tube is unsuitable for 0.1% accuracy below 1 μA beam current. In the final circuit the only valve pins connected to the condenser are the plates of three 6AL5 diodes.

2. Description of the Circuit

Current from the target is used to charge the 0.1 μF condenser C_1, which is a polystyrene type KTTE7125 manufactured by Jensen of Copenhagen. It has very low leakage and dielectric absorption. As the plate of the diode V_1a approaches 100 V, the resistive impedance of this valve decreases. Now the valves V_2 and V_3 constitute a fast trigger circuit whose feedback loop is formed by C_2, V_1a, and C_3. Therefore, at some definite voltage close to zero across V_1a, the feedback factor around the loop will exceed unity and the circuit will trigger. This will momentarily turn V_2 on hard and cut off V_3; the consequent large positive pulse appearing on the grid of V_4 will initiate discharge of

[1]) G. M. B. Bouricius and F. C. Shoemaker, Rev. Sci. Instr. 22 (1951) 183;
R. J. Helmer and A. Hemmendinger, Rev. Sci. Instr. 28 (1957) 649.

[2]) R. Kelner, J. W. Gray and B. Chance, Waveforms, M.I.T. Rad. Lab. Series, Ed. B. Chance *et al.* (McGraw-Hill, 1949) 77.

the condenser C_1 via valves V_4 and V_5. This will open the feedback loop at V_1a, but in the meantime a large positive pulse will have reached the grid of V_2 from the cathode of V_4. Thus the discharge is maintained by the DC feedback around the loop V_2, V_3, V_4; and although V_3 will again conduct on discharge of the condenser C_7, the gain of V_4 is kept low by forcing it to draw positive grid current through R_{12}. Thus the AC gain is insufficient to cause oscillation.

A second trigger circuit is necessary to stop the above discharge process when the voltage across the condenser C_1 reaches zero. The leakage current between heater and cathode of a diode is too great to permit the use of a normal trigger circuit, so the condenser is connected to the plate of the diode V_9a. This valve cannot conduct during the charging cycle, because its cathode is clamped above 100 V by the cathode follower valve V_8. However on triggering V_2, this clamp is released and the cathode of V_9a drops rapidly until it catches up on the steadily falling plate. The plate and cathode fall together until the plate of V_9a approaches zero, whereupon the plate of V_9b will start to conduct. The resultant negative pulse on the grid of V_{10} is amplified and used to turn V_{11} on hard; this momentarily drops the grid of V_4. The positive feedback then existing around the loop V_4, V_2, V_3 will drop the plate voltage on V_3. Consequently when the grid of V_4 rises again it will only attain its orginal state, wherein V_4 is cut off and so all feedback loops are open. The rise in voltage on the plate of V_2 will turn on V_8 which in turn cuts off both sides of V_9.

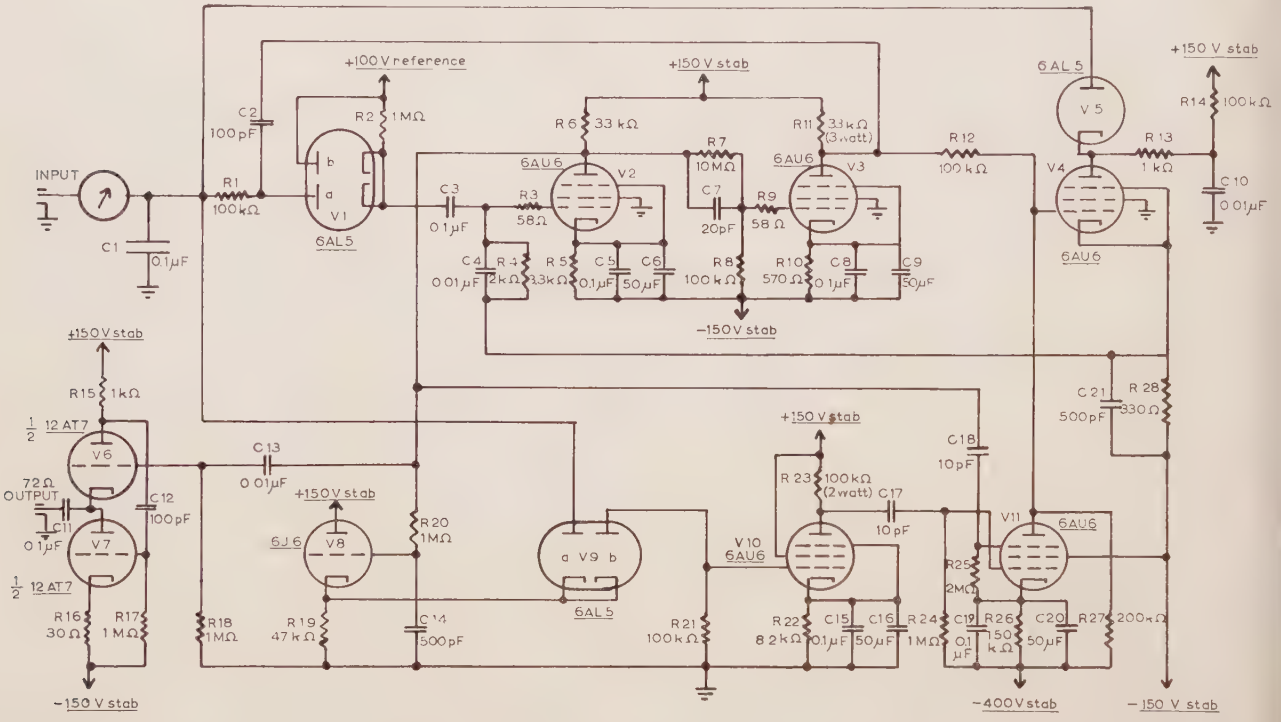

Because the initial drop in cathode potential at V_9 is able to feed through the plate to cathode capacity of V_9b, it is necessary to stop a resultant negative pulse from turning off the discharge. This is done by delaying the signal to V_8 by means of the integrating network of R_{20} and C_{14}, and at the same time putting a large negative signal on the suppressor of V_{11}. Thus by the time the spurious pulse has reached V_{11} this valve is cut off. The differentiating time of C_{18} and R_{25} is sufficiently short for V_{11} to conduct again before the switch-off pulse arrives.

The combinations R_4 and C_4, R_{28} and C_{21} were necessary to limit the high frequency gains of the various feedback loops, to prevent oscillation.

For beam currents above 1 μA, it is possible to

select a 6AU6 valve whose leakage is suitable (< 1 mμA) under the operating conditions of V_4, such that V_5 is not needed. However for currents less than this value the low leakage (< 0.1 m μA) of a selected 6AL5 diode is needed. The current drawn through R_{13} ensures that when V_4 is cut off the voltage on its plate will rise immediately to that on the top of C_{10}, thus cutting off V_5 with some certainty. As C_{10} charges up the cathode of V_5 rises so that it is always above the plate potential.

The critical parameter of V_1a is the slope of its characteristic, which is equivalent in practice to a critical current. V_1b is used solely to stabilize against drift of the characteristic with heater current. In the case of V_9 this is unnecessary because the common cathode of V_9a and V_9b automatically stabilizes the critical value of V_9a plate potential at which V_9b will commence conduction.

100 volt negative square pulses of duration 0.00 μ second (the discharge time) appear at the output of the White cathode follower formed by V_6 and V_7.

All incoming high and low tension lines are filtered for high frequencies. The three 6AL diodes, which were selected for low leakage, are supported in rubber grommets so as to eliminate base leakages. The total leakage current is about 0.1 m μA. The linearity and consistency of response were measured by recording the time between output pulses, as read on an electronic timer, for a measured constant DC input. The time between pulses for any given current is constant within 0.1% and the response is linear (i.e. constant value of counts/μC) to the same accuracy from 0.1 μA up to 20 μA. The drift in calibration of about 0.1% per week is attributable to drift in the reference voltage and a calibrating voltage source.

The circuit has no provision for maintaining the current collector at ground potential. Such a provision could be added, but is unnecessary if there is sufficient insulation and suppression of secondary electrons at the collector.

Acknowledgements

I would like to thank Professor Sir Leslie Martin, Associate Professor C. B. O. Mohr, Professor D. N. F. Dunbar and Dr. B. M. Spicer for their interest in this project.

NUCLEAR INSTRUMENTS AND METHODS 12 (1961) 198; NORTH-HOLLAND PUBLISHING CO.

LETTERS TO THE EDITOR

FURTHER COMMENTS ON ACCIDENTAL COINCIDENCES IN FAST-SLOW COINCIDENCE SYSTEMS

E. BROOKS SHERA†

Department of Physics, Western Reserve University, Cleveland, Ohio

Received 4 March 1961

In a recent article[1]), methods were presented for the determination of the accidental coincidence rate in two-fold fast-slow coincidence systems. In the analysis presented, recognition was made of the random coincidences resulting from a finite slow coincidence circuit resolving time. The chance rate was calculated on the basis of signals from one of the inputs of the slow coincidence circuit randomly coincident with correlated signals at the other two inputs, as well as uncorrelated signals at all three inputs. Such an analysis is appropriate to a simple three-fold coincidence circuit.

A two-fold fast-slow circuit cannot be treated in this manner since a signal from the fast coincidence circuit implies that events have occurred in both detectors and therefore this signal cannot be considered statistically independent of signals at the other two inputs. In the analysis of ref.[1]) for the fast-slow system, this tacit assumption of independence leads to the omission of a term due entirely to the finite resolving time of the fast coincidence circuit. The form of this term is

$$N^{12} = 2t_f N_1 N_2$$

where $2t_f$ is the resolving time of the fast coincidence circuit and N_1, N_2 are the counting rates from the amplitude selectors. This term, whose magnitude can be determined by inserting an appropriate delay in either input to the fast coincidence circuit, represents a major contribution to the actual random rate in most experiments.

When estimating the magnitudes of the remaining accidental terms, those derived by Mayer-Kuckuk and Nierhaus, the effect of dead times in the detectors and in the electronic circuitry before the slow coincidence circuit should not be neglected. These terms represent processes in which two successive events occur in the same detector within the resolving time of the slow coincidence circuit. If the detector or circuitry is inoperative for an interval following an event, the accidental counting rate from such processes will be correspondingly reduced. Indeed, if the dead time of the detectors is longer than the resolving time of the slow coincidence circuit, these processes contribute nothing to the random rate. Any attempt to measure the magnitude of these terms by inserting delays at the inputs to the slow coincidence circuit, thereby eliminating all real coincidences, disturbs the time relation between events which are counted as accidental coincidences. The effect of the dead times is thereby altered. Thus, random rates determined in this manner are not truly representative of normal operation of the system.

† Supported in part by the National Science Foundation and the Department of Defense through the U.S. Air Force Office of Scientific Research.

[1]) T. Mayer-Kuckuk and R. Nierhaus, Nucl. Instr. and Meth. 8 (1960) 76.

NUCLEAR INSTRUMENTS AND METHODS 12 (1961) 199–200; NORTH-HOLLAND PUBLISHING CO.

HIGHER ORDER EVENTS IN COINCIDENCE COUNTING

R. E. BELL

Radiation Laboratory, McGill University, Montreal

Received 12 April 1961

Recently in this journal, Paul[1]) has discussed "higher order chance coincidences in a fast-slow coincidence arrangement". It is our purpose to argue that these higher order events are not necessarily to be regarded as chance coincidences, that they are not a special property of fast-slow circuits, and that they can be largely eliminated in a simple way.

The most common of the events described by Paul is the second order one in which a fast coincidence, true or chance, is associated with a slow pulse in one channel that correctly enters its assigned pulse height range, and by a slow pulse in the other channel that does not. This latter pulse is promoted into effectiveness by the chance occurrence of another slow pulse that enters the pulse height range within the slow resolving time. Since there is no reason for the slow resolving time to be longer than the pulses being sorted by the slow pulse height selectors, this process scarcely differs from the ordinary pileup effect in which a chance slow pulse adds enough of its amplitude to the unsuitable pulse to make it suitable (or even subtracts, if positive pulses are followed by negative undershoots). In any case the result is that a previously rejected event is accepted owing to faulty pulse height selection in one channel (second order events) or both (third order events). (Paul argues that events of order higher than the third need not be considered.) Whether a higher order event is to be regarded as a true or a chance coincidence is properly decided, as always, by whether the original fast event was a true or a chance coincidence; experimentally there is no way of deciding for any one event. Paul omits consideration of the similar pileup process by which an originally acceptable pulse is promoted *out* of the acceptable range. Both kinds of higher-order processes will occur, the balance between them depending on circumstances. Paul's quantities ${}_3C''_t$ and ${}_3C''_r$, which we have just been discussing, may therefore be positive or negative.

The only thing wrong with the higher order events that are recorded is that they have faulty pulse height selection. The effect occurs in the slow channels and therefore is not a special property of fast-slow circuits; it occurs in ordinary coincidence circuits, and indeed in elementary single channel counting as well. We therefore argue that these events ought not to be classified as chance coincidences. They can be largely eliminated by an auxiliary circuit in each channel that rejects any coincidence event accompanied by closely spaced pulses in that channel. This "pileup detector" scheme, briefly described by Bell and Jørgensen[2]), accomplishes its result without appreciable change in counting rates or resolving times. The higher order events are also very much affected by the presence of dead times in the apparatus; Paul specifically excluded dead time effects from his treatment. Both these considerations show that the events discussed are not chance coincidences in the ordinary sense.

Paul writes the total observed coincidence rate (his equation (11) with one subscript omitted) as

$$C = C^{\mathrm{t}} + (C''_{\mathrm{t}} + C'''_{\mathrm{t}}) + (C' + C''_{\mathrm{r}} + C'''_{\mathrm{r}}) ,$$

where C^{t} is the ideal true coincidence rate, C''_{t} and C'''_{t} are true fast coincidences of wrong pulse height promoted into acceptance by second order and third order processes, C' is the ideal chance rate,

[1]) H. Paul, Nucl. Instr. and Meth. 9 (1960) 131.

[2]) R. E. Bell and M. Jørgensen, Can. J. Physics 38 (1960) 652.

and C_r'' and C_r''' are chance fast coincidences promoted by second and third order processes. Under the idealized conditions of Paul's discussion, a delay inserted in one fast channel allows us to observe $D = (C' + C_r'' + C_r'''$, as Paul points out. Thus one is left with $(C - D) = C^t + C_t'' + C_t'''$. We argue that in many cases this adequately represents the true coincidence rate of the experiment and no further measurements are necessary. On the other hand, the experimenter may need to know the precise extent to which wrong pulse heights are contributing to his results, or correct pulse heights are being excluded. This determination can be made on the slow pulse height selectors themselves, with the same "pileup time" (or resolving time) as in the main experiments. The effect will be seen as a slight smearing out at high counting rates of the sharply defined pulse height window seen at low counting rates. Paul's program for making an equivalent determination involves the results of seven different delay measurements, as well as the original measurement, and still leaves two other quantities to be measured before the final result is known (see his equation (34))†. In addition his result gives no idea of the distribution in true pulse height of the higher order events, and applies to a somewhat idealized case.

Many of the remarks made here apply also to an earlier and less detailed discussion by Mayer-Kuckuk and Nierhaus[3]).

† Paul's equation (33) should have a single minus sign in the middle of the right hand side, not a double minus sign. In his equation (34), the first term on the right should be ${}_3C$, not ${}_3C^t$.

[3]) T. Mayer-Kuckuk and R. Nierhaus, Nucl. Instr. and Meth. **8** (1960) 76.

NUCLEAR INSTRUMENTS AND METHODS **12** (1961) 201–202; NORTH-HOLLAND PUBLISHING CO.

PROPOSAL FOR A STORAGE RING FOR RELATIVISTIC CHARGED PARTICLES

R. EVANGELISTI and G. SACERDOTI

CNEN-Laboratori Nazionali di Frascati

Received 18 March 1961

A device suitable for storing charged particles, such as electrons or positrons, in a ring is proposed: the basic principle, believed to be new, follows.

In fig. 1 the diagram of the storage ring is shown: the ring is composed of two magnet sections and three RF cavities C_1, C_2 and C_3. The latter are tuned to a multiple of the particle revolution frequency, which depends only on the magnetic field due to the magnets.

It is easily seen that if:

$$I - n_1 = n_2 - I = a^2 < a^2_{\max}(\theta) \, .$$

1. The particle revolution is energy-independent.

2. The system has focusing properties as regards both vertical and horizontal oscillations.

3. Variations of the stable orbit radius depend on energy as

$$\frac{|y|}{R_0} = \frac{|\Delta E|}{E} \frac{I}{a^2} \, .$$

4. If a perturbation is introduced, changing the direction of particle velocity of $x_1 = \mathrm{d}y/\mathrm{d}\theta$, the variation ΔT of the revolution period is:

$$\Delta T = K x_1$$

(where K is a constant independent of θ, the azimuth of the perturbation).

5. due to perturbation x_1, the energy of the particle moving in a closed orbit intersecting the middle orbit at $\theta = \theta_1$, is:

$$E_0 + H(\theta_1)\, x_1$$

that is the particle energy is perturbed by a factor $H(\theta_1)x_1$.

The effect of the RF system is as follows:

a. the magnetic field of C_2 (due to the inherent gradient of the electric field) changes the direction of particle velocity.

b. the electric field of C_3 has an analogous effect.

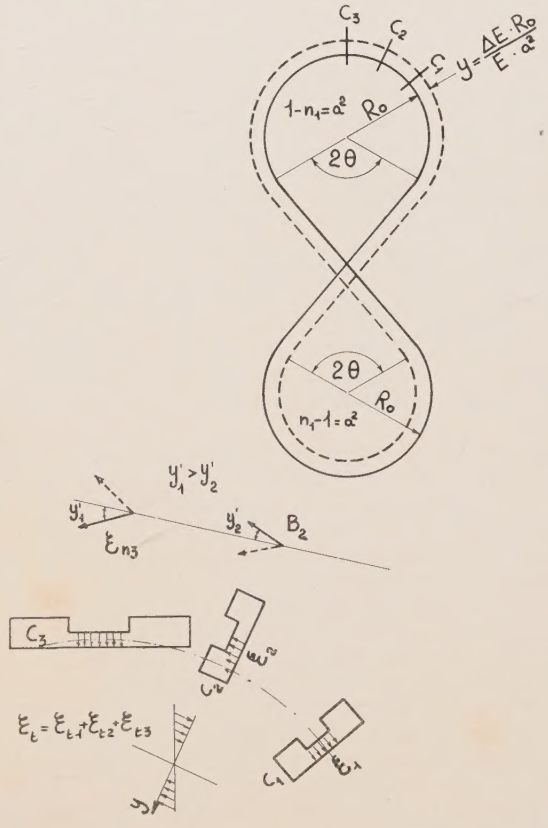

Fig. 1. Storage ring diagram.

c. the electric fields due to C_1, C_2 and C_3 change particle energy proportionally to the distance from the equilibrium orbit.

If C_3 is in the ring's magnetic field, it may be seen that, with a suitable choice of the amplitude and phase of the RF, the equations of motion become:

$$\frac{d\alpha}{dn} = -G_0^2 \sin\alpha$$

$$\frac{d(E - E_0)}{dn} = -(E - E_0 - \Delta E_1)\, G_1^2 \cos\alpha$$

$\Delta E_1 = H \sin\alpha$

n = number of turns.

One can see that:

$$E \to E_0 \quad \text{and} \quad \alpha \to 0 \qquad \text{for } n \to \infty .$$

It may be interesting to note that particles are influenced by a pseudo-Poynting vector $E_3 \times B_2$, which has a constant direction and versus. The particle trajectory is curved during interaction. An analogous situation exists when the particle radiates: also in this case the Poynting vector is in the direction of motion and particles are captured in the storage rings.

NUCLEAR INSTRUMENTS AND METHODS **12** (1961) 203–204; NORTH-HOLLAND PUBLISHING CO.

BOOK REVIEWS

ATOMIC ENERGY WASTE, ITS NATURE USE AND DISPOSAL, edited by E. Glueckauf. Butterworth & Co., London, and Interscience Publishers Inc., New York, 1961. xi + 420 pp. 95s.

The problem of how to deal with radioactive waste products has not earlier attracted so much interest compared to the importance of the matter. Every new book on the subject is therefore welcome. In this book a group of authors, mainly from the Harwell radiochemical group, present special articles, altogether giving a detailed description of the present status of this field. In spite of the title, the book is worth studying also by pure nuclear physicists. The first quarter of the book contains a clear presentation of the basic physical facts of radioactivity.

The book is divided into parts, each part containing one or more articles. The first part deals with fission and fission products with special attention to the alpha emitters. Part 2 contains articles on the important matter of radiation effects, on materials as well as on living organisms. In part 3, the legal aspects of the waste problem are presented. Part 4, which is the largest and also most important, deals with the operations involved in treatment of radioactive waste. Various methods are described and many references are given. It should be noted also that the experimental nuclear physicist in a university laboratory can learn many useful methods from this chapter. Fission products as sources of radiation are discussed in part 5. Finally, in part 6, industrial and agricultural use of radioactive isotopes are described.

All articles in the book contain very clear diagrams and tables, thus presenting the material in the most efficient way. As an example of the details included in the first part, one can mention that selection rules for beta- and gamma-transitions and tables of conversion coefficients are presented.

One minor critical remark: one cannot find anything about the known reactor accidents in the past years and what measures were taken on these occasions. Reactor accidents are of course not normal situations but once there, one does need some information about disposal of atomic waste.

Some minor misprinting does not change the impression that the book is more than worth reading by all reactor people and also by other nuclear physicists.

TORSTEN LINDQVIST

ADVANCES IN ELECTRONICS AND ELECTRON PHYSICS, Volume XII. Photo-Electronic Image Devices. Academic Press, New York and London, 1960.

The 1960 volume of this series of year-books, reviewing the allied field of electronics and electron physics, is entirely devoted to image tubes and related devices and contains the proceedings of a conference in this field held in London in September 1958. Two fields of research where the interest for image tubes is now abundant is nuclear physics and astronomy. In nuclear physics image tubes are used with luminescent particle-track chambers and a few papers in the book treat this application.

The astronomical application of photo-electronic image devices for study of weak images is based on the fact that the quantum efficiency of photocathodes is two orders of magnitude better than that of photographic plates. If all photoelectrons can be registered this means shorter exposure time for the same statistical accuracy (number of grains), which is essential for resolving objects from background fluctuations. Other objections to plates are saturation for large exposures and loss of sensitivity at low levels. One of the first papers describe A. Lallemand's original work which involved detecting the photoelectrons with nuclear plates in the same chamber as the photocathode. Later papers treat modifications of this arrangement. Then follow descriptions of image intensifiers using cascaded stages with luminescent screen-photocathode sandwiches, and of intensifiers using transmission type secondary emission multipliers and also tubes using electron multiplication in a large number of mechanically separated channels. Disturbances from thermionic and field emission are treated. Image tubes in nuclear physics are discussed in papers by P. E. Condon and A. Roberts and by M. Perl and L. Jones who in particular consider the regenerative image intensifier using optical feedback.

The remaining half of the book is devoted mainly to devices where information about the picture is gained by electronic scanning, as in television camera tubes. Papers treat the intensifier orthicon and the CPS emitron and their application for the study of weak, astronomical objects. The charge integration property of the latter tube is discussed and it is found that by cooling the tube data integration during several hours is possible. Next follow papers on simple photo-electronic storage tubes which use optical scanning and on camera tubes specially designed for integrating and storing weak images. Two papers treat the theory of signal-to-noise in the different television camera tubes, with application to image storage. In later papers the use of image tubes for investigation of diffraction patterns and for study of weak patterns in electron microscopes are discussed. One paper describes a camera tube for studying infrared images and in four papers X-ray image intensifying systems for medical applications are discussed.

The book gives detailed information about image devices, the technique of using them and also about tube construction. Unfortunately solid state image intensifiers are not included. The papers in the book are well coordinated. Perhaps it could be remarked that the kind of review articles which have made up the volumes of previous years necessarily give a more condensed and uniform treatment of a subject.

P. A. TOVE

NUCLEAR REACTOR CONTAINMENT BUILDINGS AND PRESSURE VESSELS (Proceedings of International Symposium at the Royal College of Science and Technology, Glasgow), ed. A. S. Thomson *et al.* Butterworths, London, 1960. viii + 572 pp. some 250 figs. 100 s.

The first Symposium on Nuclear Reactor Containment Buildings and Pressure Vessels was held at Glasgow from 17th to 20th May, 1960. The subject touches on many faculties of science and technology, but the main stress was this time put on containment philosophy, design and construction of steel containment shells and pressure vessels.

The contributions have been divided into six sections—introductory reviews, design studies and stress analysis, shell research, construction and testing, open topics, and summaries from different viewpoints. The problems treated are understandably centered upon conditions and practice in the United Kingdom and mostly seen from the standpoint of the design and construction engineer. The relative merits of concrete and steel as materials for containment buildings are treated, concrete being viewed with a probably justified scepticism. The outlook for concrete may be somewhat brighter, though, if the described method of controlled release to the outer atmosphere is used instead of containment (at an inner overpressure) of fission products after a hypothetical accident. The need for a U.K. code of practice is discussed in several papers, and the difficulties in formulating such a code is very evident.

Most of the book must interest the designer, but especially the first section, the excellent summaries in the last and the description of test procedures in the fourth section has much to give all those concerned with reactor operation and safety. One could wish that there had been still another section discussing containment buildings and pressure vessels in their functions as links in a chain of safety arrangements, contrasted against the risks they are to protect against.

STIG O. W. BERGSTRÖM

DIRECTORY OF NUCLEAR REACTORS, Vol. III; RESEARCH, TEST AND EXPERIMENTAL REACTORS (Supplement to Vol. II). 354 pages (International Atomic Energy Agency, IAEA, Vienna 1960) U.S. $4, 24 s.

The third volume of IAEA's reactor directory is a continuation of the second one and contains data of about one hundred research, test and experimental reactors. Information is compiled and the reactors are grouped in the same way as in the previous two volumes.

Among the reactors to be found in this volume can be mentioned the Borax family, the Russian IRT swimming pool oxide fuel reactor series, the nineteen American AGN low power solid homogenous reactors and the PRTR reactor experiment. Some reactors are still missing e.g. HWCTR and Dragon.

It is noticed with satisfaction that heat fluxes in this volume throughout are reported both in W/cm^2 and Btu/ft^2hr. The dates of information of the reactors are in most cases from 1960, and the directory is accordingly quite up to date.

IAES's reactor directory meets in a successfull way the need for easily available information about reactors of different types. It is hoped that the intention to issue further supplements will be carried through.

MATTS STRÅÅT